Université de Montréal

Mechanical Simulation of the Endovascular Repair of Abdominal Aortic Aneurysms

par David ROY

Institut du Génie Biomédical, Faculté de Médecine

Thèse présentée à la Faculté de Médecine en vue de
l'obtention du grade de Docteur en Génie Biomédical

novembre, 2014

Membres du jury

Président-rapporteur:

Carl-Éric Aubin	Professeur, École Polytechnique de Montréal

Directeur:

Gilles Soulez	Professeur, Université de Montréal, CR-CHUM

Co-directeur:

Claude Kauffmann	Chercheur, Université de Montréal, CR-CHUM

Membre de jury:

Natalia Nuño	Professeure, École de technologie supérieure de Montréal

Membre externe:

Elena Di Martino	Professeure, Université de Calgary

Représentant de la doyenne de la Faculté:

Éric Thorin	Chercheur, Institut de cardiologie de Montréal

"Life smiles to audacious ones."
Alexander the Great

"Il n'y a que les missions impossibles qui réussissent."
Commandant Jacques-Yves Cousteau

"Wennschon, dennschon!"

To my uncle and my father who suffered from aneurysms.

Résumé

Ce travail de thèse porte sur la simulation du déploiement des prothèses vasculaires de type stent-graft (SG) lors de la réparation endovasculaire (EVAR) des anévrismes de l'aorte abdominale (AAA). Cette étude se présente en trois parties: (i) tests mécaniques en flexion et compression de SG couramment utilisés (corps et jambage de marque Cook) ainsi que la simulation numérique desdits tests, (ii) développement d'un modèle numérique d'anévrisme, (iii) stratégie de simulation du déploiement des SG.

La méthode numérique employée est celle des éléments finis. Dans un premier temps, une vérification du modèle éléments finis (MEF) des SG est realisée par comparaison des différents cas de charge avec leur pendant expérimental. Ensuite, le MEF vasculaire (AAA) est lui aussi vérifié lors d'une comparaison des niveaux de contraintes maximales principales dans la paroi avec des valeurs de la littérature. Enfin, le déploiement est abordé tout en intégrant les cathéters.

Les tests mécaniques menés sur les SG ont été simulés avec une différence maximale de 5,93%, tout en tenant compte de la pré-charge des stents. Le MEF de la structure vasculaire a montré des contraintes maximales principales éloignées de 4,41% par rapport à un modèle similaire précédemment publié. Quant à la simulation du déploiement, un jeu complet de SG a pu être déployé avec un bon contrôle de la position relative et globale, dans un AAA spécifique pré-déformé, sans toutefois inclure de thrombus intra-luminal (TIL). La paroi du AAA a été modélisée avec une loi de comportement isotropique hyperélastique.

Étant donné que la différence maximale tolérée en milieu clinique entre réalité et simulation est de 5%, notre approche semble acceptable et pourrait donner suite à de futurs développements. Cela dit, le petit nombre de SG testés justifie pleinement une vaste campagne de tests mécaniques et simulations supplémentaires à des fins de validation.

Key words: anévrisme, aorte, abdominale, stent-graft, déploiement, simulation.

Abstract

This thesis work is concerned with the simulation of the deployment of stent-graft (SG) vascular prostheses in abdominal aortic aneurysms (AAA) during endovascular repair (EVAR). This study is composed of three main parts: (i) mechanical tests in bending and compression of frequently used SG (body and leg from Cook) as well as the numerical simulation of these tests, (ii) development of a numerical AAA model, (iii) strategy of simulation of SG deployment.

The finite element method is used. In a first step, a verification of the finite element model (FEM) of SG is performed by comparison of the different load cases with their experimental counterparts. Subsequently, the vascular FEM is also verified in terms of maximal principal constraints in the wall against values available in the literature. Finally, the deployment is investigated while taking the catheters into account.

The mechanical tests performed on the SG were simulated with a maximal difference of 5.93%, while accounting for the pre-load in stents. The FEM of the vascular structure showed maximal principal stresses that were 4.41% far from the ones found in the literature for a similar model. Regarding the simulation of SG deployment, a complete set of SG could be deployed with a good control of the relative and global position into a specific and pre-deformed AAA, however, no intra-luminal thrombus (ILT) was included. The AAA wall was modeled with an isotropic hyperelastic constitutive law.

In the clinical setting, the maximum tolerated difference between reality and simulation is 5%, therefore, our approach seems acceptable, and could give rise to further developments. However, the small amount of tested SG justifies a wide campaign of additional mechanical tests and simulations for the sake of validation.

Key words: aneurysms, aorta, abdominal, stent-graft, deployment, simulation.

Acknowledgements

I owe my father the very first feeling of gratitude, because while I was involved in this thesis I couldn't see him before he died. And because, thank to his inheritance, I could finish this work.

I need to deeply thank my director of research, Dr. Gilles Soulez, who gave me a chance to make come true my wish, in addition to his support in every aspect.

I also want to express my grateful thanks to my co-director of research, Dr. Claude Kauffmann, for his constant focus on the right questions, before looking for any reply.

Many people, directly and indirectly, from the lab and from far away, gave me their support and good thoughts. They all deserve a special place in my heart for what they offered.

My sincere and full consideration goes to Catherine McDonald for establishing beyond the veil this wonderful link with my loved ones. And God bless them for their guidance and true love.

Last, but not least, I would like to thank my co-worker, Florian, for his patient initiation to linux, and for bringing a relaxed and free mindset.

The financial support from Fonds de Recherche du Québec Santé (grant FRQ-S 20241) is gratefully acknowledged.

List of acronyms

AAA	abdominal aortic aneurysm
AA	abdominal aorta
BC	boundary condition
B-SG	body stent-graft
DD	delivery device
DOF	degree of freedom
EVAR	endovascular repair
FE	finite element
FEA	finite element analysis
FEM	finite element method
FSS	flow shear stresses
HGO	Holzapfel-Gasser-Ogden
ID	inner diameter
ILT	intraluminal thrombus
L-SG	leg stent-graft
OD	outer diameter
PS	patient-specific
SEDF	strain energy density function

SG	stent-graft
SI	système international
VMTK	vascular modeling toolkit
VSMC	vascular smooth muscle cells
ZPG	zero pressure geometry

List of symbols

D	Bulk modulus related parameter in HGO strain energy density function for AAA
D_1	Bulk modulus related parameter in Ogden strain energy density function for ILT
E_{316L}	Stainless steel 316L Young's modulus
$E_{G\theta}$	Nominal graft Young's modulus along the stent-graft circumferential direction
E_{Gz}	Nominal graft Young's modulus along the stent-graft axial direction
E_{NiTi}	Nitinol Young's modulus (linear behavior)
E_{pre}	Young's moduli accounting for pre-tension in stents
$G_{Gz\theta}$	Nominal graft shear modulus in $z\theta$ plane
G_{Gzr}	Nominal graft shear modulus in zr plane
$G_{G\theta r}$	Nominal graft shear modulus in θr plane
J	Jacobian determinant characterizing the volumetric variation
K	Bulk modulus
$K_{G\theta\theta}$	Transverse shear stiffness related to $\tilde{G}_{G\theta r}$
$K_{Gz\theta}$	Transverse shear stiffness in $z\theta$ plane
K_{Gzz}	Transverse shear stiffness related to $\tilde{G}_{Gzr}$
U	Strain energy density function
α	Angle made by the families of collagen fibers with the circumferential direction
α_1	Exponent in Ogden strain energy density function for ILT

$\bar{I}_1$	First invariant of the deviatoric part of the right Cauchy-Green tensor
$\bar{I}_{4(11)}$	Fourth invariant of the deviatoric part of the right Cauchy-Green tensor
$\bar{I}_{4(22)}$	Sixth invariant of the deviatoric part of the right Cauchy-Green tensor
$\boldsymbol{\sigma}$	Cauchy stress tensor
$\gamma_{z\theta}$	Graft in-plane shear angle
λ	Mechanical stretch
μ_1	Shear modulus in Ogden strain energy density function for ILT
ν_{316L}	Stainless steel 316L Poisson ratio
$\nu_{Gz\theta}$	Graft Poisson's ratio with a stretch along the stent-graft axial direction
$\nu_{G\theta z}$	Graft Poisson's ratio with a stretch along the stent-graft circumferential direction
ν_{NiTi}	Nitinol Poisson's ratio
ρ_{316L}	Stainless steel 316L density
ρ_{NiTi}	Nitinol density
$\tau_{z\theta}$	Graft in-plane shear stress
$\mathbf{A}_i$	Orientation of the families of collagen fibers ($i = 1, 2$)
$\mathbf{B}$	Left Cauchy-Green tensor
$\mathbf{C}$	Right Cauchy-Green tensor
$\mathbf{E}$	Green-Lagrange strain tensor
$\mathbf{F}$	Deformation gradient tensor
$\mathbf{I}$	Identity matrix
$\mathbf{S}$	Second Piola-Kirchhoff stress tensor
$\mathbf{X}$	Reference (undeformed) configuration
$\mathbf{x}$	Current (deformed) configuration

$\tilde{E}_{G\theta}$ Graft Young's modulus along the stent-graft circumferential direction (affected by thickness reduction)

$\tilde{E}_{Gz}$ Graft Young's modulus along the stent-graft axial direction (affected by thickness reduction)

$\tilde{G}_{Gzr}$ Graft shear modulus in zr plane (affected by thickness reduction)

$\tilde{G}_{G\theta r}$ Graft shear modulus in θr plane (affected by thickness reduction)

$\tilde{\rho}_G$ Graft density (affected by thickness reduction)

$\tilde{t}$ Graft current thickness (affected by thickness reduction)

t_0 Graft thickness at rest

c $\cos\alpha$, α being the orientation of collagen fibers with regard to the circumferential direction

Contents

General introduction

Abdominal aortic aneurysms, as dilations of the infra-renal aorta (Figure 1), represent a life threatening illness. Indeed, AAA rupture leads to serious complications and death in more than 50% of the cases. AAA rupture was identified as the 13^{th} leading cause of death in the USA in 2005 for Caucasians between 60 and 85 (Sakalihasan et al., 2005). The origins (and development) of this abnormal condition still remain uncertain, however, there is a strong correlation with the following factors: smoking habits, hypertension, family history, foods rich in lipids, sedentary lifestyle.

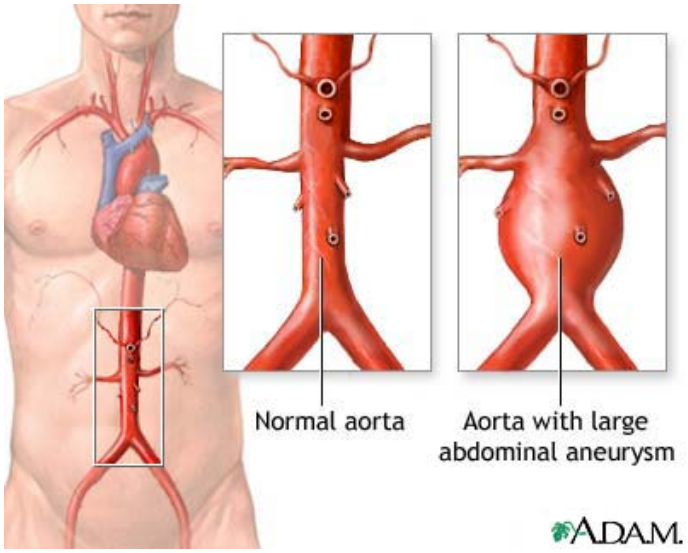

Figure 1: Illustration of an healthy aorta and a typical abdominal aortic aneurysm (A.D.A.M. document, available online: http://www.ncbi.nlm.nih.gov, consulted on 2014-12-27).

Clinicians recommend surgical intervention when the maximal diameter is 55 mm (the mean diameter of healthy abdominal aortas being 20 mm) and when the growth rate is over 5 mm every 6 months (Greenhalgh and Powell, 2008).

Usually, AAA are treated with an "open" surgery in which a vascular prosthesis (tubular

surgical tissue or *graft*) is stitched directly on the vessel (Figure 2). Such a prosthesis excludes the aneurysmal sac from blood pressure, thus limiting the rupture risk.

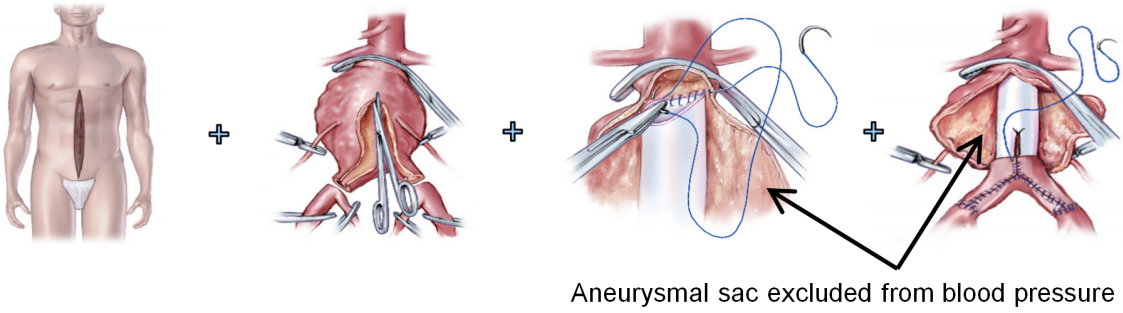

Figure 2: Open surgery of Abdominal Aortic Aneurysms (Amblard, 2006).

The endovascular repair of AAA as a less invasive alternative was first introduced by Dr. Parodi in 1992 for patients who cannot undergo the classic open surgery without a significant risk of mortality and morbidity. The technique consists in guiding stent-grafts (SG) in a percutaneous mode via catheters introduced in the femoral artery (groin area), up to the diseased area where these SG are deployed by removing the sheath that keeps them compressed and constrained against the catheters (Figure 3).

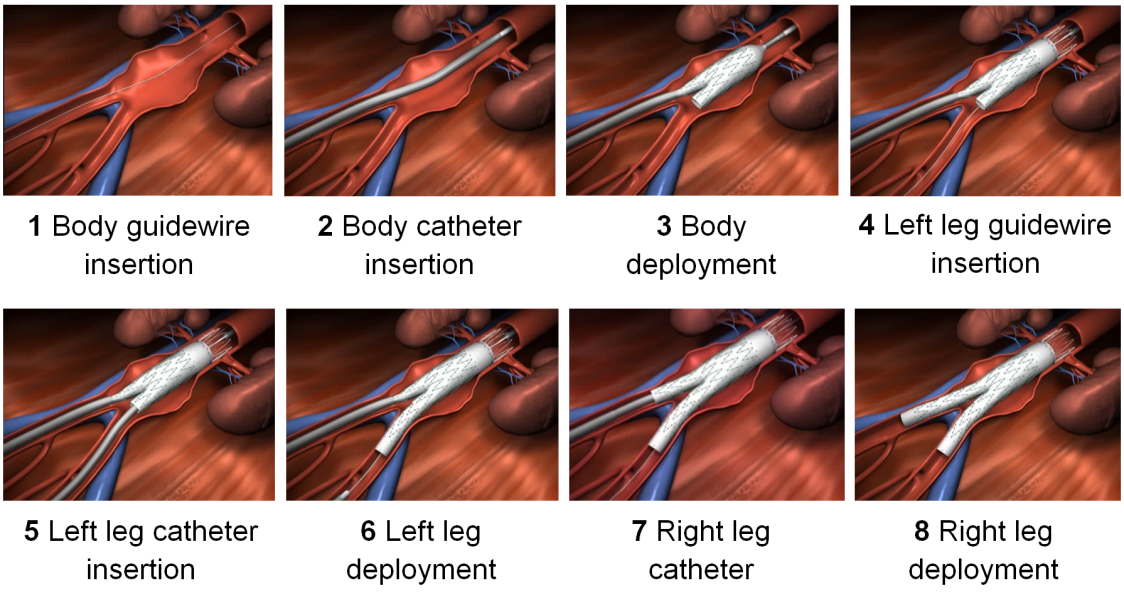

Figure 3: Endovascular repair of Abdominal Aortic Aneurysms (Cook document, available online: http://www.youtube.com/watch?v=ZC_afpYTRxw, consulted on 2014-05-20).

In fact, the proximal and distal sections of SG must be deployed on healthy regions to

avoid type I endoleaks, i.e. when the blood flows back into the aneurysmal sac, making its path between the proximal and distal sections of the SG and vessel wall.

A SG is a graft surrounded by metallic spring-like supports called *stents*, and the actual prosthesis is a set of several SG, typically a body, and two legs extending in the iliac arteries after the aortic bifurcation. This is depicted in figure 3, where the body is first deployed below the renal arteries (steps 1 to 3), followed by the left leg (steps 4 to 6) and finally the right leg (steps 7 to 8). The assembly of a SG and its corresponding catheter is called *delivery device* (DD).

The open surgery, though invasive, ensures better results on the long term whereas endovascular repair (EVAR), despite considerable improvements since 1992, still implicates a regular follow-up and might lead to complications such as endoleaks (Figure 4), obstruction and kinking (SG collapse and section area reduction).

Currently, SG sizing and selection are based on 3D reformations of contrast-enhanced CT scanners. The luminal centerlines of the aorta and iliac arteries are first extracted. On these centerlines, the operator can define manually the diameter and length of the SG components to ensure a significant coverage of the aneurysm, while avoiding occlusion of side arteries (renal, internal iliac). It is essential to obtain an adequate sealing at the proximal and distal landing zones by applying a systematic over sizing of the SG (10 to 15% in diameter).

In order to better select SG in standard catalogues for a given patient and predict the potential complications above mentioned, simulations of SG implantation can be performed with the necessary level of accuracy. This is especially useful in the case of tortuous vascular geometries, with narrowed iliac arteries and in presence of calcifications, because the geometric planning alone is not enough to anticipate the final position of the whole prosthesis in such particular and complex configurations. In any case, the iliac arteries undergo large deformations once the catheters are inserted.

Aside from the development of *intervention planning* tools, simulations may serve to improve the design of future SG (reducing fatigue failures, endoleaks and kinking) as well as assessing vessel peak stresses. Also, numerical analyses could be used for training purposes, i.e., to teach residents/fellows the consequences of implanting specific SG in a given patient.

Only a few studies (De Bock et al., 2012; Demanget et al., 2013) have addressed to some extent the complex simulation of SG deployment, however, only a single leg or body were virtually implanted, as opposed to a typical set of a body and two legs. In addition these studies were performed with quite simple geometries while in reality AAA are often

significantly tortuous, and important boundary conditions such as the spine, internal iliac arteries and surrounding organs were not taken into account. Therefore, it can be stated that the simulation of SG deployment is just developing and many improvements still need to be accomplished before any transfer to the clinical routine.

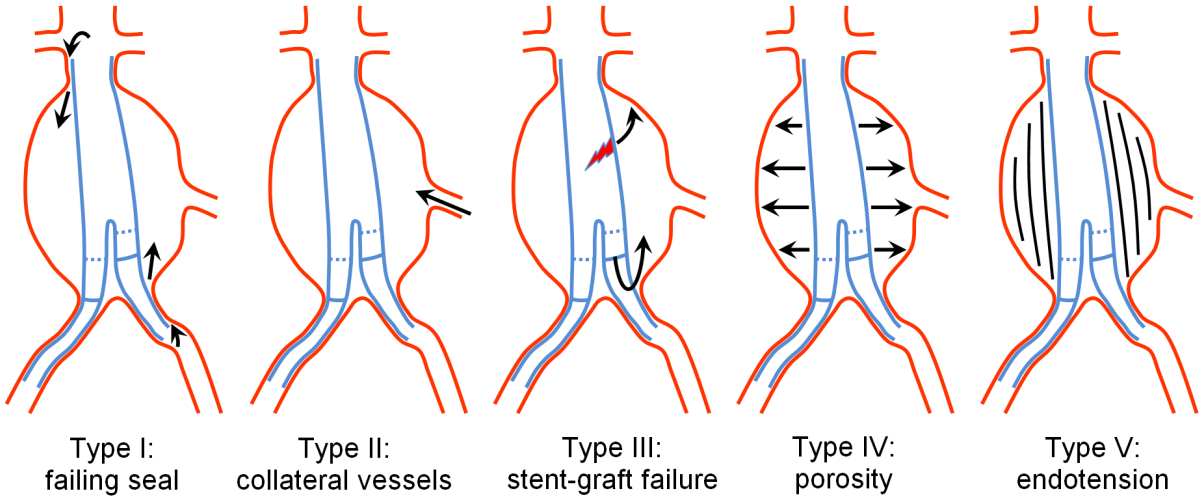

Figure 4: Types of endoleak.

This thesis has 3 parts (Figure 5) and 5 chapters.

Part I presents the finite element modeling of SG and an experimental verification. A comparison is performed between the experimental and numerical results. Python scripts reproducing the most used SG from the Cook catalogue are described.

Part II explains the development of the AAA numerical model, i.e. its geometrical reconstruction from medical imaging segmentations along with a spine representation, the elaboration of an anisotropic hyperelastic model with adapted parameters for the Holzapfel-Gasser-Ogden (HGO) model implemented in the finite element analysis (FEA) software Abaqus (SIMULIA, Providence RI, USA), and finally a Python script that generates a fully defined AAA finite element model (FEM) in terms of geometry, materials and boundary conditions.

Part III depicts a new strategy to simulate the deployment of SG in AAA. The methodology to simulate a SG deployment into a pre-deformed vessel is presented. Finally, a plug-in is proposed to automatize the developed workflow.

To conclude this research, the following recommendations can be formulated

- The vessel can be approximated with shell elements to improve the numerical efficiency

of the model (shorter time resolution).

- Accounting for the pre-deformed configuration of the vessel due to the presence of catheters not only makes the subsequent deployment simulation closer to the clinical reality, but also reduces the distortion in the elements representing the graft. Including this pre-deformed configuration might be of special relevance when considering highly tortuous geometries, because the final solution at equilibrium may be different from a deployment in the geometry corresponding to the original CT-scan.

- The pre-tension in stent-grafts can be approximated by specifically increasing the Young's modulus of the different stents.

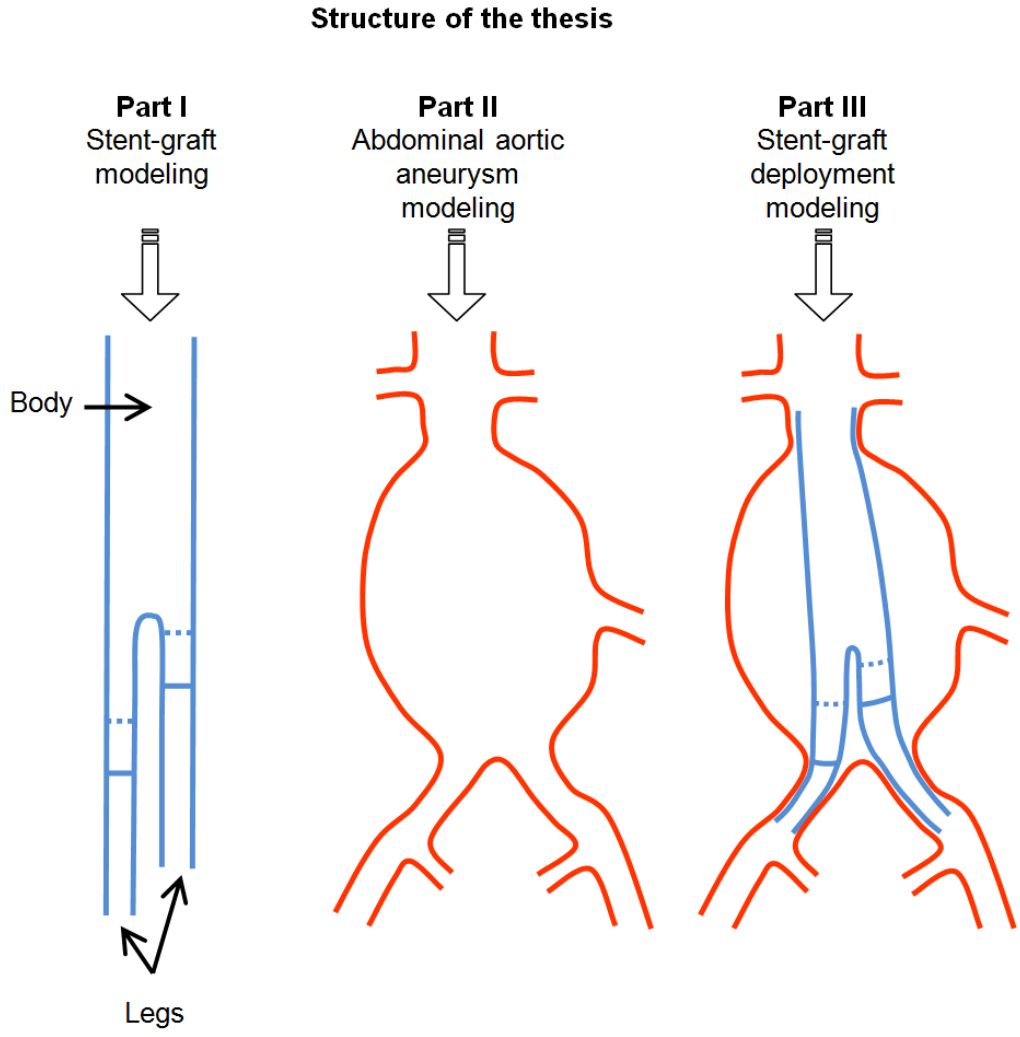

Figure 5: Development in each part of the thesis.

Literature review

Stent-graft simulation

In the early studies involving SG, the ones were modeled as continuous tubular shapes having equivalent linear elastic mechanical properties, i.e. $E_{eq} = 5$ to $15\,\text{MPa}$ and $\nu_{eq} = 0.27$, and $E_{eq} = 50\,\text{MPa}$ and $\nu_{eq} = 0.45$ (Li and Kleinstreuer, 2005b; Amblard et al., 2009).

However, this simplified modeling has a serious limitation when an accurate mechanical response is needed to predict the complications related to EVAR. Indeed, the spring-like mechanical behavior of slender stents cannot be faithfully represented with a continuous medium such as a tubular surface. This is why more detailed SG models were introduced, in particular by Capelli et al. (2010), and Demanget et al. (2012a) (Figure 6).

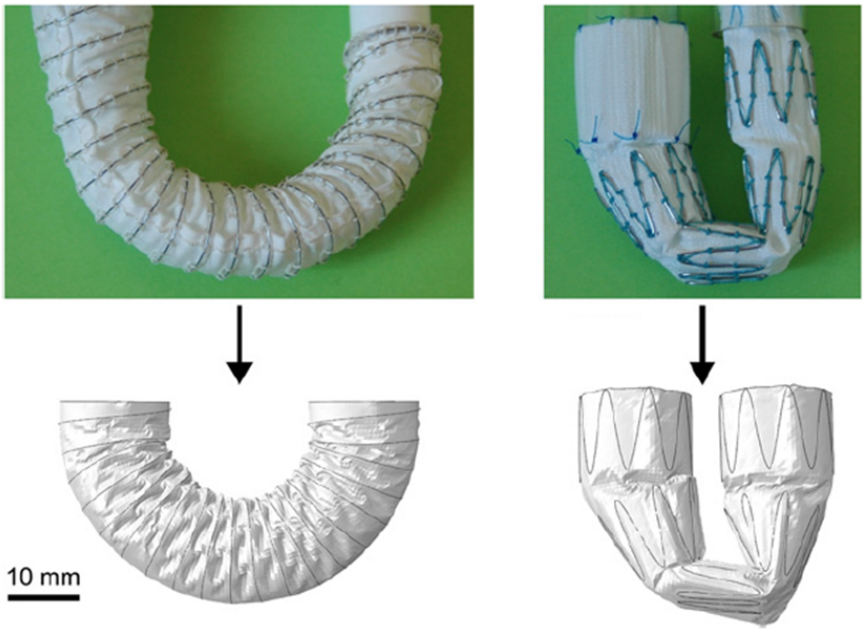

Figure 6: First realistic simulation of leg stent-grafts undergoing a pure bending (Demanget et al., 2012a). Reproduced with the permission of Elsevier.

Later on, this advanced model was validated with experimental tests, as can be seen in Figure 7.

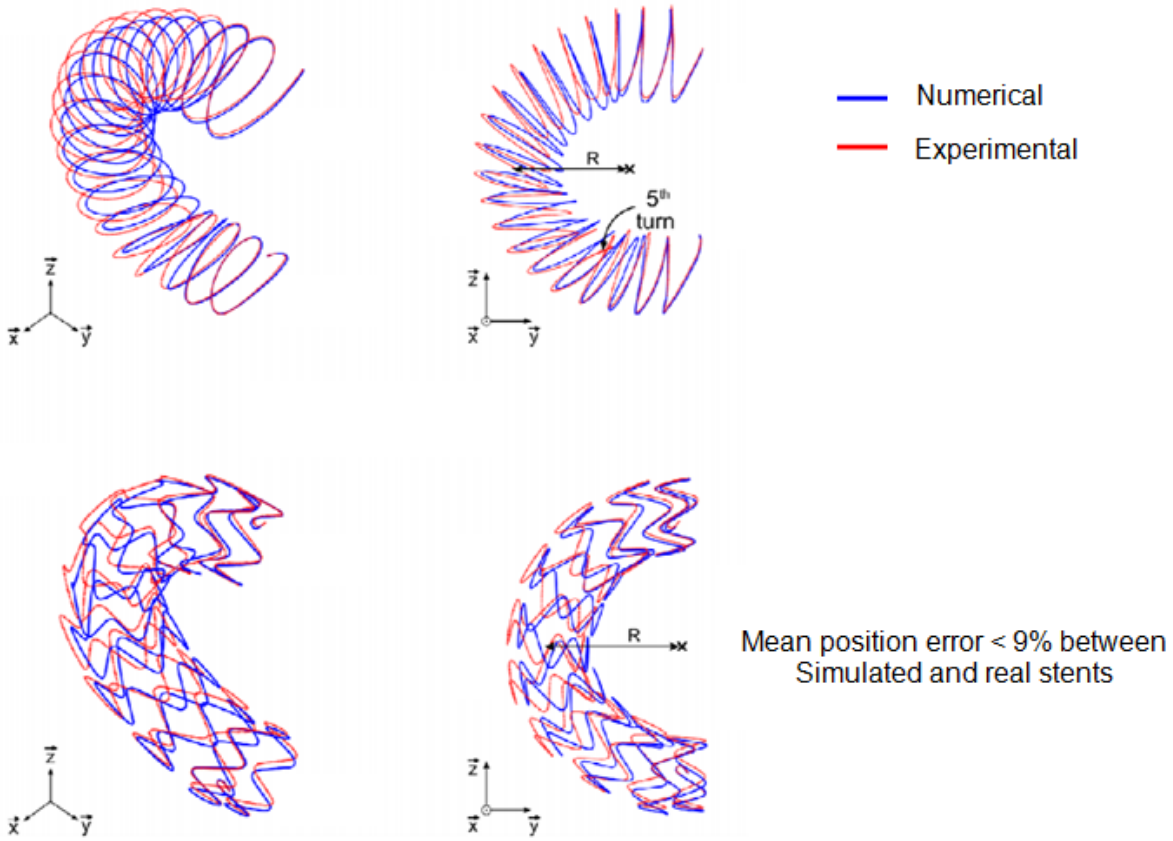

Figure 7: Experimental validation of stent-graft simulation (Demanget et al., 2012b). Reproduced with the permission of Elsevier.

These models included the graft and stents as separate entities with well distinguished finite element modeling (shell and beam elements respectively), different mechanical properties and contact to simulate their attachment via sutures. Nonetheless, the fact that the stents expand radially upon removal from the prosthesis, thus their inherent pre-tension, has not been addressed yet in the current literature.

The latter concept of pre-tension in SG is important to incorporate in advanced SG modeling in order to faithfully reproduce the radial stiffness. Eventually, this would allow to better predict endoleaks once such SG models will be introduced in soft arteries in more complex simulations.

Also, a strategy based on CT-scans (X-Ray) to rebuild the geometry of any SG coming from different commercial brands (Cook Medical, Medtronic, Cordis, etc.) was introduced

by Demanget et al. (2012b). Indeed, the shape of the stents can clearly be identified in 3D because of their high density, which allows an easy geometric segmentation and finite element discretization. The graft can then be simply added as a tubular surface matching the position of each stent.

Simulation of abdominal aortic aneurysms

In a first and rough approximation, the arterial wall can simply be modeled with a linear elastic material. In particular Kaladji et al. (2013) recently used equivalent Young's moduli of 2 MPa, 5 MPa and 10 MPa to implement minimally calcified, calcified and highly calcified arteries respectively. With regard to calcifications, Marra et al. (2006) provided significant details in terms of composition, morphology and mechanical properties.

However, the AAA being constituted by soft tissues, among which bundles of collagen fibers, exhibits a strong non-linear mechanical behavior characterized by exponential-like stress-strain curves. These tissues offer an increasing resistance while the bundles of collagen fiber are progressively taut. A pioneering experimental study (uniaxial tensile tests) of the this behavior was presented by Raghavan et al. (1996), with an isotropic interpretation since the circumferential and longitudinal stiffnesses were deemed similar at that time. Moreover, based on these results, Raghavan and Vorp (2000) later derived a strain energy density function, or hyperelastic constitutive law.

More recently, Vande Geest et al. (2006) demonstrated the potential strong anisotropic response of AAA, from biaxial tests performed on specimen samples given by 26 donors. And several anisotropic hyperelastic constitutive laws were then devised from these outcomes, by means of multiple non-linear regressions (Rodríguez et al., 2008; Basciano and Kleinstreuer, 2009; Xenos et al., 2010). This said, anisotropic hyperelastic models imply an accurate knowledge of the orientation of collagen fibers for a given patient, which is not the case from CT-scans. For this reason Humphrey and Holzapfel (2012) warned against using blindly these constitutive laws. Humphrey and Holzapfel (2012) also stressed the current lack of accuracy in defining non-invasively the distribution of the thickness wall.

Viscoelasticity in AAA wall modeling can be neglected because the aorta is a proximal artery (with regard to the heart), with a large diameter and less vascular smooth muscle cells in the media layer. In contrast, medium-size arteries such as femoral and cerebral are considered viscoelastic (Holzapfel and Ogden, 2003).

Another important part of AAA is the intraluminal thrombus. Its mechanical properties were first interpreted as linear elastic with a Young's modulus of 0.11 MPa and a Poisson's

ratio of 0.45 (Di Martino et al., 2001), and then as isotropic hyperelastic (Gasser et al., 2008). These relatively simplified models led some authors to overestimate the ILT "protective" effect, and conclude that *Von Mises* stresses in the vessel wall were reduced up to 40% (Van Dam et al., 2008). However, it was shown clinically that the pressure was often almost constant throughout the ILT structure (Schurink et al., 2000), which indicates a porous nature. Such a porosity was modeled by Toungara (2011).

SG deployment simulation

The simulation of SG deployment is quite complex because of large deformations and elaborated kinematics, and it's only recently that a few preliminary studies could be completed.

First of all, De Bock et al. (2012) could simulate the deployment of a body only, and in a straightforward geometry, which outcome was in good agreement with a soft vascular phantom made of silicone. Also, Demanget et al. (2013) could simulate the deployment of a leg only in a tortuous iliac artery, but the author mentioned significant difficulties due to distortion in the graft elements that had to be both compressed and bent along the delivery device or catheter (Demanget, 2012).

Therefore, until recently, there was no relatively complete simulation, i.e. including at least the three components of the prosthesis (one body and two legs).

Nonetheless, Bock (2014) wrote a book published by the University of Gent (no peer-review) in which quite a complete model was presented. The ILT and calcifications were included. But no pre-load was modeled, neither to simulate the blood pressure nor to approximate the pre-tension in stents. And most importantly, the pre-deformed configuration of the AAA was not modeled (Figure 8).

Accounting for the pre-deformed configuration of the AAA prior to simulate any SG deployment, might be of paramount importance to provide a solution that is closer to the clinical reality, as noted by Demanget (2012). This might also lead to a different final equilibrium, especially in the case of tortuous geometries, like the one presented by Demanget et al. (2012a) (Figure 9), hence the interest of performing simulations.

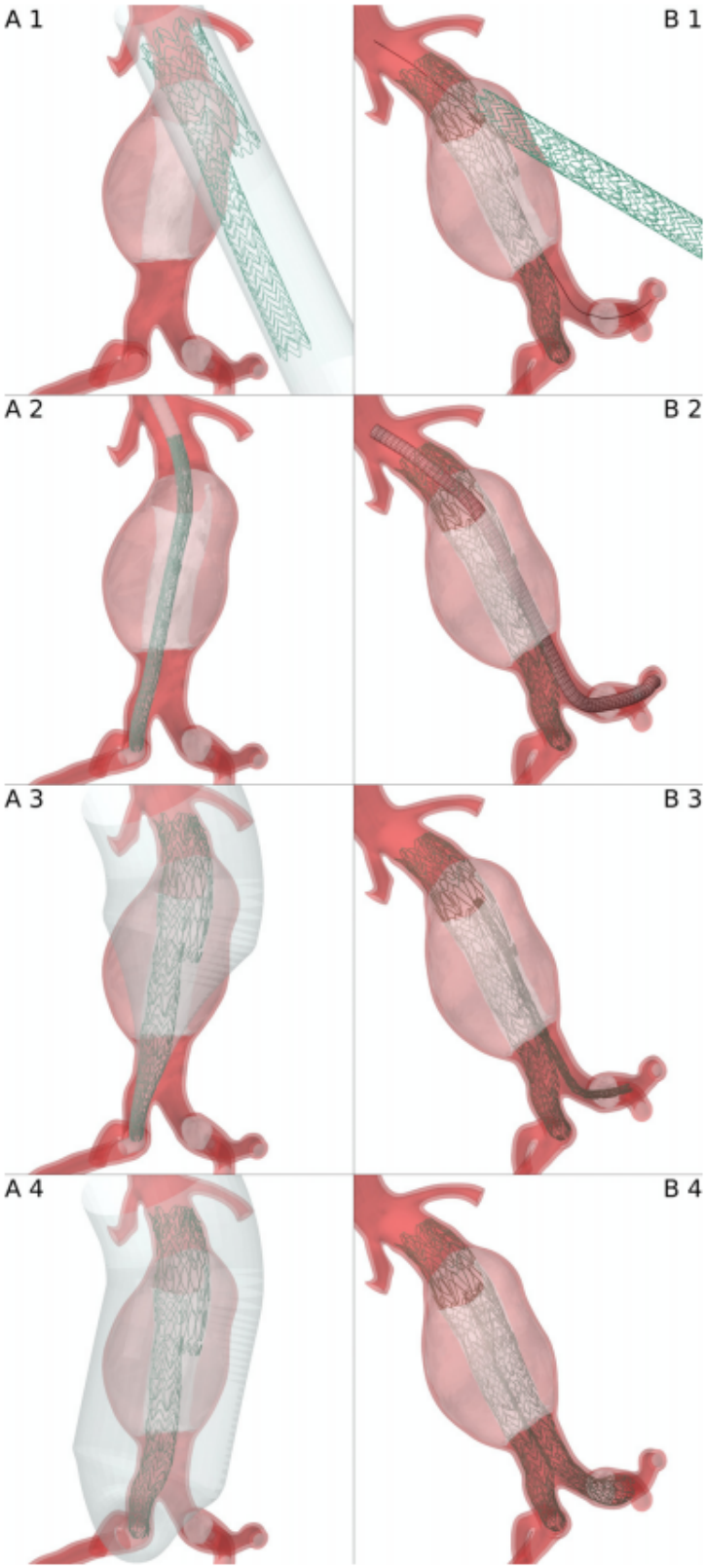

Figure 8: Stent-graft deployment simulation by Bock (2014).

Figure 9: Abdominal aortic aneurysm with a highly tortuous left iliac artery making an angle close to 180° (Demanget et al., 2012a). Reproduced with the permission of Elsevier.

Thesis objectives

The complete simulation of SG implantation in AAA is a recent and active topic of research, it embraces several sub-domains of research such as medical imaging, SG modeling, AAA biomechanics and modeling, along with experimental verification (based on one or a few samples/phantoms) and validation (based on a significant number of samples/phantoms). Therefore, a great deal of knowledge and development is necessary to achieve this goal.

Over the last few years, the modeling and validation of SG improved significantly (Demanget et al., 2012a,b). Now the stents and grafts are discretized separately with shell elements and beam/solid elements respectively, whereas SG were previously modeled with only shell elements and an equivalent homogeneous linear elastic and isotropic material (Li and Kleinstreuer, 2005a), thus discarding their composite non-linear and anisotropic nature. However, only legs were intensively developed, but bodies did not receive the same attention.

The literature related to AAA biomechanics is vast and ever-growing, a large number of isotropic and anisotropic hyperelastic models exist, nevertheless the latter are not obvious to implement because the directions corresponding to collagen fibers need to be specified. There is no gold standard regarding the orientation of collagen fibers, Vande Geest et al. (2008) projected the centerline on the wall to define local coordinate systems, and Mortier et al. (2010) built local coordinate systems on edges of well-shaped hexahedral elements, but the latter is no longer reliable with less regular elements. Besides, the strain energy density functions (SEDF) modeling hyperelastic behaviors are implemented via subroutines written in Fortran, which is tedious and error prone.

With regard to the simulation of SG implantation itself, De Bock et al. (2012) deployed a body only, whereas Demanget et al. (2013) deployed a leg only. Therefore, there is still no robust method to deploy a full prosthesis, typically, a body and two legs, with a good control of their relative position while taking into account the deforming effect of the catheters.

The objectives of this thesis are as follows

1. Regarding SG, reproduce numerically the displacements observed in mechanical tests (flexions, compressions) with a maximum difference of 5%. SG frequently used in the clinical practice must be considered.

2. Develop a framework to reconstruct AAA geometries and generate the corresponding FEM with appropriate (anisotropic) materials and boundary conditions (BC). Substantiate that the developed model provides stresses close to published/recognized values with a maximum difference of 5%.

3. Elaborate a strategy to simulate SG deployment with the following arbitrary requirements (arbitrary because no standard or recurrent criteria could be found in the literature for this context):

    - The difference of renal artery ostia displacements observed in reality (*in vivo* or *in vitro*) and in simulation should be $< 2\,\text{mm}$ in 95% of the cases.
    - Among predefined markers (points in space), the mean difference of AAA displacements observed in reality (*in vivo* or *in vitro*) and in simulation should be $< 5\,\text{mm}$ in 95% of the cases.
    - The simulation should be able to predict the final length and landing zone positions of SG with a maximum difference of 5 mm in 95% of the cases.
    - Account for the deforming effect of the catheters prior to SG deployment.
    - The overall workflow should be made as automatic as possible.

The main hypothesis stems in the fact that the present technology in terms of finite element analysis is capable to faithfully reproduce SG deployment in a pre-deformed or straightened AAA by catheters. This way the SG should undergo less distortion, thus helping analyses to complete without difficulty, as opposed to enforce fully crimped SG to further fit a tortuous centerline, which led to numerical instabilities in the latest studies (Demanget, 2012).

This work finds itself in the continuity of numerical studies devoted to AAA, SG and SG deployment simulations, in an effort to integrate the previous achievements into a unified workflow. The main objective and expected contribution/novelty lies in presenting an original, accurate and robust prediction of SG implantation in AAA, as a tool to better

understand and improve the EVAR procedure. This should be done at least for a single patient-specific geometry, as a proof of concept.

The exposed techniques should inspire other and better EVAR virtualizations.

Part I

Stent-graft modeling

Chapter 1

Mechanical tests performed on stent-grafts

1.1 Introduction

Mechanical tests performed on SG with the purpose of determining their global mechanical behavior are scarce in the literature. Bending tests, and their numerical reproduction, were first published by Demanget et al. (2012b) concerning two legs of last generation, i.e., Aorfix (Lombard Medical, Didcot, United Kingdom) and Zenith Spiral-Z (Cook Medical, Bloomington IN, USA). Also, it is worth mentioning a study from Vad et al. (2010) which allowed identifying dynamic coefficients of friction of SG pulled out of polymeric cylinders. Therefore, there are still no experimental tests conducted on both bodies and legs, and for load cases other than pure bending. This chapter presents the outcomes of two Zenith SG (body and leg) submitted to bending and compression load cases. These results provided substantial experimental data for the verification of the corresponding numerical models, which will be demonstrated in chapter 2.

1.2 Methods to characterize the mechanical behavior of stent-grafts

The two Zenith SG considered here were a body (B-SG) and a leg (L-SG) with respective references TFFB-28-125-ZT and TFLE-12-73-ZT (Figure 1.1). For the B-SG, different sections can be defined, i.e. section 1 that contains the hooks, section 2 which is the proximal landing zone that is supposed to ensure a good seal contact with the vessel, then

section 3 above the bifurcations, and sections 4 and 5 below the bifurcation. Similarly, one defines the proximal section 4 for the L-SG, which is introduced into the body, then section 5, and finally section 6 which is the distal landing zone. Section 6 is also supposed to guarantee a good seal contact with the vessel. These sections are illustrated in Figure 1.1.

Even if the leg was not from the last generation this did not preclude a verification to be done later on with its numerical counterpart. The involved stents were made of stainless steel 316L and the grafts were made of polyethylene terephthalate (PET) - so-called Dacron® - with a plain woven fabric structure as depicted in Figure 1.2.

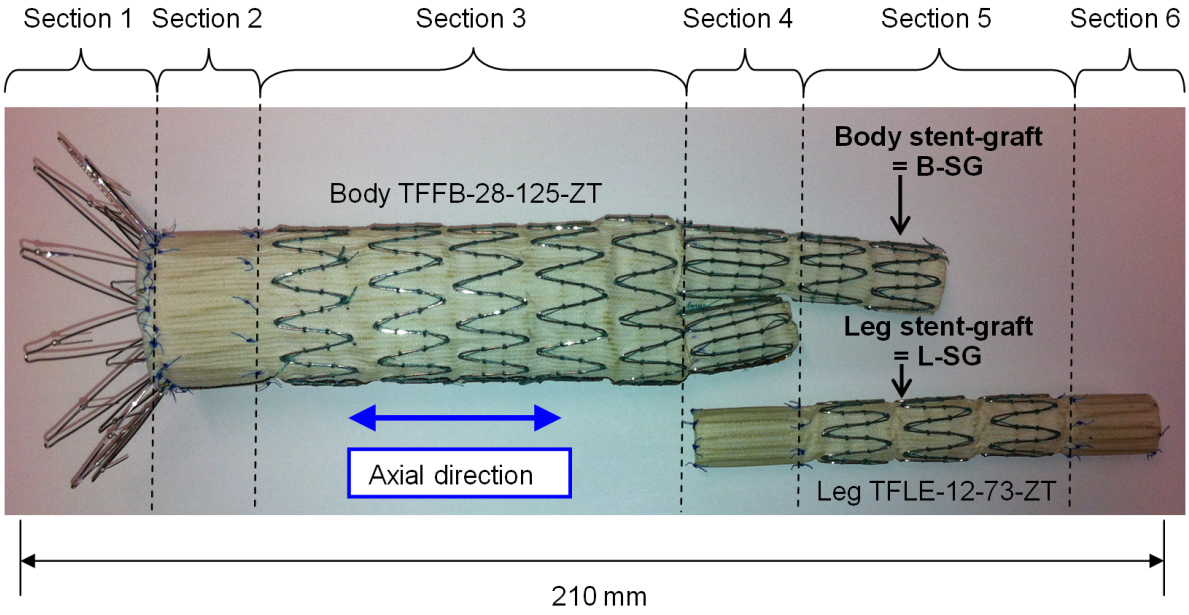

Figure 1.1: Tested stent-grafts (body TFFB-28-125-ZT, leg TFLE-12-73-ZT).

Aside from the tests performed on both the B-SG and L-SG, the mechanical response of the graft was analyzed under uniaxial tensile tests, since this component of the SG structure is generally not clearly defined in the literature.

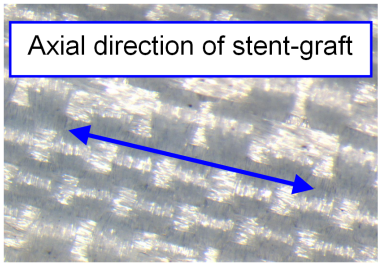

Figure 1.2: Plain woven structure of the graft.

1.2.1 Non-destructive tests on individual stent-grafts

These tests were conducted with a Bose EnduraTEC ELF 3200 uniaxial testing machine (Eden Prairie MI, USA) and a dynamometer of precision ± 0.05 mm. Since no norm was found to test SG, an arbitrary protocol was elaborated. Thus, typical loading modes were performed, which was deemed sufficient for the sake of validation. The following load cases were studied

Simple bending	(applied to L-SG and B-SG)
Three point bending	(B-SG)
Axial compression	(B-SG)

All displacements and forces are summarized in the Table I.

1.2.1.1 Leg simple bending

The L-SG was only submitted to a simple bending load case, with its proximal section fully fixed and a transversal force imposed at the distal section which magnitude was manually controlled by means of the dynamometer. The corresponding displacement of the proximal tip was then recorded (Figure 1.3).

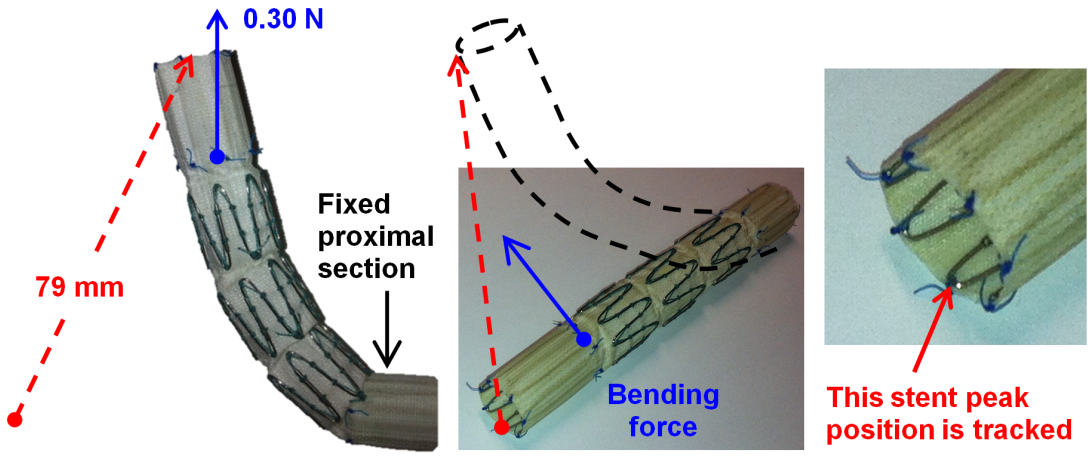

Figure 1.3: Simple bending test on a leg TFLE-12-73-ZT.

1.2.1.2 Body simple bending

Similarly, the B-SG was simply bent with its proximal section fully fixed and a transversal force imposed at each side of section 4 via the same dynamometer (Figure 1.4).

1.2.1.3 Body three-point bending

The B-SG was submitted to a three-point bending load case so as to achieve an arbitrary deviation of 70°, thus a given displacement was imposed manually and the corresponding force was recorded with the tensile machine above mentioned (Figure 1.5).

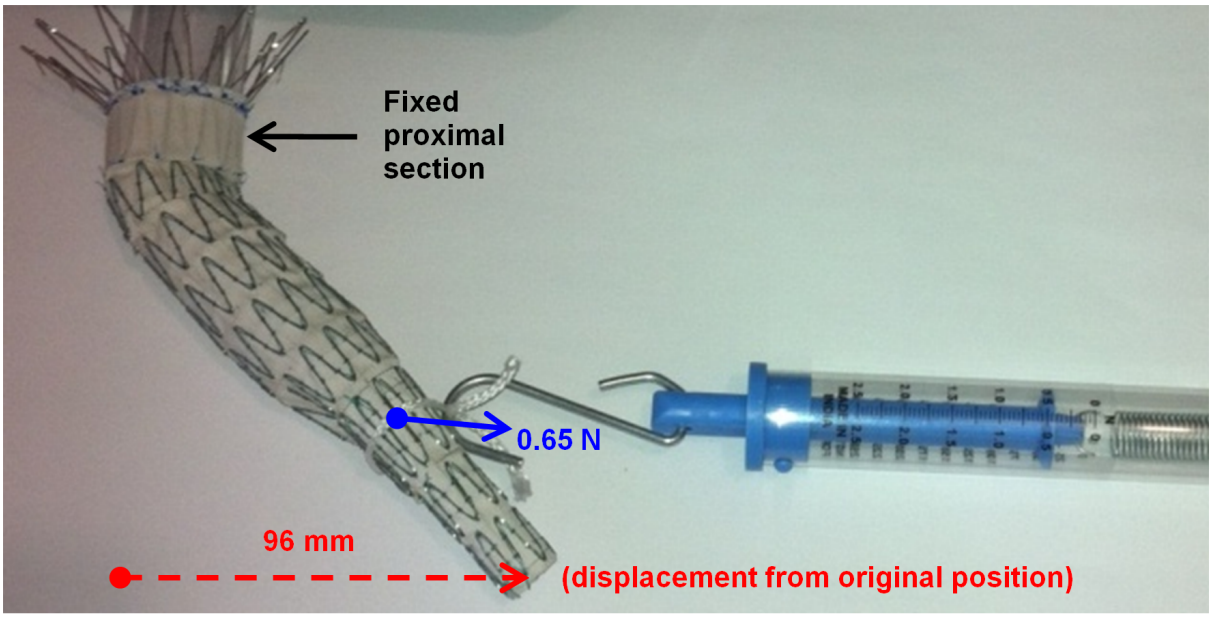

Figure 1.4: Simple bending test on a body TFFB-28-125-ZT.

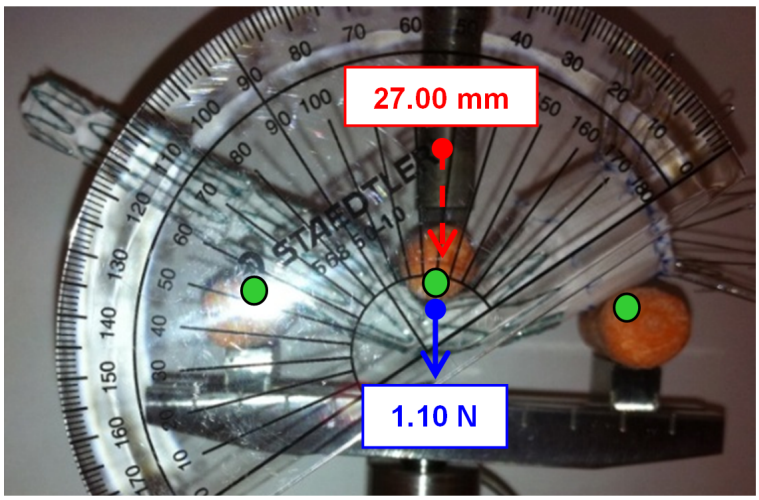

Figure 1.5: Three-point bending test on a body TFFB-28-125-ZT.

1.2.1.4 Body axial compression

It was deemed necessary to cover the case of axial compression in order to better understand the axial stiffness of typical SG, and later better predict complications such as prosthesis migration or collateral vessels occlusion. The B-SG was submitted to an axial displacement of 12 mm which is the maximum travel allowed by the tensile machine, and the corresponding force was recorded at equilibrium (Figure 1.6). This test was not intended to reproduce an actual typical vertical deformation, which is still not well known at this time. But rather to capture the trend of the vertical stiffness over a controlled distance, and for the sake of validation only.

A descending speed of $5\,\mathrm{mm\,min^{-1}}$ was imposed to ensure a quasi-static mechanical response (Gent, 2000).

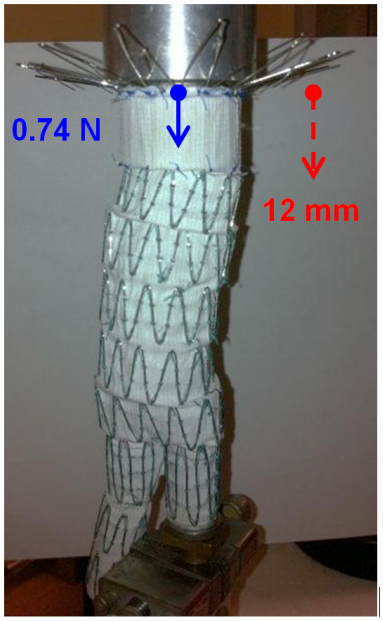

Figure 1.6: Axial compression test on a body TFFB-28-125-ZT.

1.2.2 Destructive tests on a stent and graft samples

Both transversal and radial stent stiffnesses are naturally linked, however, any experimental characterization of the latter is quite more complex due to instability and friction while trying to shrink a specimen located in a device such as shown in Figure 1.7. Therefore, only a transversal compression test was performed for simplicity, and it was assumed that a numerical model being in agreement with such a test, would automatically have the right

radial stiffness also.

Figure 1.7: Device designed to characterize the radial stiffness of stents.

To make sure the transversal compression test would not be biased by any side effects, a bare stent was extracted from the B-SG (section 2) and simply compressed over 12 mm by means of our tensile machine.

Regarding the determination of the graft mechanical properties, there was no other choice than cutting specimen samples from one of the SG. Actually the proximal section (section 2) of the B-SG was cut because this area is free of sutures, which could have distorted the outcomes.

1.2.2.1 Bare stent transversal compression

Figure 1.8 depicts how the bare stent was simply loaded between two plane and polished metallic surfaces. No friction was modeled in this test because no significant displacement was observed during the test. And once again, this test was arbitrarily designed since no testing norm was found for this particular context.

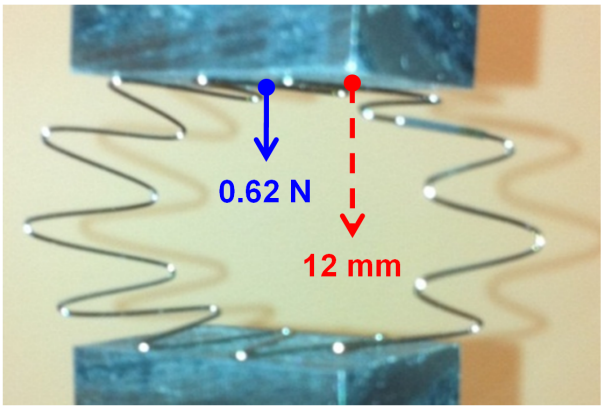

Figure 1.8: Transversal compression test on the stent from a body TFFB-28-125-ZT (proximal section).

1.2.2.2 Graft characterization

The graft is known to be strongly anisotropic (Demanget et al., 2012a), so specimen samples were cut along the axial and circumferential directions to determine the corresponding Young moduli E_{Gz} and $E_{G\theta}$ with reference to a cylindrical coordinate system having its Z-axis along the axial direction. Additional samples allowed identifying both Poisson's ratios $\nu_{Gz\theta} = |(\Delta L_\theta / L_\theta)/(\Delta L_z / L_z)|$ and $\nu_{G\theta z} = \nu_{Gz\theta} E_{G\theta}/E_{Gz}$, where L_z and L_θ are the sample dimensions exposed in Figure 1.9.

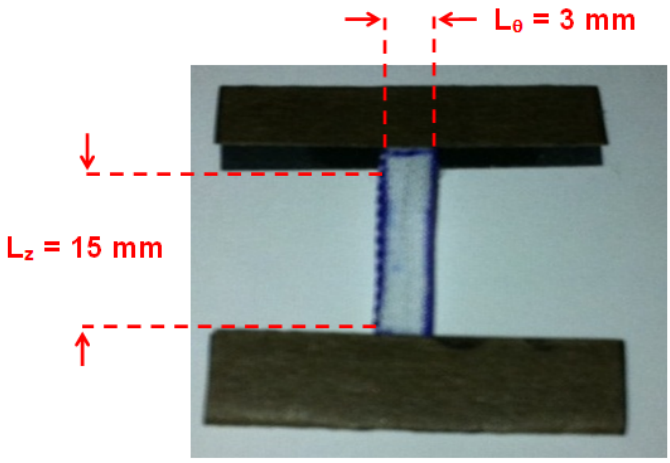

Figure 1.9: Graft specimen sample (made of Dacron®) fixed with sandpaper and cyanoacrylate glue.

Also, 45° oriented samples were cut to determine the shear modulus $G_{Gz\theta}$. These samples were 3 mm wide and 15 mm long, as per the ASTM D882 norm for thin plastic sheets.

Since some samples were initially used to assess how well they were fixed to the tensile machine via sand paper and cyanoacrylate glue to avoid any sliding from the jaws, a limited number of them could actually be used to perform the tests and no averaging operations were possible.

Every sample was stretched up to rupture, at a speed of $5\,\mathrm{mm\,min^{-1}}$.

The protocol to define $G_{Gz\theta}$ is detailed in Figure 1.10, with dimensions $D = 12\,\mathrm{mm}$ and $L_0 = 2.12\,\mathrm{mm}$. This brought a satisfying first approximation, however, for the sake of accuracy, a *picture-frame* test apparatus should be used provided a larger piece of graft would be available. Unfortunately, graft providing companies are usually reluctant to send substantial samples other than to SG manufacturers directly.

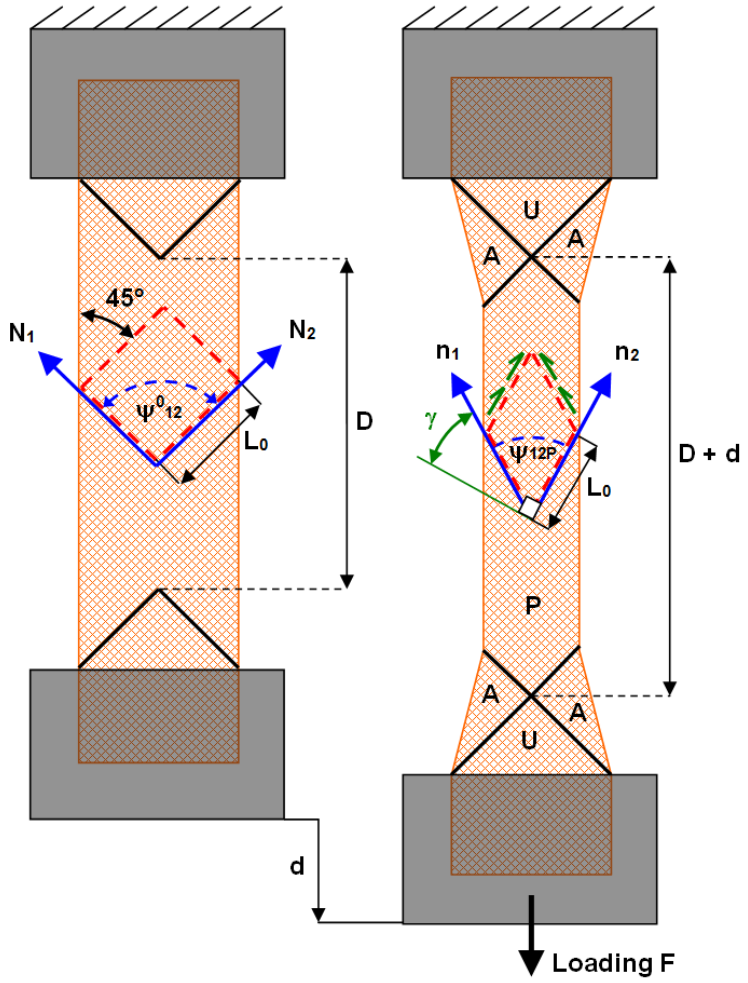

Figure 1.10: Protocol for the determination of graft shear modulus.

$G_{Gz\theta}$ can be expressed by combining the following equations

$$\gamma_{z\theta} = \frac{\pi}{2} - 2\arccos\left(\frac{D+d}{\sqrt{2}D}\right) \tag{1.1}$$

$$\gamma_{z\theta} = \frac{\tau_{z\theta}}{G_{Gz\theta}} \tag{1.2}$$

$$F = 2\tau_{z\theta} L_0 t_0 \sin\left(\frac{\pi}{4} - \frac{\gamma_{z\theta}}{2}\right) \tag{1.3}$$

into

$$G_{Gz\theta} = \frac{F}{2L_0 t_0 \sin\left(\frac{\pi}{4} - \frac{\gamma_{z\theta}}{2}\right)\gamma_{z\theta}} \tag{1.4}$$

where $\gamma_{z\theta}$ (shown as γ in Figure 1.10) is the (in-plane) shear deformation angle, $\tau_{z\theta}$ the corresponding shear stress, and t_0 the initial graft thickness.

Equation 1.1 was provided by Galliot and Luchsinger (2010), and equation 1.3 comes from Abaqus 6.10 documentation (manual `ANALYSIS_3.pdf`, page 20.4.1-18).

1.3 Results of tested stent-grafts and graft samples

1.3.1 Mechanical behavior of stent-grafts

The forces and displacements associated with each test performed on both the L-SG and B-SG are summarized in Table I. Later on, detailed results will be presented in particular for the axial compression on the B-SG.

Table I: Summary of results from non-destructive tests performed on SG.

	Force (Newton)	Displacement (mm)
L-SG simple bending	0.30	79
B-SG simple bending	0.65	96
B-SG three-point bending	1.10	27
B-SG axial compression	0.74	12
B-SG transversal compression	0.62	12

1.3.1.1 Body axial compression

This load case is characterized by graft buckling (sudden collapse of axially loaded slender structures), far before any plastification, and with two jumps at 0.6 N and 0.8 N.

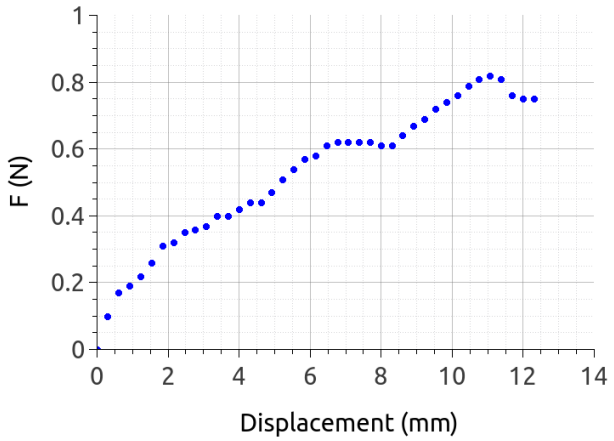

Figure 1.11: B-SG buckling during axial compression.

1.3.1.2 Body transversal compression

This load case showed that stents made of 316L steel behave like *linear* springs, even when submitted to large displacements (Figure 1.12), which allowed some material simplifications regarding their FEM. Large displacements occur when a structure is deformed by more than 10% of its characteristic dimensions.

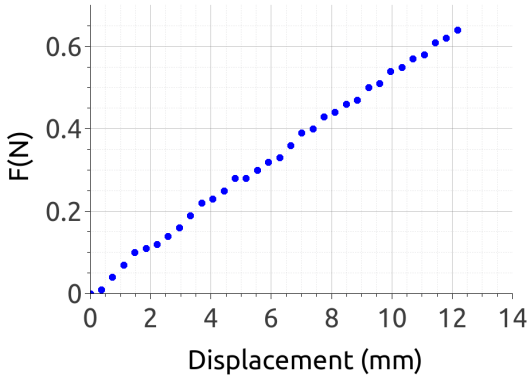

Figure 1.12: Linear spring-like behavior of B-SG proximal stent during transversal compression.

1.3.2 Graft mechanical properties

Experimental stress-strain curves derived from the uniaxial tests are presented in Figure 1.13.

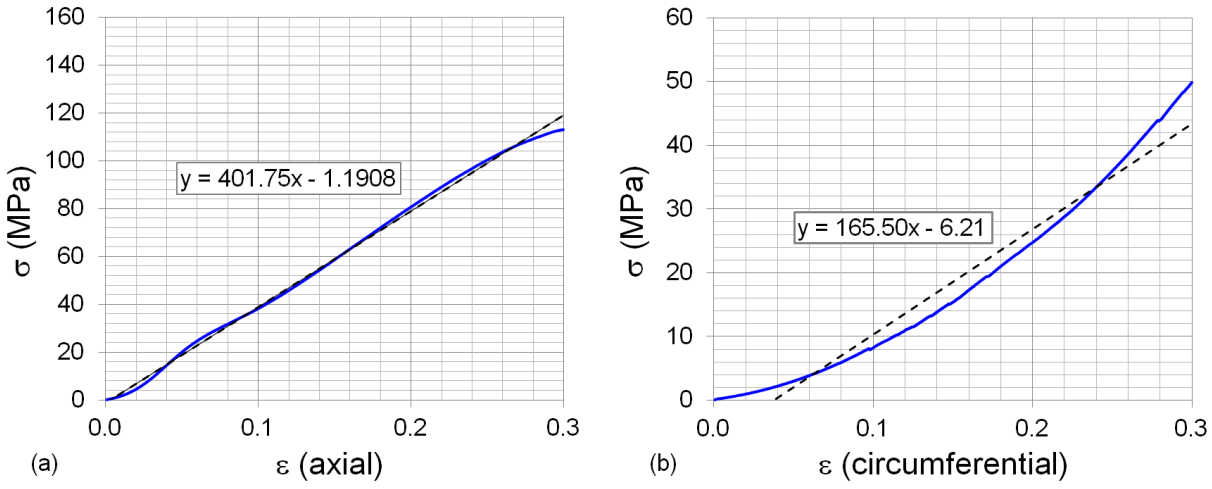

Figure 1.13: Graft Young moduli (from true strains and stresses). (a) Along the stent-graft axial direction. (b) Along the stent-graft circumferential direction.

Engineering (or nominal) stresses (force per unit undeformed area) and engineering strains were converted into Cauchy (or true) stresses (force per unit deformed area) and true strains, as $\sigma_{tru} = \sigma_{nom}\,(1 + \epsilon_{nom})$ and $\epsilon_{tru} = \ln(1 + \epsilon_{nom})$ respectively. Hence the graft Young moduli were inferred from the mean slope of trendlines, i.e. $E_{Gz} \cong 402\,\text{MPa}$ and $E_{G\theta} \cong 165\,\text{MPa}$. A linear relationship was chosen to define the graft Young moduli (Figure 1.13) because the graft does not exhibit large deformations in service. Therefore, this relationship is sufficient to capture its initial stiffness.

The graft thickness t_0 was measured with an electronic caliper and was found to be $0.2\,\text{mm}$.

With regard to Poisson's ratios, the following values could be find:

$$\nu_{Gz\theta} = |(\Delta L_\theta / L_\theta)/(\Delta L_z / L_z)| = |(-0.5/3)/(6/15)| \cong 0.42,$$

$$\nu_{G\theta z} = \nu_{Gz\theta} E_{G\theta} / E_{Gz} = 0.42 \cdot 165/402 \cong 0.17.$$

The shear modulus $G_{Gz\theta}$ could be evaluated from equations 1.1 to 1.4, based on force-displacement pairs gathered during the test. The graft structure reorganized itself while being stretched, which resulted in the Figure 1.14 where $G_{Gz\theta}$ appears to be dependent on γ.

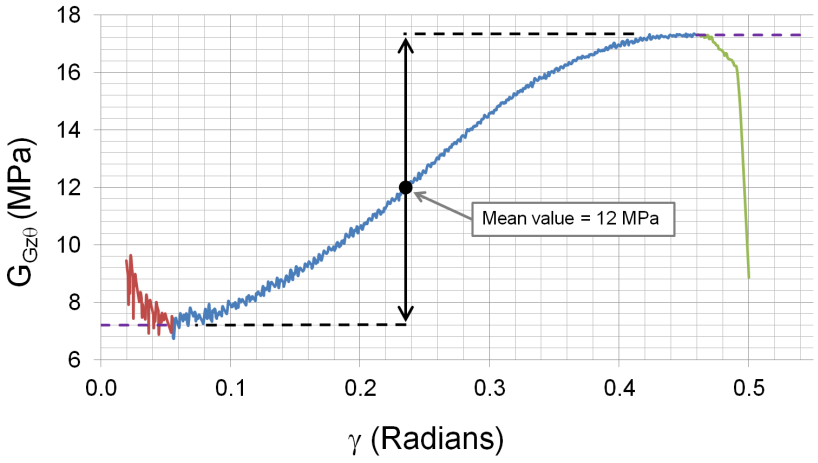

Figure 1.14: Graft shear Modulus.

In order to fix a single value, the mean value between the lower and upper asymptotic extrema was considered, i.e. roughly $7\,\text{MPa}$ and $17\,\text{MPa}$ respectively. Therefore, $G_{Gz\theta}$ was fixed to $12\,\text{MPa}$. More specifically, the curve presented in Figure 1.14 is divided into three regions that are colored respectively in red, blue and green. The first one in red corresponds to a weak and fuzzy initiation of the load, the blue region represents the phase

during which the sample was actually taut, and finally the green one depicts a typical failure.

The derived mechanical properties of the graft are gathered in Table II.

Table II: Summary of graft mechanical properties derived from tests.

Nominal Young's modulus along SG axial direction	E_{Gz}	402 MPa
Nominal Young's modulus along SG circ. direction	$E_{G\theta}$	165 MPa
Poisson's ratio with a stretch along SG axial direction	$\nu_{Gz\theta}$	0.42
Poisson's ratio with a stretch along SG circ. direction	$\nu_{G\theta z}$	0.17
In-plane shear modulus	$G_{Gz\theta}$	12 MPa

1.4 Discussion

The macroscopic mechanical behavior of typical SG, as well as a first set of graft mechanical properties could be established. However, only two specimens could be analyzed.

Besides, the L-SG (TFLE-12-73-ZT) is now obsolete, and the latest generation of SG from Cook Medical has a central Spiral-Z stent made of nitinol (metal alloy of nickel and titanium). However, this did not preclude the verification process presented in chapter 2.

A better protocol could have been designed to test SG in bending, for instance an additional tool could have been realized to perform four-point bending tests. Also, no pure radial compression was performed on any bare stent because of expected instability, but it is worth mentioning an original method developed by Johnston et al. (2010). In the latter, the authors could radially compress some SG wrapped in a Mylar® film constrained by two rollers, as shown in Figure 1.15.

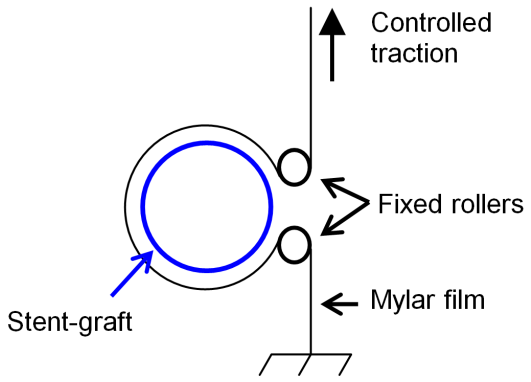

Figure 1.15: Device for radial compression of stent-grafts (Johnston et al., 2010). Reproduced with the permission of Elsevier.

Finally, a more accurate method to determine the graft in-plane shear modulus could have been used, such as presented by Galliot and Luchsinger (2010), bearing in mind that this would be a substantial development.

1.5 Conclusion

In spite of the limitations above stated, these preliminary results allowed to feed the numerical models of SG with quite realistic parameters, and get involved in their respective verification against experimental results, which is the purpose of chapter 2.

Chapter 2

Realistic finite element model of stent-grafts

2.1 Introduction

An early introduction of stent-grafts together with AAA in numerical analyses is due to Li and Kleinstreuer (2005a), but then the SG were fairly simple homogeneous structures. Later on, while simulating percutaneous pulmonary valves, Capelli et al. (2010) published quite a realistic model of the prosthesis involved, thus elaborating a composite structure with well differentiated graft and stent components. More recently, two commercial leg SG were accurately modeled and their mechanical behavior in simple bending was compared (Demanget et al., 2012a), moreover, the same authors later provided an experimental verification of the same study (Demanget et al., 2012b).

However, there is still no verification of experimental results versus numerical ones regarding a more complex structure such as a B-SG, and only simple bending load cases were studied (Demanget et al., 2012a). The axial load case is critical to make sure any numerical model faithfully reproduces complex buckling modes. Also, the graft influence in pure radial compression is still not addressed in the literature, and this is another critical aspect when pretending to simulate type I endoleaks.

In this thesis, these load cases were treated numerically and a thorough comparison with the corresponding experimental tests is presented. Also, the very important concept of *pre-tension*, so far eluded in the literature, was treated as well. This chapter finally explains how the automatic generation of verified numerical SG can be done for the most frequently used bodies and legs from a recent catalogue from Cook Medical (2013).

All the results presented in this thesis work were generated with Abaqus 6.10-1.

2.2 Explicit finite element method

All along this work the Abaqus explicit solver was used for its robustness to simulate the three non-linearities (non-linear materials, large deformations and contacts) combined all together. Abaqus was originally developed for advanced non-linear solid mechanics simulation. In explicit schemes, values known at time n are processed to obtain the corresponding values at time $n+1$. These schemes are conditionally stable and the numerical errors are proportional to the time step and the square of the space step. Such a tool is required to simulate the complex behavior of realistic SG, in particular the *Zenith Flex AAA* bodies and *Zenith*® *Spiral-Z*™ *AAA Iliac* legs considered hereafter.

2.2.1 Stents geometries

The bodies and legs are presented in Figures 2.1 and 2.2. A quick glance at these figures allows identifying basically three typical stent geometries, i.e. the bards (section 1 in Figure 1.1), cylindrical Z stents and Spiral-Z stents. One could add a fourth type by considering the funnel-shaped Z stent just above every body bifurcation, and this particular stent is transitioning from a circular section to an elliptic one. Both Z and Spiral-Z stents might be constructed by means of a sine function and a combination of a sine plus a parametric spiral function respectively (Demanget, 2012).

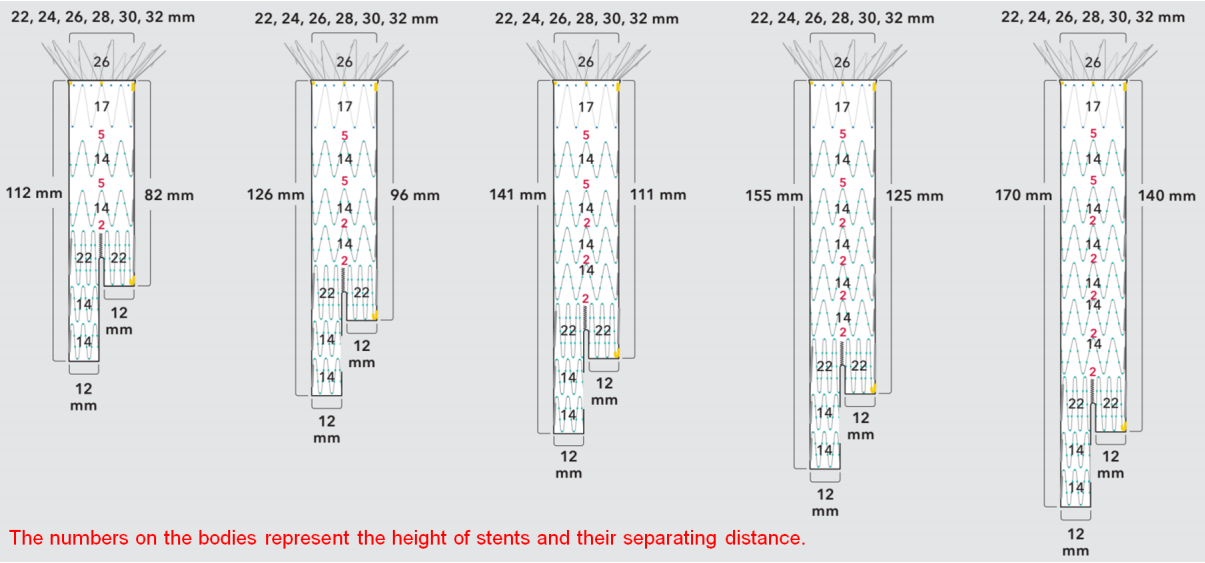

Figure 2.1: Bodies *Zenith Flex AAA* TFFB-22-82-ZT to TFFB-32-140-ZT from Cook Medical (Cooks documents).

This can also been achieved by linking some points (peaks and valleys) with a spline,

which allows generalizing the design of more complex geometries such as barbs/hooks, funnel-shaped Z stents and even full Spiral-Z stents with their evolutive radius and eccentricity.

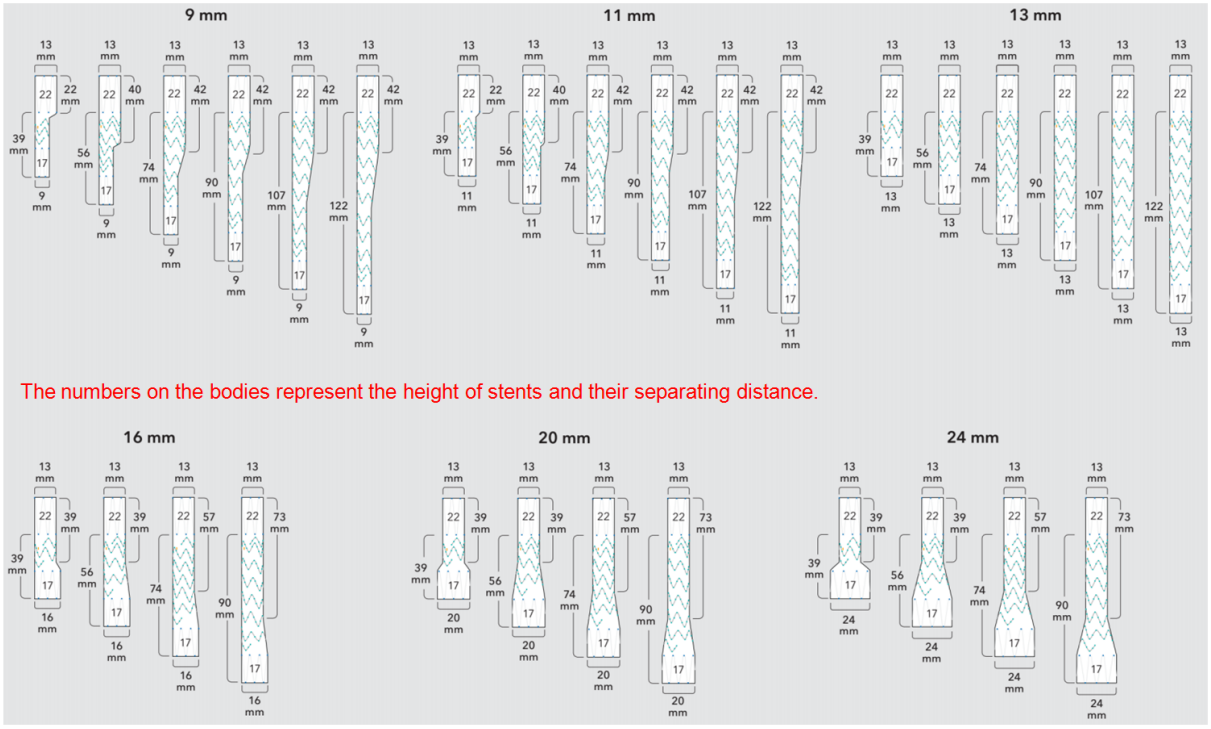

Figure 2.2: Legs *Zenith*® *Spiral-Z*™ *AAA Iliac* ZSLE-9-39-ZT to ZSLE-24-90-ZT from Cook Medical (Cooks documents).

A close collaboration with Cook Medical representatives allowed a fine tuning of the stent design by incorporating key particularities such as the exact stent geometry and thickness for a given SG. Here, it can only be reported that the mean gauge is 0.4 mm, but no more information is unveiled since these details are confidential.

For the sake of demonstration, the complete set of stents for a body TFFB-28-125-ZT and a leg ZSLE-16-74-ZT were generated and are displayed in Figure 2.3. In this figure, one can appreciate the changing radius of the Spiral-Z stent, from 13 mm at the proximal section to 16 mm at the distal one, as well as its eccentricity of $(16 - 13)/2 = 1.5$ mm. Some Python scripts were written to generate the right points according to the actual geometry. In this case, the Spiral-Z stent has a constant radius over a given length and an evolutive radius over its remaining length, but there could be up to three such zones of constant and evolutive radius (legs with distal radii 9 mm and 11 mm). This aspect is managed by the script above mentioned.

It is worth considering these details in order to fully capture the mechanical response

of Spiral-Z stents because they do not kink as much as Z stents, and preserve a more regular and open section in tortuous vessels. In fact, Spiral-Z stents are a mix between Z stents and *pure* spiral stents, so they benefit from both the buckling resistance of Z stents and superior flexibility in bending of pure spiral stents as demonstrated experimental and numerically by Demanget et al. (2012a,b).

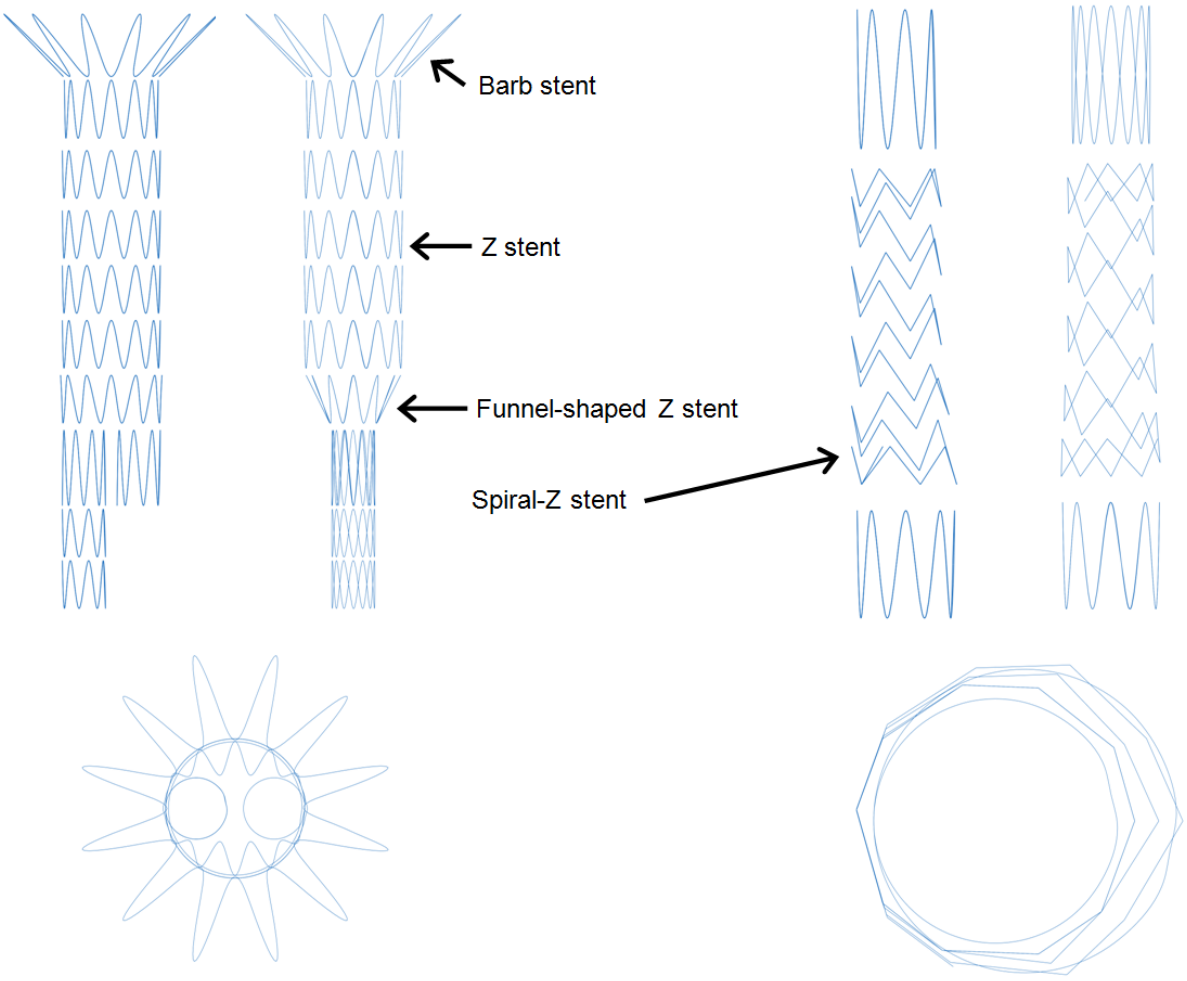

Figure 2.3: Generated stents for a body TFFB-28-125-ZT and a Leg ZSLE-16-74-ZT.

2.2.2 Grafts geometries

In the following, typical graft geometries are briefly presented (Figure 2.4). In particular, one can see typical zones with constant or evolutive radius. These geometries are surfaces passing through the middle of the graft thickness. Later on, the material is added on both sides, after meshing the part.

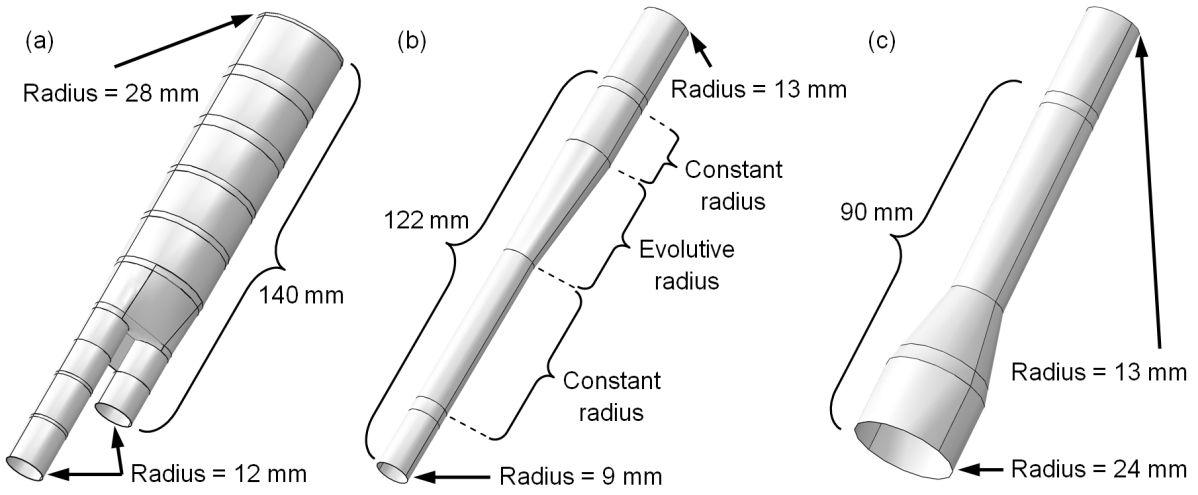

Figure 2.4: Generated grafts. (a) Body TFFB-28-140-ZT. (b) Leg ZSLE-9-122-ZT. (c) Leg ZSLE-24-90-ZT.

2.2.3 Stents materials

All stents are made of stainless steel 316L, except Spiral-Z stents that are made of nitinol (not experimentally tested). The mechanical properties of stainless steel 316L are given in Table III and are not further elaborated. However, nitinol deserves longer explanations.

Table III: Stainless steel 316L mechanical properties (UNS S31600 and UNS S31603).

Young's modulus	E_{316L}	193 000 MPa
Poisson's ratio	ν_{316L}	0.3
Density	ρ_{316L}	8000 kg m^{-3}

Nitinol exhibits two particular properties: shape memory and superelasticity. Shape memory is the capability to undergo a permanent deformation at a given temperature, and recover the original shape once heated above the characteristic *transformation temperature*. Superelasticity simply means that these alloys have a stiffness around one order of magnitude less than other (classic) metals. The corresponding mechanical properties are presented in Table IV and Figure 2.5 shows the loading and unloading paths on a typical stress-strain curve.

Therefore, a complex material modeling would be necessary with an implementation via a user-defined subroutine (VUMAT in Abaqus/Explicit). Which until the version 6.08 of Abaqus, implied modeling stents made of nitinol with solid elements in so far as the formulation available for beam elements was not supporting such non-linear behavior. This

is why a use of solid elements can be found in certain studies (Demanget et al., 2012a,b, 2013), whereas beam elements could be employed in more recent ones (De Bock et al., 2012).

Table IV: Nitinol mechanical properties (Kleinstreuer et al., 2008; Sampaio et al., 2006).

Austenite elasticity	E_A	51 700 MPa
Austenite Poisson's ratio	ν_A	0.3
Martensite elasticity	E_M	47 800 MPa
Martensite Poisson's ratio	ν_M	0.3
Transformation strain	ϵ^L	0.063
Loading	$(\partial\theta/\partial T)_L$	652.7
Start of transformation loading	σ_L^S	600 MPa
End of transformation loading	σ_L^E	670 MPa
Reference temperature		37 °C
Unloading	$(\partial\theta/\partial T)_U$	652.7
Start of transformation unloading	σ_U^S	288 MPa
End of transformation unloading	σ_U^E	254 MPa
Start of transformation stress in compression	σ_{CL}^S	900 MPa
Volumetric transformation strain	ϵ_V^L	0.063
Strain limit	ϵ_{max}	12%
A_f temperature		20 °C

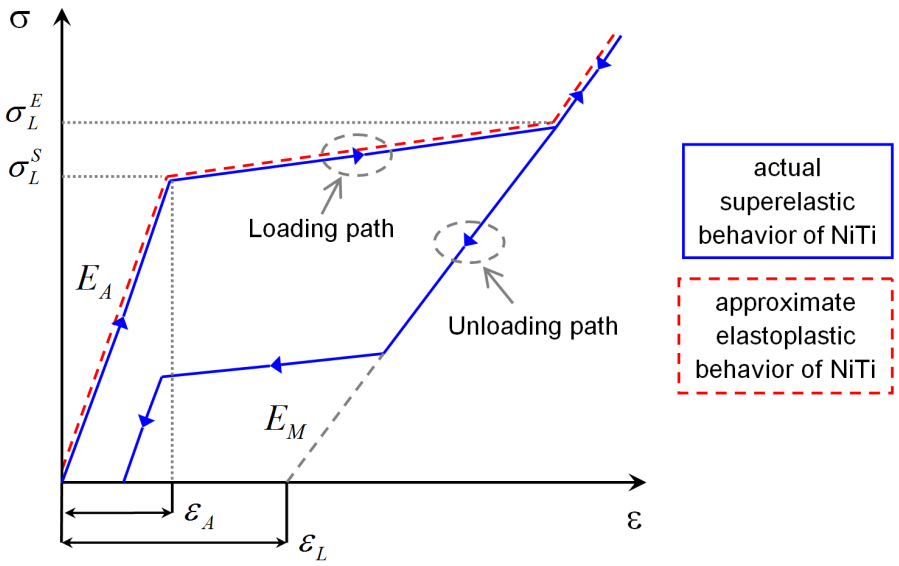

Figure 2.5: Nitinol stress-strain curve (Demanget et al., 2012b). Reproduced with the permission of Elsevier.

As a matter of fact, a Spiral-Z stent always recovers its shape by compressing it manually (isotherm loading), even after a large deformation mimicking its position along a DD. So the full superelastic behavior was not considered, neither any elastoplastic approximation, which would have led to unrealistic permanent deformations. A linear behavior was rather assumed, and based on the parameters available in Table IV a new set of simplified properties was defined (Table V). The density of nitinol can be found in ASM (2009) on page 95. The substantiation of this assumption is deferred to chapter 5.

Table V: Nitinol simplified mechanical properties (linear behavior assumption).

Young's modulus	E_{NiTi}	50 000 MPa
Poisson's ratio	ν_{NiTi}	0.3
Density	ρ_{NiTi}	6490 kg m^{-3}

In an attempt to better treat large deformations, one could be tempted to substitute the properties from Table V for an hyperelastic equivalent. Unfortunately, there is no hyperelastic formulation for beam elements in Abaqus/Explicit.

Last but not least, this simplified approach allowed a natural and simple correction of all stents Young's modulus to account for their pre-tension by the graft, as shown later on in section 2.5.

2.2.4 Graft material

Graft structural behavior is best described by an orthotropic elastic model with in-plane stresses, ideally modeled with shell elements. Following the nomenclature introduced in chapter 1, only the values of E_{Gz}, $E_{G\theta}$, $\nu_{Gz\theta}$, $G_{Gz\theta}$, G_{Gzr} and $G_{G\theta r}$ are required to define an orthotropic material, with r subscript corresponding to the radial direction of SG. The plane stress condition is $\sigma_{rr} = 0$. In this case the stress-strain relations for the in-plane components of the stress and strain are of the form (lamina in Abaqus nomenclature)

$$\begin{pmatrix} \epsilon_z \\ \epsilon_\theta \\ \gamma_{z\theta} \end{pmatrix} = \begin{pmatrix} 1/E_{Gz} & -\nu_{Gz\theta}/E_{Gz} & 0 \\ -\nu_{Gz\theta}/E_{Gz} & 1/E_{G\theta} & 0 \\ 0 & 0 & 1/G_{Gz\theta} \end{pmatrix} \begin{pmatrix} \sigma_{zz} \\ \sigma_{\theta\theta} \\ \tau_{z\theta} \end{pmatrix} \tag{2.1}$$

The shear moduli G_{Gzr} and $G_{G\theta r}$ are included for modeling transverse shear deformation in a shell. Though intuitively these two last parameters do not seem to influence much the graft out-of-plane behavior since the one is free to fold like any other fabric, the graft actually has a non-negligible transverse shear stiffness, otherwise a strip of graft hold

horizontally from one side only would completely collapse under the gravity, which is not the case. These parameters cannot be determined easily experimentally, and there is no other way than running trial simulations (FEM of complete body and leg against experimental results previously gathered) until the optimum values are found. This process is extremely tedious and is not exposed here, so the optimum values are provided beforehand directly and will be taken for granted from now on (Table VI). But before that, additional properties and concepts must be presented in detail, in particular what is called *artificial thickness reduction*.

2.2.4.1 Artificial thickness reduction

If one attempts to simulate a graft structure with material properties obtained from tests or even derived from known materials, it would behave as a plate having a similar stiffness in tension and compression, whereas a fabric offers no or little resistance in compression (buckling). Hence the need to "relax" the out-of-plane stiffness, which is directly related to the bending stiffness. To do so, the *Kirchhoff-Love* plate theory provides a useful clue in the expression of bending stiffness

$$D = \frac{Et^3}{12(1-\nu^2)} \tag{2.2}$$

where E is Young's modulus, t the thickness and ν Poisson's ratio. It can be immediately seen that the thickness is a powerful lever to allow a folding behavior without modifying the intrinsic mechanical properties of the graft. Thus, artificially reducing the graft thickness by a given factor is an elegant solution to tackle the problem. To determine this factor some authors presented an original and simple method, so-called *nail test*, consisting in reproducing numerically the bending deflection of a one-side encastred strip submitted to gravity (Demanget et al., 2012a). However, this method revealed inaccurate and after a series of trial simulations, an optimum factor of 10 was found. In the following, parameters affected by thickness reduction have a tilde sign.

Therefore, the nominal graft thickness of $t_0 = 0.2\,\text{mm}$ was reduced to $\tilde{t} = 0.02\,\text{mm}$. Obviously Young's and shear moduli were increased by the same factor so as to achieve an equivalent in-plane stiffness. Poisson's ratios were not affected.

With regard to $G_{Gz\theta}$, increasing its value led to unrealistically stiff SG, so $G_{Gz\theta}$ kept its nominal value of 12 MPa.

A substantial effort was devoted to identify the optimum values of $\tilde{G}_{Gzr}$ and $\tilde{G}_{G\theta r}$; 100 MPa and 50 MPa respectively, because there is no obvious method to define these

values experimentally. And the corresponding transverse shear stiffnesses were given by

$$K_{Gzz} = \frac{5}{6}\tilde{G}_{Gzr}\tilde{t}, \quad K_{G\theta\theta} = \frac{5}{6}\tilde{G}_{G\theta r}\tilde{t} \quad \text{and} \quad K_{Gz\theta} = 0.0 \tag{2.3a,b,c}$$

Transverse shear stiffnesses are not affected by thickness reduction because decreased thickness and increased shear moduli cancel their effect.

2.2.4.2 Density

Explicit schemes are designed to solve dynamic problems, so the material density is required. The graft density was assessed by weighting a specimen sample. This parameter is naturally affected by thickness reduction, so its nominal value of $635\,\mathrm{kg\,m^{-3}}$ was multiplied by 10 in all analyses in order to conserve the same total mass.

The whole set of graft mechanical properties is summarized in Table VI.

Table VI: Summary of all graft mechanical properties accounting for a thickness reduction factor of 10 (parameters affected by thickness reduction have a tilde sign).

Young's modulus along SG axial direction	$\tilde{E}_{Gz}$	$4020\,\mathrm{MPa}$
Young's modulus along SG circ. direction	$\tilde{E}_{G\theta}$	$1650\,\mathrm{MPa}$
Poisson's ratio with a stretch along SG axial direction	$\nu_{Gz\theta}$	0.42
In-plane shear modulus	$G_{Gz\theta}$	$12\,\mathrm{MPa}$
Shear modulus in zr plane	$\tilde{G}_{Gzr}$	$100\,\mathrm{MPa}$
Shear modulus in θr plane	$\tilde{G}_{G\theta r}$	$50\,\mathrm{MPa}$
Transverse shear stiffness related to $\tilde{G}_{Gzr}$	K_{Gzz}	$1.67 \times 10^{-3}\,\mathrm{MPa\,m}$
Transverse shear stiffness related to $\tilde{G}_{G\theta r}$	$K_{G\theta\theta}$	$8.33 \times 10^{-4}\,\mathrm{MPa\,m}$
Transverse shear stiffness in $z\theta$ plane	$K_{Gz\theta}$	$0.0\,\mathrm{MPa\,m}$
Density	$\tilde{\rho}_G$	$6350\,\mathrm{kg\,m^{-3}}$

2.2.4.3 Grafts orientation

In the numerical SG the graft must be oriented according to the material description given above, thus respecting its anisotropy.

Figure 2.6 shows the graft orientation for both a B-SG and L-SG. Particular attention must be paid regarding the orientation of every B-SG bifurcation to avoid erroneous finite elements orientation.

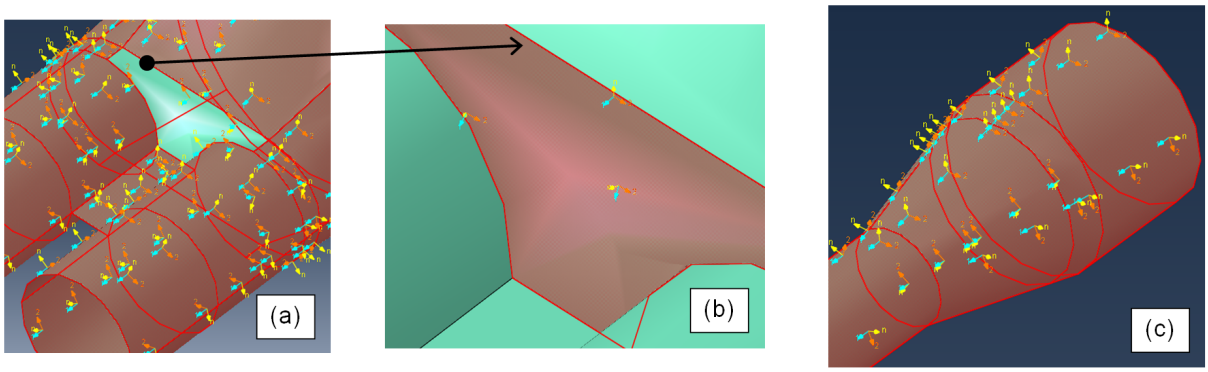

Figure 2.6: Grafts orientation. (a) Global view of a body TFFB-28-140-ZT. (b) Detailed bifurcation of a body TFFB-28-140-ZT. (c) Global view of a leg ZSLE-24-90-ZT. Local z and θ axes are represented by blue and orange vectors respectively.

2.2.5 Stent mesh

Stents were meshed with linear beam elements (B31 in Abaqus nomenclature) and an element size of 0.7 mm (giving 5636 elements and 5636 nodes for a body TFFB-28-125-ZT), which was close to the average optimum size of 0.57 mm reported by De Bock et al. (2012). This formulation brought numerical efficiency and remained accurate.

2.2.6 Graft mesh

As already mentioned in section 2.2.4 the graft was meshed with shell elements (Demanget, 2012), as opposed to membrane elements that have absolutely no resistance in compression neither transverse shear stiffness and would collapse unrealistically. In particular a 4-node doubly curved linear shell element with full integration (four Gauss points), enhanced hourglass control and finite (large) in-plane strains capability ("S4" element in Abaqus nomenclature) was considered. This element integrates thin and thick shell formulations based on the *Kirchhoff-Love* and *Mindlin-Reissner* theories of plates respectively. The *Mindlin-Reissner* theory is valid with a maximum ratio of thickness to global characteristic dimension of the considered structure of one tenth, which was the case with a reduced thickness of 0.02 mm and a minimum SG diameter of 9 mm. Regarding the finite element scale, Abaqus tolerates a maximum aspect ratio of thickness to element minimum edge/-diagonal length equal to 1, which was again the case with a prescribed element size of 0.5 mm. The dependence of the results on the mesh size is studied in section 2.3. Reduced shell elements (S4R) could have been used for the sake of efficiency, but fully integrated elements were considered, in a context of verification.

2.2.7 Numerical parameters

In this section the following key numerical parameters/settings are presented and their use is substantiated when appropriate

Explicit stable time increment	Smooth amplitude
Contact	Mass scaling
Damping	Units

2.2.7.1 Explicit stable time increment

Explicit schemes are *conditionally stable*, meaning that their time increment must remain below a certain threshold to ensure a successful convergence and completion of the analysis. The time increment is restricted to

$$\Delta t \leq \min\left(L^{el}\sqrt{\frac{\rho}{\lambda+2\mu}}\right) \tag{2.4}$$

where the minimum is taken from over all elements in the mesh, L^{el} is a characteristic length associated with an element, ρ is the density of the material in the element, and λ and μ are effective Lamé's constants for the material in the element. λ and μ can be derived from Young's modulus and Poisson's ratio.

2.2.7.2 Contact

Abaqus offers the so-called *general contact* algorithm to manage all possible contacts between any number of entities meshed with rigid, solid, shell or even beam elements, including self-contact which is particularly useful for the graft. Friction might also be prescribed where necessary, especially between a SG and another object such as a sheath or a tool, but a simple frictionless tangential friction property is more appropriate when a studied SG does not enter in contact with any other entity.

Regarding the connection between both the graft and associated stents, the facing nodes are constrained in the three translational degrees of freedom (DOF) over a controlled distance (*tie constraint* in Abaqus nomenclature).

This technique to approximate the real sutures is demonstrated in Figure 2.7. In the same figure a set of nodes pertaining to the barb stent is also identified to further simulate hooks rigidly linked to the arterial wall after deployment.

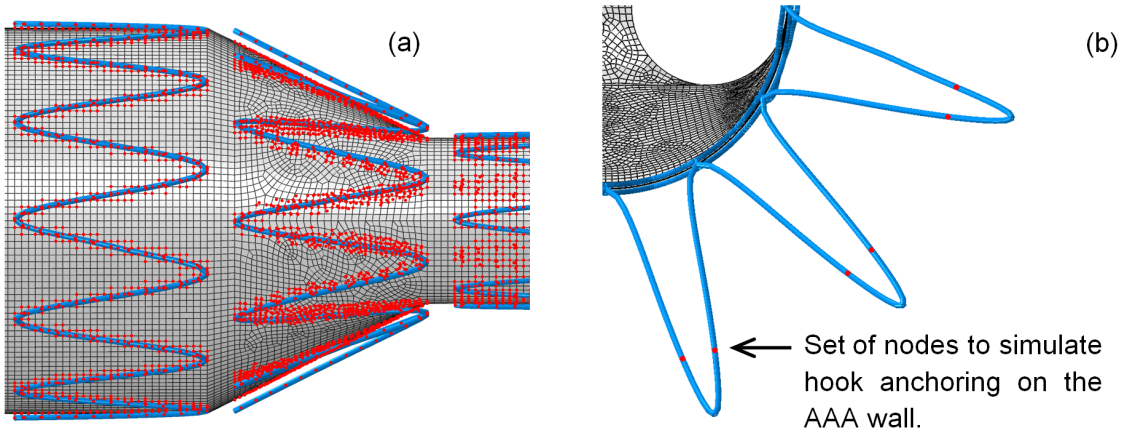

Figure 2.7: Stent-graft nodes attributed to particular constraints and contact (body TFFB-28-140-ZT). (a) Nodes involved in constraints between the graft and stents to simulate sutures. (b) Set of nodes from the barb stent to simulate hooks.

2.2.7.3 Damping

Some degree of *Rayleigh* damping was introduced to stabilize the numerical models. Actually, only the mass proportional damping term (α damping in Abaqus nomenclature) was considered, which did not penalize much the numerical performance. Indeed, optimal α damping values of $5.0\,\mathrm{s}^{-1}$ and $25.0\,\mathrm{s}^{-1}$ were applied to the B-SG and L-SG respectively. These values were obtained by performing sensibility studies when the mechanical tests were reproduced numerically (see section 2.3) until reaching a smooth curve of deformation energy, i.e. free of unrealistic noise. This direct method to identify the right values was preferred over a more theoretical assessment, because structural damping is far from trivial to approximate for such complex geometries and mix of materials.

2.2.7.4 Smooth amplitude

Performing analyses with an explicit solver implies that quasi-static results should be obtained when the simulated event is slow by nature, as opposed to a (dynamic) crash test for instance. Thus, inertia should play a negligible role, which is the case in this study. The accepted criterion for quasi-static results is that the kinetic energy must not exceed 5% of the total energy of deformation (Kim et al., 2002), but 10% is acceptable for very large deformations.

This is why loads and BC are to be applied as smoothly as possible to help meeting this criterion. Practically, this is achieved via a sigmoid function.

2.2.7.5 Mass scaling

Explicit schemes are robust, but extremely slow since they are based on a very large number of small time increments. To reduce the resolution time, it is common to recourse to the concept of *mass scaling*. In light of equation 2.4, it becomes apparent that "artificially" increasing the density increases the stable time increment, which in turn reduces the resolution time. However, the amount with which the density is increased must be carefully controlled in order to keep the solution quasi-static. For instance, if the density is increased by a mass scaling factor of 10 000, the resolution time is roughly reduced by 100, provided the "energetic" criterion above introduced is satisfied. Mass scaling factors are very problem-dependent, and in this thesis work it ranged from 100 to 100 000, depending on the concerned structure, either the AAA of SG.

2.2.7.6 Units

In this document all the parameters and physical values are presented in SI units, however in the numerical models a set of units that generates larger values was used to avoid numerical issues on certain platforms or computers due to near-zero values. In this set lengths are in mm, forces in mN (milliNewton), masses in kg and stresses in kPa.

2.3 Numerical reproduction of the experimental tests performed on stent-grafts

2.3.1 Leg simple bending

The proximal section (section 4 from Figure 1.1) was fully fixed, and the bending load of 0.30 N was distributed on the distal stent (Figure 2.8).

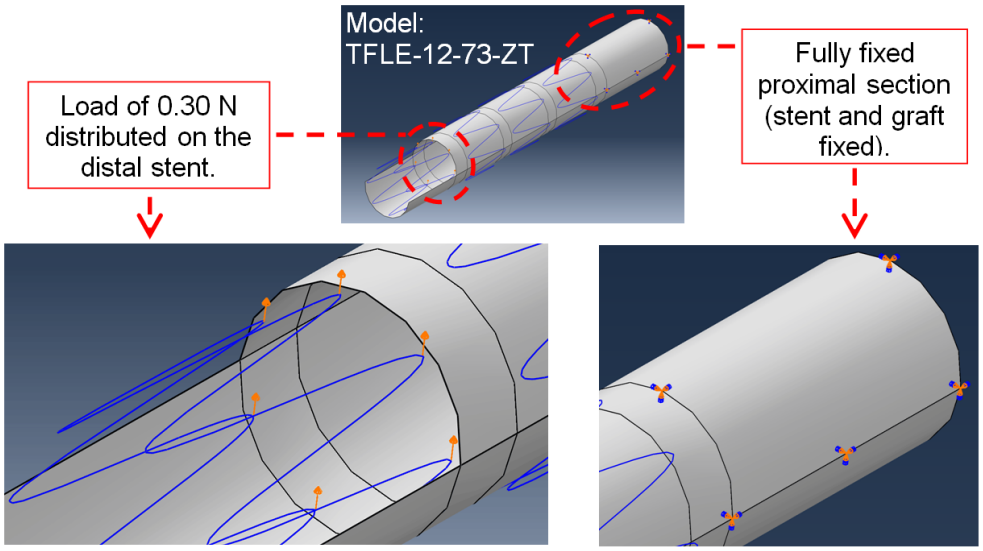

Figure 2.8: Simulation of the simple bending of the leg: boundary condition and load.

A virtual displacement of around 78 mm could be observed numerically (Figure 2.9).

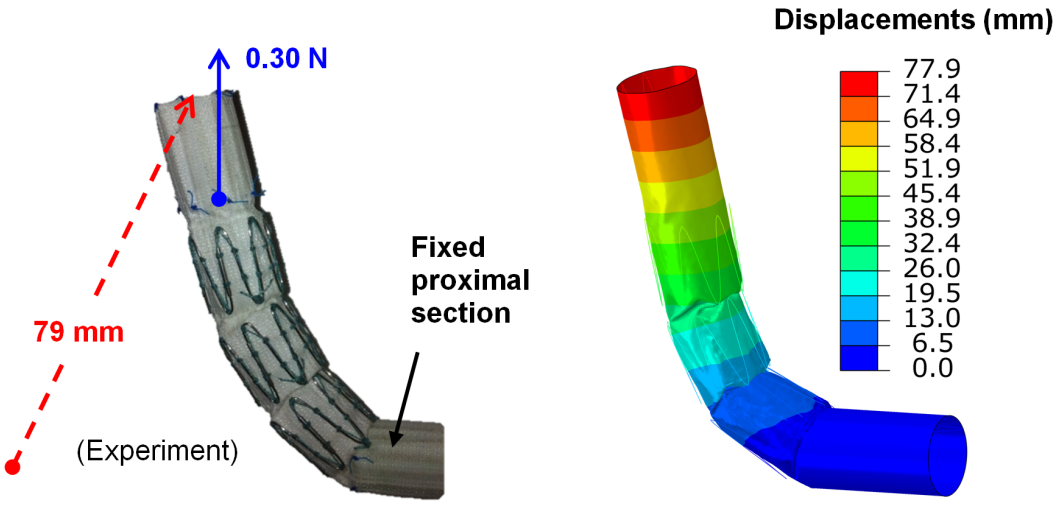

Figure 2.9: Comparison of experimental and numerical resultant displacements from a simple bending test for a leg TFLE-12-73-ZT.

Moreover, a displacement of 78.9 mm could be reproduced by changing the mesh size to 0.12 mm for the graft, which also means that the results do not depend on mesh refinement. The solution is "mesh size independent".

2.3.2 Body simple bending

Real SG are not perfect geometries like their virtual model. In particular, the graft is not strictly cylindrical and forms random corrugations between each pair of stents (irregular diameter). This is depicted in Figure 2.10(a).

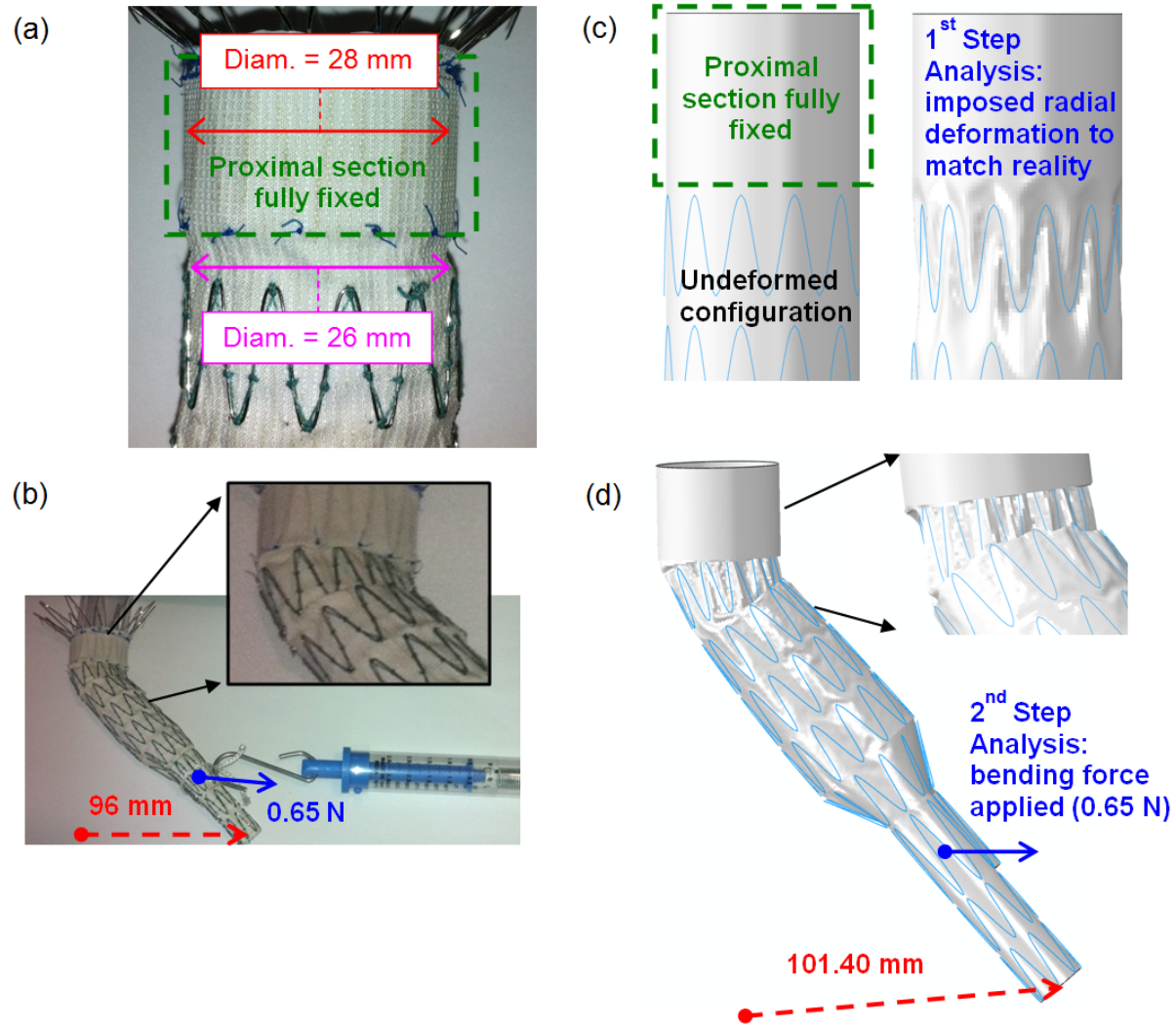

Figure 2.10: Comparison of experimental and numerical resultant displacements from a simple bending test for a body TFFB-28-125-ZT. (a) Real diameter discrepancy. (b) Experimental displacement. (c) Numerical diameter discrepancy. (d) Numerical displacement.

Such discrepancies have a non-negligible effect on the non-linear response of the simulated B-SG, mainly because they are located where the maximum bending moment causes the largest deformations. Therefore, a similar diameter variation was reproduced in a first step (Figure 2.10(b)). The actual bending loads were applied in a second step, allowing a displacement in good agreement with experiments.

2.3.3 Body three-point bending

The vertical displacement was measured at the center of the superior support. This configuration involved supports made of a polymer and for the sake of accuracy, a kinetic coefficient of friction of 0.6 was accounted for. This value is based on the study from Vad et al. (2010) who investigated experimental and numerically such coefficients for several brands of SG.

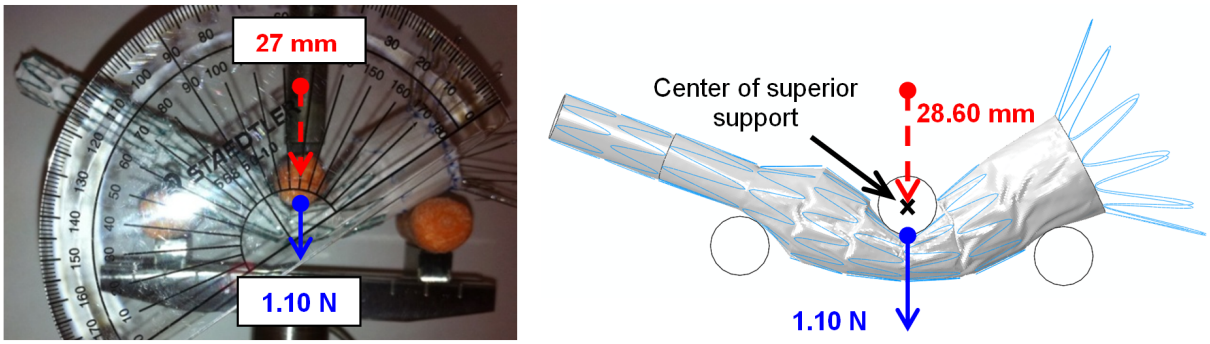

Figure 2.11: Comparison of experimental and numerical resultant displacements from a three-point bending test for a body TFFB-28-125-ZT.

A sensibility study was conducted on this model to make sure the results were independent from variations of the prescribed element size. The stents element size was first halved from 0.7 mm to 0.35 mm, which increased the global vertical displacement by 5.35%. Also, the graft element size was halved from 0.5 mm to 0.25 mm (keeping a size of 0.7 mm for the stents), which decreased the global vertical displacement by 4.43%. Thus, the model provided a solution that was reasonably independent from the element size (differences around 5% being acceptable).

2.3.4 Body axial compression

A strong buckling obviously occurred during this load case and made the solution quite noisy (Figure 2.13), however the response ended up stabilizing itself when the final equilibrium was obtained.

The usual order of magnitude of the simulated events (*time period* in Abaqus nomenclature) is about one second, and this was the case in general in this thesis, unless otherwise stated. For this particular load case, two analyses were conducted with prescribed time periods of 2 s and 6 s, and were stopped at 1.5 s and 2 s respectively after the total imposed displacement of 12 mm was reached and constant vertical reactions of 1.0 N and 0.5 N were observed. A 2 s time period is quite standard, whereas a 6 s time period is more "quasi-static concerned". Finally, the mean response of $1.0 + 0.5 = 0.75$ N was considered, knowing that this deformation mode would need additional investigation.

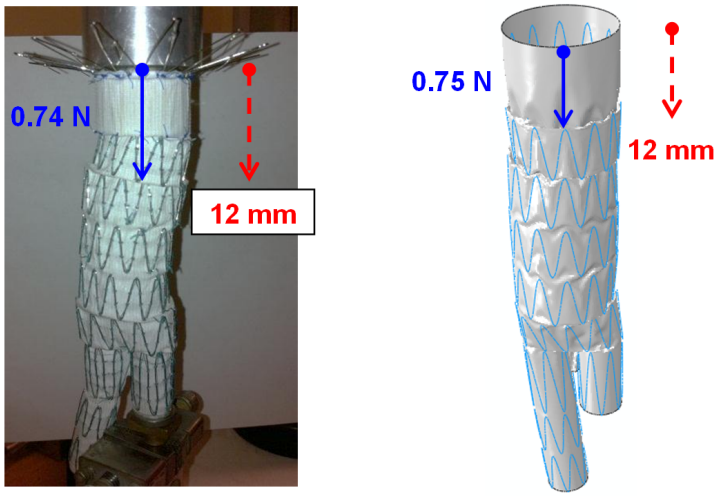

Figure 2.12: Comparison of experimental and numerical resultant displacements from an axial compression test for a body TFFB-28-125-ZT.

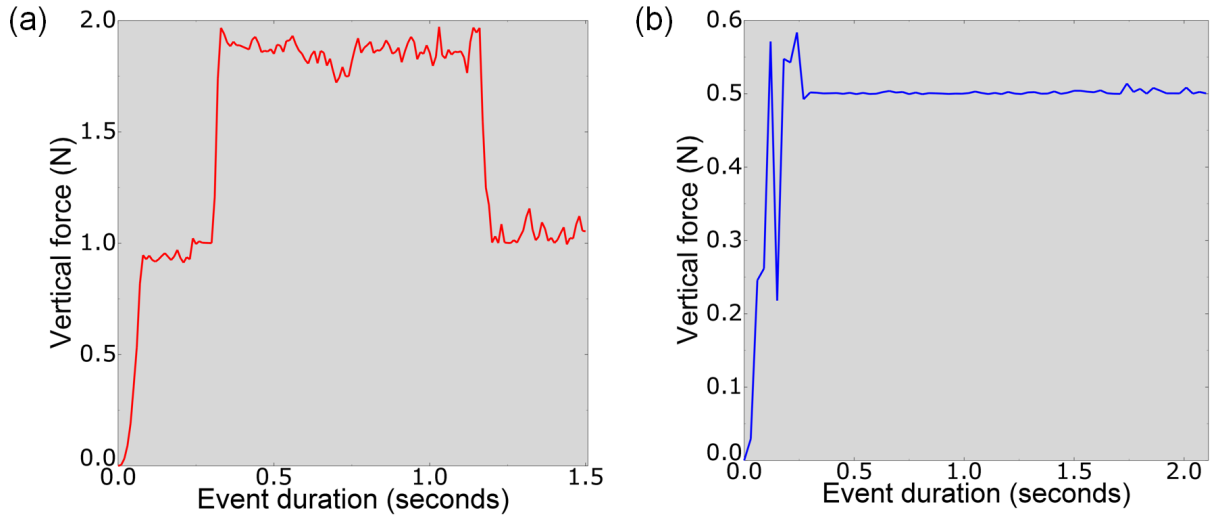

Figure 2.13: Reaction forces from axial compression tests for a body TFFB-28-125-ZT. (a) Prescribed time period of 2 s. (b) Prescribed time period of 6 s.

2.3.5 Bare stent transversal compression

This load case is straightforward. Since a slender structure with a negligible surface of contact was simulated, no friction was modeled. A fairly low difference of 3.23% could be observed between the experimental and numerical results.

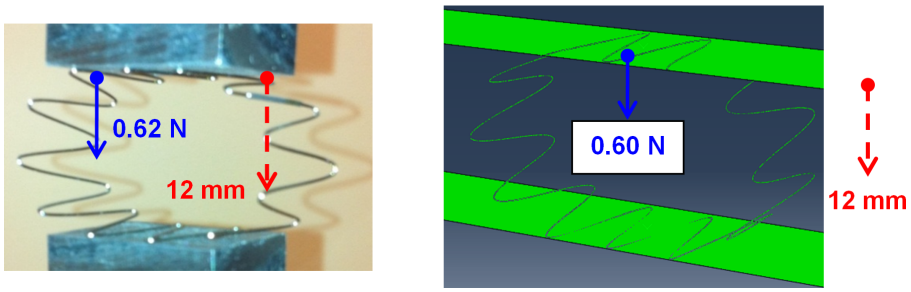

Figure 2.14: Comparison of experimental and numerical resultant displacements from an transversal compression test for a body TFFB-28-125-ZT.

2.3.6 Bare stent radial compression

This load case was conducted numerically only, assuming that the "pure" radial compression validity was covered by the well reproduced transversal compression test.

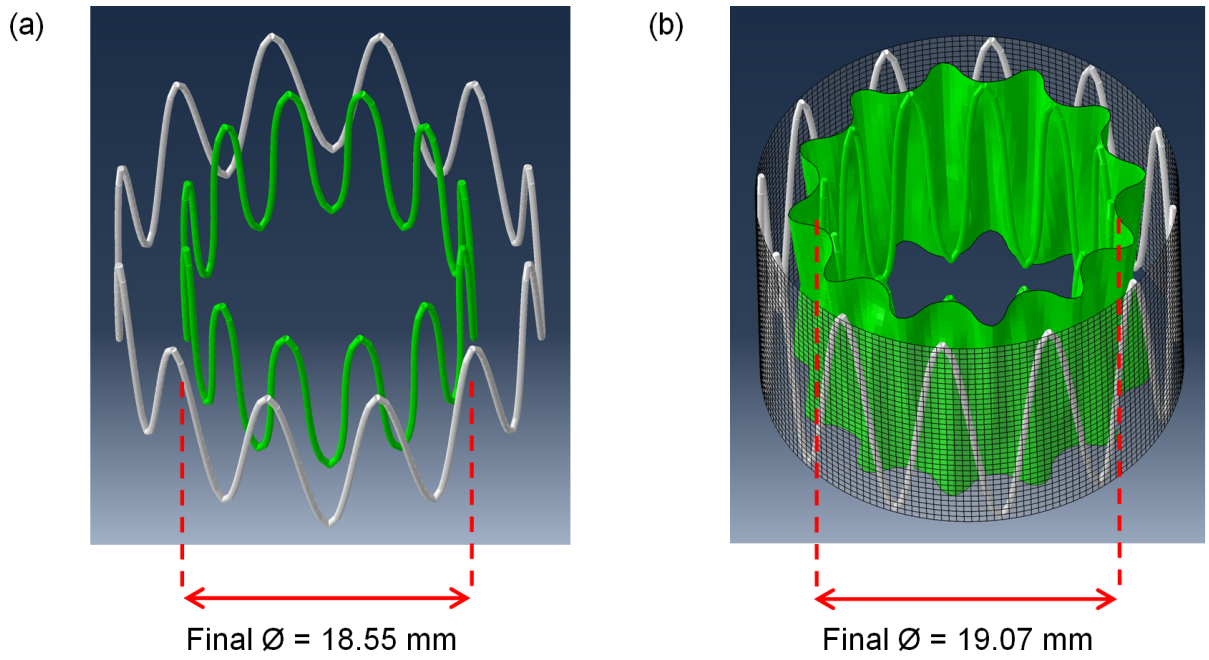

Figure 2.15: Numerical influence of the graft on a body TFFB-28-125-ZT proximal section submitted to a force of 6.24 N in radial compression (undeformed meshes in white). (a) Bare stent. (b) Stent-graft section.

Doing so, a fair comparison was possible while avoiding the difficulties and expected inaccuracies from an experimental test due to instability and friction. Here these aspects were well controlled. The body proximal section, with a nominal diameter of 28 mm was submitted to a total radial force of 6.24 N distributed over the stent nodes. As depicted in Figure 2.15 the bare stent and (full) SG section diameters were reduced to 18.55 mm and 19.07 mm respectively. This represents a difference of 2.80% (between two numerical results only), the graft has a negligible influence on the radial stiffness.

Such result is important for clinicians who are mainly concerned with the radial compliance of both the proximal and distal sections of the prosthesis. As can be seen in Figure 2.15(b), the graft naturally folds, which is crucial to anticipate type I endoleaks. Experimental and numerical results are compared in Table VII. The maximum difference of 5.93% comes from the three-point bending load case performed on the B-SG.

Table VII: Comparison of experimental and numerical results (Measured against Simulated). Forces (F) and Displacements (D) units are Newton and mm respectively.

	Imposed	Measured	Simulated	Difference (%)
L-SG simple bending	F 0.30	D 79	D 78	1.27
B-SG simple bending	F 0.65	D 96	D 101.40	5.62
B-SG three-point bending	F 1.10	D 27	D 28.60	5.93
B-SG axial compression	D 12	F 0.74	F 0.75	1.35
B-SG transversal compression	D 12	F 0.62	F 0.60	3.23

2.4 Comparison and discussion of experimental and numerical results

Despite the non-linearities dealt with during these tests, a maximum difference of 5.93% could be reached between both the experimental and numerical outcomes. This is close to the clinical tolerance of 5% usually considered in the present context. However, if this was a satisfying *verification* allowing to investigate the next steps towards virtual stenting, some additional tests might be needed on a larger number of specimen samples and performed by several analysts to achieve a definitive *validation*. Moreover, some tests like B-SG and L-SG simple bending may be realized with specific tools/protocols rather than manually and equipped with a simple dynamometer. Also, additional numerical analyses should be done regarding the axial compression load case, particularly with a wider range of prescribed time periods, typically from 6 s to 20 s.

2.5 Modeling of the pre-tension in stent-grafts

Actually, in the above development, a *relative* comparison was done, which was correct since a linear relationship between deformation and applied force was assumed. Indeed, force variations were applied while discarding the pre-tension already present in the stents that are radially compressed by a graft of inferior diameter.

To investigate further, the stents from the previously tested B-SG (TFFB-28-125-ZT) and L-SG (TFLE-12-73-ZT) were extracted. Therefore they naturally expanded to recover their unloaded diameter, which is presented in Figure 2.16.

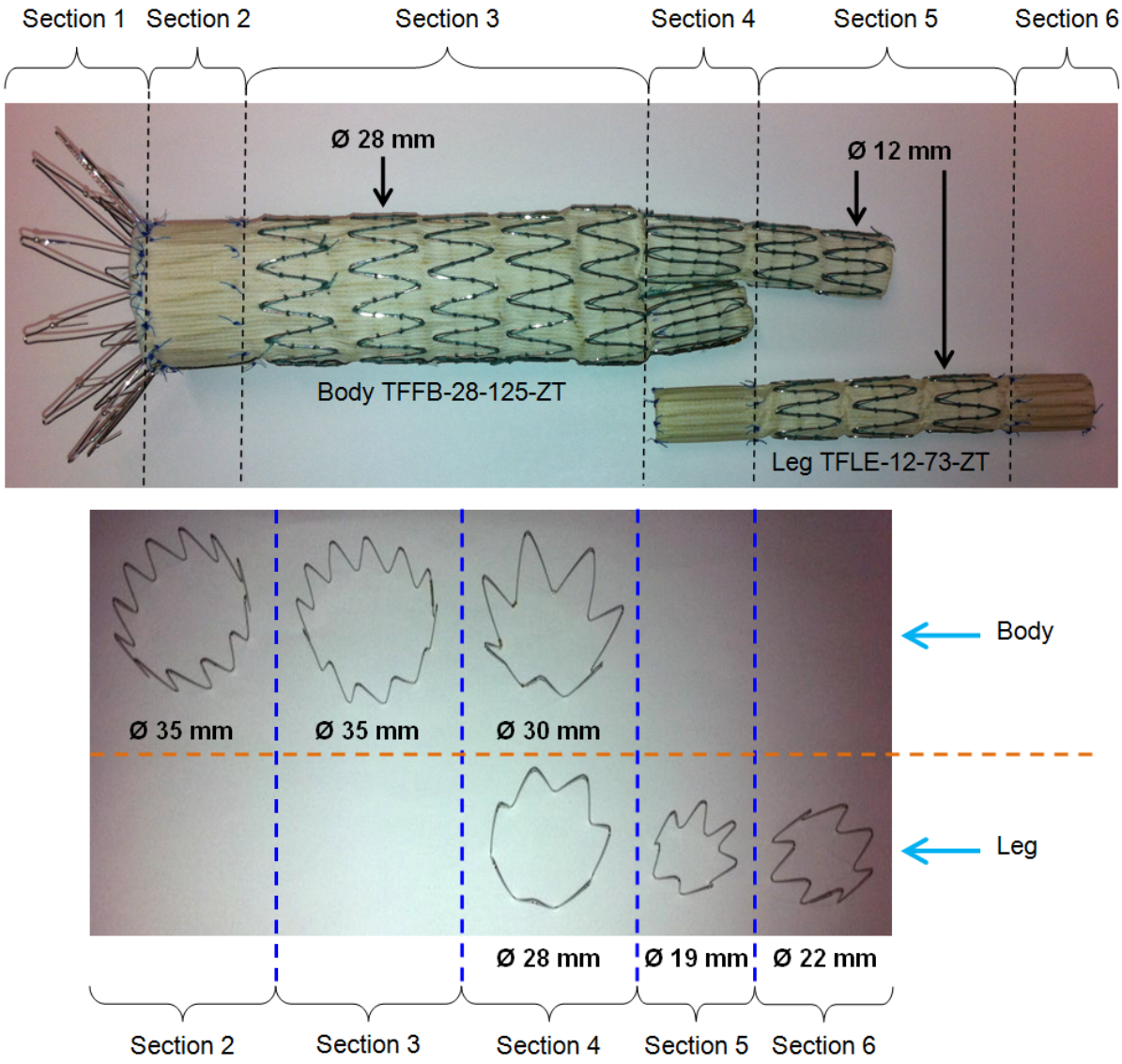

Figure 2.16: Diameter of freely expanded stents to illustrate their pre-tension state.

The easiest way to account for pre-tension is increasing the Young's modulus of each stent, knowing that the bending stiffness of beams linearly depends on the Young's modulus.

In a first step, the linear relationship between the radial force and diameter reduction for the proximal section of the B-SG was demonstrated numerically, for a diameter reduction to 70% of its nominal diameter of 28 mm. This is illustrated in Figure 2.17.

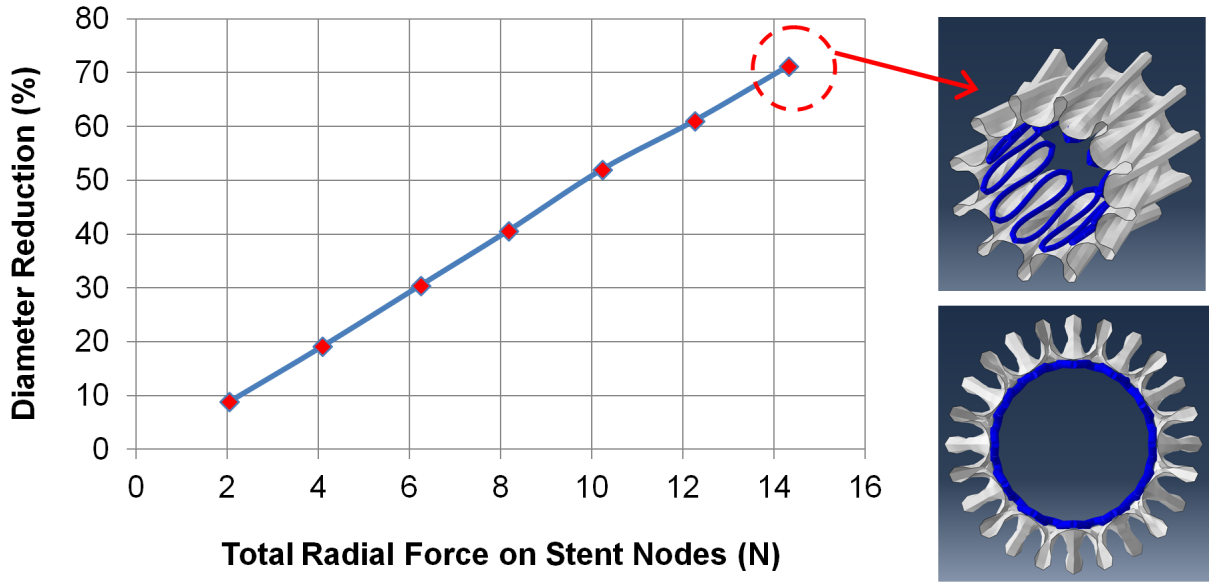

Figure 2.17: Relation between the total radial force and diameter reduction for the proximal section of the body TFFB-28-125-ZT (nominal diameter of 28 mm). No initial pre-tension considered. Radial force distributed on the 312 nodes of the stent.

Then, virtual stents corresponding to B-SG TFFB-28-125-ZT and L-SG TFLE-12-73-ZT sections were created, actually two variations of each of them, i.e. expanded and pre-tensioned. Pre-tensioned variations just had the same diameter as observed for each SG, but no initial or residual stresses were introduced, thus the term "pre-tensioned" just refers to a geometry. Then all expanded stents were radially compressed to half the nominal pre-tensioned SG diameter and the resulting radial forces were recorded. Finally, the diameter of all corresponding pre-tensioned stents was reduced to the same "target" diameter with (iteratively) increased Young's moduli E_{pre}, until reaching the same radial reaction force (Figure 2.18). Equivalent Young's moduli for pre-tension modeling ensure correct radial stiffnesses to be applied on the vessel wall during deployment simulations.

The results are gathered in Table VIII.

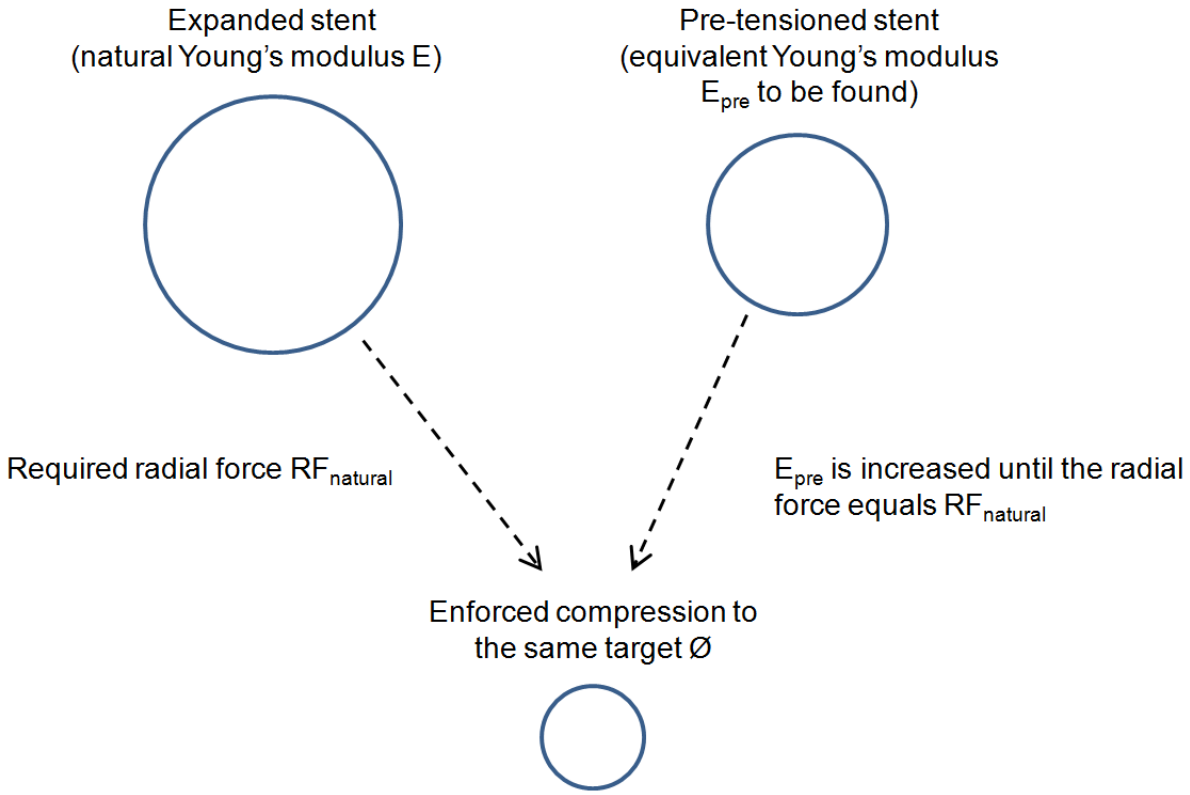

Figure 2.18: Illustration of the strategy to determine the pre-tension in stent-grafts.

Table VIII: Determination of Young's moduli accounting for pre-tension in stents from a body TFFB-28-125-ZT and a leg TFLE-12-73-ZT (assuming Z stents made of nitinol for the leg section 5). E_{init} stands for the initial Young's modulus and F_r for the radial force. F_r values are similar between expanded stents and pre-tensioned ones because an equivalent stiffness was successfully achieved to simulate the pre-tension (at the same target Ø). This correction applies at least to the range of diameter reduction in which a linear behavior was demonstrated above. SS and Ni correspond to Stainless Steel and Nitinol respectively

		Target Ø	Expanded stent			Pre-tensioned stent	
		(mm)	Ø (mm)	E_{init} (MPa)	F_r (N)	E_{pre} (MPa)	F_r (N)
Body	Section 2	14	35	193 000 (SS)	9.876	272 000	9.866
	Section 3	14	35	193 000 (SS)	17.131	267 500	17.134
	Section 4	6	30	193 000 (SS)	4.637	666 000	4.641
	Section 5	6	19	193 000 (SS)	9.786	349 290	9.764
Leg	Section 4	6	28	193 000 (SS)	11.234	569 100	11.200
	Section 5	6	19	50 000 (Ni)	2.449	84 000	2.451
	Section 6	6	22	193 000 (SS)	15.666	368 200	15.666

In an average sense, the 316L steel Young's modulus is increased from 193 000 MPa to the (mean) value of 415 000 MPa, and the nitinol one from 50 000 MPa to 84 000 MPa. *Thus, a rule of thumb to estimate Young's moduli accounting for pre-tension in stents is doubling initial values.* For the sake of simplicity, the L-SG Z stents from section 5 was made of nitinol rather than 316L steel, so the results could be generalized to Spiral-Z stents made of nitinol as it is the case for the latest generation of L-SG. This approximation was made since Spiral-Z stents do not expand purely radially, and because an exact modeling is far from trivial.

This is a very important aspect of SG modeling, so far neglected in the literature, to achieve a realistic diameter recovery and radial stiffness of SG in deployment simulations.

Obviously, a more realistic pre-tension modeling is possible via multi-step analyses by actually compressing all the stents, and releasing them *in situ* while simulating the sutures with "sticky" contacts. But this level of complexity is left for further detailed investigations.

2.6 Python script to generate stent-graft models automatically

Building finite element models of SG is quite a substantial task, therefore two Python scripts were written to do so in an efficient manner. With these scripts it is possible to generate the FEM corresponding to bodies *Zenith Flex AAA* (models TFFB-22-82-ZT to TFFB-32-140-ZT) and legs *Zenith Spiral-Z AAA* (models ZSLE-9-39-ZT to ZSLE-24-90-ZT) from Cook Medical (Figures 2.1 and 2.2). Actually, this is done in just a few seconds, as opposed to about half a day if done manually.

The code was organized in subordinate functions creating generic stents and a main function creating the graft, stent-graft assembly, materials, tie constraints (mimicking sutures), and mesh for each SG model. The scripts for the bodies and legs have about 3500 and 6500 lines respectively, so it is decently not possible to present them in this document. However, a short "user manual" is presented in Appendix A.

2.7 Conclusion

This first part covered the experimental mechanical characterization and finite element (FE) modeling of SG. Although a large scale validation was not possible due to a limited number of specimen samples, and also because of limited available time, a thorough verification

was however conducted on a typical B-SG and L-SG. The maximum difference achieved between experimental and numerical data, i.e. 5.93% is close to the clinical target of 5%. The second part will be dedicated to AAA modeling, from medical imaging (3D) segmentation to mechanical analysis via the FE method.

Part II

AAA modeling

Chapter 3

Finite element model of AAA

3.1 Introduction

3.1.1 Generalities about healthy aortas

Let's start with a description of healthy abdominal aortas, that are composite structures constituted of three layers, i.e. the (innermost) intima, media and adventitia (Figure 3.1).

The intima replies to stimuli coming from both the blood and cellular matrix. It hosts the endothelium, a monolayer of endothelial cells. The latter manages the vasoconstriction and vasodilation by controlling vascular smooth muscle cells (VSMC) and their growth. Endothelial cells are anti-thrombotic, play a key role in angiogenesis (regeneration of damaged vessels) and in the selective permeability of anti-inflammatory cells from blood to the vessel wall.

The media is the domain of VSMC organized in musculo-elastic concentric layers. VSMC are surrounded by a conjunctive tissue made in majority of elastic fibers (elastin) and collagen fibers. The elastin is responsible of the aortic capability to resume its shape after stretching or contracting, and its production is associated to VSMC. Collagen fibers provide the aorta structural integrity and rigidity.

The adventitia wraps the media of a conjunctive tissue mainly made of collagen. The latter is produced by sparse fibroblast cells. The adventitia also has nerves and the vasa vasorum that is a network of capillaries bringing oxygen and nutrients. Thus, VSMC located in the media are fed from both the intima and adventitia.

Arteries can be classified into two categories; muscular and elastic. Muscular arteries (coronary, femoral, splenic and renal arteries) have no elastic fibers, and VSMC ensure their vasomotor function. On the other hand, elastic arteries (aorta, large supra-aortic

arterial trunks and iliac arteries) are characterized by a media layer that is rich in elastic fibers which ensure the arterial compliance. The abdominal aorta is clearly elastic, and explains the *Windkessel* effect (at the systolic peak 40% of the expelled blood is stored in the "elastically" deformed vessel, and sent back to the circulation during the diastole period after the artery resumes its undeformed shape, thus converting elastic energy into kinetic energy and eventually ensuring a continuous flow).

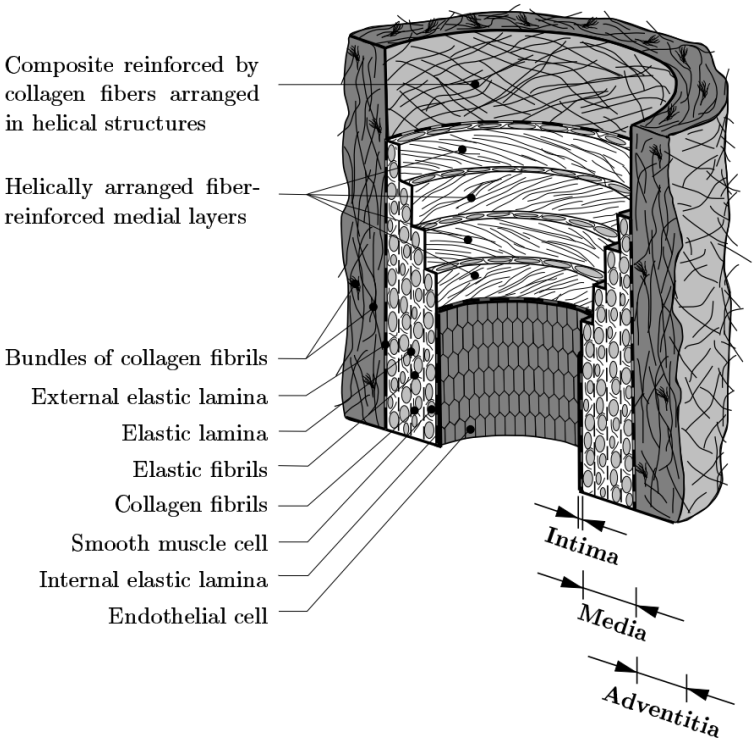

Figure 3.1: Histological composition of the aorta (Holzapfel et al., 2000). Reproduced with the permission of Elsevier.

Between 2003 and 2004, some clarifications were made regarding the viscoelasticity of arteries. It was found that this property is related to the proportion of VSMC (Van Oijen, 2003). Holzapfel and Ogden (2003) indicates that viscoelasticity can be neglected for aortic modeling, since the aorta is a proximal artery with a large diameter and contains less VSMC in the media layer, than medium-size vessels, such as femoral and cerebral arteries, which are considered viscoelastic. However, in the general study of arteries the viscoelastic behavior is important, especially for dynamic and fluid-structure analyses because it might modify the frequency response. Viscoelasticity is also very important in elastography.

For these reasons the aorta was considered to be elastic, thus following the general trend of using hyperelastic models, as observed in the literature (Fung, 1993; Holzapfel et al.,

2000; Weisbecker et al., 2012), even if some authors implemented interesting viscoelastic models (Quaglini et al., 2004; Amblard et al., 2009).

3.1.2 About AAA

In AAA the maximal diameter can reach 120 mm and the wall thickness usually lies in a range of 1.5 to 2 mm (Toungara, 2011). Actually, with the present technology, it is not possible to extract accurate values for the wall thickness distribution. As already mentioned, the genesis of AAA is still an important topic of research, but it is known that pulse waves have an amplified echo in bifurcations, which combined with hypertension, explain the frequency of vascular dilations in the aortic and cerebral bifurcations. Subsequently, the departure from cylindrical shapes is likely to trigger blood stagnation and recirculation, hence leading to the formation of ILT in 75% of the cases (Harter et al., 1982). In addition, the low shear stresses induced by blood recirculation reduce the production of nitric oxide (NO_2) that acts as vasodilator, platelet aggregation inhibitor and anti-inflammatory substances producer.

There are still controversial opinions about the ILT "protective" effect. Indeed, seen as a homogeneous and elastic material (Li et al., 2008; Van Dam et al., 2008), the ILT may reduce wall stresses in AAA by acting as pressure "shield", however it is actually porous and a fraction of blood is transmitted to the AAA. In fact, it was clinically shown that the pressure throughout the ILT is almost constant (Schurink et al., 2000). The latter argument mitigates the "cushion" effect attributed to the ILT (Li et al., 2008; Van Dam et al., 2008). In addition, the ILT reduces the flow shear stresses (FSS), thus also anti-inflammatory substances, and weakens the wall by hypoxemia. A porous ILT model based on Darcy's law was presented by Toungara (2011), but clinical studies are still needed to identify realistic porosities and permeabilities.

Significant changes in the AAA structure were reported by He and Roach (1994), and the following results were found over 8 aneurysms; the volume fraction of elastin decreased from 22.7% to 2.4%, the volume fraction of VSMC decreased from 22.6% to 2.2% and the volume fraction of collagen and ground substance altogether increased from 54.8% to 95.6%. This explains the loss of vascular elasticity associated with this pathology, and further justifies that viscoelasticity can be neglected for the specific study of AAA. The biomechanical models best describing the aorta hyperelastic behavior are based on strain energy density functions (SEDF). A first isotropic model was devised by Raghavan and Vorp (2000), after a previous publication providing uniaxial stress-strain curves along the axial and circumferential directions (Raghavan et al., 1996). In parallel, Holzapfel et al.

(2000) introduced an anisotropic model, but it was only after Vande Geest et al. (2006) published the (only) available biaxial stress-strain curves that anisotropic models could be nourished with experimental data, and implemented into FEA packages. Since then, several variations of the original anisotropic model were presented (Rodríguez et al., 2008; Basciano and Kleinstreuer, 2009; Xenos et al., 2010; Ferruzzi et al., 2011). Here it should be mentioned that, at the moment, there are no experimental data about aneurysmal iliac arteries, but only about healthy aged ones (Schulze-Bauer et al., 2003).

Calcifications are also often present within the arterial wall. Marra et al. (2006) provided useful informations about stiffness (hardness and Young's modulus) after a detailed analysis of micromorphology and mechanical properties of vascular calcifications. Maier et al. (2010) conducted comparative numerical analyses involving several degrees of calcifications, i.e. "non-calcified", "disperse calcifications", "highly calcified" and "pure calcification", which surprisingly relieved that calcifications reduce the average wall stress by up to 59.2%. This goes against previous assumptions that calcifications would act as stress concentrators, in particular Speelman (2009) claimed that stresses could be increased by up to 20%. In this study, no calcifications were modeled.

3.1.3 Contributions

Anisotropic models might be considered for clinical validations, however the plethora of variations available in the literature makes the selection difficult. Besides, these models and associated parameters can only be implemented via subroutines written in Fortran, which is a tedious and error-prone task. Therefore, the anisotropic so-called "Holzapfel-Gasser-Ogden" (HGO) model already available in Abaqus was considered in this study. Doing so, the corresponding parameters were determined after a multiple non-linear regression on published biaxial tests (Vande Geest et al., 2006), which is explained in section 3.3.1. Anisotropy is related to the orientation of collagen fibers, and it was found that the methods presented so far were not robust neither accurate enough for real tortuous vascular geometries. Therefore, a more robust and innovative technique for collagen fibers orientation was devised, and is the object of section 3.3.2.

FEM are needed to simulate large displacements accurately, as well as wall stresses for rupture risk assessment, especially for complex geometries. Real-time solutions are only possible with haptic models that are purely based on mass-spring-damper systems, but these models are not as accurate as the ones based on the finite element method.

3.2 AAA Geometry reconstruction from medical imaging modalities

Retrieving the vascular 3D geometry is quite time consuming in itself since it generally involves a cascade of specialized applications. The necessary workflow is described hereafter.

3.2.1 Segmentation of AAA lumen and ILT

First of all, both the lumen and ILT envelopes were extracted from the medical imaging software distributed by Object Research Systems (ORS, Montréal, Canada). A plug-in dedicated to the segmentation was developed by Kauffmann et al. at CR-CHUM (pending patent ♯ US60/938,078). Its accuracy to provide measurement of AA maximal diameter and volume was previously validated. As a matter of example let's consider the anonymized case H1025269 extracted from the University of Montréal Hospital Research Center (CR-CHUM) database. ORS allows an automatic extraction of the lumen (Figure 3.2). As long as enough contrast agent was injected during a scan acquisition, the resulting mesh - made of triangular facets - is well defined. Such a mesh is the direct output from ORS and just defines the geometry, it is not yet a "finite element" mesh.

The proximal section is located above the celiac trunk and the distal one should ideally be slightly below the inguinal ligament, which will later be the lower limit of the finite element meshed domain (so this section plane is roughly horizontal).

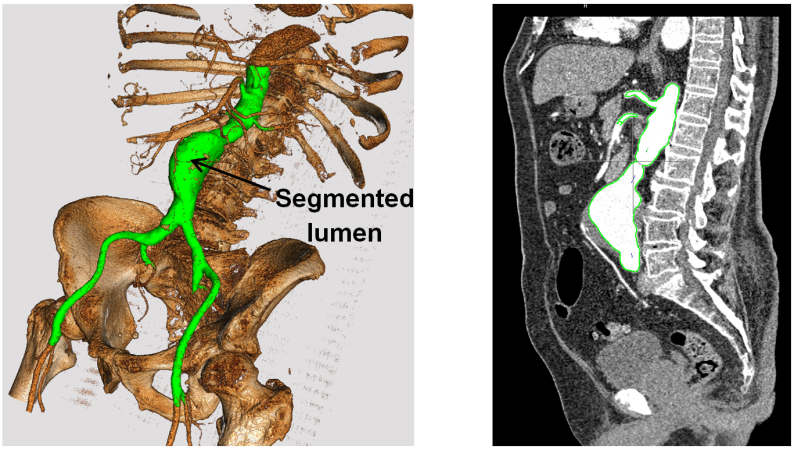

Figure 3.2: Patient-Specific AAA segmented lumen (case H1025269 from CR-CHUM database).

Regarding the ILT segmentation, this is a semi-automatic task in which one has to manually define the envelope via "snakes" defined by spline curves in 8 planes. There are

three guidelines to perform a successful ILT segmentation:

1. As shown in Figure 3.3(a) by the vertical red lines, the proximal and distal limits of the segmentation domain should be strictly confined to the space occupied by the ILT. This avoids disturbing penetrations of the ILT and lumen envelopes in the next steps.

2. Again referring to Figure 3.3(a) the snakes should stay away from the centerline to avoid "folded" ILT envelopes, and facilitate the subsequent closing operation to generate the corresponding volume. Also, where the ILT and lumen envelopes intersect, the intersection angle i should remain between 30° and 40°. An intersecting angle below 30° leads to really flat tetrahedral finite elements, whereas above 40° the vessel becomes too irregular. The Lumen and ILT envelopes need to intersect so the actual ILT volume can later be determined by means of Boolean operations (lumen volume subtracted from ILT volume), and meshed with tetrahedral finite elements.

3. As depicted in Figure 3.3(b), the ILT and lumen envelopes should meet smoothly and in an almost tangent fashion where they intersect (at every transversal plane). This is actually a corollary of the preceding guideline.

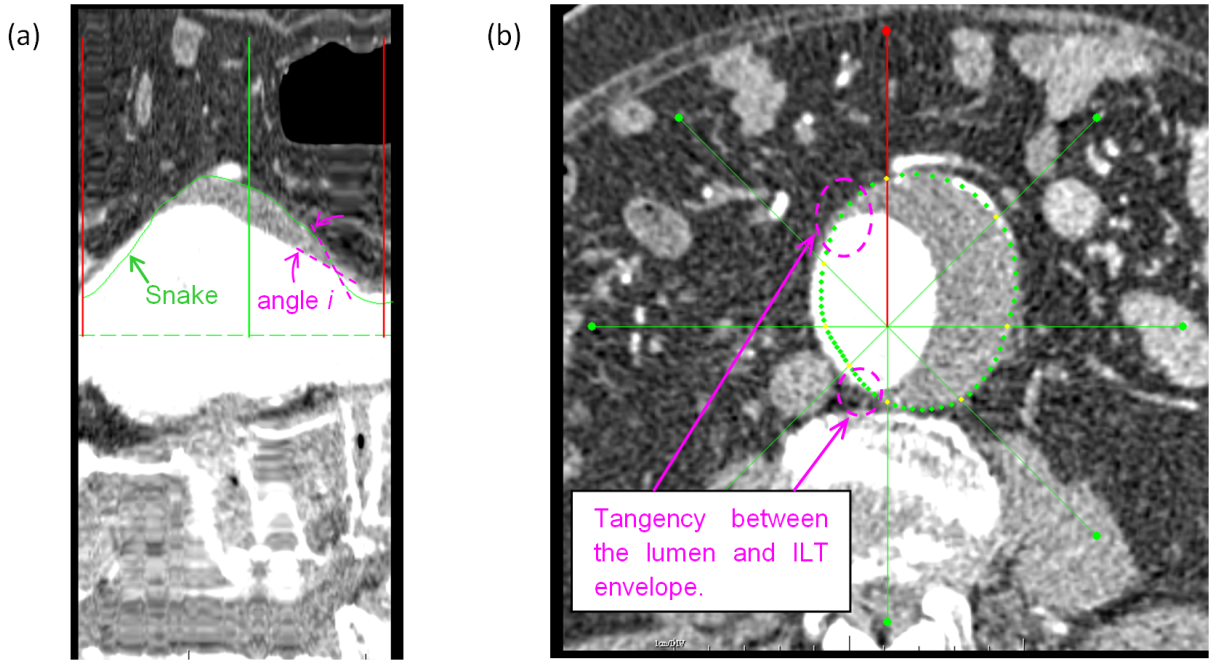

Figure 3.3: Patient-specific AAA segmented ILT (case H1025269 from CR-CHUM database). (a) Snake definition in the anterior plane. (b) ILT envelope.

In Figure 3.4(b) the end section of a typical ILT envelope is represented, it should ideally be as regular/circular as possible, which makes easier any subsequent closing operation.

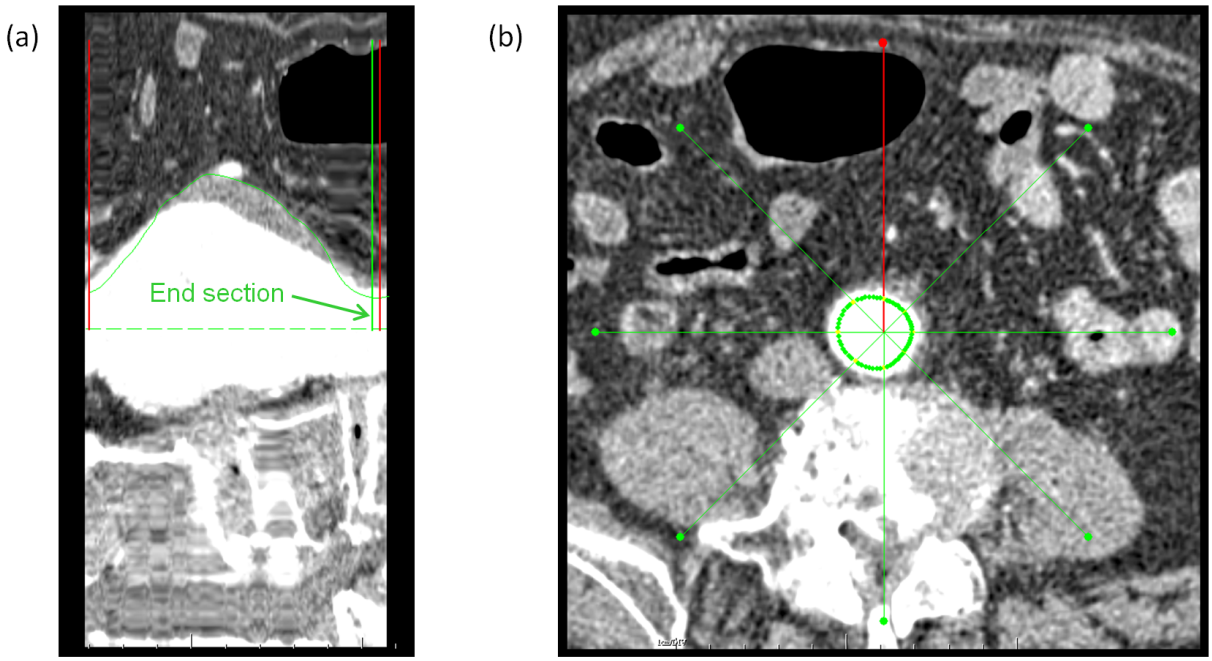

Figure 3.4: Typical end section of a patient-specific AAA segmented ILT (case H1025269 from CR-CHUM database). (a) Sagittal plane. (b) Transversal plane.

The next step after both the lumen and ILT envelopes are retrieved from ORS is to clean (removing any unwanted or unrealistic vascular feature), close and smooth these envelopes, which in turn makes possible the actual reconstruction into "native" Abaqus models for finite element meshing and analysis. This is done with the open source application Meshlab.

3.2.2 Cleaning and smoothing of AAA geometries

Many times the direct output/segmentation from medical imaging applications might be quite noisy, and therefore some cleaning and remeshing are needed. There exists a plethora of open source and commercial applications to do so, but here Meshlab was found to be adapted and versatile enough to meet the goal.

The optimal sequence of cleaning, closing and smoothing operations is presented in detail in Appendix B, but here a few points are to be explained in detail.

First of all, the closing operation is necessary to define the centerlines properly. Indeed this is achieved with a set of algorithms provided by the open source application VMTK (Vascular Modeling Toolkit). Algorithms from the VMTKCenterlines module rely on point

clouds and this is why it is better to avoid any large hole or open section, so a maximum of information about the geometry is treated. All smoothing operations must follow the closing ones so enough vertices are built in each proximal and distal sections, which allows the selection of source and target points that are truly on centerlines (Figure 3.5(b)). The latter requirement only holds for the lumen envelope because the centerlines are based on this geometry only, which will be illustrated in section 3.2.4. Closing the lumen and ILT envelopes is also important for Abaqus to generate the corresponding volumes. There should be strictly no holes at all, whereas in theory, a little hole (a single missing facet for instance) would not preclude the centerlines to be computed properly (since the associated algorithms only rely on point clouds).

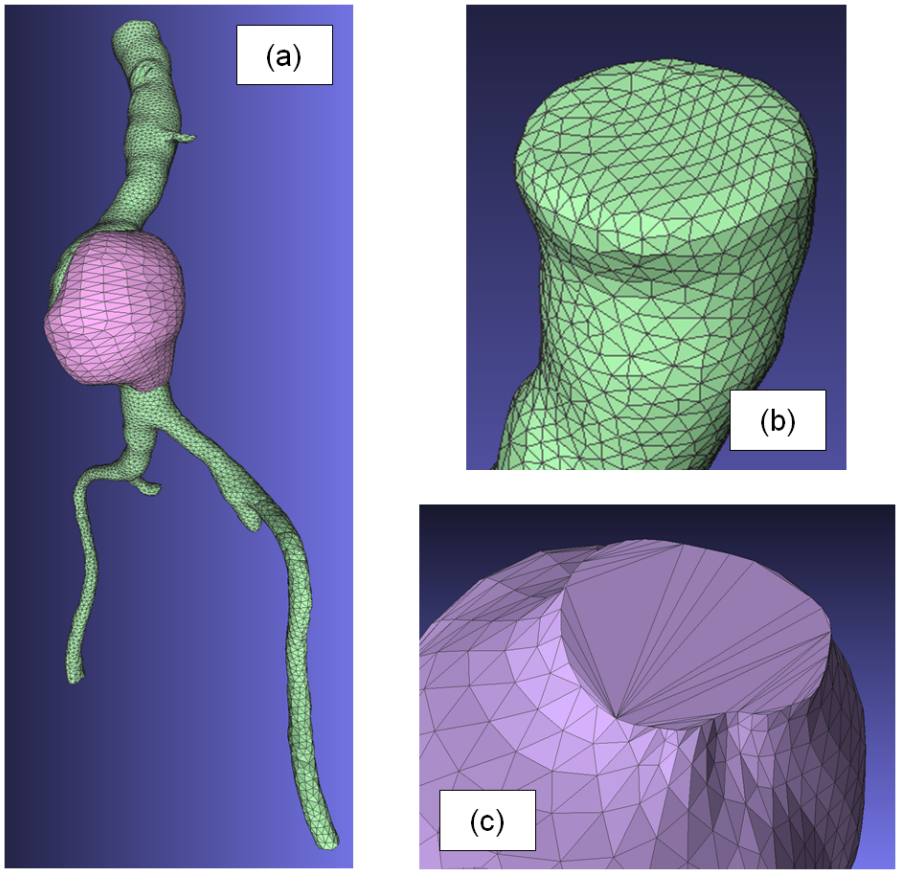

Figure 3.5: Example of ideal Lumen and ILT segmentations in Meshlab (case H1025269 from CR-CHUM database). (a) Meshes (lumen: 6986 vertices, 13 968 facets / ILT: 1095 vertices, 2186 facets). (b) Detail of the lumen proximal section. (c) Detail of the ILT proximal section.

Typical segmentations from ORS contain a large number of vertices and triangular facets, and the Python script designed to reconstruct the geometry in a native Abaqus

format (triangular facet wise) does not support such amount of data. Therefore, the vertices must be merged to a certain extent in order to reduce the model size, and based on experience there should remain about 11 000 vertices and 22 000 facets for the lumen. After merging the vertices, the associated facets are obviously coarser but the Abaqus "virtual topology" tool compensates this effect by creating a continuous smooth surface that can be cut and meshed with triangular or quadrilateral shell elements of controlled size, independently of the triangular segmentation coming from ORS and later modified in Meshlab. This workflow eventually allows using the full Abaqus toolbox on a native single surface (cutting, merging and meshing).

All face normals must point outward, so Abaqus can create volumes by filling the inner domain, otherwise it would attempt to fill the outer one, thus indefinitely, and would fail. This can be done in Meshlab by re-orienting all faces coherently, however this is rarely required as Meshlab properly orientates all faces by default. An inverted face usually appears with a dark color.

In Figure 3.6 the intersection of the lumen and ILT envelopes is clearly presented.

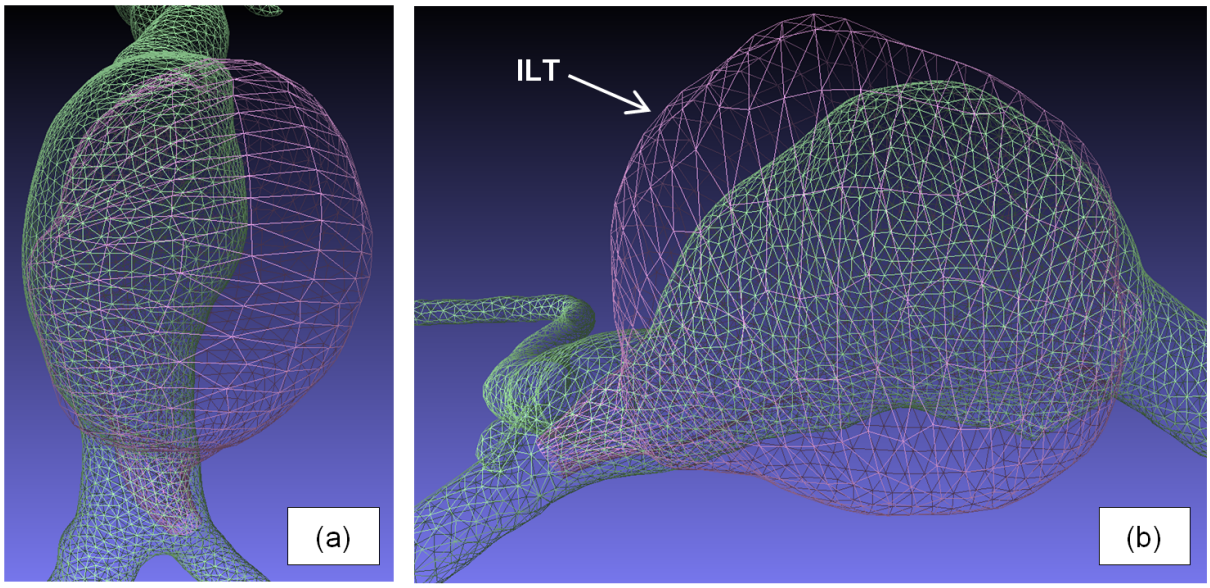

Figure 3.6: Intersection of lumen and ILT envelopes in Meshlab (case H1025269 from CR-CHUM database). (a) Front view. (b) Side view.

Once the lumen and ILT geometries are properly defined, they might be used as input for a Python script that will actually build the AAA wall and ILT as an Abaqus native surface and volume respectively. The actual ILT volume is derived by subtracting the lumen volume from the initial ILT volume extracted from the CT-scan (Figures 3.6, 3.7). Also, the actual AAA wall is derived from combining the lumen and ILT envelopes.

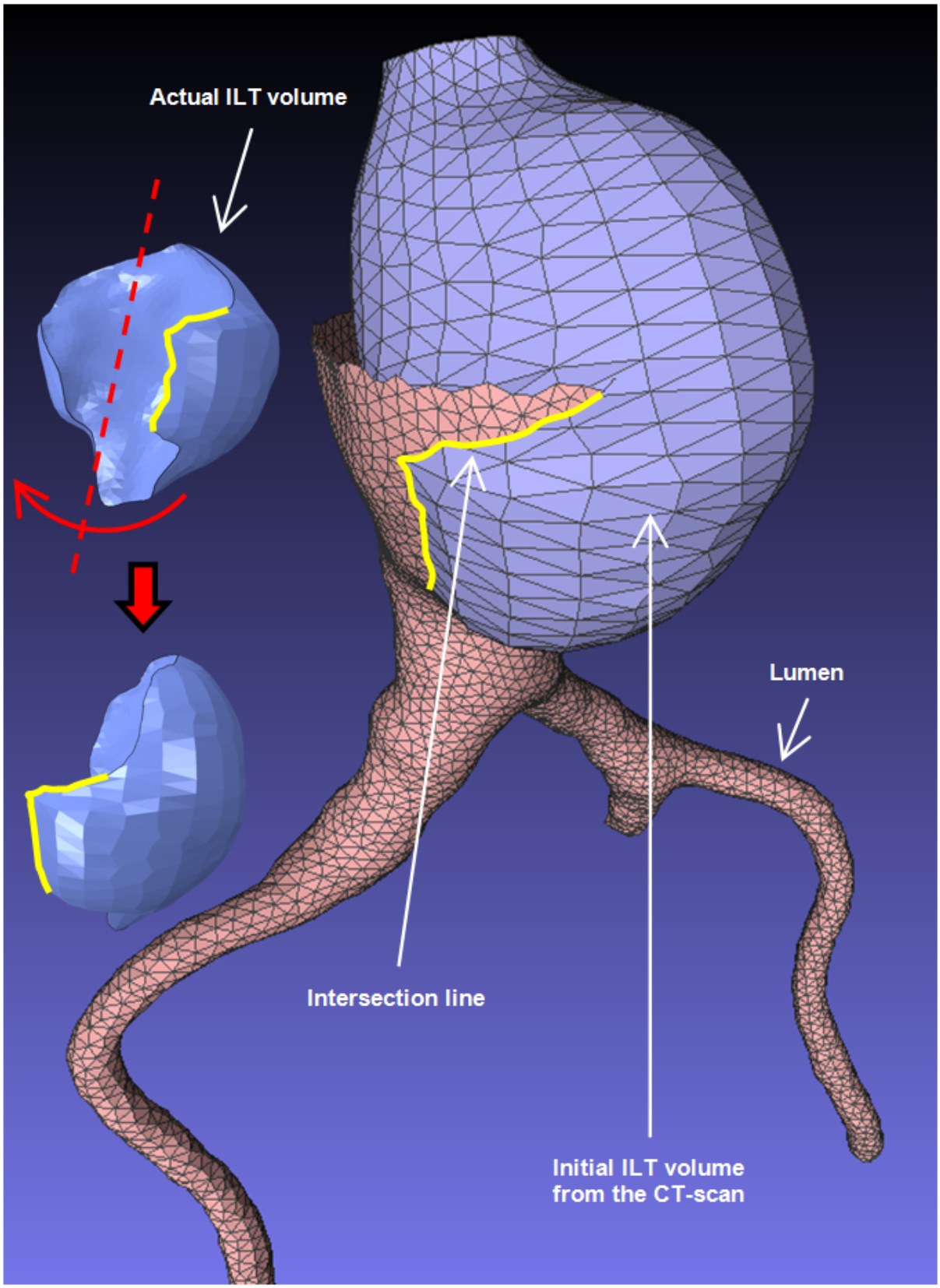

Figure 3.7: Intersection of the lumen and initial ILT volumes to define the actual ILT volume in Abaqus via a Boolean operation (case H1025269 from CR-CHUM database).

3.2.3 Python script to create a native geometry in Abaqus

Importing geometries directly from Meshlab to Abaqus results in geometries made of triangular facets that have a purely geometrical nature, i.e. this is not yet a "finite element mesh" incorporating the mechanics/physics of the AAA wall. Thus, if used as is, the finite element mesh would be supported/seeded by the initial facets sides, which would lead to a totally uncontrolled finite element mesh (Figure 3.8). Only triangular elements could be produced with very little control on their size, in fact no larger element size than the original facets could be prescribed. However this control is very needed to adjust the ratio of thickness to the typical element size (side or diameter length), and meet the criterion from the *Mindlin-Reissner* theory of thick surfaces, already mentioned for graft modeling. In parallel, one may avoid small elements in order not to decrease unnecessarily the stable time increment according to equation 2.4.

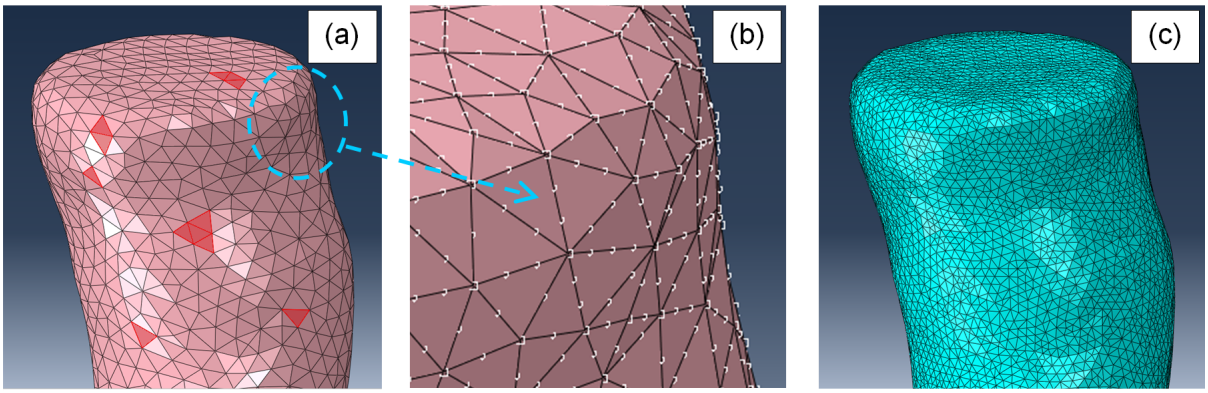

Figure 3.8: Clumsy AAA mesh without using a single continuous geometry (case H1025269 from CR-CHUM database). (a) Facets from Meshlab. (b) Mesh seed of the same facets. (c) Uncontrolled and clumsy mesh.

To solve this problem, the initial facets can be merged. But doing this manually would be quite tedious, therefore a Python script was written to make this task automatically and quickly. This script first performs some Boolean operations on the lumen and ILT envelopes/volumes, in order to extract the actual AAA wall surface. Then it merges the facets defining the AAA wall surface and ILT volume, thus resulting in geometries that can be cut and meshed at will. These merging steps are made possible by the "virtual topology" tool available in Abaqus. This "flexible" modeling strategy is illustrated in Figure 3.9.

AAA geometries are also defined by their centerlines. Indeed, being able to "map" AAA and their main collateral vessels in terms of centerlines is of primary importance to

measure their length and select the most suitable SG, but also to apply algorithms for collagen fibers orientation in anisotropic modeling, catheter interaction and deployment simulation. This is the object of the next section.

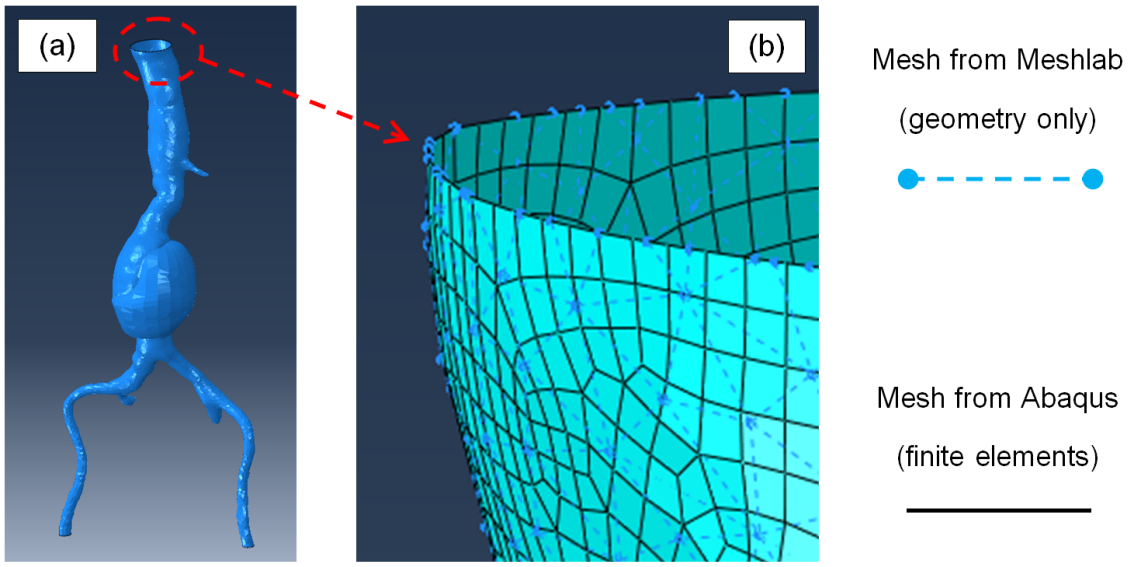

Figure 3.9: Improved AAA mesh using a single continuous geometry (case H1025269 from CR-CHUM database). (a) AAA wall as a single surface, obtained after a "virtual topology" operation. (b) Controlled finite element mesh, independent from the original triangular facets.

3.2.4 AAA centerlines and side branches

As indicated in section 3.2.2 VMTK is the ideal tool to define vascular centerlines. Not only points along the centerlines are provided, but also the mean diameter of the vessel at every point.

In Windows operating system, one can enter VMTK command lines in an interface named PypePad. The optimum sequence of commands, and how to execute them is detailed in Appendix C. Figure 3.10 shows how the source and target points are selected, as well as the conventional order in which targets are selected. This convention is arbitrary, but helps identifying centerlines for each vessel branch. Figure 3.10(a) justifies why it is important to have enough points on the ending sections, particularly the proximal one.

Even though VMTK offers the option to automatically detect the source and target points on open geometries, one would then loose the advantage of selecting targets in a specific order (manually), hence closed geometries are needed to do so.

Obviously the centerlines have to be computed with the lumen geometry (Figure 3.10),

but one could use the AAA wall as an approximation if not possible otherwise, depending on the ILT level of symmetry.

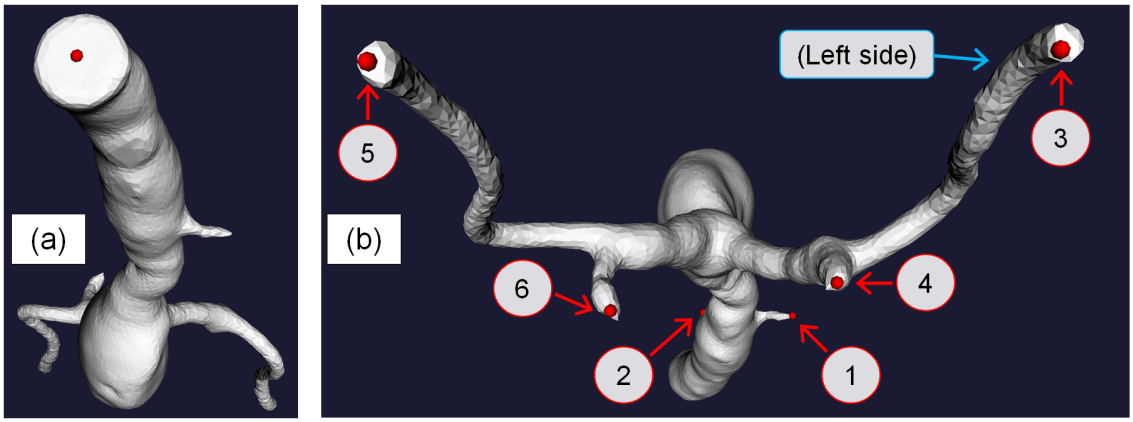

Figure 3.10: Selection of the source and target points in VMTK (case H1025269 from CR-CHUM database). (a) Source point. (b) Target points by conventional order of selection.

Eventually VMTK returns the associated data file listing all points, their coordinates as well as the local diameter of the related vessel branch. However, for each vessel branch the corresponding centerline starts from the same source and goes to each target point, thus duplicating every overlapping points as much as branches are defined, typically 6 (Figure 3.10(b)). Therefore, another Python script was designed to sort out the data file and export the centerline for each branch to Abaqus with a tolerance of 2.0 mm (Figure 3.11).

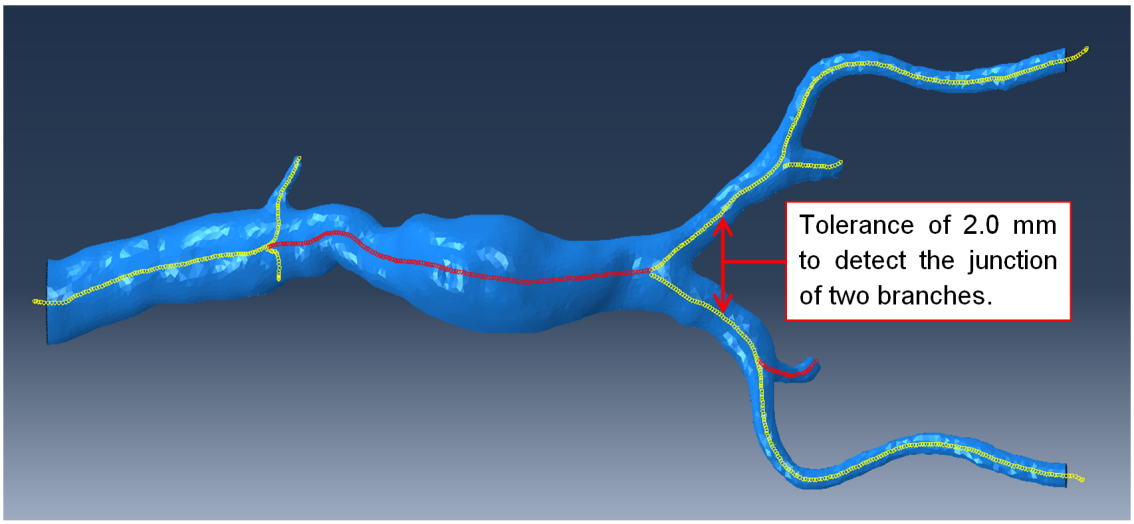

Figure 3.11: Centerline construction for each vessel branch in Abaqus (case H1025269 from CR-CHUM database). The central and right internal iliac branches are highlighted in red.

3.2.5 Creation of a rigid surface representing the spine

The spine constitutes the last entity which geometry can easily be extracted from CT scans (Figure 3.12). It represents a rigid constraint to any AAA backward movement, and was included in the FEM. Additional techniques about surrounding organs modeling is provided in section 3.5.4.

The employed strategy merely consists in picking some points along the spine from the original CT scan (sagittal plane). These points are then imported in Abaqus and a spline is created and extruded over 100 mm. Finally, the created spine (rigid) surface is located aside the AAA according to the real position, which is achieved after some matricial operations (translation and rotations). As can be seen in Figure 3.12, the only guideline is to define the upper border of the spine to be slightly over the AAA mesh (at least 10 mm), in order to avoid any contact issue later on in the analysis.

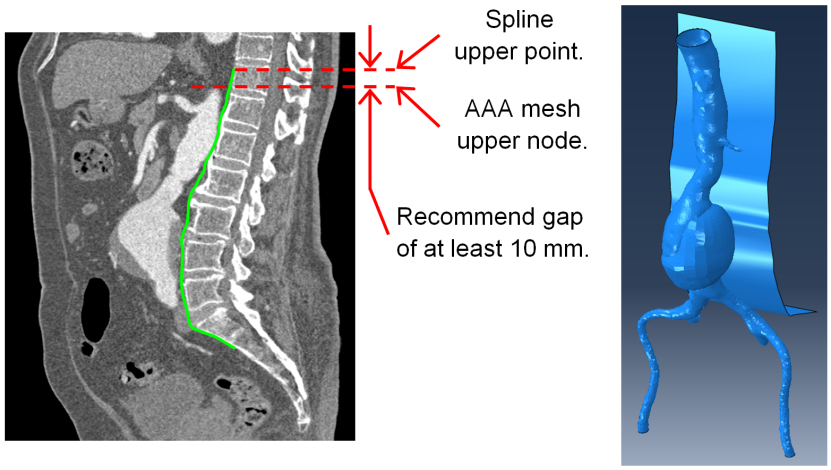

Figure 3.12: Spine reconstruction in Abaqus (case H1025269 from CR-CHUM database).

This completes the geometrical definition of the vascular environment, and the next section is devoted to materials definition, in particular for the AAA wall.

3.3 AAA biomechanics

3.3.1 Anisotropic strain energy function and its parameters for AAA

Let's gradually introduce the formalism of non-linear biomechanics for the hyperelastic modeling of AAA via anisotropic SEDF. An hyperelastic material is characterized by a non-linear and reversible stress-strain curve, thus deprived of any significant plastic behavior, and therefore, may undergo large deformations before rupture. These materials are mostly incompressible. SEDF simply represent the stored elastic energy per unit of reference volume, based on which stresses and strains can be derived.

The motivation to develop anisotropic models as opposed to isotropic ones, comes from the first comprehensive uniaxial tensile tests performed on AAA specimen samples (Raghavan et al., 1996; Thubrikar et al., 2001), that showed different replies along the circumferential and axial directions. This trend was later confirmed by biaxial tensile tests performed in particular by Vande Geest et al. (2006), who also showed that only healthy abdominal aortas can be considered isotropic.

3.3.1.1 General theoretical background

The first term to be defined at this stage is the deformation gradient tensor, or simply deformation gradient $\mathbf{F} = d\mathbf{x}/d\mathbf{X}$, between a reference (undeformed) configuration $\mathbf{X}$ and a current (deformed) configuration $\mathbf{x}$ (Figure 3.13). In its most general form $\mathbf{F}$ stands as

$$\mathbf{F} = \begin{pmatrix} \frac{\partial x_1}{\partial X_1} & \frac{\partial x_1}{\partial X_2} & \frac{\partial x_1}{\partial X_3} \\ \frac{\partial x_2}{\partial X_1} & \frac{\partial x_2}{\partial X_2} & \frac{\partial x_2}{\partial X_3} \\ \frac{\partial x_3}{\partial X_1} & \frac{\partial x_3}{\partial X_2} & \frac{\partial x_3}{\partial X_3} \end{pmatrix} \tag{3.1}$$

The components of this tensor are the stretches, defined as ratios between the deformed and undeformed lengths. When the base coordinate system is principal, its stretches reduce to the principal ones, and the deformation gradient matrix can be written

$$\mathbf{F} = \begin{pmatrix} \lambda_1 & 0 & 0 \\ 0 & \lambda_2 & 0 \\ 0 & 0 & \lambda_3 \end{pmatrix} \tag{3.2}$$

The left and right Cauchy-Green tensors can then be defined as $\mathbf{B} = \mathbf{F}\mathbf{F}^T$ and $\mathbf{C} = \mathbf{F}^T\mathbf{F}$ respectively. The anisotropy stems in accounting for the collagen fibers orientation, and usually two "families" of collagen fibers are sufficient to describe the biomechanical behavior of arteries (Holzapfel et al., 2000). The directions of these two families in the reference configuration are defined by unit vectors $\mathbf{A}_i$ $(i = 1, 2)$; $\mathbf{A}_1 = (\cos\alpha, \sin\alpha, 0)$ and $\mathbf{A}_2 = (\cos\alpha, -\sin\alpha, 0)$, as illustrated in Figure 3.14.

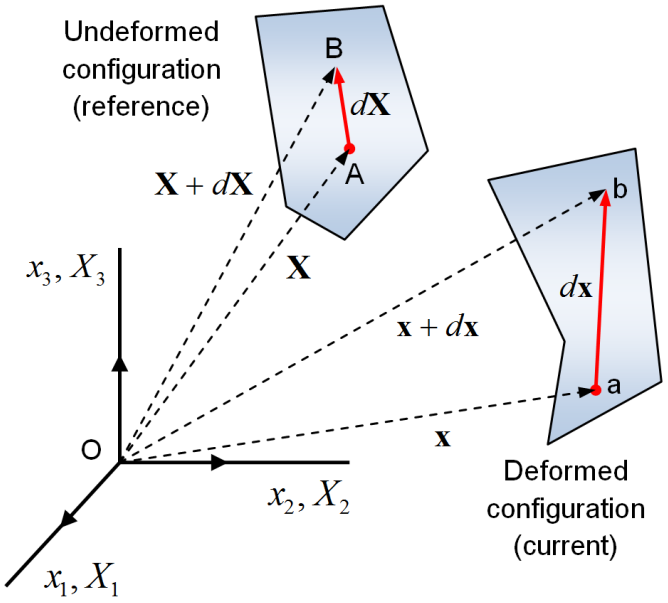

Figure 3.13: Definition of the deformation gradient.

It can now be postulated that The SEDF U depends on the right Cauchy-Green tensor and both families of collagen fibers directions

$$U = U(\mathbf{C}, \mathbf{A}_i) \tag{3.3}$$

This general formulation can be further decomposed into a volumetric elastic response U_{vol} (changing volume) and an isochoric elastic response U_{iso}, i.e.

$$U = U_{vol}(J) + U_{iso}\left(\bar{I}_1, \bar{I}_{4(11)}, \bar{I}_{4(22)}\right) \tag{3.4}$$

where $J = \det\mathbf{F}$ is the Jacobian determinant characterizing the volumetric variation of the material, and $\bar{I}_1$, $\bar{I}_{4(11)}$, $\bar{I}_{4(22)}$ are the invariants of the deviatoric (isochoric) part of the right Cauchy-Green tensor

$$\overline{\mathbf{C}} = J^{-\frac{2}{3}}\mathbf{C} \tag{3.5}$$

J and these invariants can be expressed as

$$J = \lambda_\theta \lambda_z \lambda_r \tag{3.6}$$

$$\bar{I}_1 = \mathrm{tr}\left(\overline{\mathbf{C}}\right) = \lambda_\theta^2 + \lambda_z^2 + \lambda_r^2 \tag{3.7}$$

$$\bar{I}_{4(ii)} = \overline{\mathbf{C}} : \mathbf{A}_i \otimes \mathbf{A}_i = \mathbf{A}_i \overline{\mathbf{C}} \mathbf{A}_i \qquad (i = 1, 2) \tag{3.8}$$

$$\bar{I}_{4(11)} = \bar{I}_{4(22)} = c^2 \lambda_\theta^2 + \left(1 - c^2\right) \lambda_z^2 \tag{3.9}$$

$$c = \cos \alpha \tag{3.10}$$

Again, α is the angle made by the families of collagen fibers with the circumferential direction, λ is the material stretch and the indices θ, z and r stand for the circumferential, axial and radial directions respectively. There is no summation of the indices i and j. Because soft tissues are assumed incompressible the condition $J = \lambda_\theta \lambda_z \lambda_r = 1$ prevails.

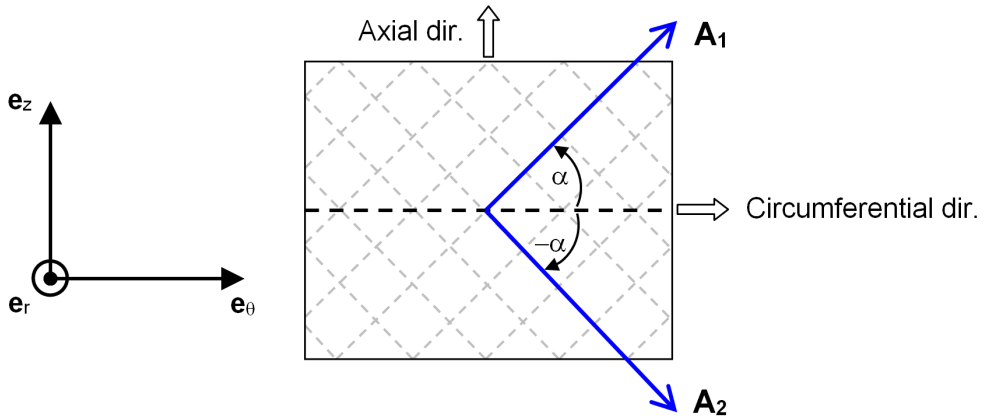

Figure 3.14: Symmetrical orientation of the two families of collagen fibers.

In non-linear mechanics the stress and strain fields are expressed in terms of the second Piola-Kirchhoff stress tensor ($\mathbf{S}$), and Green-Lagrange strain tensor ($\mathbf{E} = (\mathbf{C} - \mathbf{I})/2$, $\mathbf{I}$ being the identity tensor) respectively. Both tensors are related to the SDEF U via

$$\mathbf{S} = \frac{\partial U}{\partial \mathbf{E}} = 2 \frac{\partial U}{\partial \mathbf{C}} \tag{3.11}$$

Moreover, the Cauchy stress tensor (true stress = force per unit deformed area) can be derived from the second Piola-Kirchhoff stress tensor (engineering stress = force per unit undeformed area) from

$$\boldsymbol{\sigma} = J^{-1} \mathbf{F} \mathbf{S} \mathbf{F}^{\mathrm{T}} \tag{3.12}$$

Since we are only concerned with the in-plane components of the vascular wall, equation 3.11 can simply be restated as

$$S_\theta = \frac{1}{\lambda_\theta}\frac{\partial U}{\partial \lambda_\theta} \tag{3.13}$$

$$S_z = \frac{1}{\lambda_z}\frac{\partial U}{\partial \lambda_z} \tag{3.14}$$

Similarly, the in-plane components of the Green-Lagrange strain tensor are

$$E_\theta = \left(\lambda_\theta^2 - 1\right)/2 \tag{3.15}$$

$$E_z = \left(\lambda_z^2 - 1\right)/2 \tag{3.16}$$

This concludes the general formulation of stress and strain derivation from anisotropic SEDF. Let's now present the HGO model specifically.

3.3.1.2 HGO model formulation

There are basically two categories of SEDF formulation; "strain-based" where Green's strains are considered ($U = U(\mathbf{E})$), and "invariant-based" depending on the right Cauchy-Green tensor invariants and the unit vectors defining the directions of the fibers (equation 3.3). The HDO model is invariant-based and has the form

$$U = C_{10}\left(\bar{I}_1 - 3\right) + \frac{1}{D}\left(\frac{J^2-1}{2} - \ln J\right) + \frac{k_1}{2k_2}\sum_{i=1}^{2}\left\{\exp\left[k_2\left\langle\overline{E_i}\right\rangle^2\right] - 1\right\} \tag{3.17}$$

$$\overline{E_i} = \kappa\left(\bar{I}_1 - 3\right) + (1 - 3\kappa)\left(\bar{I}_{4(ii)} - 1\right) \tag{3.18}$$

In equation 3.17 the different terms have the following types of response

$C_{10}\left(\bar{I}_1 - 3\right)$	isotropic isochoric (elastin contribution)
$\frac{1}{D}\left(\frac{J^2-1}{2} - \ln J\right)$	isotropic volumetric (general compressibility)
$\frac{k_1}{2k_2}\sum_{i=1}^{2}\left\{\exp\left[k_2\left\langle\overline{E_i}\right\rangle^2\right] - 1\right\}$	anisotropic (collagen fibers contribution)

The Macauley bracket operator $\langle\cdot\rangle$, defined as $\langle x\rangle = (|x| + x)/2$ selects only positive (tensile) strains.

The parameter D is related to the bulk modulus K by $K = 2/D$, and for a near incompressible behavior a value of $1 \times 10^{-6}\,\mathrm{kPa}^{-1}$ is recommended for D, as per Abaqus 6.10 documentation (manual `BENCHMARKS.pdf`, page 3.1.7-5). Here it is worthy to mention that using shell elements in Abaqus ensures per see a full incompressible response, as opposed to solid elements.

At this stage the following parameters need to be identified by a multiple non-linear regression on the earlier mentioned biaxial experimental stress-strain curves (Vande Geest et al., 2006): C_{10} (kPa), k_1 (kPa), k_2 (dimensionless), κ (dimensionless) and α (degrees). The parameter κ ($0 \leq \kappa \leq 1/3$) describes the level of dispersion in the fiber directions (Gasser et al., 2006). If $\rho(\Theta)$ is the orientation density function that characterizes the distribution (normalized number of fibers with orientations in the range $[\Theta, \Theta + d\Theta]$ with respect to the mean direction), the parameter κ is defined as

$$\kappa = \frac{1}{4}\int_0^{\pi} \rho(\Theta)\sin^3\Theta d\Theta \tag{3.19}$$

It is also assumed that all families of fibers have the same mechanical properties and the same dispersion. When $\kappa = 0$, the fibers are perfectly aligned (no dispersion). When $\kappa = 1/3$, the fibers are randomly distributed and the material becomes isotropic, which corresponds to a spherical orientation density function.

More explicit and simplified expressions of U, S_θ and S_z for the HGO model are provided in Appendix D.

3.3.1.3 Determination of the HGO model parameters

The approach to identify such parameters relies on minimizing the error between the experimental second Piola-Kirchhoff stresses presented by Vande Geest et al. (2006) (Figure 3.15) and the ones predicted by the HDO model, for similar Green-Lagrange strains. From the original data presented in Figure 3.15 one can clearly appreciate how AA provide almost isotropic responses whereas AAA are significantly stiffer in the circumferential direction. This could be interpreted as an adaptation to counteract the hoop/circumferential stresses that are twice as large as in the axial direction for a cylinder, after the Laplace's law.

Thus the error function reads

$$error = \sum_{\text{point p=1}}^{n} \left[\left(S_{\mathrm{p},\,\theta}^{experience} - S_{\mathrm{p},\,\theta}^{model} \right)^2 + \left(S_{\mathrm{p},\,z}^{experience} - S_{\mathrm{p},\,z}^{model} \right)^2 \right] \tag{3.20}$$

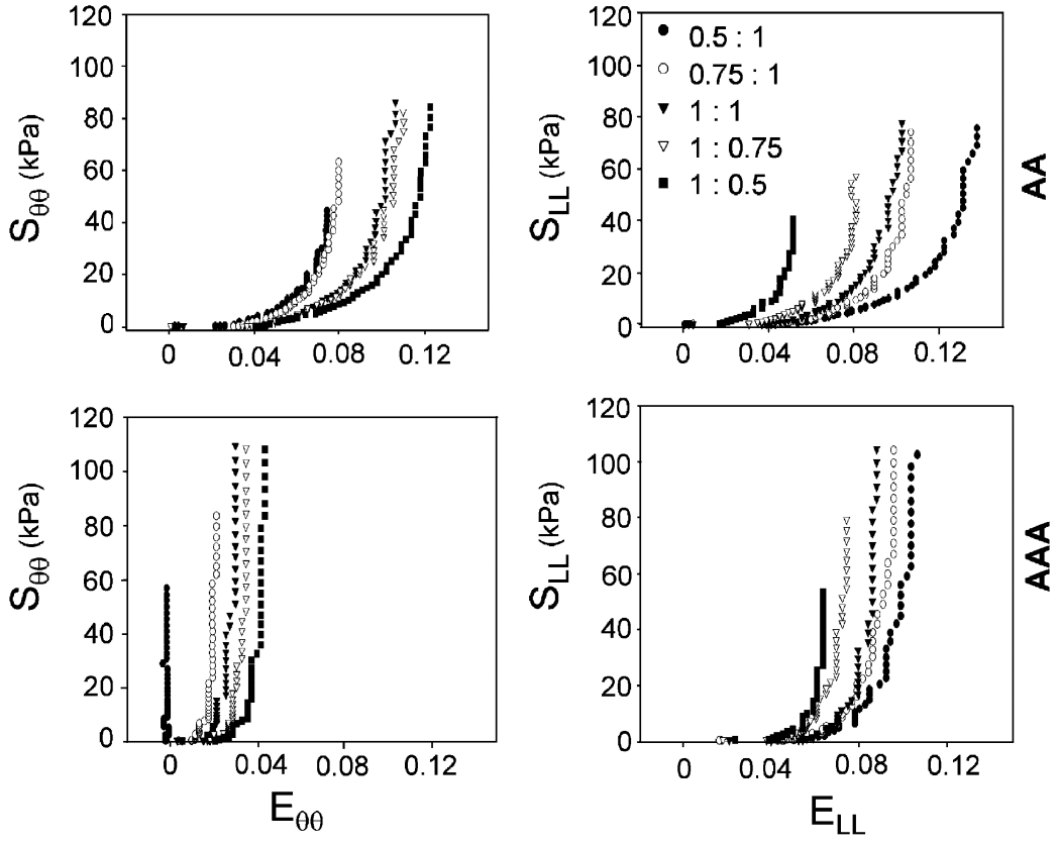

Figure 3.15: Experimental biaxial stress-strain curves from 26 AAA and 8 age-matched (healthy) abdominal aortas (AA), for different circumferential to axial tensile force ratios $T_\theta : T_z$ (Vande Geest et al., 2006). Reproduced with the permission of Elsevier.

The best fit computation was performed on all (10) curves simultaneously with a Simulated Annealing (direct search) algorithm available in Mathematica 8.0 (Wolfram Research Inc., Champaign IL, USA). This type of algorithm was preferred to the (classically used) Levenberg-Marquardt algorithm, because the latter is based on the gradient and may lead to local minima, whereas the former guarantees a global minimum. The results are presented in Table IX.

Table IX: Optimized parameters for the HGO model after a best fit of stresses on experimental data (Vande Geest et al., 2006).

C_{10} (kPa)	k_1 (kPa)	k_2 (-)	κ (-)	α (degrees)
1.100×10^{-6}	2853.630	9321.990	0.325	5.000

C_{10} has a low value, which can be associated to the known phenomenon of elastin loss. One can also notice that κ value is close to the theoretical bound of 1/3, which in

theory corresponds to an almost isotropic material, but here the predominant parameters responsible of the anisotropy are k_1 and k_2. The orientation of collagen fibers defined by $\alpha = 5.0°$ is consistent with the literature (Rodríguez et al., 2008; Xenos et al., 2010).

As a matter of verification, the original stresses and the ones predicted by the HGO model with the obtained optimum parameters are plotted in Figure 3.16 for every ratio $T_\theta : T_z$.

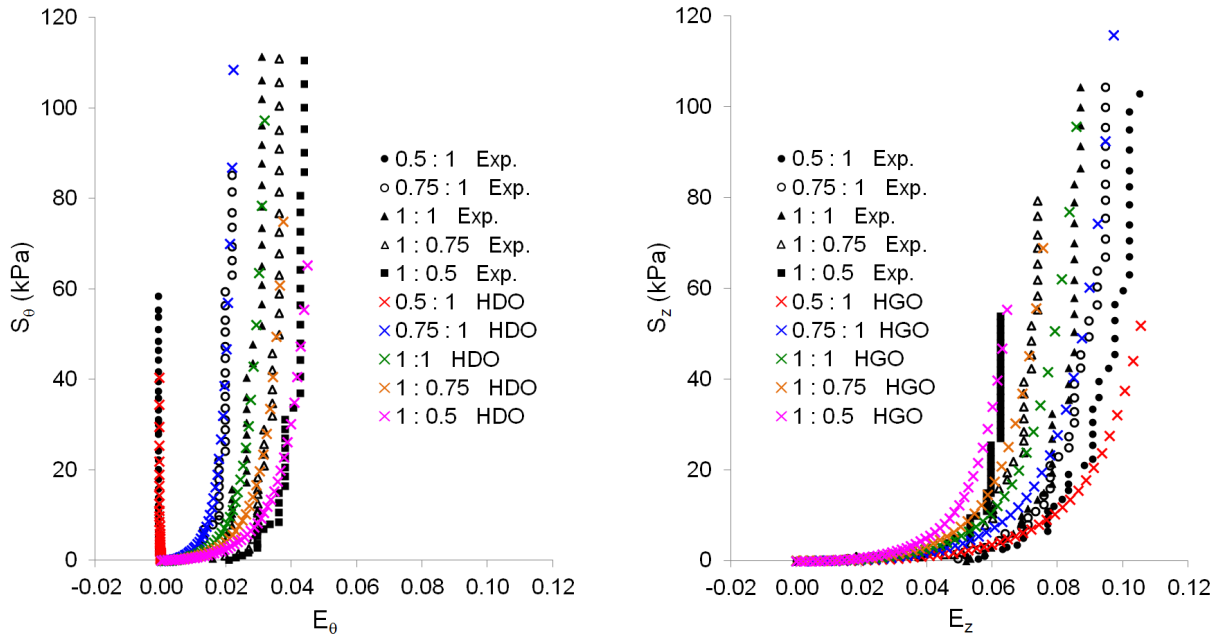

Figure 3.16: Comparison of experimental and predicted stresses given by Vande Geest et al. (2006) and the HGO model respectively (Roy et al., 2014).

Taking into account all the fitted curves, a global coefficient of determination $R^2 = 0.857$ was found.

Since explicit solvers require the density to be defined for all the involved materials, a value of $1200\,\mathrm{kg\,m^{-3}}$ was considered for the AAA wall (Scotti and Finol, 2007).

3.3.1.4 Isotropic hyperelastic model

Based a total of 64 cadaveric samplings Raghavan et al. (1996) plotted stress-strain curves (Figure 3.17) corresponding to the circumferential and axial directions, and interpreted these outcomes as an isotropic expression of AAA biomechanics.

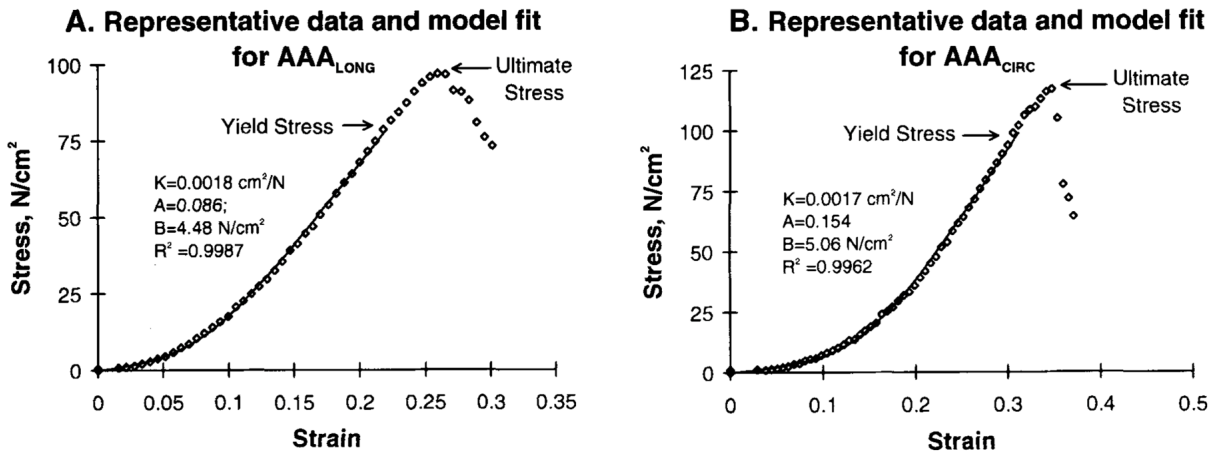

Figure 3.17: Stress-Strain curves from Raghavan et al. (1996) for an isotropic modeling of AAA. Reproduced with the permission of Elsevier.

Later on the same authors built an isotropic SEDF from their initial findings with the following expression (Raghavan and Vorp, 2000)

$$U = \alpha \left(\bar{I}_1 - 3 \right) + \beta \left(\bar{I}_1 - 3 \right)^2 \tag{3.21}$$

where $\alpha = 174\,\text{kPa}$ and $\beta = 1881\,\text{kPa}$.

Though it was shown that AAA clearly have an anisotropic response, this isotropic model is still widely used as a first satisfying approximation.

3.3.2 Innovative method to orientate the collagen fibers

The above development of anisotropic SEDFs conveys the necessity to properly orientate the two families of collagen fibers, which must be done element-wise for the sake of accuracy.

3.3.2.1 State-of-the-art for collagen fibers orientation

In the literature there are mainly two methods to do so. The first one relies on local coordinate systems built on the centerline and then projected onto the AAA wall, which will be improved later on in this thesis work. The second method relies on well shaped hexahedral elements - so-called “brick” elements - on which local coordinate systems are constructed, however this is no longer affordable with triangular or tetrahedral elements, and in general when modeling tortuous geometries involving more distorted elements. These two strategies are illustrated in Figure 3.18.

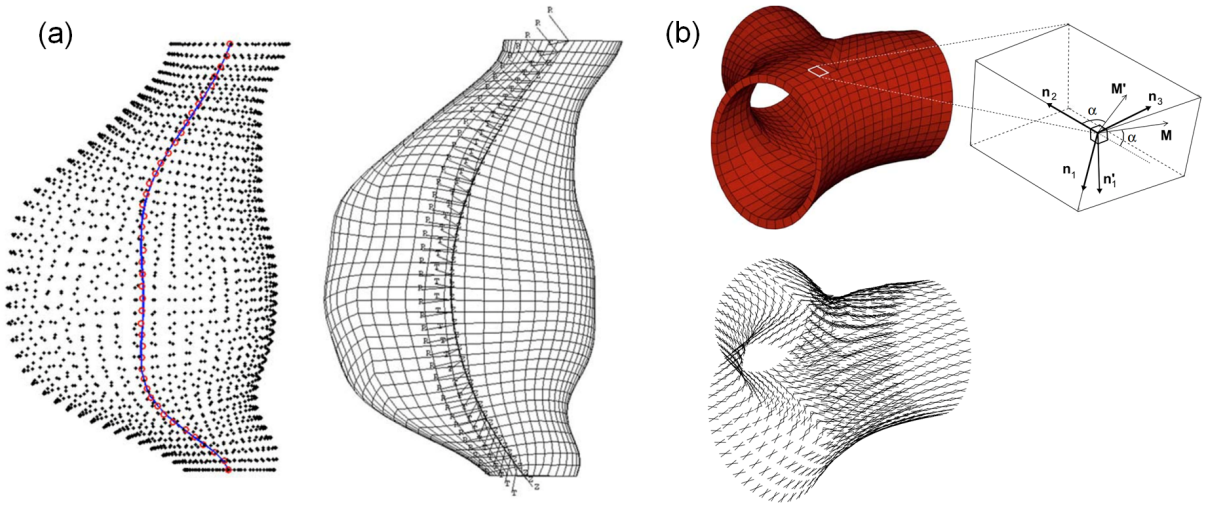

Figure 3.18: Classic strategies for collagen fibers orientation. (a) Local coordinate systems projected from the centerline (Vande Geest et al., 2008). (b) Local coordinate systems supported by regular hexahedral elements (Mortier et al., 2010). Reproduced with the permission of Elsevier.

3.3.2.2 Improved method

A more robust strategy to orientate the two families of collagen fibers was devised; by projecting the local centerline branches on each element, as done by Vande Geest et al. (2008), but also by introducing the concept of "cone of selection".

To start with let's consider the Figure 3.19 where a single element is represented, along with the closest centerline branch. In order to define a local coordinate system related to this element and then prescribe the orientation angle α as depicted in Figure 3.14, three points a, b and c have to be determined as per Abaqus 6.10 documentation (manual `ANALYSIS_1.pdf`, page 2.1.1-2). Here, we redefine these points as follows

point c is the local origin,

point a lies along the local X-axis,

point b lies along the local Y-axis.

Also, the plane equation of the element needs to be assessed, which can be done via the three points A, B and C, A being the middle point of nodes 1 and 2. Such equation has the well known form $Dx + Ey + Fz + G = 0$, whose first three coefficients can be determined via the Cramer's rule and the fourth one by a simple substitution

$$
\begin{aligned}
D &= (y_B - y_A)(z_C - z_A) - (z_B - z_A)(y_C - y_A) \\
E &= (z_B - z_A)(x_C - x_A) - (x_B - x_A)(z_C - z_A) \\
F &= (x_B - x_A)(y_C - y_A) - (y_B - y_A)(x_C - x_A) \\
G &= -Dx_A - Ey_A - Fz_A
\end{aligned}
\tag{3.22}
$$

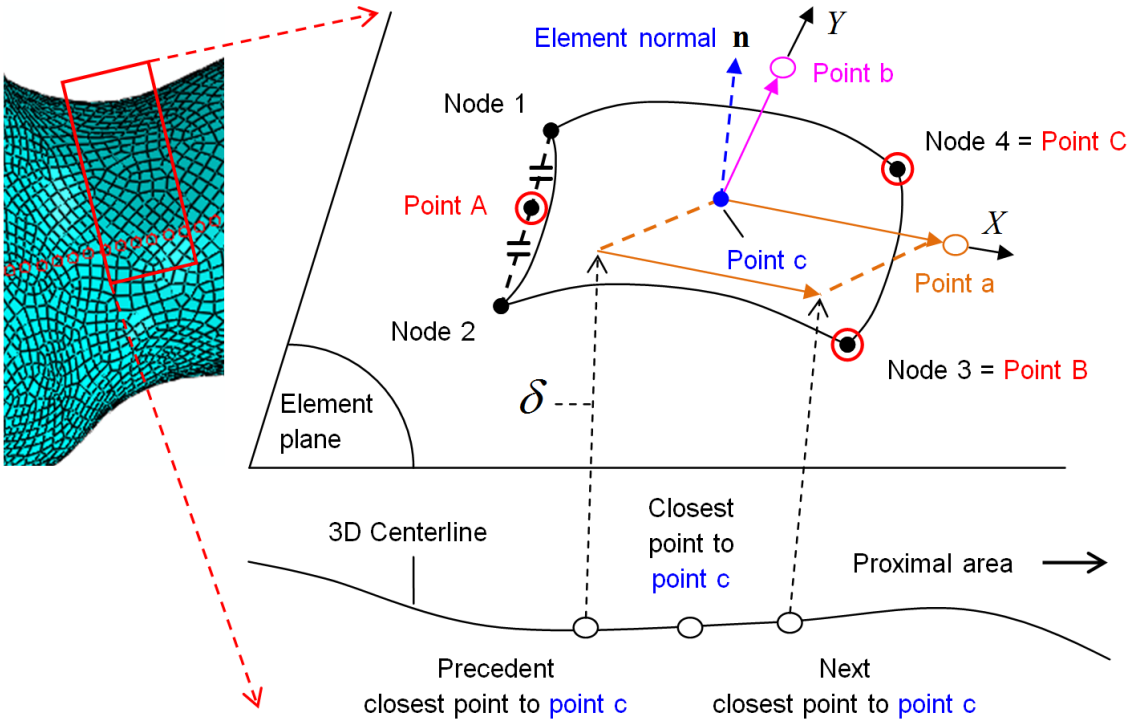

Figure 3.19: Definition of local coordinate system for each element (Roy et al., 2014).

With reference to point c the three closest points from the centerlines are identified by means of a Python script. Then the projection vectors of the "precedent" and "next" closest points on the element plane are defined as $\delta\mathbf{n}$, where δ is the minimum distance from these points to the plane and $\mathbf{n}$ is the plane normal vector.

Hence, point a can be defined along the local X-axis according to Figure 3.19.

$$\delta\mathbf{n} = \frac{|Dx_p + Ey_p + Fz_p + G|}{\sqrt{D^2+E^2+F^2}} \begin{pmatrix} \dfrac{D}{\sqrt{D^2+E^2+F^2}} \\ \dfrac{E}{\sqrt{D^2+E^2+F^2}} \\ \dfrac{F}{\sqrt{D^2+E^2+F^2}} \end{pmatrix} = \frac{|Dx_p + Ey_p + Fz_p + G|}{D^2+E^2+F^2} \begin{pmatrix} D \\ E \\ F \end{pmatrix} \tag{3.23}$$

The unit vectors are

$$\mathbf{i} = \frac{\mathbf{ca}}{\|\mathbf{ca}\|}, \quad \mathbf{j} = \mathbf{k} \times \mathbf{i} \quad \text{and} \quad \mathbf{k} = \frac{\mathbf{AB} \times \mathbf{AC}}{\|\mathbf{AB} \times \mathbf{AC}\|} \tag{3.24}$$

but the vector **cb** need not be a unit vector, and can be simply defined as

$$\mathbf{cb} = (\mathbf{AB} \times \mathbf{AC}) \times \mathbf{ca} \tag{3.25}$$

With

$$\mathbf{AB} \times \mathbf{AC} = \begin{pmatrix} (y_B - y_A)(z_C - z_A) - (y_C - y_A)(z_B - z_A) \\ (x_C - x_A)(z_B - z_A) - (x_B - x_A)(z_C - z_A) \\ (x_B - x_A)(y_C - y_A) - (x_C - x_A)(y_B - y_A) \end{pmatrix} = \begin{pmatrix} I \\ II \\ III \end{pmatrix} \tag{3.26}$$

and

$$\mathbf{cb} = \begin{pmatrix} (z_A - z_C)\,II - (y_A - y_C)\,III \\ (x_A - x_C)\,III - (z_A - z_C)\,I \\ (y_A - y_C)\,I - (x_A - x_C)\,II \end{pmatrix} = \begin{pmatrix} x_b - x_c \\ y_b - y_c \\ z_b - z_c \end{pmatrix} \tag{3.27}$$

we finally obtain the coordinates of point b

$$\begin{cases} x_b = x_c + (z_A - z_C)\,II - (y_A - y_C)\,III \\ y_b = y_c + (x_A - x_C)\,III - (z_A - z_C)\,I \\ z_b = z_c + (y_A - y_C)\,I - (x_A - x_C)\,II \end{cases} \tag{3.28}$$

However, while identifying the closest points to a given element center (point c), there is a potential issue arising when the former are located on the centerline of another vessel branch than the centerline actually related to the considered element. This situation is

illustrated in Figure 3.20 where a particular element on a large AAA bulb is closer to the "iliac centerline" than the "AAA centerline". Therefore, an additional criterion is needed for the script to isolate the right centerline branch for each element. In order to enforce the script to fetch closest points that are on the right side of the vessel, one may constrain the angle β made by the element normal and the vector defined by the element center and the current centerline point, to have a minimum value. By experience, a reasonable minimum value of 110° was found to meet this goal, thus β should remain in the range $[110°, 180°]$. But this value might be adjusted depending on the geometry, for instance 110° seems adequate for convex shapes whereas 30° might better suit concave ones. Hence a "cone of selection" is defined, i.e. only the points that are within this geometrical domain are good candidates to become the "closest" points of a given element.

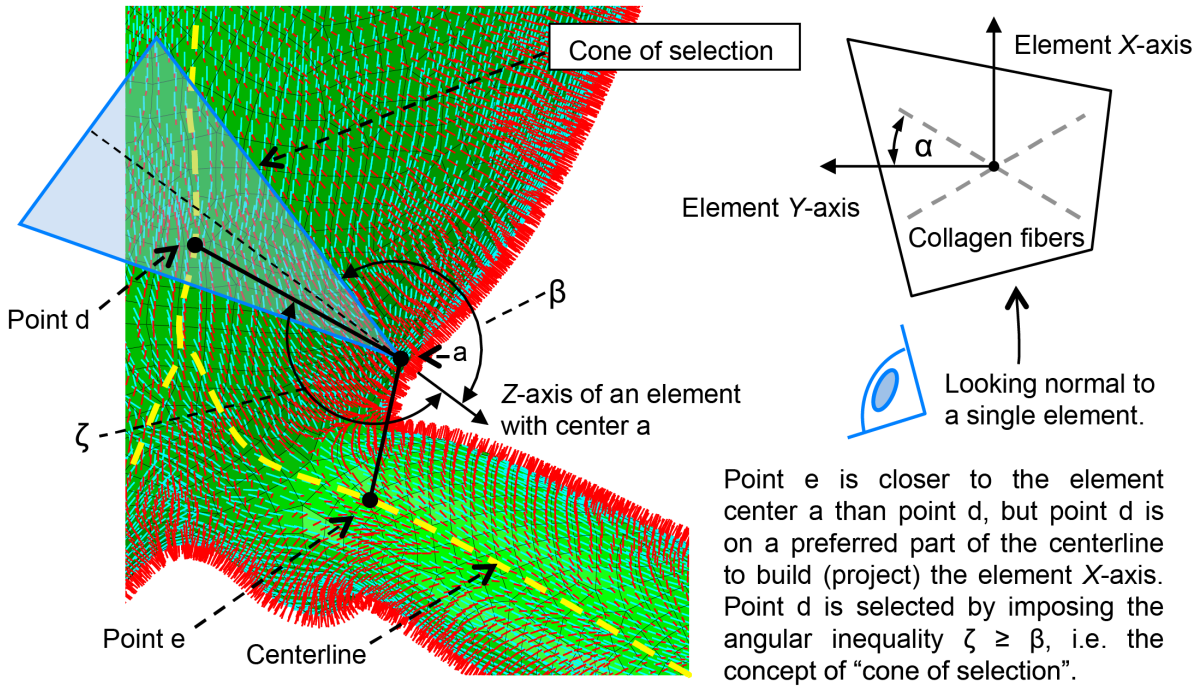

Figure 3.20: Element-wise orientation of collagen fibers and cone of selection (Roy et al., 2014).

Proceeding with this selection a relatively accurate local coordinate system is built for every single element, which is depicted in Figure 3.20. Local X and Y axes are represented with blue and red directions respectively. Obviously the local X-axes are, at best, projections of each centerline branch, and minor discrepancies might occur inevitably at junctions. But since the centerline branches are smooth, their projections are smooth as well, which minimizes errors naturally. As presented in chapter 4 dedicated to the

validation of AAA anisotropic models, there were no discontinuity in the stress field after pressurization of the vessel.

The collagen fibers can finally be oriented locally and symmetrically with an angle α with regard to the local Y-Axis.

3.3.3 Residual stresses in AAA wall

There are non-negligible residual stresses in healthy arteries (Holzapfel et al., 2007). Therefore, one needs to assess whether or not residual stresses must be accounted for in AAA. After Greenwald et al. (1994) residual stresses are mainly located in the elastin (in the media) for healthy arteries, however, He and Roach (1994) reported that the media decreases by 91% in terms of volume fraction in AAA. As a consequence, residual stresses were assumed not relevant in AAA.

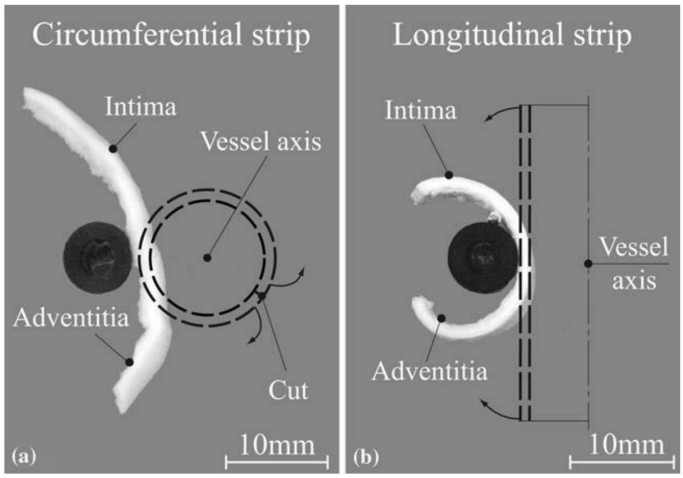

Figure 3.21: Opening angles of cut healthy arteries (Holzapfel et al., 2007). Reproduced with the permission of Elsevier.

In addition, after attending 5 open surgeries for an assessment of the opening angle (Hôtel-Dieu Hospital, Montréal, 2012), no significant opening was observed, which confirmed the hypothesis.

3.3.4 Isotropic strain-energy function to simulate the ILT

The ILT most often accompanies the AAA wall and clearly influences its biomechanical behavior as a whole. Therefore, a faithful geometrical and material modeling must be adopted.

The ILT usually exhibits three layers called luminal, medial and abluminal from inside to outside (Figure 3.22).

Each layer is considered isotropic and Wang et al. (2001) initially proposed the following hyperelastic model

$$U = c_1 \left(\bar{I}_2 - 3\right) + c_2 \left(\bar{I}_2 - 3\right)^2 \tag{3.29}$$

where $\bar{I}_2 = \frac{1}{2}[\mathrm{tr}(\overline{\mathbf{C}})^2 - \mathrm{tr}(\overline{\mathbf{C}}^2)]$ is the second invariant of the right Cauchy-Green tensor, with specific values of c_1 and c_2 for the luminal and medial layers, but not for the abluminal layer that was too degraded.

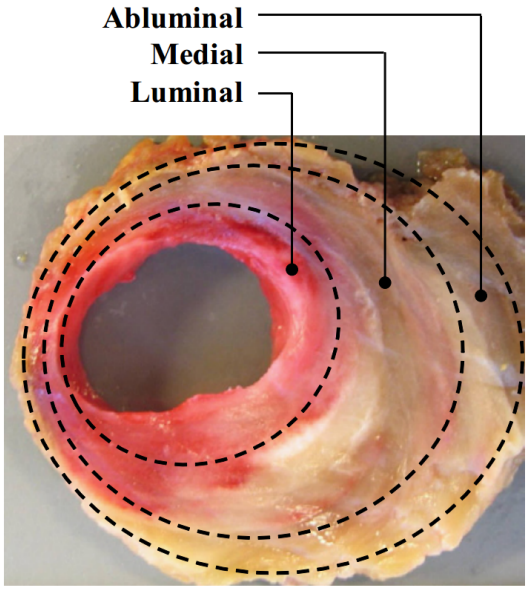

Figure 3.22: Layers of the intra-luminal thrombus (Gasser et al., 2008).

More recently, Gasser et al. (2008) provided a one parameter Ogden-like SEDF for each of the three layers

$$U = c \sum_{i=1}^{3} \left(\lambda_i^4 - 1\right) \tag{3.30}$$

with the material parameter c of the luminal, medial and abluminal layers being quantified to 2.62 kPa, 1.98 kPa and 1.73 kPa respectively. This formulation characterizes the overall ILT and will be adopted in this study. It can be represented in Abaqus by a first order Ogden SEDF of general form

$$U = \sum_{i=1}^{N} \frac{2\mu_i}{\alpha_i^2} \left(\lambda_1^{\alpha_i} + \lambda_2^{\alpha_i} + \lambda_3^{\alpha_i} - 3\right) + \sum_{i=1}^{N} \frac{1}{D_i} \left(J - 1\right)^{2i} \tag{3.31}$$

where λ_i are the deviatoric principal stretches and N, μ_i, α_i and D_i are material parameters. In particular μ_i is related to the shear modulus, and D_i to the bulk modulus as previously stated for the HGO model.

A first order Ogden SEDF is characterized by $i = 1$, hence equation 3.31 reduces to

$$U = \frac{2\mu_1}{\alpha_1^2}\left(\lambda_1^{\alpha_1} + \lambda_2^{\alpha_1} + \lambda_3^{\alpha_1} - 3\right) + \frac{1}{D_1}\left(J - 1\right)^2 \tag{3.32}$$

Based on equation 3.30 a mean material parameter c_m can be defined for the whole ILT, as well as $\mu_1 = c_m\alpha_1^2/2$. The parameters finally used with equation 3.32 for the ILT are summarized in Table X.

Table X: Parameters of the Ogden strain energy density function representing the ILT.

α_1 (-)	c_m (kPa)	μ_1 (kPa)	D_1 $\left(\text{kPa}^{-1}\right)$
4	2.11	16.88	1×10^{-6}

Finally, in this study a density of $1080\,\text{kg}\,\text{m}^{-3}$ was considered for the ILT (Wang et al., 2001).

3.4 Finite element mesh for AAA

Building a robust finite element mesh/discretization is a key step to avoid excessive element distortion during large displacements analyses. This premise prevails for both the AAA wall and ILT, however the former needs a special attention since shell elements convey some technical constraints/limitations as exposed in the following section.

The dependence of the solution to AAA and ILT mesh size, measured in terms of displacements of pressurized AAA, is addressed in chapter 4.

3.4.1 AAA wall mesh

Shell elements were used in this work mainly because of the difficulty to mesh the complex geometry of AAA with solid elements. The latter lead to initially interpenetrated elements that consistently fail during the very first stages of any FEA. Besides, solid elements are far less efficient than shells, which would restrict our potential of finding within the large scope of SG deployment simulation. And shell elements ensure an incompressible behavior whereas a perfect or even nearly incompressibility is less easily achieved with continuum (solid) elements (Ní Annaidh et al., 2013). However, the AAA wall should ideally be

meshed with solid elements because AAA are 3D continua, especially when the tissues are inflamed which implicates large thicknesses (up to 20 mm).

In particular, linear shell elements (S4) were considered, and for a reason already mentioned in section 2.2.6; as long as the wall thickness does not exceed one tenth of a characteristic arterial dimension, typically its local diameter, the *Mindlin-Reissner* theory provides acceptable solutions. This is the case if we consider an aortic wall thickness of 1.5 mm with a minimum diameter of 15 mm, and 1 mm thick iliac artery wall with a minimum diameter of 8 mm.

Having substantiated the range of applicability of shell elements with regard to the available theoretical background, it still remains to address the validity of this strategy on the element scale. For the whole vascular geometry (aortic and iliac branches) a prescribed element size of 1 mm was necessary to capture adequately tortuous geometries. Since Abaqus allows a maximum aspect ratio of thickness to element minimum edge/diagonal length equal to 1 (via the option "max ratio = 1"), the actual thickness must be "artificially" modified. Therefore, with real mean aortic and iliac thicknesses of 1.5 mm (Raghavan et al., 2000; Scotti and Finol, 2007; Rodríguez et al., 2008) and 1 mm respectively, a reduction factor of 2 was applied to meet this requirement. This led to aortic and iliac thicknesses of 0.75 mm and 0.5 mm respectively, in the numerical models. Indeed, the 1 mm thickness of iliac arteries came from a ratio of outer diameter to wall thickness of 7.7 for human aged iliac arteries observed by Schulze-Bauer et al. (2003), and based on a minimum diameter of 8.0 mm measured on the geometry at hand (case H1025269 from CR-CHUM database). Hence the thickness $8.0\,\text{mm}/7.7 = 1.04\,\text{mm} \cong 1.0\,\text{mm}$.

Finally, in order to maintain the same initial in-plane or membrane stiffness, this reduction factor had to be balanced by an increase of the material parameters in the same proportion. In fact, parameters that have a dimension of pressure are increased, whereas parameters that have a dimension of inverse pressure are decreased. Also, the material density is increased.

Again, reduced linear shell elements (S4R) could be considered for efficiency purposes, but all analyses were performed with integrated elements in a context of verification, which is the object of chapter 4.

3.4.2 ILT mesh

Linear tetrahedral elements (C3D4 in Abaqus nomenclature) with a prescribed size of 1.5 mm were used to mesh the ILT volumetric domain. Also, the interior elements had an increased size ("Moderate growth" option) for optimum numerical efficiency (Figure 3.23).

The next important aspect of AAA modeling is concerned with the applied boundary conditions, i.e. how the vessel is tethered, loaded by blood pressure and how it interacts with its surrounding medium.

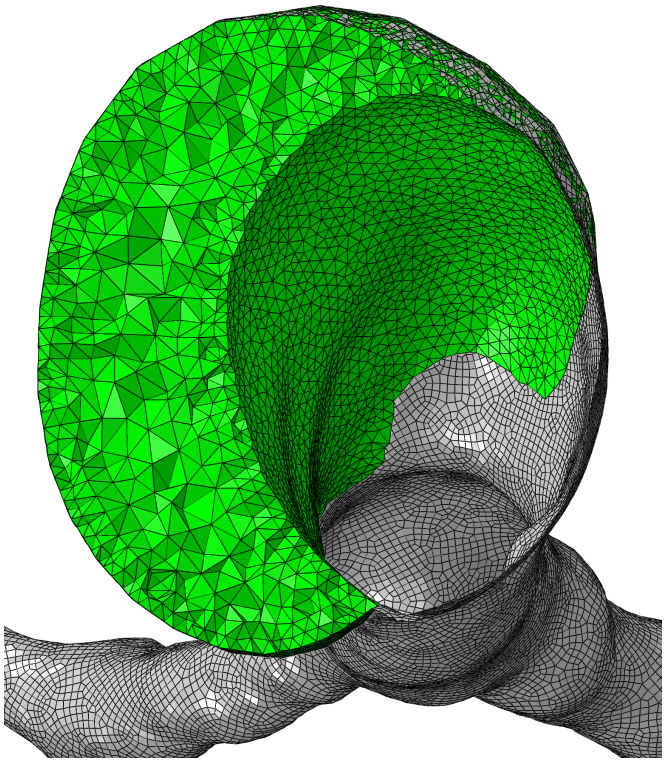

Figure 3.23: Typical AAA and ILT meshes, respectively with linear quadrilateral shell elements and linear tetrahedral solid elements.

3.5 Boundary conditions

Realistic boundary conditions are not trivial to establish in the complex modeling of AAA. This section will present the approximations made in this study.

3.5.1 Constrained degrees of freedom at proximal and distal AAA ends

The abdominal aorta is strongly tethered proximally due to its proximity with the diaphragm, and distally as it is attached by the inguinal ligament (Figure 3.24). However, in the numerical model these sections were circumferentially and axially constrained in local coordinate systems, thus allowing the vessel to freely expand radially, which avoided unrealistic stresses.

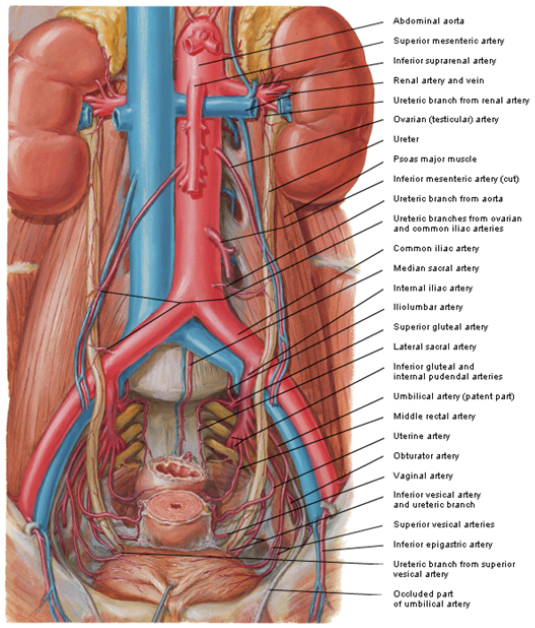

(Ref.: Netter Atlas, plate 328)

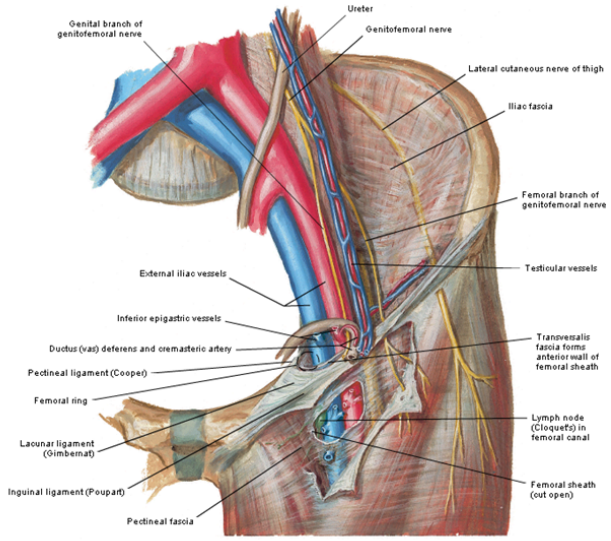

(Ref.: Netter Atlas, plate 252B)

Figure 3.24: Abdominal cavity anatomy.

The main collateral vessels such as renal and internal iliac arteries must be represented to some extent, at least as landmarks to prevent any occlusion in the context of EVAR treatment. The question remains whether or not these vessels must be attached.

3.5.2 Internal iliacs represented with non-linear springs

After a clinical consultation (radiologists, vascular surgeons) it was decided to leave unattached the renal arteries, but to constrain the internal iliac arteries. Indeed, as can be seen in Figure 3.24, the internal iliacs are significantly ramified shortly after the iliac bifurcation, thus constituting a strong intermediate connection in our global vascular geometry.

The simplest approximation to this link is a non-linear spring mimicking the corresponding force versus displacement relationship. Since the internal iliac arteries most often remain healthy during AAA growth, the non-linear spring was designed with experimental data performed on healthy tissues. Although Schulze-Bauer et al. (2003) provided several anisotropic SEDF related to healthy aged iliac arteries, an isotropic model was preferred since only the axial component was needed. Therefore, the isotropic model of healthy aorta presented in figure 5 from Raghavan et al. (1996) (see Figure 3.25) was considered, i.e. the stress-strain curve named “NORMAL-long” along with the related equation

$$\epsilon = \left(K + \frac{A}{B+\sigma}\right)\sigma \tag{3.33}$$

where $K = 3 \times 10^{-4}\,\mathrm{kPa}^{-1}$, $A = 0.223$ (dimensionless) and $B = 89.3\,\mathrm{kPa}$.

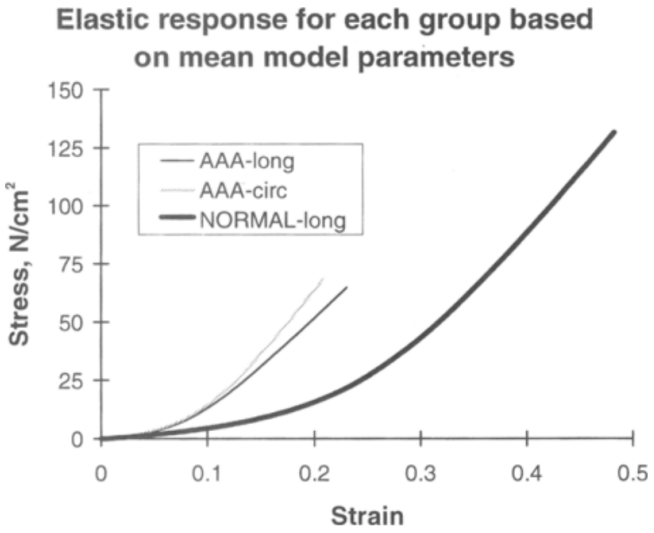

Figure 3.25: Uniaxial stress-strain curves (up to yield strength) based on mean correlated parameters for each group; AAA-long, AAA-circ and NORMAL-long (Raghavan et al., 1996).

In order to derive the force versus displacement relationship let's start with the basic definition of a spring-like stiffness for a soft continuum sample

$$k = \frac{F}{\Delta L} = \frac{F}{\epsilon L} = \frac{A_s E}{L} \tag{3.34}$$

where A_s and E are the cross section area and Young's modulus respectively. Moreover, Young's modulus can be derived from equation 3.33

$$E = \frac{1}{\dfrac{\partial \epsilon}{\partial \sigma}} = \frac{1}{\left(\dfrac{-A}{(B+\sigma)^2}\right)\sigma + \left(K + \dfrac{A}{(B+\sigma)}\right)} \tag{3.35}$$

At this point an estimation of typical cross section areas and lengths of iliac arteries was needed. Such estimates, and computed mean values and standard deviations were extracted from our database (Table XI). With a mean thickness of 1.3 mm (Schulze-Bauer et al., 2003) for healthy iliac arteries, a mean cross section area $A_s = 28.16\,\mathrm{mm}^2$ was computed based on a mean diameter of 6.89 mm.

Table XI: Typical diameters and lengths of internal iliacs (from CR-CHUM database).

Anonymized Patient ID	Diameter (mm)	Length (mm)
1025269	6.45	11.30
1119887	5.00	22.00
828515	5.50	24.53
572411	7.05	28.89
1119046	5.24	22.88
1045943	7.64	52.74
1349336	11.38	37.35
	mean $\pm$ std. dev.	
	6.89 ± 2.20	28.53 ± 13.24

Based on Figure 3.25 strains in the range [0.00, 0.50] were considered, with an increment of 0.05. Subsequently the corresponding Cauchy stresses (σ), tangent Young's moduli (E), non-linear stiffness (k) and forces (F) were computed from equations 3.35 and 3.34 respectively (Table XII).

Table XII: Definition of a non-linear spring representing internal iliacs: computed Cauchy stresses, tangent Young's moduli, stiffness coefficients and forces.

ϵ (-)	$\epsilon L = \Delta L$ (mm)	σ (kPa)	E (kPa)	k (mN mm^{-1})	F (mN)
0.00	0.00	0	0	0	0
0.05	1.43	22	521	515	734
0.10	2.85	54	786	776	2213
0.15	4.28	103	1189	1174	5023
0.20	5.71	175	1708	1685	9616
0.25	7.13	273	2214	2186	15588
0.30	8.56	394	2596	2562	21926
0.35	9.98	530	2842	2805	28009
0.40	11.41	677	2995	2956	33726
0.45	12.84	829	3090	3050	39153
0.50	14.26	985	3152	3111	44376

For the sake of completeness a compressive stiffness should also be prescribed, however, dealing with soft tissues, it cannot be the exact opposite of the tensile stiffness. Therefore, 10% of the tensile stiffness was arbitrarily attributed to the compressive stiffness (Table XIII), which is depicted in Figure 3.26. A non null compressive stiffness stabilizes the solution.

Table XIII: Non-linear spring definition for internal iliacs: compressive and tensile stiffnesses.

Compressive stiffness		Tensile stiffness	
ΔL (mm)	F (mN)	ΔL (mm)	F (mN)
0.00	0	0.00	0
−1.43	−73.4	1.43	734
−2.85	−221.3	2.85	2213
−4.28	−502.3	4.28	5023
−5.71	−961.6	5.71	9616
−7.13	−1558.8	7.13	15 588
−8.56	−2192.6	8.56	21 926
−9.98	−2800.9	9.98	28 009
−11.41	−3372.6	11.41	33 726
−12.84	−3915.3	12.84	39 153
−14.26	−4437.6	14.26	44 376

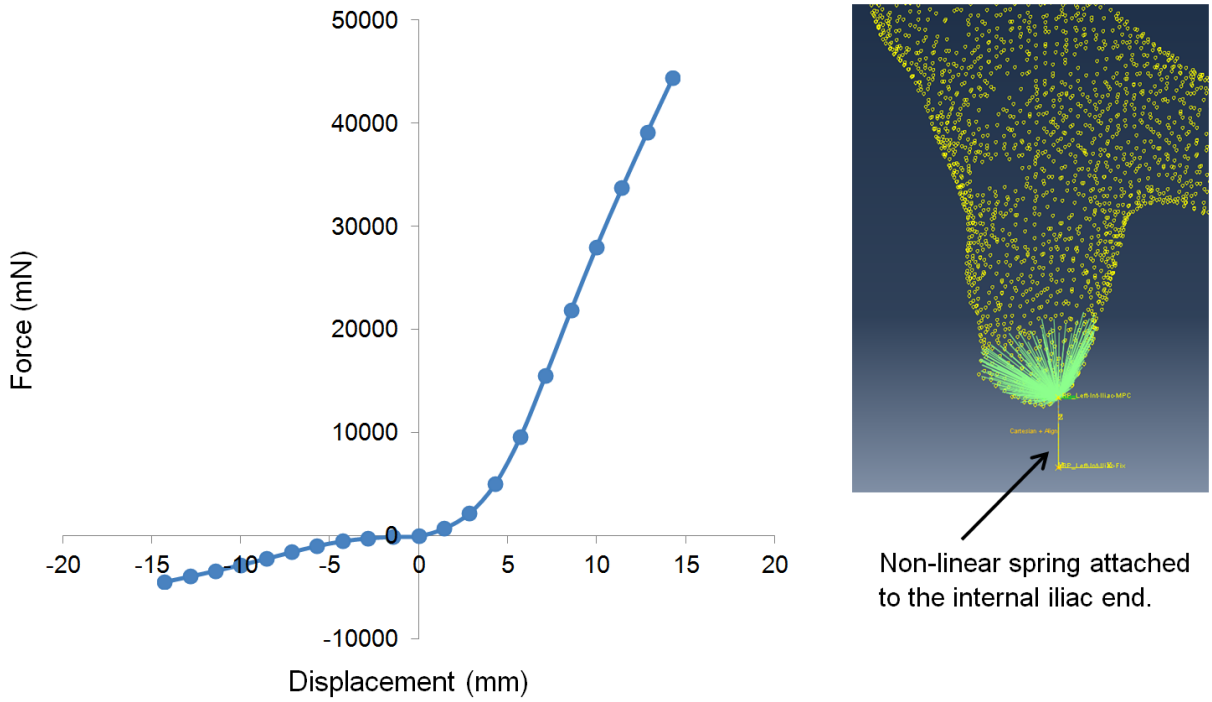

Figure 3.26: Non-linear spring mimicking the ramification stiffness of internal iliacs (applied in all three directions).

This approximation of collateral vessels is only a glimpse of a much broader research field dedicated to the simplified modeling of surrounding organs, trying to conciliate accuracy and efficiency. The next section presents additional techniques.

3.5.3 Surrounding organs

This topic is quite complex and probably the most efficient solutions rely on multi-dimensional modeling, thus combining conventional FEM with so-called "0D" and "1D" idealizations based on equivalent RLC circuits. These models allow detailed FEM to be enhanced with sophisticated solid and/or fluid boundary conditions. For instance Moireau et al. (2012) could simulate a complex fluid-structure analysis in an aortic arch while accounting for the surrounding organs (spine included) via a combination of springs and dashpots distributed along the vessel.

Another strategy is adding a layer of solid elements with adequate equivalent viscoelastic properties around a vessel meshed with shell elements (Harewood et al., 2010). However, such models might implicate a larger number of solid elements to achieve a satisfying accuracy, not to mention the associated degradation of performance.

The mechanical properties of abdominal organs were assessed experimentally by Brown et al. (2003); Rosen et al. (2008) on porcine tissues (bladder, gallbladder, large and small intestines, liver, spleen and stomach). Also, Maaß and Kühnaptel (1999) presented a useful table of mechanical properties for some human abdominal organs and tissues (Figure 3.27).

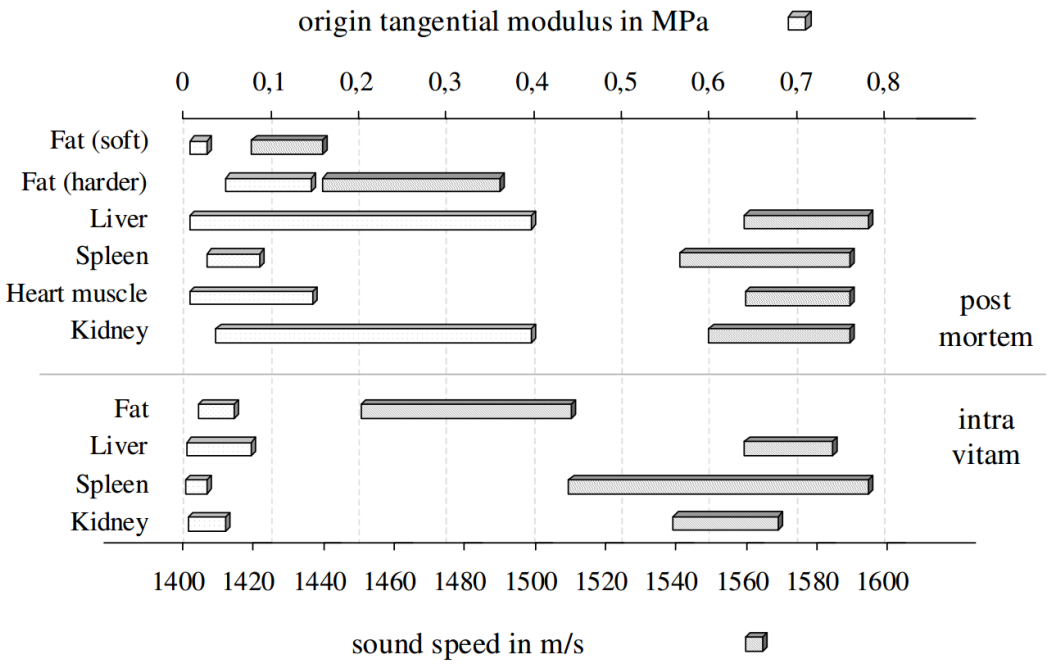

Figure 3.27: Young's modulus and characteristic sound speed of some human abdominal tissues (Maaß and Kühnaptel, 1999).

In this thesis work, the abdominal pressure was simply prescribed on the AAA outer

face, which is known to be around 12 mmHg, as reported by (Hinnen et al., 2005) and used by Scotti et al. (2008) in fluid-structure analyses.

Finally, it is worth mentioning that a viscous pressure might be prescribed on the AAA to simulate approximately the surrounding organs. Viscous pressure loading is most commonly applied in structural problems to damp out dynamic effects and reach a static equilibrium in a minimal number of increments. Such pressure reads

$$p = -c_v \left(\mathbf{v} - \mathbf{v}_{ref}\right) \cdot \mathbf{n} \tag{3.36}$$

where c_v is the viscosity given as the magnitude of the load, $\mathbf{v}$ is the velocity of the point on the surface where the pressure is being applied, $\mathbf{v}_{ref}$ is the velocity of a reference node (set to a null vector since there is no relative motion in our case) and $\mathbf{n}$ is the outward normal of the element at the same point. The coefficient c_v is given by ρc_d, ρ being the density of the material at the surface and c_d the value of the dilatational wave speed in the material. For an isotropic, linear elastic material

$$c_d = \sqrt{\frac{\lambda + 2\mu}{\rho}} = \sqrt{\frac{E\left(1-\nu\right)}{\rho\left(1+\nu\right)\left(1-2\nu\right)}} \tag{3.37}$$

The choice of the pressure coefficient represents a level of damping in which pressures waves crossing the free surface are absorbed with no reflection of energy back into the interior of the finite element mesh.
For typical structural problems, it is not desirable to absorb all of the energy. Typically, c_v is set equal to a small percentage (1 or 2 percent) of ρc_d, as an effective way of minimizing dynamic effects.

3.6 Assessment of AAA zero pressure geometry

The last critical aspect of AAA modeling addressed in this work is concerned with the identification of the so-called "zero pressure geometry" (ZPG). This corresponds to the virtual geometry that, once load by the blood pressure, leads to the observed *in vivo* (already loaded) geometry (from CT-scans, MRI modalities, etc.). This difficult inverse structural problem is still an active topic of research.

Some approximations were proposed (Govindjee and Mihalic, 1998; De Putter et al., 2007; Speelman, 2009; Gee et al., 2010) provided a full access to the FEA source code is granted. However, most analysts rely on commercial software's. Therefore, a few authors presented an affordable iterative solution based on "fixed point" iterations (Raghavan et al.,

2006; Bols et al., 2013). Although the latter approach is mathematically sound and elegant, and might converge toward a satisfying solution for quite simple geometries as demonstrated by Bols et al. (2013) for a mouse-specific abdominal aorta, it was found inefficient for human-specific tortuous AAA. Indeed, after a few iterations all initial irregularities are amplified, thus making concave shapes deeper and convex ones more salient, without achieving convergence (or only in a mean sense).

It was finally decided to apply only the first iteration of this strategy in order to avoid such discrepancies. This reduces to pressurizing the initial geometry (forward analysis), and subtract the displacements (backward analysis) to obtain an approximated ZPG. This is equivalent to assuming a linear mechanical behavior, which is somehow justified by the relatively low vascular deformations due to blood pressure, especially for older and likely calcified arteries.

3.7 Limitations

No calcifications were modeled in this project, mainly because the identification of the geometrical domain where they are located is not technically obvious and implicates a significant manual pre-processing. They could be visualized with an appropriate Hounsfield unit threshold, but unfortunately, it was not possible to reprogram ORS so an actual segmentation of this domain could be performed. However, the open source application ITK-snap was recently identified as a potential tool to export the 3D domain occupied by calcifications. Such a domain would be particularly useful for a 3D modeling of the AAA wall, which is not the case in this study, nevertheless the position and thickness of calcified plaques could be incorporated in shell elements by means of composite section properties (one layer for the AAA wall and another one for any calcification). The latter is quite a substantial development, and is left for future investigation.

The material properties and collagen fiber orientation were assumed homogeneous, whereas it is well known that in reality there is a significant inter and even intra-individual variation of these parameters. The same applies for the wall thickness.

An accurate modeling of the surrounding organs was not deemed possible within the scope of this project, and equivalent pressures and/or viscous pressures were considered instead. This said, multi-dimensional modeling is a promising alternative, and still deserves a substantial effort of development and validation.

Before presenting in details the numerical verification of the AAA model developed above, an attempt to make its modeling more automatic is explained in the next section.

3.8 Python script to generate AAA automatically

To alleviate the tedious task of creating from scratch a complete AAA model, a Python script was written and can be run directly from Abaqus or in batch mode. This script calls six external files whose variable name, content and extension are detailed in Table XIV.

Table XIV: Python script for automated AAA modeling: information about external files.

Variable Name	Content	Format extension
lumenPointsCSVFile	lumen points coordinates	.csv
lumenFacetsCSVFile	lumen facets connectivity with points	.csv
ILTPointsCSVFile	ILT points coordinates	.csv
ILTFacetsCSVFile	ILT facets connectivity with points	.csv
centerlinesDataFile	centerlines points issued by VMTK	.dat
spinePathControlPoints	points along the spine path	.xml

The script also receives arguments to define the spine width and its offset with regard to the AAA wall. About 15 min are necessary to complete this script, leading to a complete AAA structural definition with material properties, finite element mesh, boundary conditions and centerlines (Figure 3.28). We recommend using the version 6.10 of Abaqus to run this script, as opposed to the version 6.13 since we observed very little (undesirable) elements to be generated with the latter. This script contains more than 1100 lines of code and is not presented in this document. Finally, a typical command line to launch an analysis in batch mode (to be typed in an Abaqus Command window) has the following syntax with n CPUs running in parallel

abaqus job=inputFileName cpus=n dynamic_load_balancing.

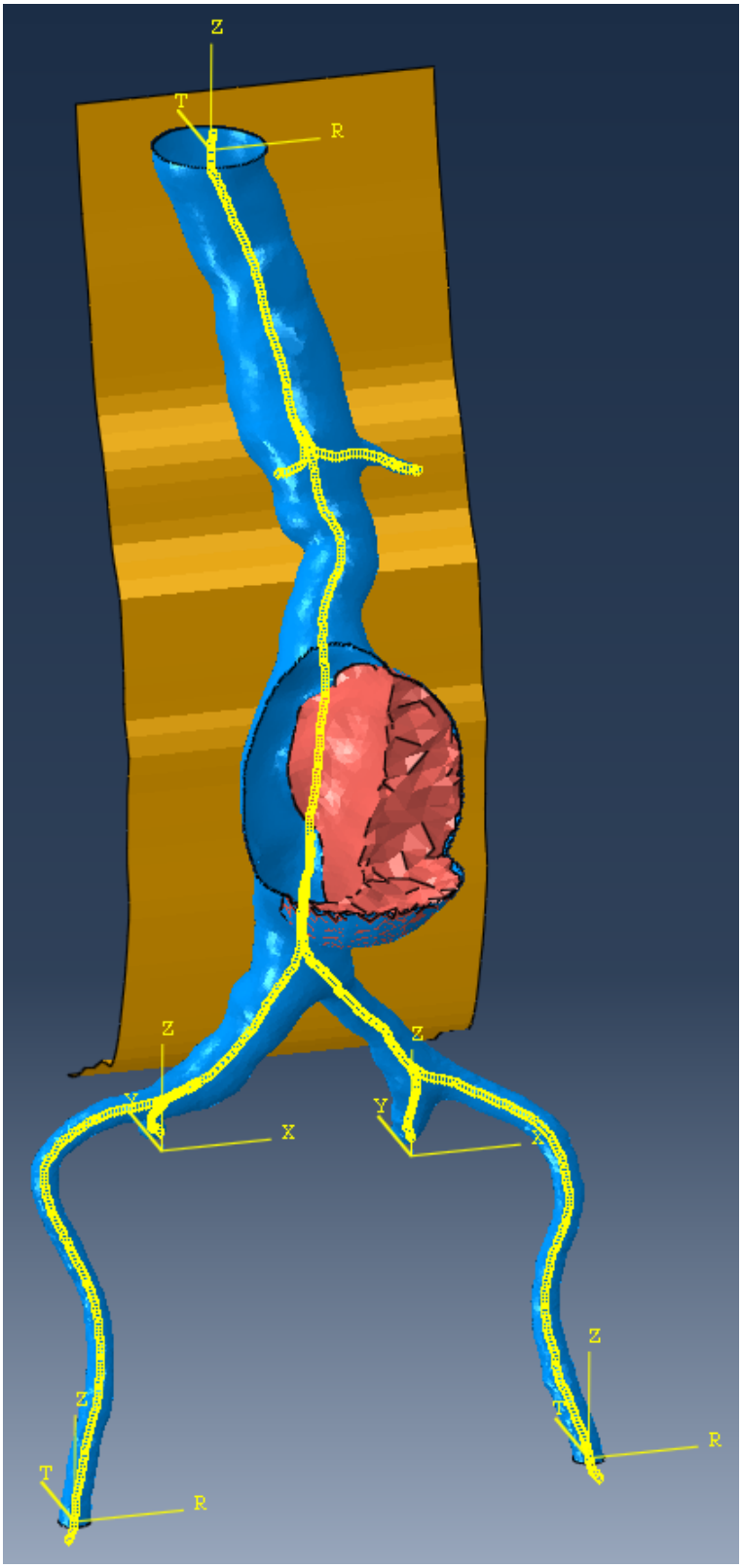

Figure 3.28: Automatically generated AAA by means of a Python script (case H1025269 from CR-CHUM database).

3.9 Conclusion

In this chapter a complete workflow of AAA modeling was described, from extracted medical images to a "ready-to-use" FEM. The biomechanical properties of both the AAA wall and ILT were thoroughly described and justified against experimental data. Although the AAA wall might be better modeled with solid elements for the specific purpose of stress assessment and rupture prediction, it is believed that relying on shell elements leads to more efficient and robust models in a context of SG deployment simulation (large displacements expected), at least in an exploring phase. Indeed, SG deployment simulation is an active topic of research, but the related literature is still scarce. In the next chapter, a series of verifications of our AAA modeling will be conducted.

Chapter 4

Verification of AAA numerical model

4.1 Introduction

A thorough validation of the above developed AAA model would have required an intensive comparison with a significant amount of clinical data, which was not affordable in the scope of this study. Therefore, a limited verification against a key reference from the literature was performed, i.e. a study from Rodríguez et al. (2008) regarding the influence of material anisotropy on mechanical stresses in AAA.

4.2 Methods

4.2.1 Geometries and materials

The proposed verification took place in three main steps with a different geometry in each case: (i) a direct stress comparison to Rodríguez et al. (2008) with the same simple virtual geometry (case 7), (ii) an indirect stress comparison to Rodríguez et al. (2008) with a first patient-specific geometry (PS1) from CR-CHUM database (knowing Rodríguez et al. (2008) did not use patient-specific geometries), and (iii) a sensitivity study to the AAA wall and ILT mesh size in terms of stresses with a second patient-specific geometry (PS2) (case H1025269 from CR-CHUM database). Cauchy stresses were considered for the AAA wall.

Only PS2 was accompanied by an ILT. Every geometry had a thickness of 1.5 mm, except below the aortic bifurcation of PS1, where a thickness of 1 mm was prescribed.

In particular, the function providing the mathematical definition of the simple virtual geometry, as proposed by Elger et al. (1996), is given as follows

$$R(Z) = R_a + \left(R_{an} - R_a - c_3 \frac{Z^2}{R_a}\right) \exp\left(-c_2 \left|\frac{Z}{R_a}\right|^{c_1}\right) \tag{4.1}$$

where c_1 is a constant taken as 5.0, c_2 and c_3 are dimensionless parameters depending on the aneurysm geometry

$$c_2 = \frac{4.605}{(0.5 L_{an}/R_a)^{c_1}}, \quad c_3 = \frac{R_{an} - R_a}{R_a \, (0.8 L_{an}/R_a)^2} \tag{4.2}$$

$R(Z)$, R_a, R_{an} and e are the radii and eccentricity respectively, as depicted in Figure 4.1.

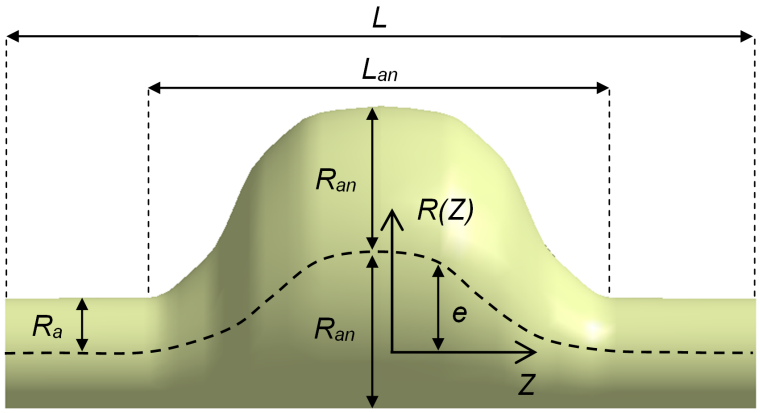

Figure 4.1: Radii and eccentricity of the simple virtual geometry (Roy et al., 2014).

Additional parameters were introduced by Rodríguez et al. (2008)

$$F_R = \frac{R_{an}}{R_a}, \quad F_L = \frac{L_{an}}{R_{an}}, \quad F_E = \frac{e}{(F_R - 1)\, R_a} \tag{4.3}$$

The value of each parameter is provided in Table XV.

Table XV: Parameters defining the virtual geometry (case 7 from Rodríguez et al. (2008)).

F_R (-)	F_L (-)	F_E (-)	R_a (mm)	R_{an} (mm)	L_{an} (mm)	L (mm)
2.75	3.00	1.00	10.10	27.78	83.33	138.32

The first step involved the anisotropic hyperelastic HGO model, as well as the isotropic SEDF from Raghavan and Vorp (2000), whereas the second and third steps involved respectively the HGO model and isotropic SEDF presented by Raghavan and Vorp (2000) for the AAA wall.

4.2.2 Numerical parameters

As mentioned in section 2.2.7 the same guidelines were followed here regarding mass scaling and smooth amplitude. For the first two steps, no mass scaling at all was prescribed in order to guarantee quasi-static results. A standard time period of 1 s was attributed.

A transverse shear stiffness of 10 kPa was attributed to shell elements representing the AAA wall, as recommended in the literature (Vande Geest et al., 2008).

4.2.3 Elements

Fully integrated linear quadrilateral elements (S4) were used in the models (simple virtual geometry, PS1 and PS2), whereas Rodríguez et al. (2008) used solid elements (simple virtual geometry).

In the third step, the AAA wall and ILT had initial mesh sizes of 1 mm and 1.5 mm respectively, the former could not be reduced because of the maximal ratio of thickness to element edge/diagonal length, so it was increased by 2, whereas the latter was divided by 2.

4.2.4 Loads and boundary conditions

All three geometries underwent a pressure of 120 mmHg. In step 1 both end sections of the simple virtual geometry were fully fixed according to Rodríguez et al. (2008), whereas in steps 2 and 3 the proximal and distal sections were axially and circumferentially fixed in local cylindrical coordinate systems, thus allowing a radial free expansion. PS1 and PS2 had non-linear springs attached to their internal iliac end sections.

4.3 Results

4.3.1 Pressurized simple virtual geometry

The simple virtual geometry was analyzed with the isotropic SEDF from Raghavan and Vorp (2000), and also with the anisotropic HGO model. Corresponding maximal principal Cauchy stresses are depicted in Figure 4.2. Clearly, maximal stresses occur along the circumferential direction, thus corresponding to the most critical hoop stresses (in nearly cylindrical structures). Peak wall stresses of 658 kPa and 759 kPa were observed for the isotropic and anisotropic models respectively. As already reported by Rodríguez et al. (2008), stresses are higher when anisotropic materials are implemented, because of the

preferential orientation of collagen fibers along the circumferential direction. Stresses are naturally increased by shapes having double curvature, hence the high stresses located where the AAA radius increases.

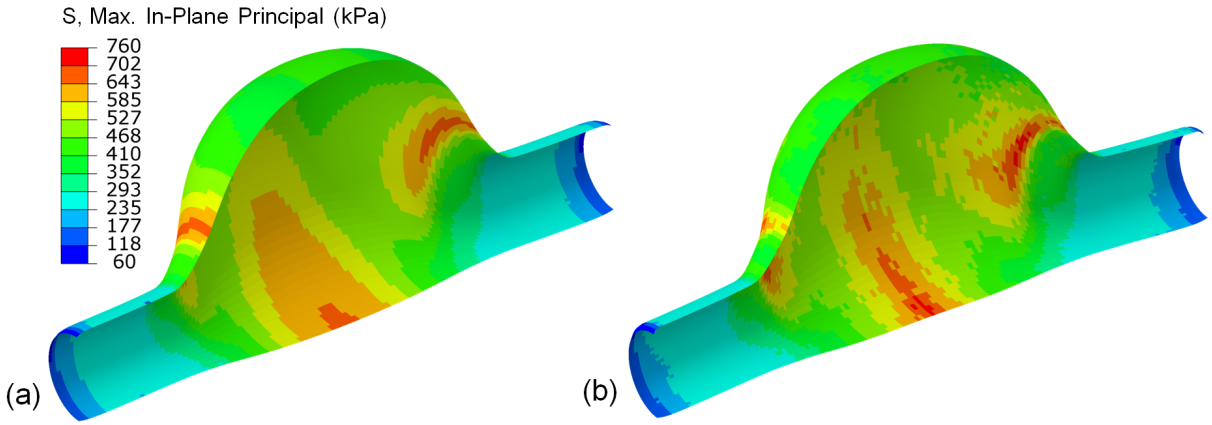

Figure 4.2: Maximal principal Cauchy stresses in the simple virtual geometry (Roy et al., 2014). (a) With isotropic material (Raghavan and Vorp, 2000). (b) With anisotropic HGO model.

4.3.2 Pressurized first patient-specific geometry

Again, presenting maximal principal Cauchy stresses (Figure 4.3), a global peak wall stress of 1087 kPa was observed in the bifurcation area. The position of this maximal value is explained by the double curvature, acting as stress concentrator.

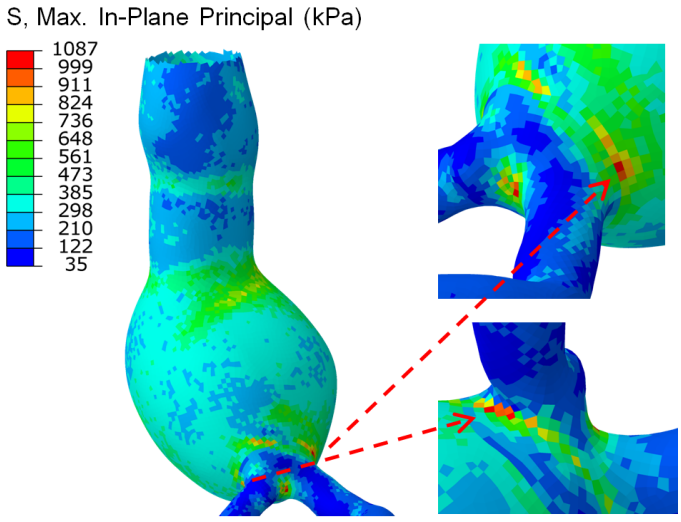

Figure 4.3: Maximal principal Cauchy stresses in the first patient-specific geometry (PS1) (Roy et al., 2014).

Maximal principal Cauchy stresses at the transition between proximal healthy abdominal aorta and AAA bulge are plotted in Figure 4.4. A local peak wall stress of 792 kPa was found in this area.

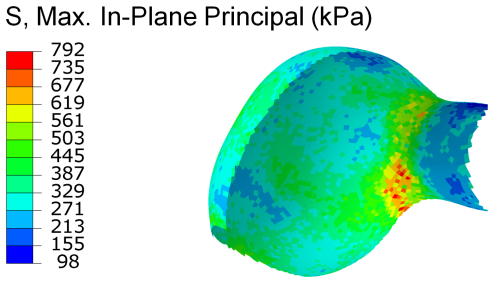

Figure 4.4: Maximal principal Cauchy stresses between proximal healthy aorta and AAA bulge of the first patient-specific geometry (PS1) (Roy et al., 2014).

4.3.3 Pressurized second patient-specific geometry

4.3.3.1 Sensitivity of AAA mesh size

Maximal principal Cauchy stresses for nominal and augmented element sizes of PS2 AAA are exposed in Figure 4.5. Maximum peak wall stresses of 756 kPa and 711 kPa were found respectively, which represented a difference of 5.95% with reference to the nominal version.

Also, one can note lower stresses at the AAA-ILT interface, that was earlier interpreted as a "cushion" effect from the ILT, which is probably not true since it might be porous.

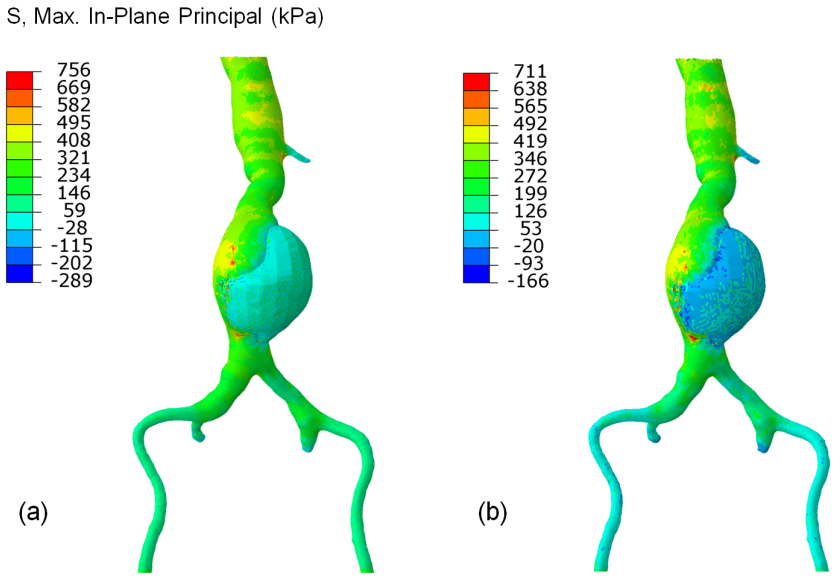

Figure 4.5: AAA mesh size sensitivity in terms of maximal principal Cauchy stresses. (a) Nominal size of 1 mm. (b) Augmented size of 2 mm.

4.3.3.2 Sensitivity of ILT mesh size

After analyzing the PS2 geometry with the nominal element size, and another version with an element size of 0.75 mm rather than 1.5 mm for the ILT, resulting Von Mises stresses could be compared (Figure 4.6). Maximal values of 8.62 kPa and 10.52 kPa were found respectively, which based on the nominal version represented a difference of 22%.

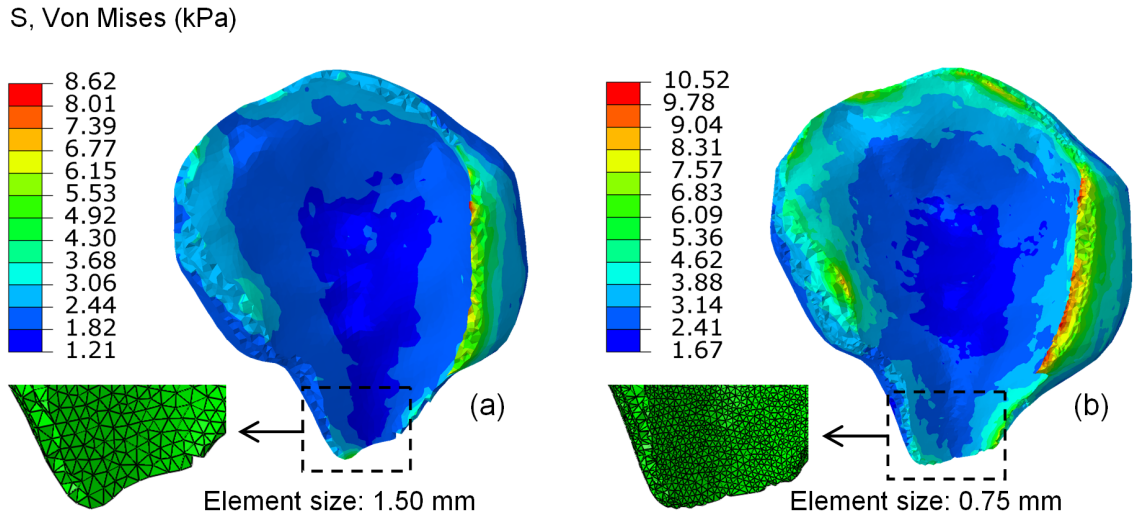

Figure 4.6: ILT mesh size sensitivity in terms of Von Mises stresses. (a) Nominal size of 1.5 mm. (b) Reduced size of 0.75 mm.

In terms of maximum displacements, the models showed 4.97 mm and 5.27 mm for the nominal and refined versions respectively (Figure 4.7). With reference to the nominal version, this represented a difference of 6%.

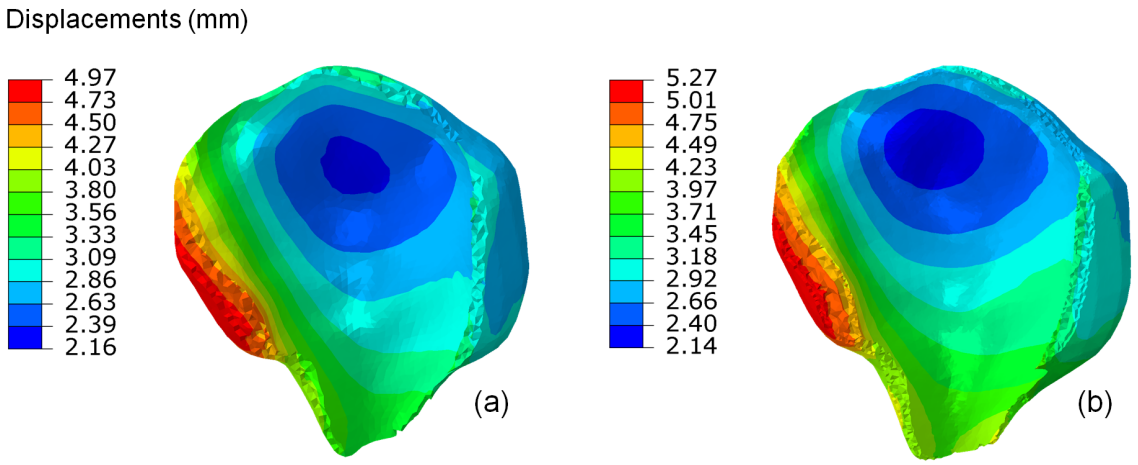

Figure 4.7: ILT mesh size sensitivity in terms of displacements. (a) Nominal size of 1.5 mm. (b) Reduced size of 0.75 mm.

4.4 Discussion

As shown in Figure 4.2(b), the peak wall stress of 759 kPa found in the simple virtual geometry made with shell elements and implementing the HGO model, compared well to 794 kPa found by Rodríguez et al. (2008) for the same geometry. This represented a difference of 4.41%. Therefore, the initial objective to demonstrate a maximum difference of 5% could be met.

Moreover, PS1 geometry implementing the HGO model, led to a local peak wall stress of 792 kPa in a region of similar double curvature compared to the simple virtual geometry.

Regarding the sensitivity of the solution to AAA mesh size, it appeared a maximal difference of 5.95% in terms of Cauchy stresses between the two versions of PS2 modeled with the nominal and augmented element sizes respectively. Hence, one could expect a lower difference between the nominal model and exact solution, probably less than 5% or very close to this threshold.

Finally, the results in nominal and refined ILT were compared in terms of Von Mises stresses, that are better adapted for continuum structures modeled with solid elements. Von Mises stresses incorporate both compressive and shear stresses in all 3 directions simultaneously. Despite a significant difference of 22%, the associated stresses were almost two orders of magnitude less than the ones occurring in the AAA wall. And a substantial mesh refinement would have been needed to reduce the difference (particularly for the nearly flat elements at the border), thus leading to unaffordable long analyses. Therefore, it was decided to consider displacements rather than stresses as validation metric, because one is mostly concerned with displacements in this project. In terms of displacement, a maximum difference of 6% was found, which is closer to the required 5%.

4.5 Conclusion

In this chapter, it was showed that well understood and implemented shell elements may perform as well as solid elements for AAA modeling, provided the arterial thickness does not exceed one tenth of the diameter.

A satisfying correlation in terms stresses and displacements was obtained with published results and according to the objectives of this work. The reached (mesh size independent) solution is a good compromise between accuracy and the efficiency allowed by shell elements.

In the third and last part, SG deployment simulations are finally addressed, based on the precedent developments on SG and AAA modeling.

Part III

SG deployment modeling

Chapter 5

Numerical approach of SG deployment

5.1 Introduction

Numerical simulations of the complete EVAR procedure are still challenging tasks. Actually, at the moment such simulations are not available, and only a few partial models exist. Prasad et al. (2013) could deploy a cylindrical body in a soft AAA, and De Bock et al. (2012) presented a bifurcated body deployment, also in a soft AAA (Figure 5.1).

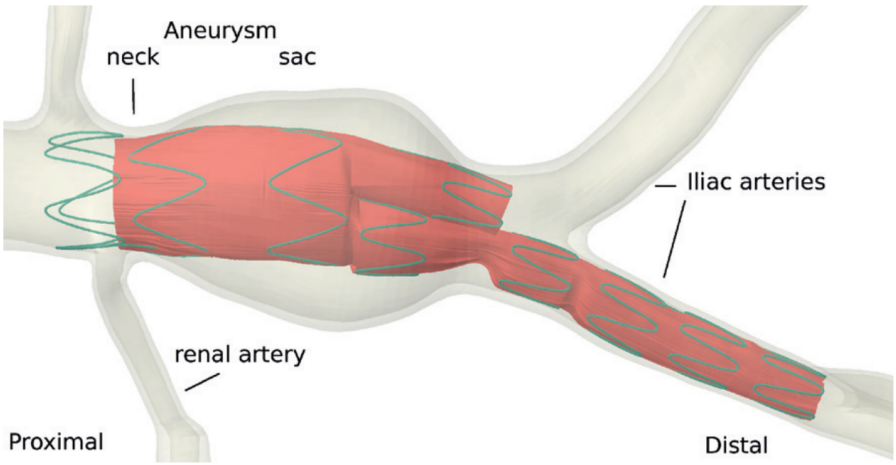

Figure 5.1: Deployment of a body SG in a virtual straight AAA (De Bock et al., 2012). Reproduced with the permission of Elsevier.

However, both studies relied on virtual and quite straight AAA geometries, besides, no leg SG were included.

On the other hand, Demanget et al. (2013) focused specifically on leg deployment in a virtual but tortuous vessel (Figure 5.2)(b), and reported a significant numerical difficulty related to element distortion in the graft.

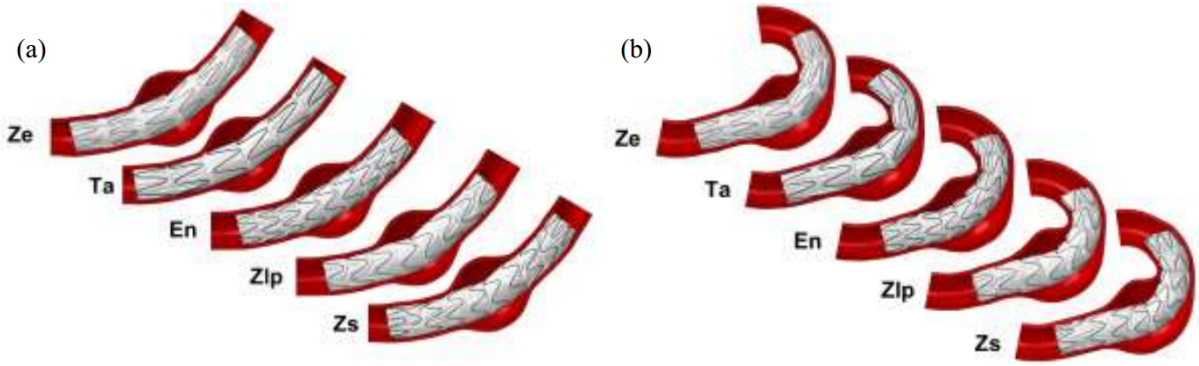

Figure 5.2: Deployment of a leg SG (Demanget et al., 2013). (a) In a virtual straight AAA. (b) In a virtual tortuous AAA. Abbreviations for commercial SG; Ze: Zenith Flex (Cook Medical), Ta: Talent (Medtronic), En: Endurant (Medtronic), Zlp: Zenith Low Profile (Cook Medical) and Zs: Zenith Spiral Z (Cook Medical).

Indeed, distortion is the main challenge when simulating such large displacements, both in the grafts compressed against their catheter, and in AAA severely straightened by catheter insertion.

In the present work, the body and legs were modeled, and deployed into a patient-specific geometry with a more pronounced degree of tortuosity. The contribution also comes from performing the deployment into a pre-deformed geometry reproducing the deformed configuration due to catheter insertion (of the pressurized ZPG). Also, an original use of connectors allowed a better control of the relative position of the SG, as well as the global positioning of the prosthesis.

These developments were condensed into a plug-in application embedded into Abaqus, as an effort toward a clinical tool for intervention planning. Also, this could be used as a training platform for young practitioners. Aside from these potential applications, for now the plug-in offers a more efficient and automated way to execute the developed workflow for new cases.

After SG and AAA characterization and modeling, the mechanical behavior of catheters in bending had to be identified in order to fully define the DD. This aspect is addressed in the following sections.

5.2 Characterization of catheter bending stiffness

Before any serious development of SG deployment simulations, the bending stiffness of typical DD (assembly of catheter, SG and guidewire) must be assessed. Regarding the available DD to realize these measurements, some still had SG whereas for others the SG had already been deployed.

5.2.1 Results of three-point bending tests on common catheters

These tests were done by means of a Bose EnduraTEC ELF 3200 tensile machine, on a guidewire *Lunderquist 260* and several body and leg DD from Cook Medical. All DD were tested at the SG location and distal location, as shown in Figure 5.3.

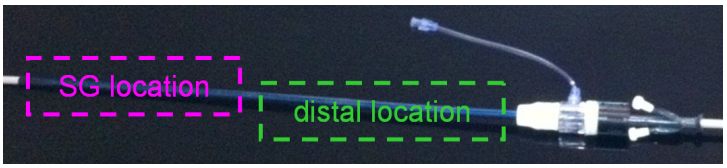

Figure 5.3: Locations where three-point bending tests were realized on catheters.

Each test was performed three times with the same material, and global equivalent Young's moduli are presented in terms of mean values and corresponding standard deviations (Table XVI). Typical setups are presented in Figure 5.4.

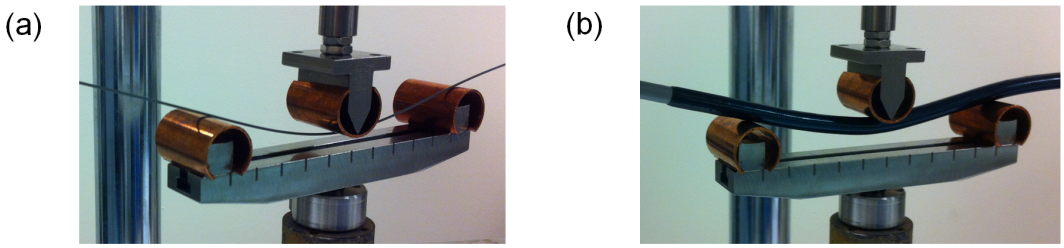

Figure 5.4: Three-point bending test performed on guidewire and catheters.

Equivalent Young's moduli were determined from classical equations

$$E = \frac{FL^3}{48yI} \tag{5.1}$$

where F is the vertical force, L the distance between the two inferior supports, y the vertical deflection and $I = \pi D^4/64$ the moment of inertia with D being the diameter. $L = 108\,\text{mm}$ in each case.

Table XVI: Equivalent Young's moduli of the guidewire (G) and typical delivery devices from Cook Medical (after three-point bending tests). Young's moduli are given as mean values and standard deviation (each test repeated 3 times).

	Tested device	Ø(mm)	with SG	E (kPa)
1	G	0.889	-	$2.030 \times 10^8 \pm 1.090 \times 10^6$
2	G + TFFB-24-111 (SG location)	6.85	yes	$3.600 \times 10^5 \pm 1.400 \times 10^4$
3	G + TFFB-24-111 (distal location)	6.85	-	$5.740 \times 10^5 \pm 4.000 \times 10^3$
4	G + TFLE-12-54 (SG location)	5.20	yes	$6.710 \times 10^5 \pm 3.800 \times 10^4$
5	G + TFLE-12-54 (distal location)	5.20	-	$1.094 \times 10^6 \pm 6.700 \times 10^4$
6	G + TFLE-12-71 (SG location)	5.20	no	$1.083 \times 10^6 \pm 3.000 \times 10^4$
7	G + TFLE-12-71 (distal location)	5.20	-	$1.084 \times 10^6 \pm 5.900 \times 10^4$
8	G + TFLE-16-88 (SG location)	5.25	no	$1.051 \times 10^6 \pm 2.900 \times 10^4$
9	G + TFLE-16-88 (distal location)	5.25	-	$1.102 \times 10^6 \pm 7.200 \times 10^4$

As a reminder, guidewires might have nitinol or stainless steel cores, both coated with polytetrafluoroethylene (PTFE) and having a flexible tip. In the present study, the available guidewire clearly had a stainless steel core, given its equivalent Young's modulus.

Based on these preliminary results, mean properties (diameter, equivalent Young's modulus and equivalent density) could be defined for main body and leg outer catheters (outer referring to the largest diameter). Also, the inner catheter portion, i.e., where the diameter had its smallest value and allows storing SG prior to deployment, could be defined (see Figure 5.5). This development is detailed in the next section.

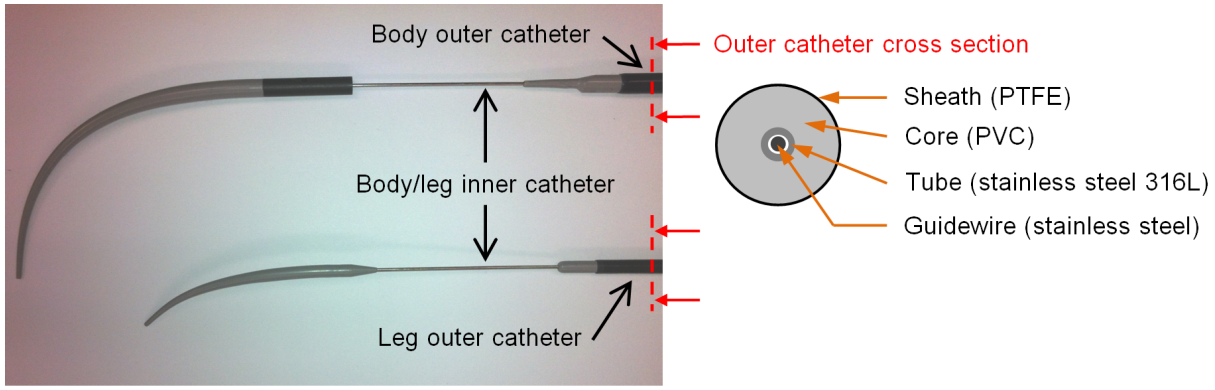

Figure 5.5: Typical body and leg catheters: cross section and composition. PTFE and PVC stand for polytetrafluoroethylene and polyvinyl chloride respectively.

5.2.2 Specific properties of body and leg catheters

5.2.2.1 Body outer catheter

Since only one main body catheter could be tested, the data from line 3 of Table XVI was assumed to be the mean diameter and mean Young's modulus. Regarding density assessment, the following "mixing" rule was used

$$\rho_m = \frac{\sum_{i=1}^{n} \rho_i A_i}{\sum_{i=1}^{n} A_i} \tag{5.2}$$

where A_i represents the cross section area of each part. Details of this computation are presented in Table XVII. A similar density was assumed for both the tube and guidewire.

Table XVII: Computation of equivalent density for main body outer catheters. ID and OD stand for inner diameter and outer diameter respectively. Densities for PTFE and PVC came from *www.fluortek.com* (consulted on 2014-06-14) and *http://en.wikipedia.org/wiki/Polyvinyl_chloride* (consulted on 2014-06-14) respectively.

Part	ID (mm)	OD (mm)	A (mm^2)	Material	ρ ($kg\,mm^{-3}$)
Sheath	6.05	6.85	8.105	PTFE	2.22×10^{-6}
Core	1.25	6.05	27.520	PVC	1.23×10^{-6}
Tube + guidewire	0.0	1.25	1.227	stainless steel	8.00×10^{-6}
$\rho_m = 1.673 \times 10^{-6}\,kg\,mm^{-3}$					

5.2.2.2 Leg outer catheter

In this case, the mean diameter and mean Young's modulus were computed from lines 5, 7 and 9 of Table XVI, leading to 5.22 mm and 1.093×10^6 kPa respectively.

Similarly, the corresponding mean density was computed with the mixing rule (Table XVIII).

Table XVIII: Computation of equivalent density for leg outer catheters.

Part	ID (mm)	OD (mm)	A (mm^2)	Material	ρ ($kg\,mm^{-3}$)
Sheath	4.82	5.22	3.154	PTFE	2.22×10^{-6}
Core	1.25	4.82	17.019	PVC	1.23×10^{-6}
Tube + guidewire	0.0	1.25	1.227	stainless steel	8.00×10^{-6}
$\rho_m = 1.764 \times 10^{-6}\,kg\,mm^{-3}$					

5.2.2.3 Inner catheter portion

An outer diameter of 1.25 mm was measured for this portion, common to all catheters supporting/housing body or leg SG. The properties of stainless steel were considered for this region.

Finally, all the dimensions and properties defined above are summarized in Table XIX. A Poisson's ratio of 0.3 was attributed to all these sections, as a generic value.

Table XIX: Equivalent mean properties for typical sections of body and leg catheters.

	Ø(mm)	E (kPa)	ν (-)	ρ (kg mm^{-3})
Body outer catheter	6.85	5.740×10^5	0.3	1.673×10^{-6}
Leg outer catheter	5.22	1.093×10^6	0.3	1.764×10^{-6}
Inner catheter	1.25	1.930×10^8	0.3	8.00×10^{-6}

5.2.3 Artificial catheter properties for vascular deformation purposes

To anticipate the need of modeling the large deformations undergone by AAA upon DD/catheter insertion, a particular set of DD having the same stiffness as the above mentioned body and leg outer catheters was developed, but having a diameter of 2 mm. The benefit of that is to make easier the numerical pre-deformation of AAA structures characterized by narrowed sections.

Thus, Young's moduli and densities had to be adapted, while keeping the same Poisson's ratio obviously. In order to maintain the same stiffness, the ratio F/y was extracted from equation 5.1 and kept constant, moreover, all unchanging terms were discarded, which led to

$$E_2 = E_1 \left(\frac{D_1}{D_2}\right)^4 \tag{5.3}$$

Replacing E_1 and D_1 by the nominal values associated to the body and leg outer catheters, and setting D_2 to 2 mm, allowed to estimate the adapted Young's moduli. On the other hand, the mass of each catheter had to be kept constant, which was simply achieved by keeping constant the product ρA. Thus bringing the formula

$$\rho_2 = \rho_1 \left(\frac{D_1}{D_2}\right)^2 \tag{5.4}$$

Again, replacing ρ_1 and D_1 by the nominal values and setting D_2 to 2 mm, allowed to identify adapted values. These outcomes are gathered in Table XX.

Table XX: Equivalent properties for body and leg outer catheters with imposed diameter of 2 mm.

	E (kPa)	ρ (kg mm^{-3})
Body outer catheter "2 mm"	7.899×10^7	1.963×10^{-5}
Leg outer catheter "2 mm"	5.072×10^7	1.202×10^{-5}

5.3 Deployment strategy

The case H1025269 from CR-CHUM database served as demonstrator, the ILT of which was discarded for the sake of simplicity, and to avoid long analyses (tetrahedral elements always require more computational effort than quadrilateral ones and beam elements). Therefore, the lumen was meshed as if it was the actual vessel wall. At this point, it is reminded that the very first step is to define the ZPG of the vessel, by means of a forward-backward analysis.

5.3.1 Arterial pre-deformation

Since SG should ideally be deployed in pre-deformed AAA, in order to faithfully reproduce the clinical reality, a preliminary analysis involving only deforming catheters in a pressurized AAA must be performed. For this particular analysis, the catheter properties designed in section 5.2.3 were considered, along with a damping coefficient of 100 and a mesh size of 3 mm. This strategy is fortunate because by straightening the vascular structure, it avoids excessive element distortion in the grafts, while trying to make the pre-assembled (i.e. compressed against real catheters) prosthesis fit highly tortuous centerlines.

This analysis involved two steps; during the first one the vessel (ZPG) was pressurized (120 mmHg), while the catheters were displaced on the centerlines corresponding to the pressurized ZPG. All possible contacts were deactivated to allow the catheters to travel "through" the vessel wall. During the second step, the contacts were activated and the imposed displacements on both catheters were removed, thus releasing their stored elastic energy and deforming the vessel.

A constant mass scaling factor of 100 ensured a quasi-static solution to develop during both steps, and a time period $T = 2$ s was definitely needed during the second step to

stabilize the dynamic release of catheters. It was found that fully integrated quadrilateral shell elements (S4) helped the model to converge, as opposed to reduced elements (S4R). Although not mandatory, second-order accuracy is recommended to simulate such dynamic events, and it was done so. S3R elements could also be used, even if they are reduced and do not have second-order accuracy, but this would increase significantly the resolution time.

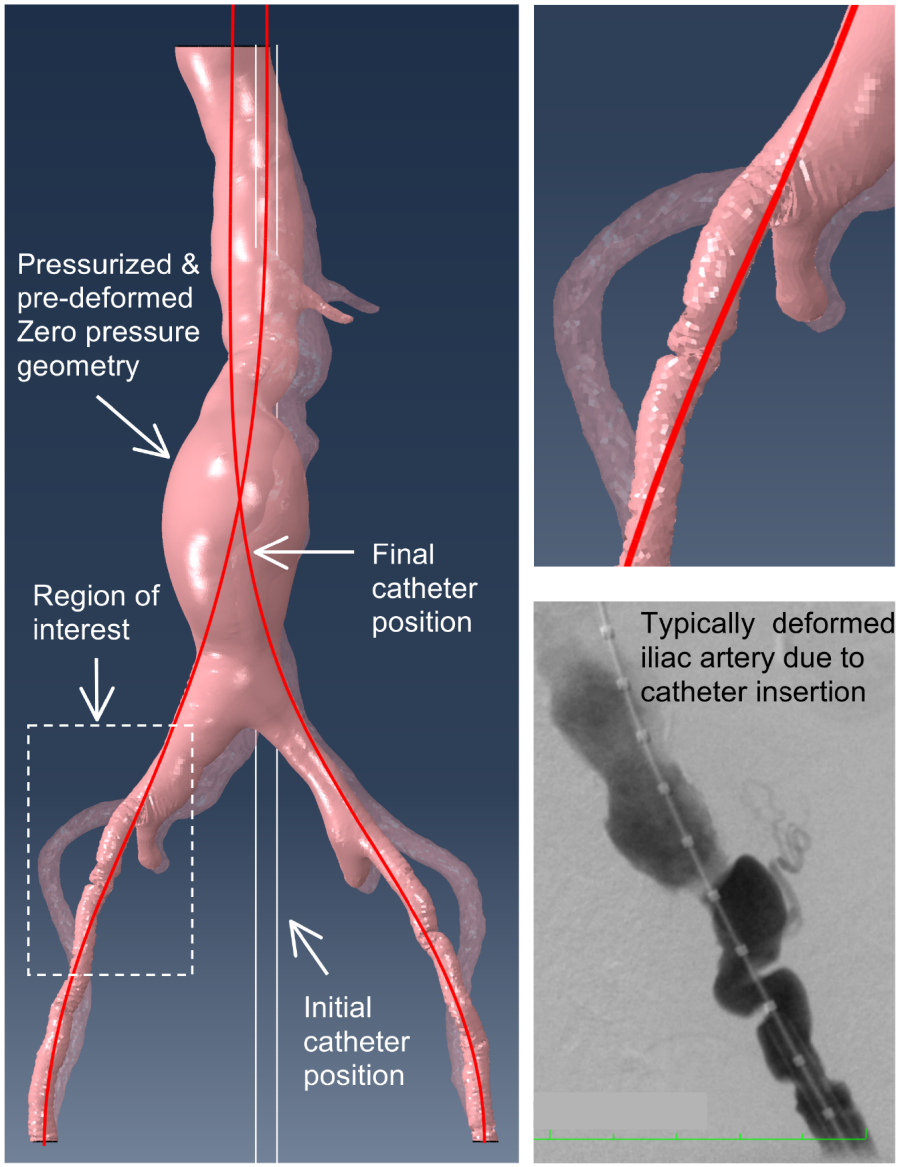

Figure 5.6: Pressurized (120 mmHg) and pre-deformed AAA (case H1025269 from CR-CHUM database) due to catheter introduction. The ILT was discarded, and the lumen was assumed to represent the vessel wall (Roy et al., 2014).

In case of instabilities at AAA end sections, the latter could be fully fixed.

5.3.2 Whole deployment model

5.3.2.1 Material adjustments

This model included the AAA, SG, catheters and sheaths. A uniform thickness of 1.5 mm was attributed to the AAA wall for simplicity. In this case the catheters were the ones developed in section 5.2.2.

All sheaths were attributed the mechanical properties found online (*www.fluortek.com*, consulted on 2014-06-14). Their nominal thickness of 0.4 mm was reduced to 0.04 mm to avoid any numerical side effect due to their natural stiffness. Thus, the parameters having a dimension of pressure or density were increased by the same factor to compensate. However, the density was adjusted after some trials in order to ensure a proper contact with SG. An arbitrary Poisson's ratio of 0.45 was attributed, knowing that perfectly incompressible materials are characterized by a Poisson's ratio of 0.50. These parameters are summarized in Table XXI.

Table XXI: Mechanical properties of shrinking sheaths. Parameters with dimension of pressure or density are affected by thickness reduction, i.e. increased by the same factor.

Reduced thickness (by a factor 10)	t	$0.04\,\mathrm{mm}$
Young's modulus	E	$5.000 \times 10^6\,\mathrm{kPa}$
Poisson's ratio	ν	0.45
Shear modulus	$G = E/(2(1+\nu))$	$1.724 \times 10^6\,\mathrm{kPa}$
Transverse shear stiffness in circumf. dir.	$K_{11} = (5/6)Gt$	$5.747 \times 10^4\,\mathrm{kPa\,mm}$
Transverse shear stiffness in axial dir.	$K_{22} = K_{11}$	$5.747 \times 10^4\,\mathrm{kPa\,mm}$
Transverse shear stiffness in in-plane dir.	K_{12}	$0.000\,\mathrm{kPa\,mm}$
Density	ρ	$1.085 \times 10^{-8}\,\mathrm{kg\,mm^{-3}}$
Expansion	α	$11.6\,\mathrm{K^{-1}}$

Additional trials allowed to identify the ideal variations of temperature that had to be applied to each sheath, i.e. $\Delta T = -0.1\,\mathrm{mm}$ for all sheaths, except for the one compressing the upper part of the body (from proximal stent with hooks down to the bifurcation) for which an optimum $\Delta T = -0.2\,\mathrm{mm}$ was found.

5.3.2.2 Benefit of connectors

A key feature of Abaqus involved in this model was the capability to impose complex kinematic relationships via connectors. These allowed

- controlling the relative position between the body and leg SG, thus avoiding them to move apart from each other,
- controlling the prosthesis (global) position along the centerlines,
- simulating the hooks anchored into the AAA wall.

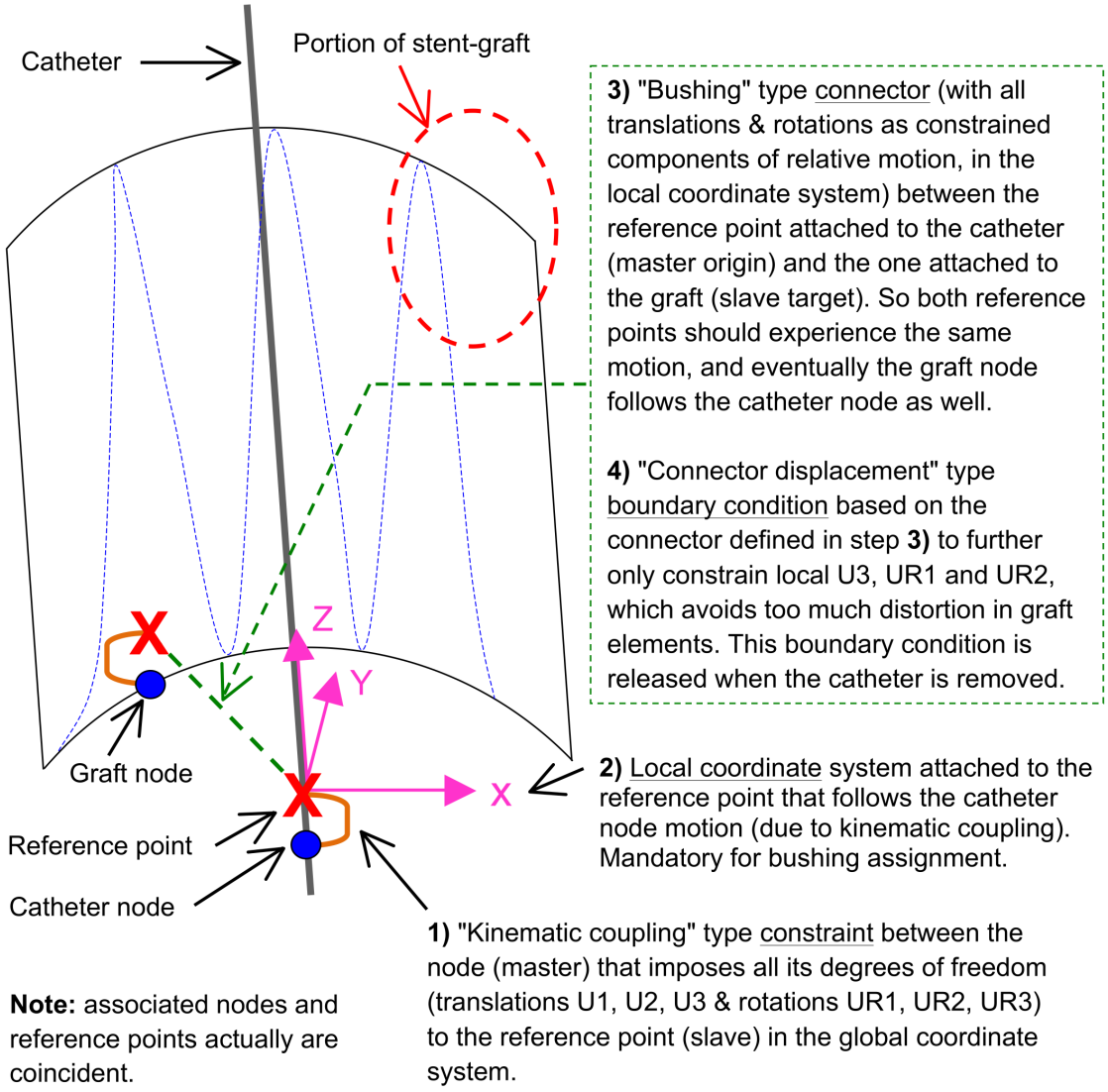

Figure 5.7: General definition of connectors. Connectors can only be defined between reference points, therefore kinematic coupling constraints must first be defined between each reference point and the adjacent node. This depicts how the connectors are defined between a catheter and a SG, and the same holds for the connectors between catheters and sheaths.

Regarding the connectors simulating the hooks anchored into the AAA, the set of nodes identified in Figure 2.7(b) was constrained to follow the motion of a reference point

attached to the vessel, along the direction shown by the centerline close to this point (after deployment). This constraint is depicted in Figure 5.8.

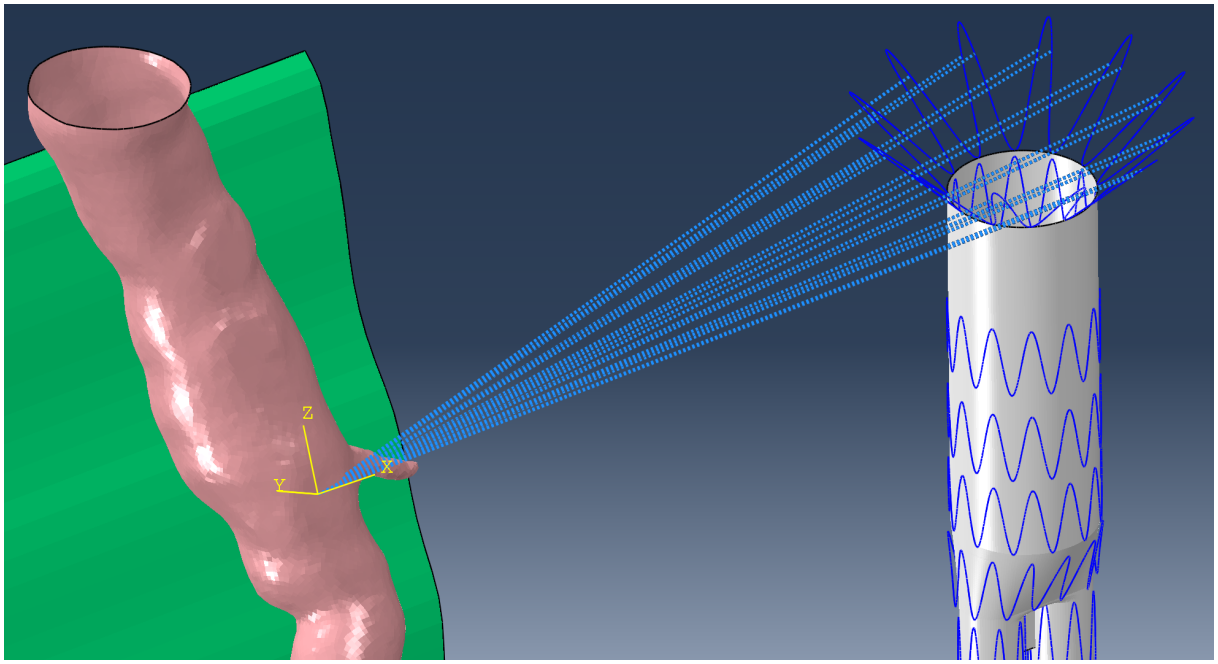

Figure 5.8: Connectors for hooks simulation. In this case, the master reference point is attached to a node of the vessel. The constraint is applied along the Z-axis of the local coordinate system attached to this reference point.

As mentioned above, a beneficial consequence of using connectors is that the position of the different SG along the centerlines can be controlled. In particular, the distance between the top of the body graft and the left renal centerline was defined as a control parameter (Figure 5.9).

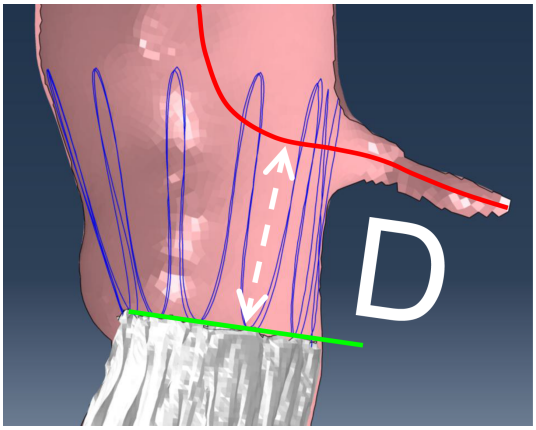

Figure 5.9: Parameter "D" to control the position of the body with respect to the centerline branch of the left renal artery.

Furthermore, the overlap distance between both legs and the body was also controlled all along the analysis. The accuracy with which the prosthesis can be located along the centerlines (in a curvilinear manner), is of the order of 1 mm. And for this reason, the catheters involved in deployment simulations have a mesh size of 1 mm. Since the catheters are undergoing controlled displacements all along the analysis, the ratio of (beam) element size to actual diameter is not important. These catheters, although defined with realistic material properties and sections, only serve to guide the prosthesis to the right desired position inside the vessel via contact.

5.3.2.3 Friction

It was found that prescribing contacts with friction might induce numerical (convergence) difficulties during the release of sheaths. For this reason, friction was introduced in the contact algorithms only at the very last step, i.e. during equilibrium. Coefficients of friction of 0.20 (Mortier et al., 2010) and 0.30 (Prasad et al., 2013) were found in the literature, so an overall mean value of 0.25 was considered in this work.

5.3.2.4 Mass scaling and time period

A constant mass scaling factor of 100 000 was applied to the whole model. Despite this high value, the model remained quasi-static when deformation was involved. This factor was found to be optimum. Indeed, the analysis still tended to fail with a factor of 40 000, whereas unrealistic dynamic effects were appearing with a factor of 1 000 000.

With regard to time period, a value of 1 s was prescribed to each step of the deployment, except during sheath removal and final equilibrium, for which optimum values of 2 s and 4 s were set respectively.

5.3.2.5 Correct pressures

In this work, a mean arterial pressure of 120 mmHg was considered to remain consistent with the current literature (Rodríguez et al., 2008). However, for further investigations, one should consider the following formula for mean pressure (http://en.wikipedia.org/wiki/Mean_arterial_pressure, consulted on 2014-07-19)

$$P_{mean} = \left(P_{sys} + 2P_{dia}\right)/3 \tag{5.5}$$

Also, once the SG are deployed, an additional (delta) pressure should be applied inside all grafts to account for the pulsatile effect of blood. This additional pressure was defined

as the difference between the systolic and mean arterial pressures

$$\Delta P_{pul} = P_{sys} - P_{mean} \tag{5.6}$$

Table XXII hereafter provides such pressures for a series of (anonymized) patients from CR-CHUM database.

Table XXII: Typical mean and pulsatile pressures, based on equations 5.5 and 5.6 respectively.

Anonymized patient ID	P_{sys} (mmHg)	P_{dia} (mmHg)	P_{mean} (mmHg)	ΔP_{pul} (mmHg)
AAA C-D 1072085	134	71	92.00	42.00
AAA P-R 6042615	124	70	88.00	36.00
AAA R-G 518516	158	81	106.67	51.33
AAA A-G 1190422	122	56	78.00	44.00
AAA J-T 6057578	118	80	92.67	25.33
AAA B-C 302698	147	78	101.00	46.00
AAA C-L 375501	122	74	90.00	32.00
AAA P-C 279950	133	72	92.33	40.67
AAA B-B 6074197	106	69	81.33	24.67
AAA PT-1184910	112	79	90.00	22.00
			mean $\pm$ std. dev.	
			91.20 ± 8.33	36.40 ± 10.05

Therefore, a pulsatile pressure of 36.40 mmHg (or 4.85 kPa) was applied inside all grafts during the equilibrium step.

Note: while developing a model with ILT, it was observed that realistically applying a pressure on the ILT itself led to a non quasi-static results. This issue could be addressed by shifting the pressure load on the whole inner face of the AAA wall (thus, as if the ILT was strongly porous).

5.3.2.6 Element type for graft modeling

Reduced triangular (linear) shell elements (S3R) were used for all grafts, as these proved to be more robust with regard to distortion. Regarding AAA, S3R elements failed during imposed pre-deformation (even transforming quadrilateral elements into triangular ones), whereas S4 elements with second-order accuracy proved to be robust enough.

5.3.2.7 Whole model

The complete model for SG deployment simulation is presented in Figure 5.10. Connectors are defined between

1. left catheter and left leg
2. left catheter and left sheath compressing both the left leg and left body leg
3. right catheter and right leg
4. right catheter and right sheath compressing both the right leg and right body leg
5. right catheter and body
6. right catheter and sheath compressing the body
7. vessel and nodes corresponding to hooks

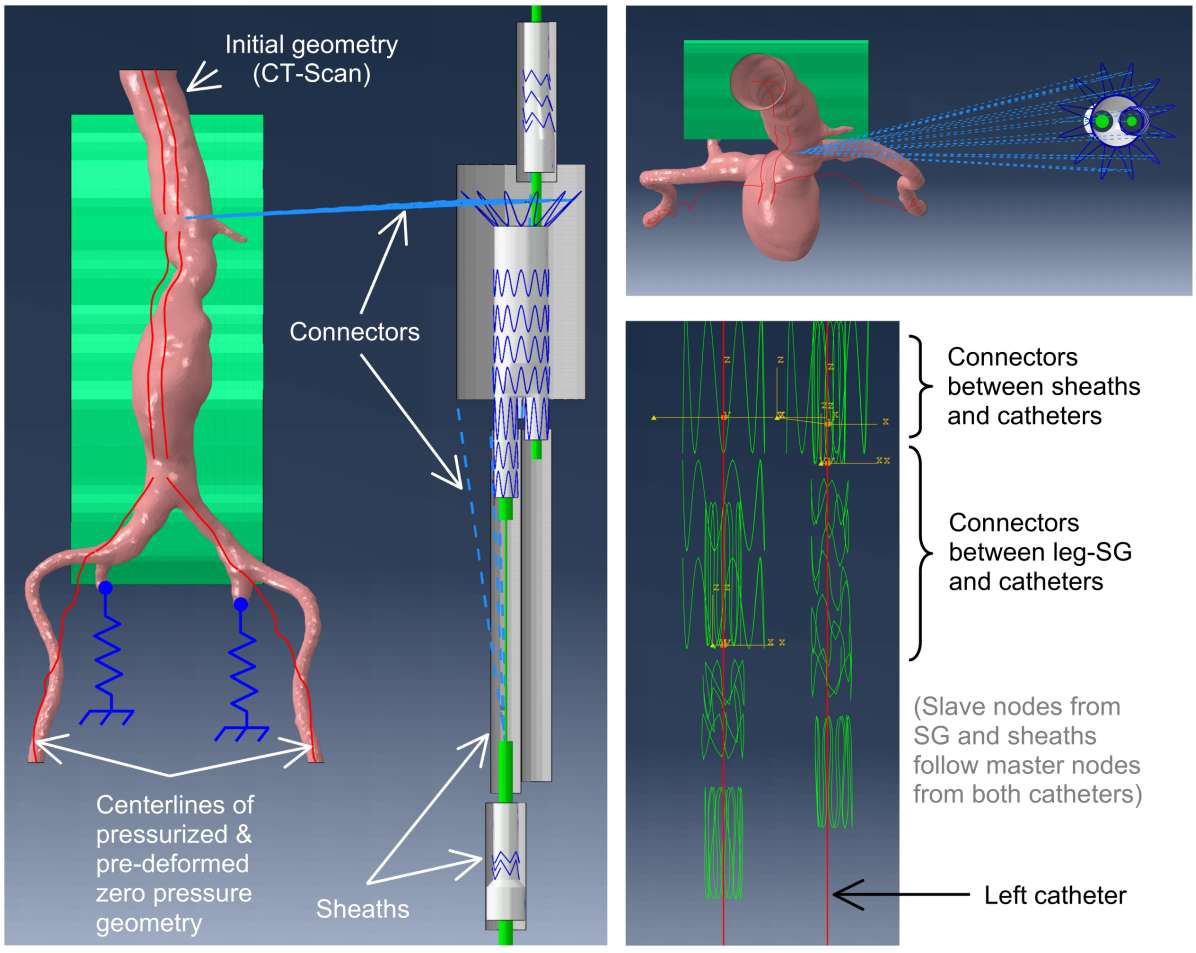

Figure 5.10: Whole model for stent-graft deployment simulation. The (Zenith) body, left and right stent-grafts have the following reference respectively: TFFB-28-111-ZT, ZSLE-16-56-ZT and ZSLE-20-39-ZT. Dual centerlines were derived from the classic "vessel" centerline, in order to fit both catheters within the AAA without geometrical clashes.

5.3.2.8 Flowchart of deployment simulation

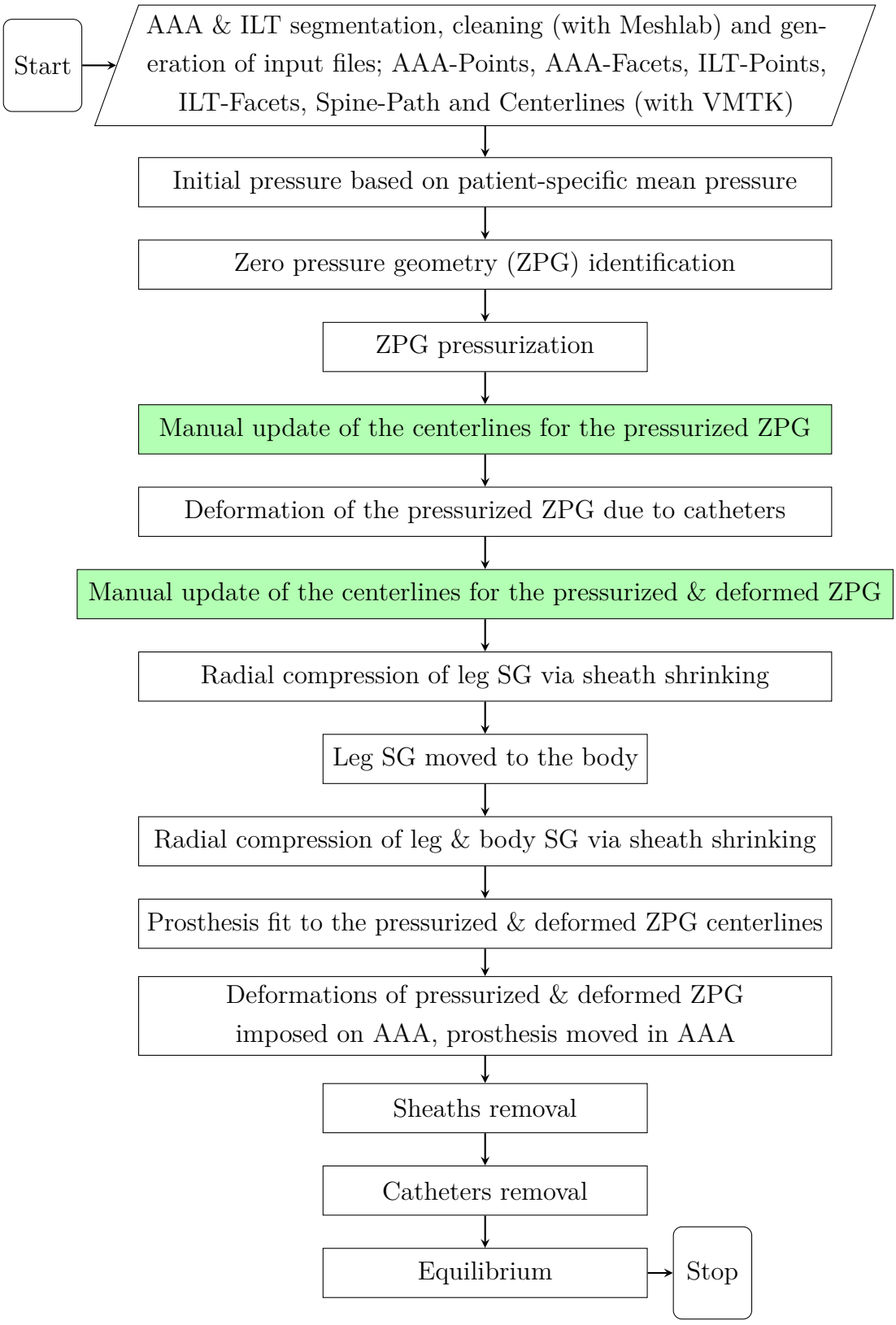

5.4 Results

5.4.1 Stent-graft deployment simulation

The sequence of SG deployment is depicted in Figure 5.11.

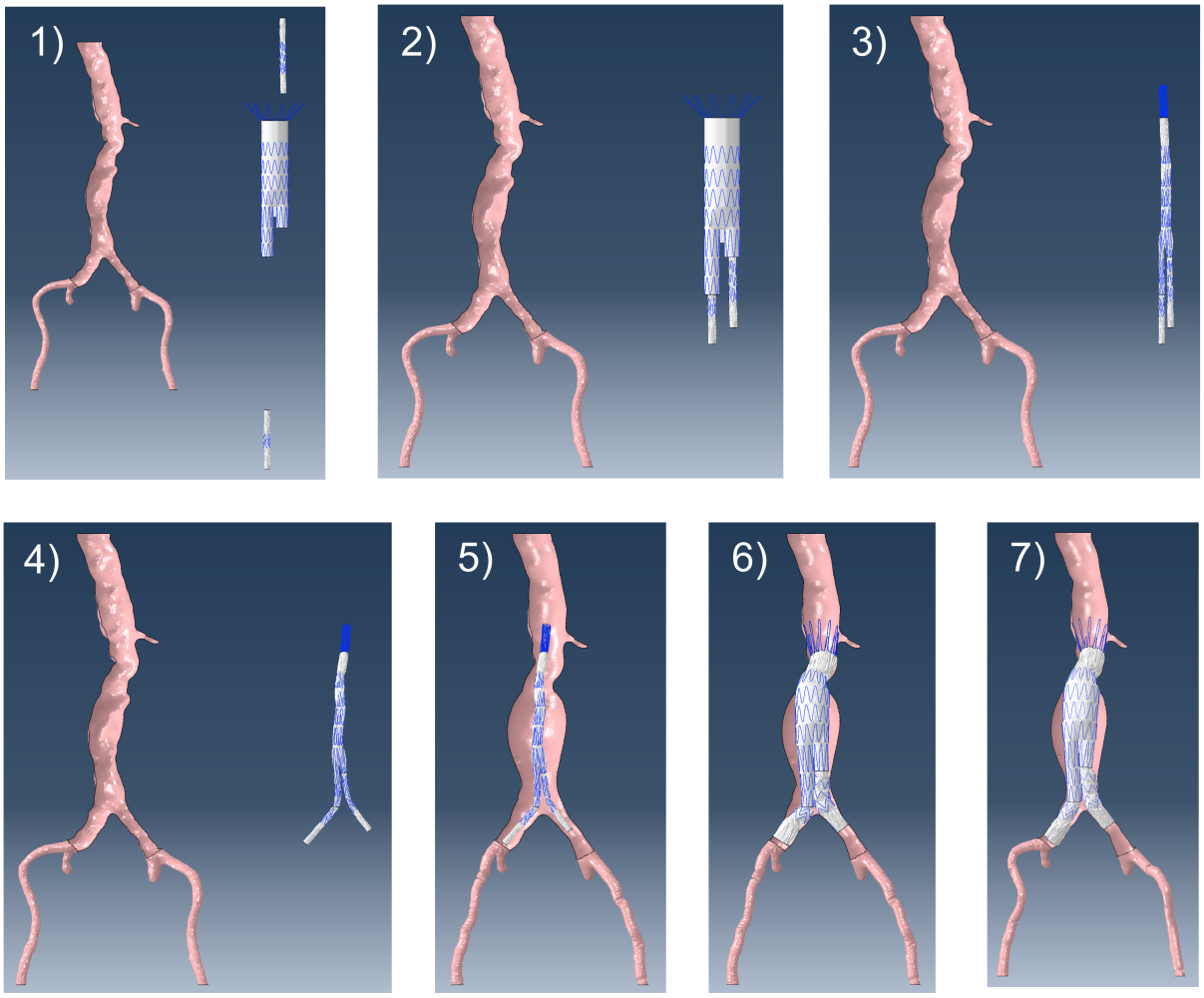

Figure 5.11: Stent-graft deployment simulation. Between pictures 4) and 5) the pre-assembled prosthesis was moved from right to left through the AAA wall (contacts deactivated). In picture 7) the final equilibrium was simulated after catheter removal, accounting for blood pressure and AAA compliance.

Having a closer look at the final equilibrium state, one can notice that some stents penetrated the graft, despite a fine mesh size of 0.7 mm for the stents and the contact controls described in Appendix E. Also, some portions of the AAA wall remained folded at the end of the equilibrium step (Figure 5.12).

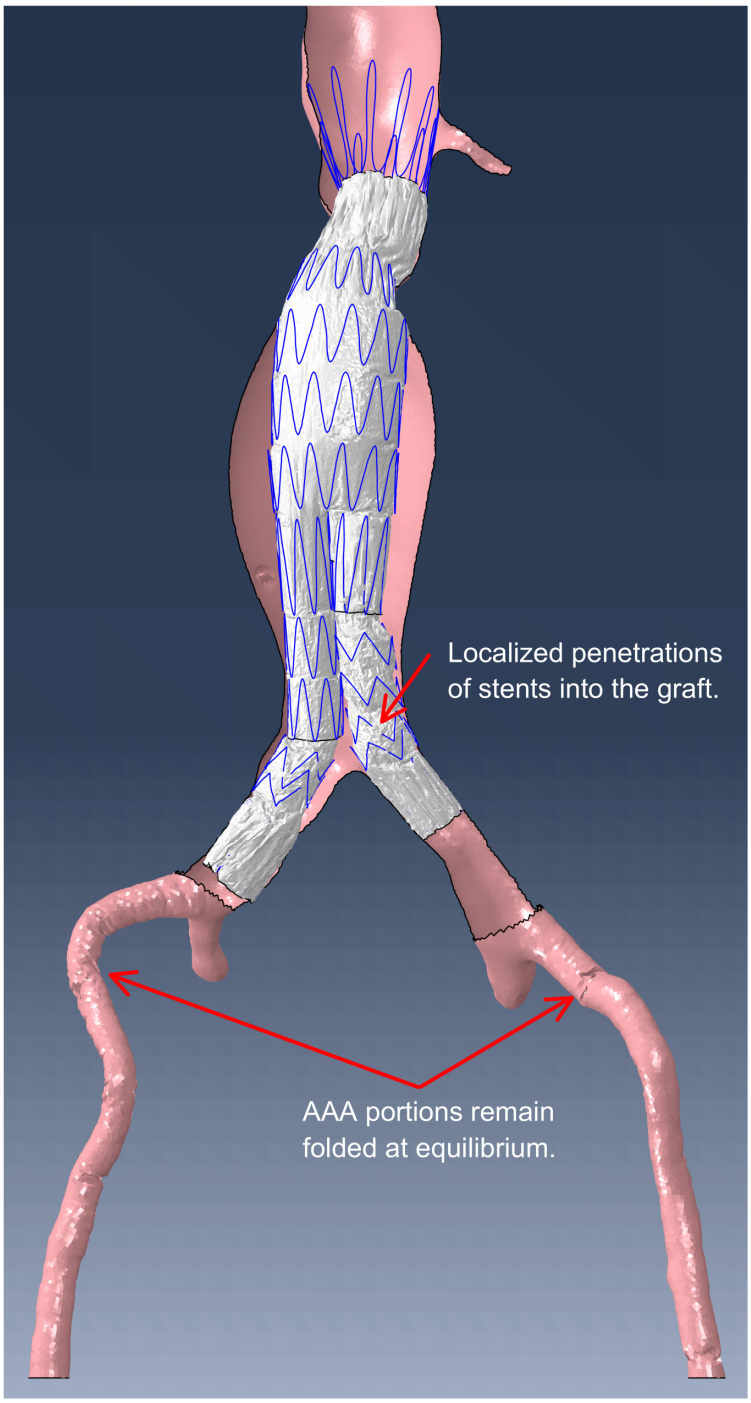

Figure 5.12: Defaults observed after final equilibrium of stent-graft deployment.

Finally, the stents looked distorted at some points, as shown in Figure 5.13, that also depicts the Von Mises stresses undergone by all the stents. Overall, these stresses remained below the yield stress of 1.70×10^5 kPa (from norm UNS S31603), but some portions were affected by stresses as high as 2.83×10^6 kPa, because of tortuous iliac arteries.

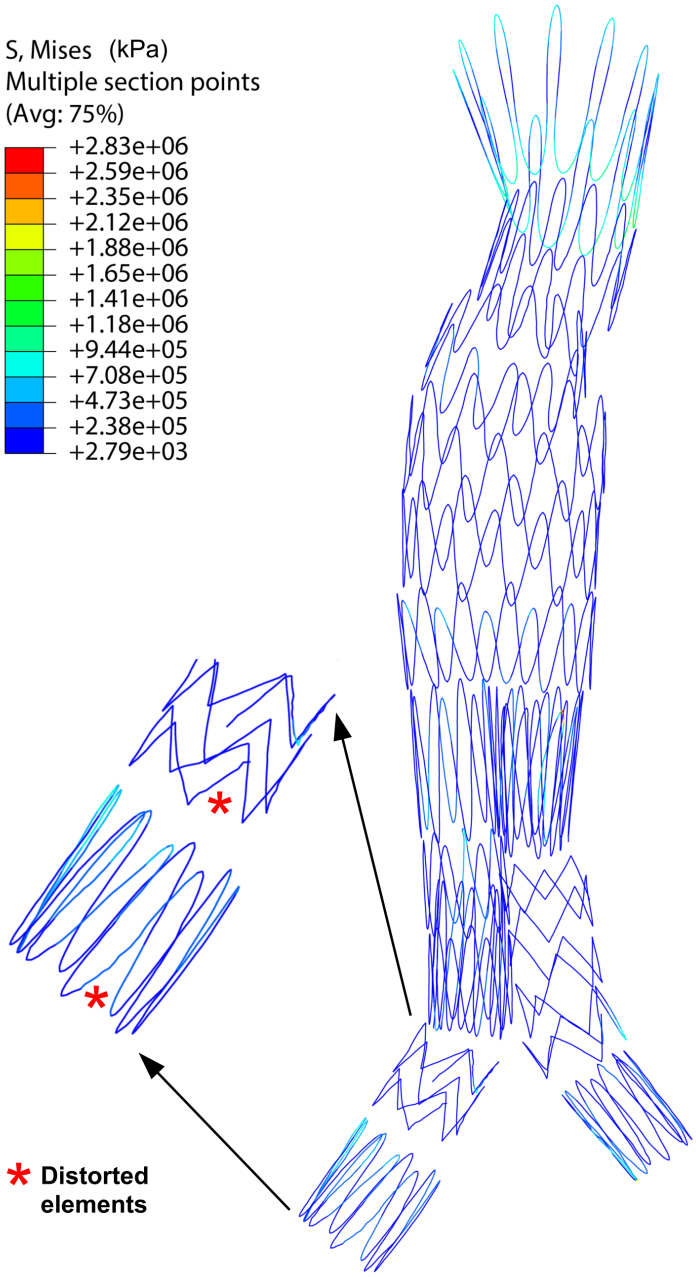

Figure 5.13: Von Mises stresses in stents after final equilibrium of stent-graft deployment.

5.4.2 Deformation energy vs. kinetic energy

The quasi-static nature of the solution is demonstrated in Figure 5.14. Here the peaks correspond to "rigid body" translations during which no or very little deformations were occurring. This does not invalidate the fact that the model behaved almost quasi-statically during the computation. Peak 1 corresponds to the compressed leg SG being moved into

the body (picture 2 in Figure 5.11). Peak 2 corresponds to the compressed prosthesis being fit on the centerlines (picture 4 in Figure 5.11), with limited deformations since these were mostly happening during the previous step. Peak 3 represents the pre-assembled prosthesis translated into the vessel (picture 5 in Figure 5.11). Peak 4 represents the removal of both catheters. Finally, the fact that the kinetic energy was momentarily superior to the deformation energy, as identified by the dotted green circle in Figure 5.14, reflects the contact between the proximal stent of the body and its (shrinking) sheath. This contact then evolved in a smoother fashion, thus reestablishing a quasi-static behavior.

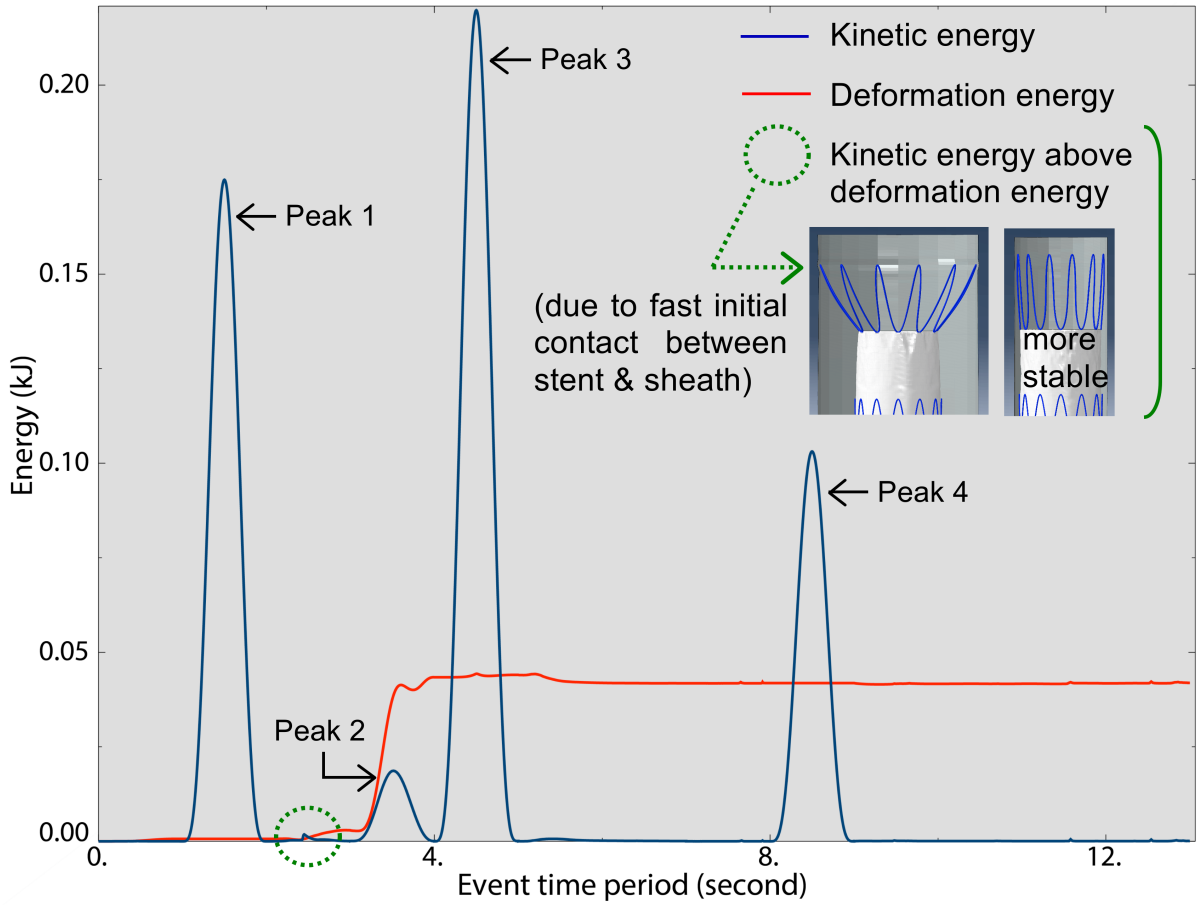

Figure 5.14: Quasi-static nature of stent-graft deployment. The peaks of kinetic energy are acceptable because they correspond to "rigid body" motions (with no or little relative deformations).

5.4.3 Time required to complete the workflow

About a week was necessary to complete the workflow on 8 CPUs (3.40 GHz), at least for the demonstrator considered in this work. No benefit was found by involving more CPUs.

5.4.4 Substantiation of the linear behavior for nitinol

It is now time to support the hypothesis of linear behavior for nitinol in the light of the complete results exposed above. From Table IV, the maximum strain of the linear elastic domain ϵ_A can be derived as $\epsilon_A = \sigma_L^S / E_A = 0.0116$, and from the SG deployment simulation one can extract the strains prior to sheath removal and after equilibrium. As a reminder, only the Spiral-Z stents are made of nitinol.

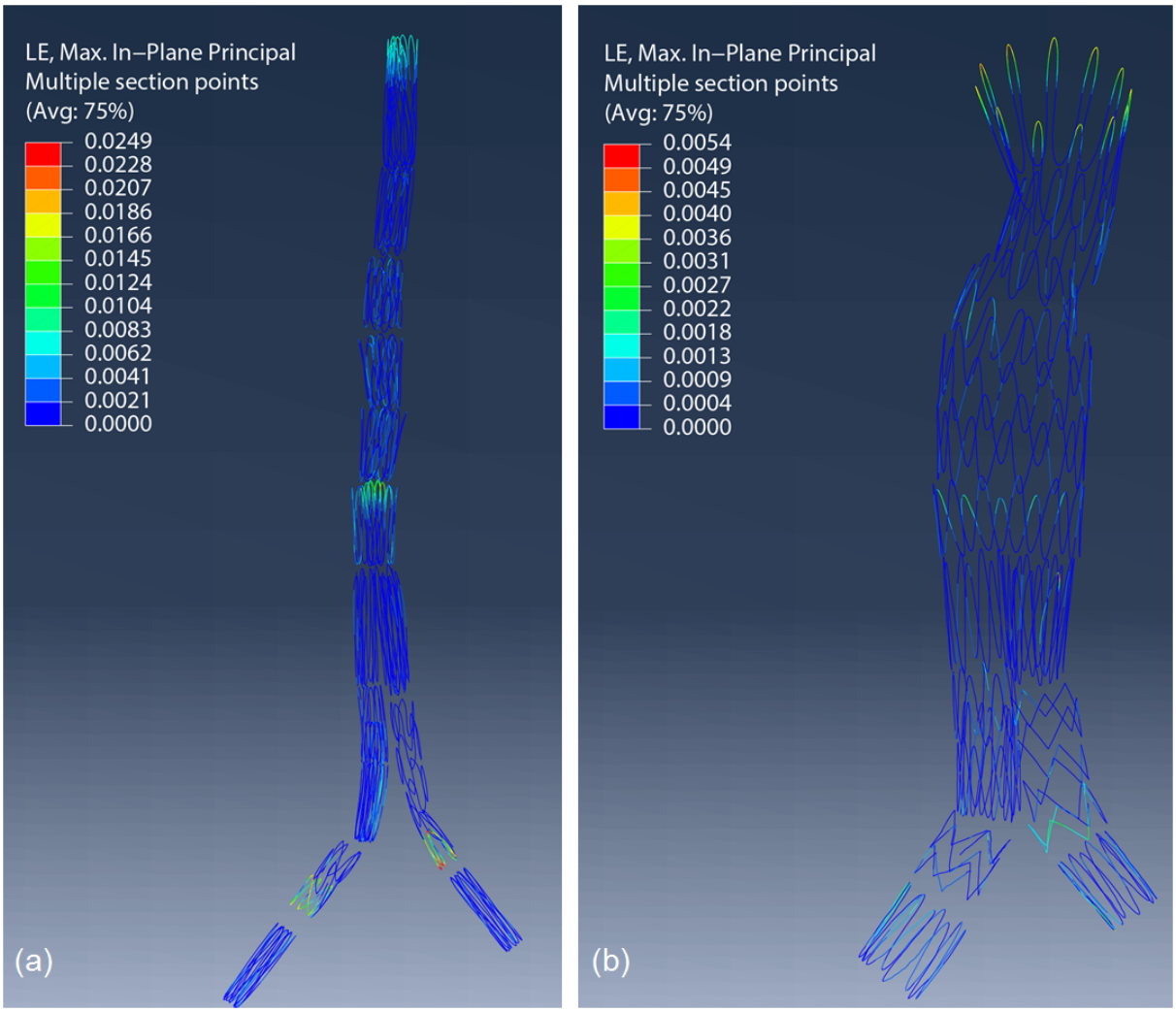

Figure 5.15: Strains in stents. (a) Before sheath removal (SG fully compressed). (b) After equilibrium. The logarithmic strains LE here depicted, are very close to the nominal strains NE ($NE = \epsilon = \exp(LE) - 1$).

From Figure 5.15(a) it can be seen that the maximum strain of 0.0249 is clearly above ϵ_A. This means that the Spiral-Z stents experience a non-linear behavior as long as they are confined into their sheath, which really does not matter in terms of mechanical response

since they are rigidly moved along with their DD. Moreover, from Figure 5.15(b) the maximum strain of 0.0054 lies below ϵ_A, meaning that the Spiral-Z stents (reversibly) came back to a linear elastic behavior during the equilibrium, which is a critical step to solve realistic displacements. Even just after sheath removal, the behavior of the Spiral-Z stents remained in the linear elastic domain as a maximum strain of 0.0045 was observed over all the stents (Figure 5.16). Therefore, it is legitimate to assume a linear behavior for all the stents made of nitinol.

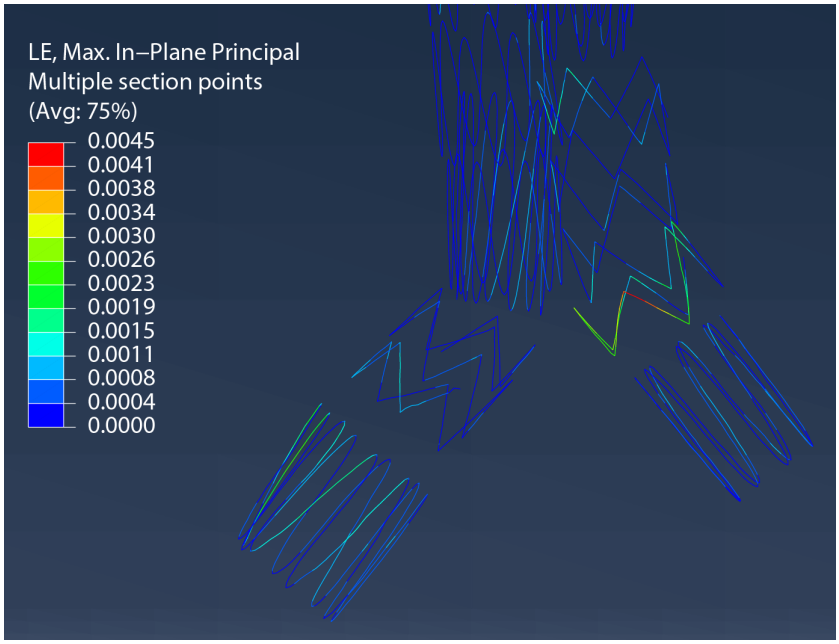

Figure 5.16: Strains in stents just after sheat removal. The logarithmic strains LE here depicted, are very close to the nominal strains NE ($NE = \epsilon = \exp(LE) - 1$).

To further support this assumption, one can refer to Demanget (2012) (page 145) who reported that nitinol stents of only 2 L-SG over 8 different models experienced a non-linear behavior during a deployment simulation in strongly angulated vessels (90° and 180°). This author also reported that none of the steel stents from these 8 L-SG models underwent any plastification. To specifically quote this experience: “Ainsi, les stents en Nitinol sont restés dans leur domaine élastique pendant la simulation excepté pour la Ta-SG et l’En-SG pour lesquelles le plateau superélastique caractéristique du NiTi a été dépassé, sans que les contraintes n’atteignent cependant la limite d’élasticité de l’alliage. Pour les stents en acier inoxidable 316L de la Ze-SG, les contraintes relevées sont bien inférieures à la limite d’élasticité du matériau et la plasticité n’est donc jamais atteinte pendant la simulation”.

5.4.5 Stent-graft deployment simulation including ILT

Eventually, a model including the ILT and also a prescribed thickness of 1 mm for the iliac arteries (while maintaining a thickness of 1.5 mm for the AAA above the iliac bifurcation) could be completed successfully. The tetrahedral elements modeling the ILT were attributed an average size of 3 mm and the "Maximum Growth" option for the inner elements, which helped reducing the resolution period.

Despite a global satisfying result (Figure 5.18), the same issues were observed as when excluding the ILT (Figure 5.17). Some areas of the AAA wall remained folded after the equilibrium step, some stents appeared highly distorted and penetration between the grafts and stents persisted.

Finally, this model completed in about two weeks on 10 CPUs (2.60 GHz).

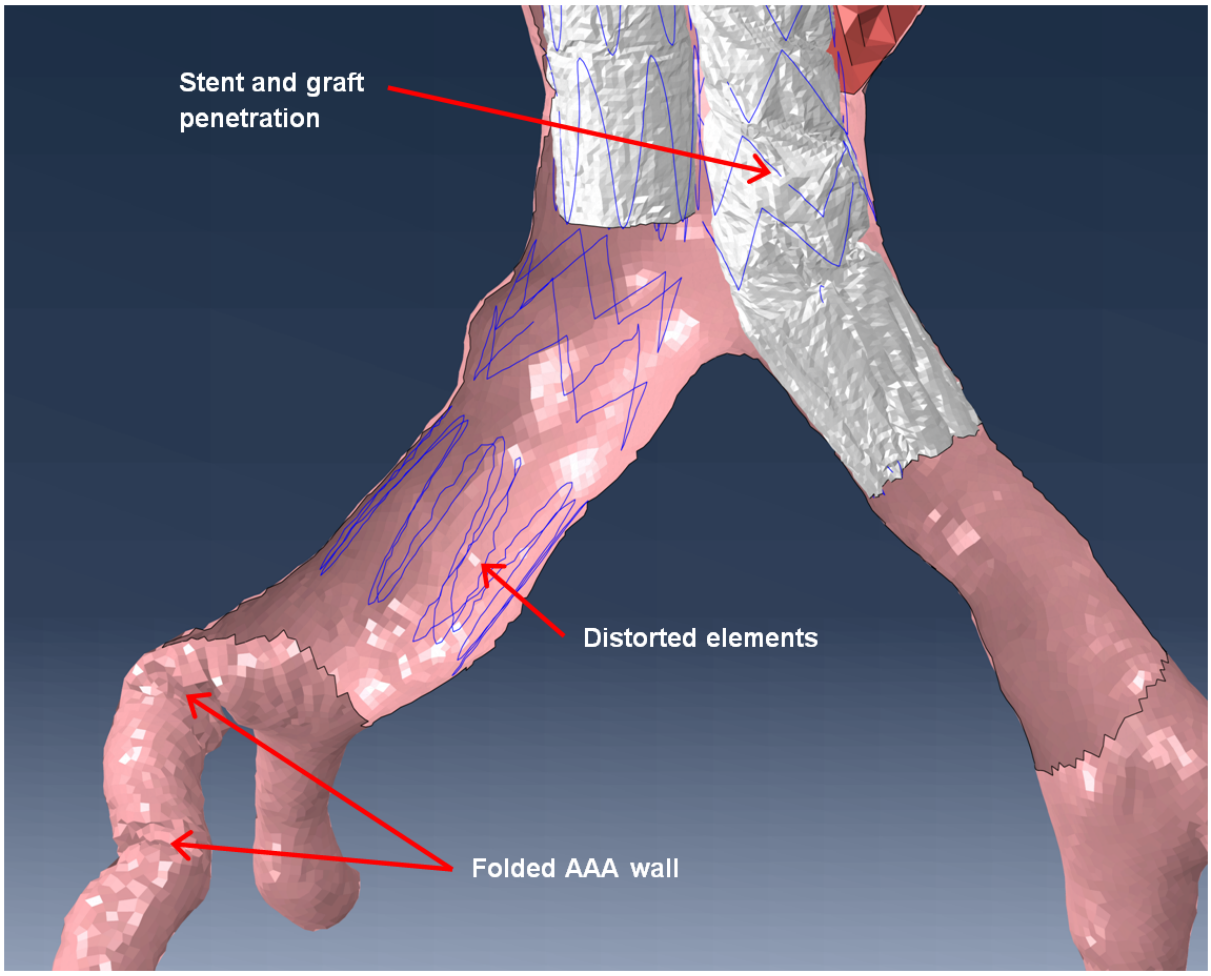

Figure 5.17: Defaults of stent-graft deployment simulation including the ILT.

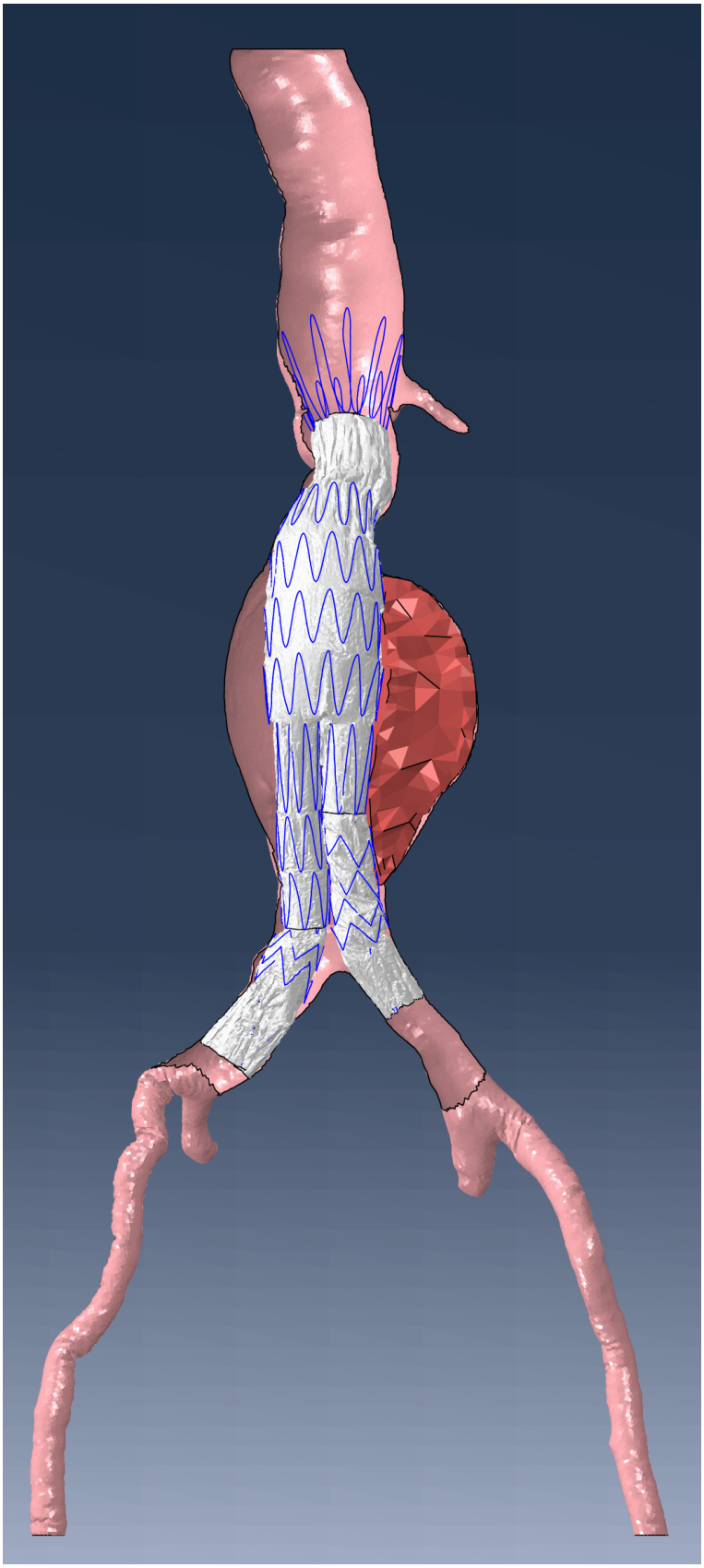

Figure 5.18: Stent-graft deployment simulation including the ILT.

5.4.6 Phantom design

The numerical simulation of SG deployment itself requires a substantial effort. However, a vascular phantom was also designed for further experimental validations (Figure 5.19). Also, the supporting box of this phantom was realized, and tested with a simple (idealized) AAA geometry made of polyurethane (Huntsman, The Woodlands, Texas, USA). Another 3D printed simple geometry was tested, and made of a commercial material named "TangoBlackPlus shore A40" (Proto3000, Woodbridge, Ontario, Canada). The true strains & stresses of the tested polyurethane and TangoBlackPlus material are given in Appendices G and H respectively.

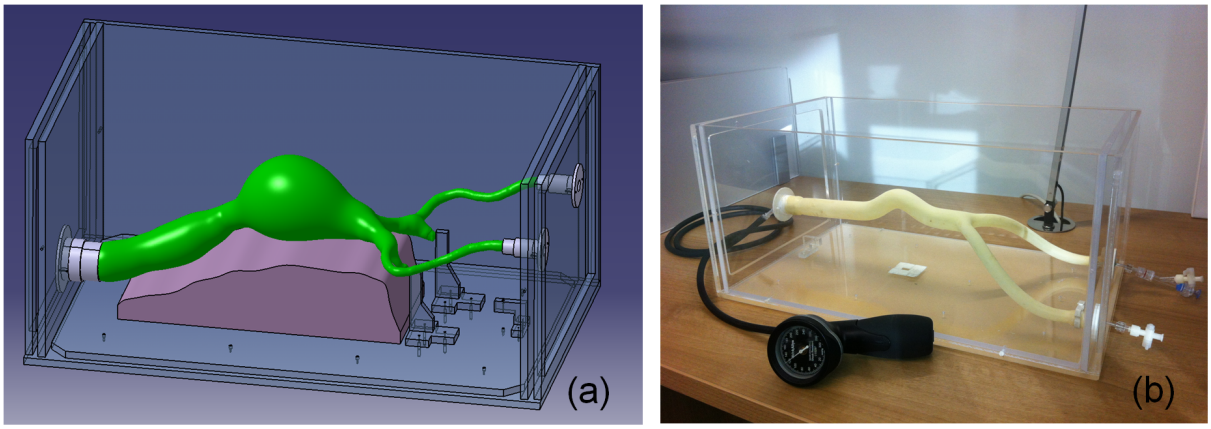

Figure 5.19: Vascular phantom. (a) Virtual model. (b) First (pressurized) prototype made of polyurethane.

5.4.7 Plug-in application EVARSim

The final goal of any biomedical development is to actually improve the way clinicians diagnose pathologies, and apply appropriate treatments. With this objective in mind, a simplified and unified graphic interface was designed.

The plug-in was named *EVARSim*, and the corresponding icon contains the Greek letters ϵ and σ that have the same initial as EVAR and simulation respectively. In addition, since ϵ and σ represent the strains and stresses respectively in solid mechanics, this reminds that the simulation is physically based. The procedure to install EVARSim is exposed in Appendix F.

EVARSim is twofold; it opens an application that is a simplified version of the classic Abaqus GUI (Abaqus CAE), in which only the relevant features/menus were conserved, and it adds the actual plug-in within the list of plug-ins already available in Abaqus (Figure 5.20).

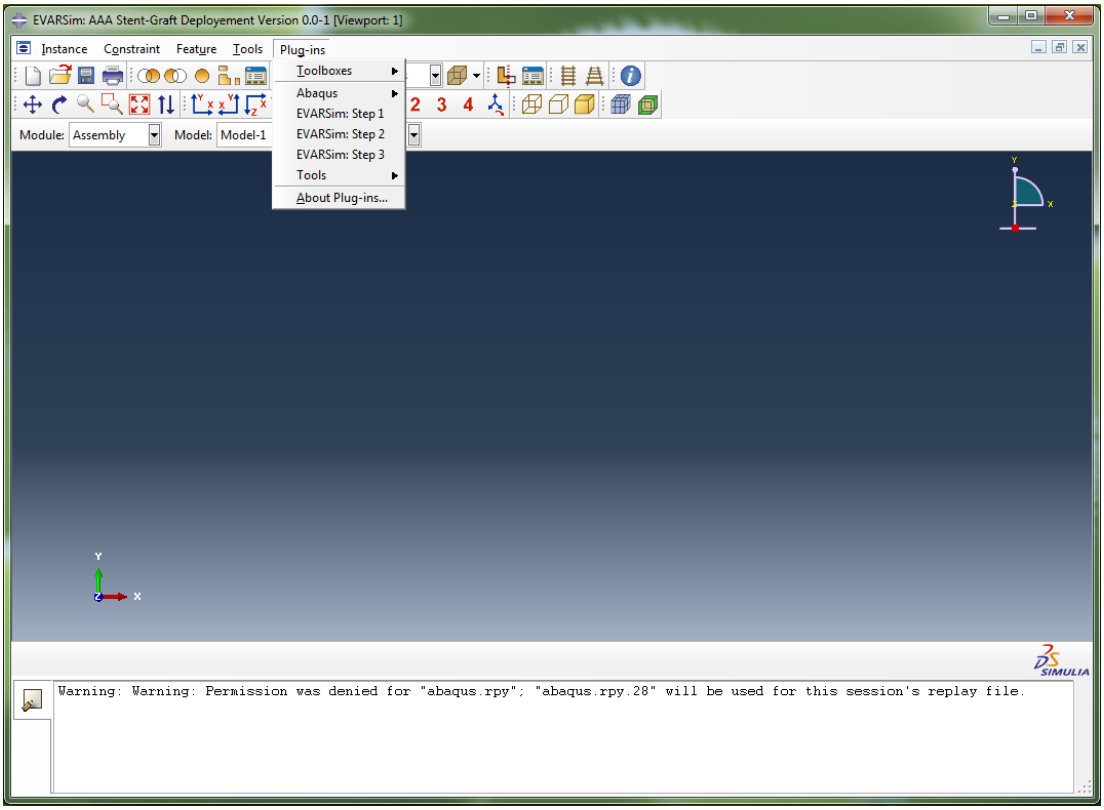

Figure 5.20: EVARSim application. The corresponding plug-in is expanded on top of the picture, with 3 steps.

As can be seen in Figure 5.20 there are three steps. The first one allows selecting the input files after the initial segmentation from CT-scans, and executes the workflow described in the above flowchart until the first manual update of the centerlines. The corresponding interface (pressing on *EVARSim: Step 1*) is depicted in Figure 5.21.

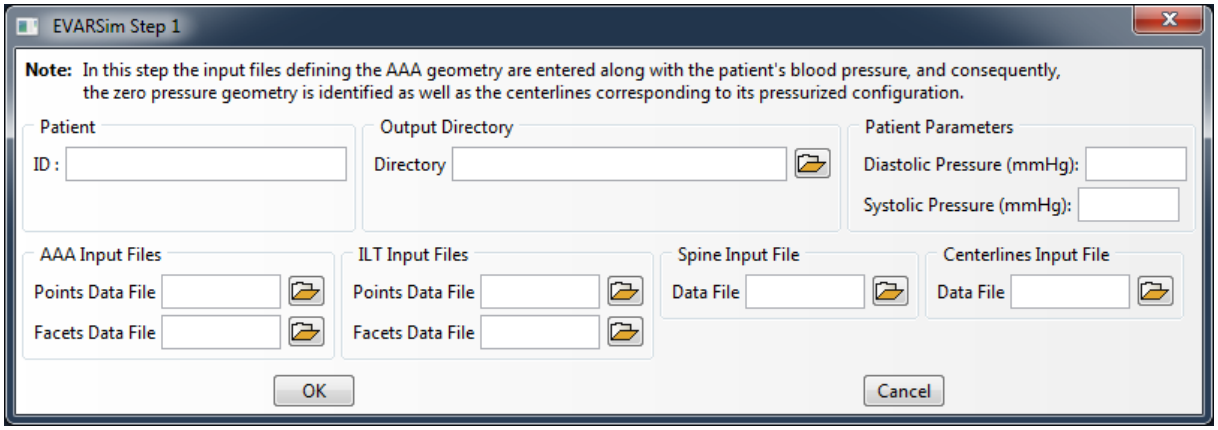

Figure 5.21: EVARSim step 1. Interface to select the input files defining the AAA geometry, and analyze the first part of the workflow.

The second step is concerned with the specific analysis intended to provide the configuration of the pressurized ZPG pre-deformed by both catheters. Thus, after the first centerlines update, one just has to click *OK* on this interface to execute this analysis (Figure 5.22).

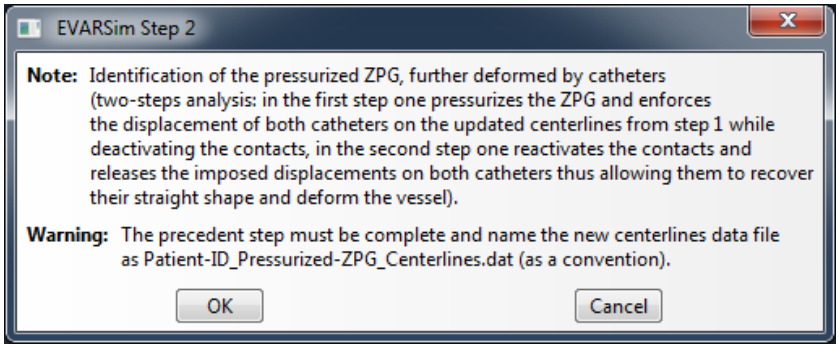

Figure 5.22: EVARSim step 2. Interface to determine the pre-deformed geometry of the AAA.

Finally, the step 3 executes the workflow starting after the second manual update of centerlines, and until the final equilibrium (Figure 5.23).

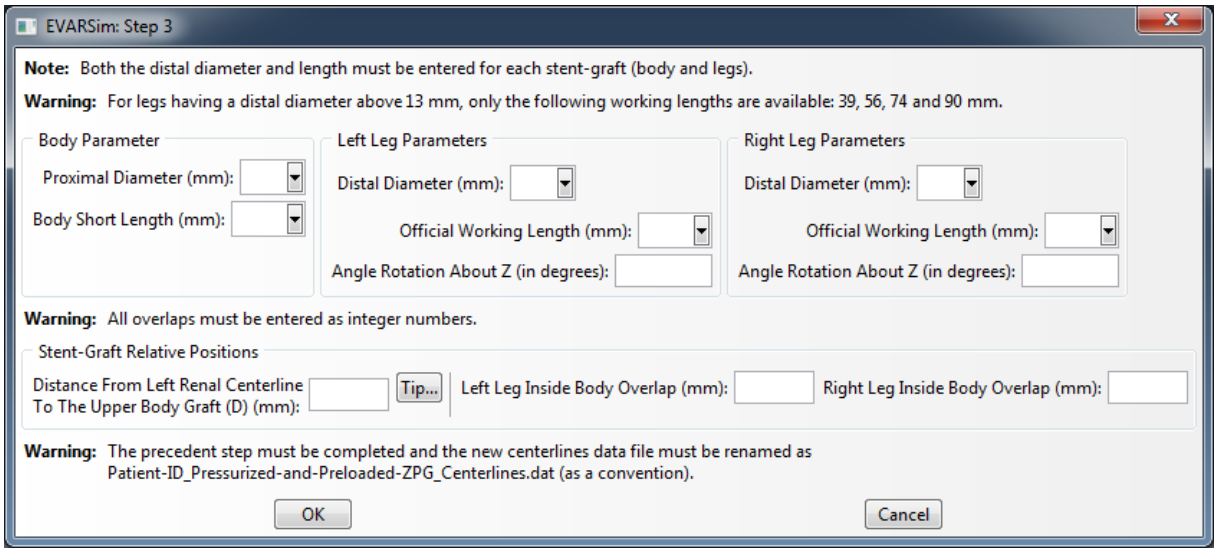

Figure 5.23: EVARSim step 3. Interface to complete the workflow after the second manual update of centerlines.

In Figure 5.23 the tip related to the definition of the distance from the left renal centerline to the upper body graft displays the picture from Figure 5.9.

5.4.8 EVARSim pre-validation

Many trials and probably debugging activities will be needed to bring EVARSim to a mature state. However, it proved to execute properly its tasks up to step 2, and at least generate and start executing the input file related to step 3 without apparent errors.

Here a pre-validation is provided for the resulting model and input file related to step 3, only in terms of initial positioning of each instance in the assembly (AAA, SG, catheters and sheaths). A series of different combinations of SG and overlaps of legs into the body were tested, and the automatic "data check" performed by Abaqus was successful in each case. The outcome of these results is presented in Table XXIII.

Table XXIII: Successful pre-validation of EVARSim for the input file of step 3, in terms of initial position (AAA, SG, catheters and sheaths) and "data check" performed by Abaqus. Diameters, lengths and angles of rotation are expressed in mm and degrees respectively.

Body		Left leg			Right leg			Left overlap	Right overlap
Ø	Length	Ø	Length	Angle	Ø	Length	Angle		
32	140	9	39	90	16	90	45	12	7
32	140	11	122	30	13	74	72	18	8
32	125	11	74	30	13	122	72	18	8
26	140	20	39	5	11	122	25	18	8
22	96	24	39	45	16	39	90	21	2
22	140	16	90	28	11	56	25	10	1
30	82	9	122	20	11	107	-70	10	5
22	82	11	107	-20	9	122	-70	10	5
22	82	24	39	-20	20	90	-70	10	5
24	96	13	90	25	24	56	90	25	12
30	96	13	107	45	20	39	90	25	12
24	125	13	56	45	11	122	90	25	12
24	96	16	56	45	9	90	90	36	25
28	111	20	56	58	9	74	36	20	8
28	96	24	74	138	24	56	8	14	16
22	111	16	90	110	16	74	30	11	17
26	82	13	90	70	13	56	40	2	18
26	111	9	56	25	24	39	30	7	3
30	125	16	39	20	20	90	28	14	16

5.5 Discussion

As mentioned above, the beam elements from stents tended to penetrate the shell elements from grafts, in particular for the legs. Even though several contact options were selected and a fine mesh size of 0.7 mm was prescribed to the stents, this penetration remained, probably due to the complex loading history happening during the workflow.

Broadly, the final equilibrium could be achieved, however, some parts of the AAA remained partially folded. This could not be improved by either increasing the time period, or decreasing the mass scaling factor.

Also, some distorted beam elements from the stents were observed at the final equilibrium. A model with plastification attributed to the 316L stainless steel was tested (Rasmussen, 2001), but obviously led to permanent deformations after sheath removal, thus precluding any further deployment. The origin of this issue did not appear clearly (too high mass scaling factor, contacts wrongly defined, etc.).

Finally, a more advanced model including the ILT, anisotropic hyperelastic HGO model and different thicknesses for the AAA bulge and iliac arteries(1.5 mm and 1.0 mm respectively), was built. Unfortunately, it could not be executed completely because of excessive distortion in the shell elements representing the AAA wall. Moreover, the separation between the two sections of different thickness (above the aortic bifurcation) was found quite complex to be determined automatically. However, the isotropic version of this model including the ILT could finally be completed successfully, even if some defaults still persisted.

5.6 Conclusion

A first complete simulation of SG deployment could be analyzed successfully with a AAA wall issued from the segmentation of a patient-specific lumen, and modeled with an isotropic hyperelastic model (Raghavan and Vorp, 2000). Despite no realistic modeling was attributed to the surrounding organs (only the spine and internal iliac arteries were simulated), an overall satisfying deployment and equilibrium state could be reached.

Conclusion and future work

General conclusion

The simulation of vascular prostheses, and particularly SG deployment, is quite demanding. One needs to simulate the AAA and parts of the abdominal architecture, in addition to the complete delivery device, i.e. SG and catheters. Also, one needs to cope with a combination of the three types of non-linearities; material non-linearity (hyperelastic modeling of the AAA wall), contacts and large displacements. In this thesis, the actual EVAR procedure could not be strictly reproduced, mainly because in reality interventionists have to push the DD (guidewire and catheter later on) back and forth until reaching the landing zone. This would have resulted in extremely complex and unstable numerical simulations, probably failing most of the time, even with an advanced modeling of the surrounding organs and tissues.

The strategy adopted here, was a compromise between numerical feasibility and a faithful consideration of the right compliance of the involved soft tissues and DD. Actually, the level of abstraction offered by the actual FEA packages, here Abaqus, made possible to translate a pre-assembled prosthesis (body and legs) from a side of the AAA directly through the vessel wall, by playing with the activation/deactivation of contacts. Even though this approach looks simple, there are indeed many technical details and pitfalls to solve before any mature workflow can be developed.

The multi-step analysis to complete such workflow implicates many trials before the set of right parameters can be identified. For instance, contacts are based on the concept of master and slave, and the former must ideally have a coarser mesh size to avoid unrealistic penetrations. This aspect alone introduces many constraints on the finite element meshes, and therefore, the hierarchy of element size must be carefully selected for the beam, shell and solid elements coming into play. Not to mention the constraints imposed by the ratio of section or thickness to global size for beam and shell elements respectively. Also, provided an explicit solver must be used for an efficient treatment of contacts, a particular

attention must be paid to the definition of mass scaling factor and time periods, that in turn determine the stable time increment of the analysis.

Moreover, two manual updates of the centerlines must be performed during the workflow to better reproduce the physiological conditions (preloaded AAA, and ZPG).

For these reasons, it was not possible to further validate the model with vascular phantoms of increasing complexity as primarily (and ambitiously) scheduled. The attention was instead focused on first developing a demonstrator, and bring a proof of concept. However, these results gave rise to an accepted funding from the Natural Science and Engineering Research Council of Canada (NSERC), which will fill the need for maturity and validation (experimental and clinical) of the workflow. This grant (CRDPJ 460903-13) will be supported by Siemens and CAE Healthcare, as industrial partners.

The contribution first resides in the experimental validation of the numerical model of SG. As detailed in chapter 2, a maximum difference of 5.93% (in displacement) was found among load cases intended to reproduce physiological deformations (bending, axial, transversal and radial compressions). The graft and its folding behavior was probably the most challenging part of this work. Also, the pre-tension of stents was modeled by a controlled increase of the Young's modulus, and in an average sense, Young's moduli must be increased by a factor 2. The main bodies and legs SG from the catalogue of Cook Medical were encoded into a Python script.

In chapter 3, the steps to reconstruct any AAA observed in a CT-scan into a native Abaqus model were fully explained. In chapter 4, the anisotropic hyperelastic HGO model attributed to the AAA wall was validated against published results. A maximum difference of 4.41% (in maximal principal stresses) was found for a similar simulation. Also, a more accurate and robust method was devised to orientate the collagen fibers, even for tortuous iliac arteries.

Chapter 5 was devoted to the simulation of SG deployment, and the demonstrator (case H1025269 from CR-CHUM database)was presented. Therefore, a full prosthesis was deployed in a patient-specific pre-deformed vessel, which was made possible by an innovative use of connectors. The connector feature defined in Abaqus provides an efficient way to prescribe complex kinematic boundary conditions. This somehow fulfills the initial statement that: "The main objective and expected contribution/novelty lies in presenting an original, accurate and robust prediction of SG implantation in AAA ...". At least in the *innovative* sense. The accuracy of the developed model will be further tested with vascular phantoms, and its robustness by considering other tortuous patient-specific geometries.

Eventually, a prototype of a plug-in application (EVARSim) was developed with the

purpose to make the workflow more automatic, and provide the basis for a potential clinical application, and possibly a training simulator for students.

In essence, the main hypothesis was that this type of simulation was possible by first establishing the pre-deformed configuration of the AAA, prior to proceed with the actual deployment. This concept is twofold: it avoids too much distortion in the shell elements constituting the grafts, and allows deploying in a pre-deformed vessel, which is closer to the clinical reality.

In chapter 5, it was finally possible to assess the total time required for this workflow to complete; approximately a week. One month usually elapses between the decision is taken for a patient to undergo an EVAR, and the intervention itself. So, provided enough machine power is available, there is plenty of time to complete several scenarios in parallel, and provide the clinicians with a valuable collection of possible outcomes, depending on SG model and selected landing zone.

In terms of publication/dissemination, a thorough literature review and vulgarization was initially published (Roy et al., 2012).

The parameters for the HGO anisotropic hyperelastic model (biomechanical simulation of AAA wall), along with the innovative strategy to improve the initial orientation of collagen fibers, were published with Professor G. A. Holzapfel (Roy et al., 2014). These results were also presented at the 4^{th} *Canadian Conference on Non-Linear Solid Mechanics* held by McGill University (Montréal, Canada) in July 2013.

The SG deployment model was first presented at the 7^{th} *World Congress of Biomechanics* in Boston (MA, USA) in July 2014, and also at the *Regional User Meeting* organized by Dassault Systèmes (distributor of Abaqus) in Chicago (IL, USA) in September 2014.

Finally, at the time of completing this thesis (December 2014), two manuscripts were close to be submitted. One regarding the experimental validation of SG simulations, and another about the proof of concept of SG deployment simulation accounting for the pre-deformed configuration of the vessel wall.

Future work

Anatomical and physiological boundary conditions

The ILT was first discarded for the sake of simplicity and because its presence makes significantly longer the required time to solve the complete model. This aspect might be improved by using a linear elastic material property, rather than an isotropic hyperelastic

one. Actually Di Martino et al. (2001) used a Young's modulus of 0.11 MPa and a Poisson's ratio of 0.45. However, such a model failed at sheath removal. The ILT should be taken into account since it is present in most of the AAA.

Similarly, calcifications were not modeled because their actual locus is randomly distributed and affected by a significant blurring effect once visualized with medical imaging modalities. Nonetheless, their mechanical effect is of paramount importance, and an effort is still needed to include them into any advanced model. Mechanical properties of calcifications have already been assessed (see in section 3.1).

The surrounding organs deserve a more accurate representation. They should ideally be simulated by means of solid elements and a viscoelastic constitutive law. One could also consider the Young's modulus of abdominal fat to start with. But doing so would require a powerful computing capability, which is now possible via supercomputers.

An additional improvement would consist in introducing anisotropic hyperelastic constitutive laws for the AAA wall in the model for SG deployment simulation.

Improved material properties for stents

Spiral-Z stents are made of nitinol, and their complex mechanical behavior was reduced to a linear elastic one to make sure the SG deployment would not be affected by permanent deformations. This assumption was motivated by the fact that most of the stents recover their initial shape after large and repeated deformations. However, for further investigations, about fatigue for instance, a most accurate material modeling would be required, probably by developing material and element user subroutines. And, once again, the beam element formulation presently implemented in Abaqus does not support hyperelastic constitutive laws. Therefore, solid elements must be used in conjunction with hyperelastic material properties, thus implicating significantly longer analyses, unless additional computing power is granted.

More accurate ZPG

Evaluating the ZPG still remains a complex "inverse problem" to solve, especially when using a commercial finite element analysis package, which prevents any direct access to the deformation tensor. A simple forward and backward analysis was performed, inspired by the "fixed point" (Bols et al., 2013), but more iterations tended to degrade the solution.

In order to bypass this issue, an original strategy based on thermal correction could be implemented. Indeed, if a single cylinder is pressurized, it is possible to make it recover its

original shape (while still pressurized) by applying a controlled thermal retraction. The same should be possible for a complex geometry such as a AAA, by attributing orthotropic expansion coefficients in the local coordinate system of each element. These coefficients being derived from a previous forward pressurization, in such a way that a uniform and fixed difference of temperature times the coefficients would equate the observed strains (in two in-plane orthogonal local directions). Insofar as the used FEA package provides this feature, it would be worth trying this approach. Then, there would be no need to search for an hypothetical ZPG, since the initial pressurized AAA geometry would be "artificially shrinked" back to a close configuration of its natural (pressurized) state observed in a CT-scan.

Error between simulation and phantoms

A maximum acceptable clinical error of 5% was established based on the oversizing of the diameter of the involved SG from 1 to 15%, and also on a maximum deviation of 6 mm to 7 mm over a typical (B-SG) length of 120 mm to 140 mm.

With such large displacements and non-linearities involved in SG deployment, a consistent validation of the numerical model can only take place via detailed vascular phantoms. This is the purpose of the NSERC collaborative grant above mentioned, over a period of 2 years. In particular, it is scheduled to validate the SG deployment model with a first rigid vascular phantom having a simple (virtual) geometry. Then, other validations will take place with soft phantoms having simple and patient-specific geometries, thus increasing progressively the complexity. Eventually, some clinical validations will be performed (three cases as a minimum).

EVARSim further validation

EVARSim is a first version and further validations are still needed, both with vascular phantoms and eventually via clinical validations. These effort and goal will be made possible by the NSERC grant above quoted. Hopefully, the created momentum will lead to a clinical application.

Bibliography

Amblard, A. (2006). *Contribution à l'étude du comportement d'une endoprothèse aortique abdominale. Analyse des endofuites de type I.* PhD thesis, Institut National des Sciences Appliquées de Lyon.

Amblard, A., Berre, H. W. L., Bou-Saïd, B., and Brunet, M. (2009). Analysis of type I endoleaks in a stented abdominal aortic aneurysm. *Med Eng Phys*, 31(1):27–33.

ASM (2009). *Materials and coatings for medical devices.* Library of Congress Control Number: 2009935433.

Basciano, C. A. and Kleinstreuer, C. (2009). Invariant-based anisotropic constitutive models of the healthy and aneurysmal abdominal aortic wall. *J Biomech Eng*, 131(2).

Bock, S. D. (2014). *A biomechanical analysis of stent graft for the treatment of abdominal aortic aneurysms.* ISBN 978-90-8578-699-3. Gent University.

Bols, J., Degroote, J., Trachet, B., Verhegghe, B., Segers, P., and Vierendeels, J. (2013). A computational method to assess the in vivo stresses and unloaded configuration of patient-specific blood vessels. *Journal of Computational and Applied Mathematics*, 246:10–7.

Brown, J. D., Rosen, J., Kim, Y. S., Chang, L., and Sinanan, M. N. (2003). In-vivo and in-situ compressive properties of porcine abdominal soft tissues. In *Studies in Health Technologies and Informatics - Medicine Meets Virtual Reality*, volume 94, pages 26–32, Newport Beach.

Capelli, C., M., T. A., Migliavacca, F., Bonhoeffer, P., and S., S. (2010). Patient-specific reconstructed anatomies and computer simulations are fundmental for selecting medical device treatment: application to a new percutaneous pulmonary valve. *The Royal Society A*, 368(1921):3027–38.

De Bock, S., Iannaccone, F., De Santis, G., De Beule, M., Van Loo, D., Devos, D., Vermassen, F., Segers, P., and Verhegghe, B. (2012). Virtual evaluation of stent-graft deployment: a validated modeling and simulation study. *J Mech Behav Biomed Mater*, 13:129–39.

De Putter, S., Wolters, B. J., Rutten, M. C., Breeuwer, M., Gerritsen, F. A., and Van De Vosse, F. N. (2007). Patient-specific initial wall stress in abdominal aortic aneuryms with a backward incremental method. *J Biomech*, 40(5):1081–90.

Demanget, N. (2012). *Analyses des performances mécaniques des endoprothèses aortiques par simulation numérique: application au traitement des anévrismes tortueux*. PhD thesis, École Nationale Supérieure des Mines de Saint-Etienne, France.

Demanget, N., Avril, S., Badel, P., Orgéas, L., Geindreau, C., Albertini, J. N., and Favre, J. P. (2012a). Computational comparison of the bending behavior of aortic stent-grafts. *J Mech Behav Biomed Mater*, 5(1):272–82.

Demanget, N., Badel, P., Avril, S., Orgéas, L., Geindreau, C., and Albertini, J. N. (2013). Simulation du déploiement d'endoprothèses dans des anévrismes iliaques tortueux. In *11e Colloque National en Calcul des Structures*, pages 1–7, France.

Demanget, N., Latil, P., Orgéas, L., Badel, P., Avril, S., Geindreau, C., Albertini, J. N., and Favre, J. P. (2012b). Severe bending of two aortic stent-grafts: an experimental and numerical mechanical analysis. *Ann Biomed Eng*, 40(12):2674–86.

Di Martino, E., Guadagni, G., Fumero, A., Ballerini, G., Spirito, R., Biglioli, P., and Redaelli, A. (2001). Fluid-structure interaction within realistic three-dimensional models of the aneurysmatic aorta as a guidance to access the risk of rupture of the aneurysm. *Medical Engineering and Physics*, 23(9):647–655.

Elger, D. F., Blackketter, D. M., Budwig, R. S., and Johansen, K. H. (1996). The influence of shape on the stresses in model abdominal aortic aneurysms. *J Biomech Eng*, 118(3):326–32.

Ferruzzi, J., Vorp, D. A., and Humphrey, J. D. (2011). On constitutive descriptors of the biaxial mechanical behavior of human abdominal aorta and aneurysms. *Journal of The Royal Society Interface*, 8(56):435–50.

Fung, Y. C. (1993). *Biomechanics, mechanical properties of living tissues*. Springer.

Galliot, C. and Luchsinger, R. H. (2010). The shear ramp: A new test method for the investigation of coated fabric shear behaviour. *J Composites*, 41(12):1743–49.

Gasser, T. C., Görgülü, G., Folkesson, M., and Swedenborg, J. (2008). Failure properties of intraluminal thrombus in abdominal aortic aneurysm under static and pulsating mechanical loads. *J Vasc Surg*, 48(1):179–88.

Gasser, T. C., Ogden, R. W., and Holzapfel, G. A. (2006). Hyperelastic modelling of arterial layers with distributed collagen fibre orientations. *Journal of The Royal Society Interface*, 3(6):15–35.

Gee, M. W., Förster, C., and Wall, W. A. (2010). A computational strategy for prestressing patient-specific biomechanical problems under finite deformation. *International Jounal for Numerical Methods in Engineering*, 26(1):52–72.

Gent, A. N. (2000). *Engineering with Rubber*. Hanser Gardner Publications, Cincinnati, 2 edition.

Govindjee, S. and Mihalic, P. A. (1998). Computational methods for inverse deformations in quasi-incompressible finite elasticity. *International Jounal for Numerical Methods in Engineering*, 43(5):821–38.

Greenhalgh, R. M. and Powell, J. T. (2008). Endovascular repair of abdominal aortic aneuysms. *N Engl J Med*, 358(5):452–501.

Greenwald, S., Rachev, A., Moore, J. E., and Meister, J. J. (1994). The contribution of the structural components of the arterial wall to residual strains. *ASME Advances in Bioengineering*, 28:63–64.

Harewood, F., Grogan, J., and McHugh, P. (2010). A multiscale approach to failure assessment in deployment for cardiovascular stents. *J Multiscale Modelling*, 02(1):1–22.

Harter, L. P., Gross, B. H., Callen, P. W., and Barth, R. A. (1982). Ultrasonic evaluation of abdominal aortic thrombus. *J Ultrasound Med*, 1(8):315–8.

He, C. M. and Roach, M. R. (1994). The composition and mechanical properties of abdominal aortic aneurysms. *J Vasc Surg*, 20(1):6–13.

Hinnen, J. W., Koning, O. H. J., Visser, M. J. T., and Van Bockel, H. J. (2005). Effect of intraluminal thrombus on pressure transmission in the abdominal aortic aneurym. *J Vasc Surg*, 42(6):1176–82.

Holzapfel, G. A., Gasser, T. C., and Ogden, R. W. (2000). A new constitutive framework for arterial wall mechanics and a comparative study of material models. *Journal of Elasticity*, 61(1-3):1–48.

Holzapfel, G. A. and Ogden, R. W., editors (2003). *Biomechanics of soft tissues in cardiovascular systems*, chapter Structural and numerical models for the (visco)elastic response of arterial walls with residual stresses, pages 109–184. Springer, New York.

Holzapfel, G. A., Sommer, G., Auer, M., Regitnig, P., and Ogden, R. W. (2007). Layer-specific 3d residual deformations of human aortas with non-atherosclerotic intimal thickening. *Ann Biomed Eng*, 35(4):530–45.

Humphrey, J. D. and Holzapfel, G. A. (2012). Mechanics, mechanobiology, and modeling of human abdominal aorta and aneurysms. *J Biomech*, 45(5):805–14.

Johnston, C. R., Lee, K., Flewitt, J., Moore, R., Dobson, G. M., and Thornton, G. M. (2010). The mechanical properties of endovascular stents: an in vitro assessment. *Cardiovasc Eng.*, 10(3).

Kaladji, A., Duménil, A., Castro, M., Cardon, A., Becquemin, J. P., Bou-Saïd, B., Lucas, A., and Haigron, P. (2013). Prediction of deformations during endovascular aortic aneurysm repair using finite element simulation. *Computerized Medical Imaging and Graphics*, 37(2):142–9.

Kim, J., Kang, Y. H., Choi, H. H., Hwang, S. M., and Kang, B. S. (2002). Comparison of implicit and explicit finite-element methods for the hydroforming process of an automobile lower arm. *Int J Adv Manuf Technol*, 20(6):407–13.

Kleinstreuer, C., Li, Z., Basciano, C. A., Seelecke, S., and A., F. M. (2008). Computational mechanics of nitinol stent grafts. *J Biomech*, 41(11):2370–78.

Li, Z. and Kleinstreuer, C. (2005a). Blood flow and structure interactions in a stented abdominal aortic aneurysm model. *Med Eng Phys*, 27(5):369–82.

Li, Z. and Kleinstreuer, C. (2005b). Fluid-structure interaction effects on sac-blood pressure and wall stress in a stented aneurysm. *J Biomech Eng*, 127(4):662–71.

Li, Z. Y., U-King-Im, J., Tang, T. Y., Soh, E., See, T. C., and Gillard, J. H. (2008). Impact of calcification and intraluminal thrombus on the computed wall stresses of abdominal aortic aneurysm. *J Vasc Surg*, 47(5):928–35.

Maaß, H. and Kühnaptel, U. (1999). Noninvasive measurement of elastic properties of living tissues. In *Computer Assisted Radiology and Surgery*, pages 865–870, Paris, France.

Maier, A., Gee, M. W., Reeps, C., Eckstein, H. H., and Wall, W. A. (2010). Impact of calcifications on patient-specific wall stress analysis of abdominal aortic aneurysms. *Biomech Model Mechanobiol*, 9(5):511–21.

Marra, S. P., Daghlian, C. P., Fillinger, M. F., and Kennedy, F. E. (2006). Elemental composition, morphology and mechanical properties of calcified deposits obtained from adbominal aortic aneurysms. *Acta Biomaterialia*, 2(5):515–20.

Moireau, P., Xiao, N., Astorino, M., Figueroa, C. A., Chapelle, D., Taylor, C. A., and Gerbeau, J. F. (2012). External tissue support and fluid-structure simulation in blood flows. *Biomech Model Mechanobiol*, 11(1-2):1–18.

Mortier, P., Holzapfel, G. A., De Beule, M., Van Loo, D., Taeymans, Y., Segers, P., Verdonck, P., and Verhegghe, B. (2010). A novel simulation strategy for stent insertion and deployment in curved coronary bifurcations: comparison of three drug-eluting stents. *Ann Biomed Eng*, 38(1):88–99.

Ní Annaidh, A., Destrade, M., Gilchrist, M. D., and Murphy, J. G. (2013). Deficiencies in numerical models of anisotropic nonlinearly elastic materials. *Biomech Model Mechanobiol*, 12(4):781–791.

Prasad, A., Xiao, N., Gong, X. Y., Zarins, C. K., and Figueroa, C. A. (2013). A computational framework for investigating the positional stability of aortic endografts. *Biomech Model Mechanobiol*, 12(5):869–887.

Quaglini, V., Pena, P., and Contro, R. (2004). A discrete-time approach to the formulation of constitutive models for viscoelastic soft tissues. *Biomech Model Mechanobiol*, 3(2):85–97.

Raghavan, M. L., Baoshun, M. A., and Fillinger, M. F. (2006). Non-invasive determination of zero-pressure geometry of arterial aneurysms. *Annals of Biomedical Engineering*, 34(9):1414–19.

Raghavan, M. L. and Vorp, D. A. (2000). Toward a biomechanical tool to evaluate rupture potential of abdominal aortic aneurysm: identification of a finite strain constitutive model and evaluation of its applicability. *J Biomech*, 33(4):475–82.

Raghavan, M. L., Vorp, D. A., Federle, M. P., Makaroun, M. S., and Webster, M. W. (2000). Wall stress distribution on three-dimentionally reconstructed models of human abdominal aortic aneurysm. *J Vasc Surg*, 31(4):760–9.

Raghavan, M. L., Webster, M. W., and Vorp, D. A. (1996). Ex vivo biomechanical behavior of abdominal aortic aneurysm: assessment using a new mathematical model. *Ann Biomed Eng*, 24(5):573–82.

Rasmussen, K. (2001). Full-range stress-strain curves for stainless steel alloys. Research report R811, The University of Sydney, Sydney, NSW, 2006, Australia.

Rodríguez, J. F., Ruiz, C., Doblaré, M., and Holzapfel, G. A. (2008). Mechanical stresses in abdominal aortic aneurysms: influence of diameter, asymmetry, and material anisotropy. *J Biomech Eng*, 130(2).

Rosen, J., Brown, J. D., De, S., Sinanan, M. N., and Hannaford, B. (2008). Biomechanical properties of abdominal organs in vivo ans postmorten under compression loads. *J Biomech Eng*, 130(2):021020.

Roy, D., Holzapfel, G. A., Kauffmann, C., and Soulez, G. (2014). Finite element analysis of abdominal aortic aneuryms: geometrical and structural reconstruction with application of an anisotropic material model. *Journal of Applied Mathematics*, 79(5):1011–1026.

Roy, D., Kauffmann, C., Delorme, S., Lerouge, S., Cloutier, G., and Soulez, G. (2012). A literature review of the numerical analysis of abdominal aortic aneurysms treated with endovascular stent grafts. *Computational and mathematical methods in medicine*, 2012:1–16.

Sakalihasan, N., Limet, R., and Defawe, O. D. (2005). Abdominal aortic aneurysm. *Lancet*, 365(9470):1577–89.

Sampaio, S. M., Panneton, J. M., Mozes, G., Andrews, J. C., Noel, A. A., Kalra, M., Bower, T. C., Cherry, K. J., Sullivan, T. M., and Gloviczki, P. (2006). Aortic neck dilation after endovascular abdominal aortic aneurysm repair: Should oversizing be blamed? *Ann Vasc Surg*, 20(3):338–45.

Schulze-Bauer, C. A., Mörth, C., and Holzapfel, G. A. (2003). Passive biaxial mechanical response of aged human iliac arteries. *J Biomech Eng*, 125(3):395–406.

Schurink, G. W. H., Baalen, J. M., Visser, M. J. T., and Van Bockel, J. H. (2000). Thrombus within an aortic aneurysm does not reduce pressure on the aneurysmal wall. *J Vasc Surg*, 31(3):501–6.

Scotti, C. M. and Finol, E. A. (2007). Compliant biomechanics of abdominal aortic aneurysms: A fluid-structure interaction study. *Computers and Structures*, 85(11-14):1097–1113.

Scotti, C. M., Jimenez, J., Muluk, S. C., and Finol, E. A. (2008). Wall stress and flow dynamics in abdominal aortic aneuryms: finite element analysis vs. fluid-structure interaction. *Computer Methods in Biomechanics and Biomedical Engineering*, 11(3):301–322.

Speelman, L. (2009). *Biomechanical analysis for abdominal aortic aneurysm risk stratification*. PhD thesis, Maastricht University, Netherlands.

Thubrikar, M. J., Labrosse, M., Robicsek, F., Al-Soudi, J., and Fowler, B. (2001). Mechanical properties of abdominal aortic aneurysm wall. *Journal of Medical Engineering and Technology*, 25:133–42.

Toungara, M. (2011). *Contribution à la prédiction de la rupture des anévrismes de l'aorte abdominale (AAA)*. PhD thesis, École Doctorale Ingénierie - Matériaux Mécanique Energétique Environnement Procédés Production, Université de Grenoble, France.

Vad, S., Eskinazi, A., Corbett, T., McGloughlin, T., and Vande Geest, J. P. (2010). Determination of coefficient of friction of self-expanding stent-grafts. *J Biomed Eng*, 132(12):121007.

Van Dam, E. A., Dams, S. D., Peters, G. M. W., Rutten, M. C. M., Schurink, G. W. H., Buth, J., and Van De Vosse, F. N. (2008). Non-linear viscoelastic behavior of abdominal aortic aneurysm thrombus. *Biomech Model Mechanobiol*, 7(2):127–37.

Van Oijen, C. (2003). *Mechanics and design of fiber-reinforced vascular prostheses*. Technische Universiteit Eindhoven.

Vande Geest, J. P., Sacks, M. S., and Vorp, D. A. (2006). The effects of aneurysm on the biaxial mechanical behavior of human adbominal aorta. *J Biomech*, 39(7):1324–34.

Vande Geest, J. P., Schmidt, D. E., Sacks, M. S., and Vorp, D. A. (2008). The effects of anisotropy on the stress analyses of patient-specific abdominal aortic aneurysms. *Ann Biomed Eng*, 36(6):921–32.

Wang, D. H. J., Makaroun, M., Webster, M. W., and Vorp, D. A. (2001). Mechanical properties and microstructure of intraluminal thrombus from abdominal aortic aneurysm. *J Biomech Eng*, 123(6):536–9.

Weisbecker, H., Pierce, D. M., Regitnig, P., and Holzapfel, G. A. (2012). Layer-specific damage experiments and modeling of human thoracic and abdominal aortas with non-atherosclerotic intimal thickening. *J Mech Behav Biomed Mater*, 12:93–106.

Xenos, M., Rambhia, S. H., Alemu, Y., Einav, S., Labropoulos, N., Tassiopoulos, A., Ricotta, J. J., and Bluestein, D. (2010). Patient-specific abdominal aortic aneurysm rupture risk prediction with fluid structure interaction modeling. *Ann Biomed Eng*, 38(11):3323–37.

List of Figures

List of Tables

Appendix A

Python scripts to generate stent-graft models

To generate bodies (valid only for models TFFB-22-82-ZT to TFFB-32-140-ZT) just go to the very last line of code in the script and replace the function arguments *mainBodyLength* and *mainBodyDiameter* by appropriate (floating) values. Possible values for *mainBodyLength* are 82.0, 96.0, 111.0, 125.0 and 140.0. Possible values for *mainBodyDiameter* are 22.0, 24.0, 26.0, 28.0, 30.0 and 32.0.

```
f_bodyStentGraftGeneration(mainBodyLength, mainBodyDiameter)
```

To generate legs (valid only for models ZSLE-9-39-ZT to ZSLE-24-90-ZT) just go to the very last line of code in the script and replace the first two function arguments *DistalIliacLegDiameter* and *workingLengthOfIliacLeg* by appropriate (floating) values. The third argument *'side'* will indicate if this is the left (contralateral) of right (ipsilateral) leg, so type 'left' or 'right' for instance (quotes must be typed). Finally, the argument *angle* provides the option to rotate the stent-graft around its vertical axis (0.0° by default). *Angle* should ideally be a real number. Possible values for *DistalIliacLegDiameter* are 9.0, 11.0, 13.0, 16.0, 20.0 and 24.0. Possible values for *workingLengthOfIliacLeg* are 39.0, 56.0, 74.0, 90.0, 107.0 and 122.0.

```
f_legStentGraftGeneration(DistalIliacLegDiameter, workingLengthOfIliacLeg,
'side', angle)
```

Both scripts can be run either graphically from Abaqus GUI (File > Run Script), or via a command line (Abaqus Command window) by typing *abaqus cae noGUI=scriptName.py*.

The latter option is far more efficient for long tasks, though the difference is not perceptible while using these scripts.

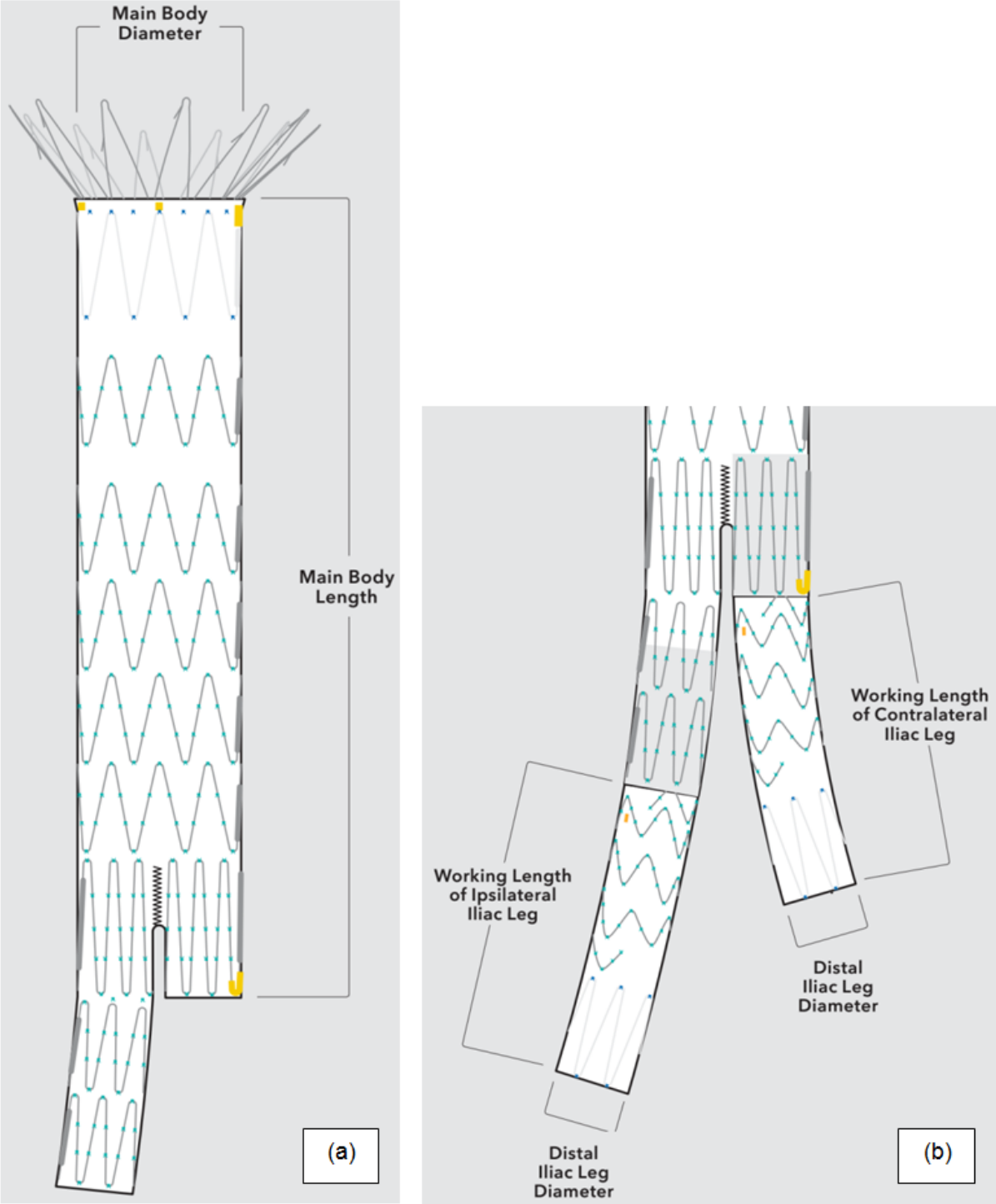

Figure A.1: Parameters needed for automatic SG generation. (a) For bodies. (b) For legs.

Appendix B

Optimal sequence of AAA geometries cleaning, closing and smoothing operations in Meshlab

After all unwanted and unrealistic vascular features (facets and associated points) are manually removed, the following sequence of operations is to be executed

Filter Tab > **Normals, Curvature and Orientation**

Transform: Scale (apply a factor 1000 to convert into mm)

Filter Tab > **Cleaning and Repairing**

Merge Close Vertices (*perc on* = 40)

Remove Duplicate Faces

Remove Duplicate Vertex

Remove Unreferenced Vertex

Remove Zero Area Faces

Select non Manifold Edges (then select the "delete the current set of selected faces and all the vertices surrounded by these faces" icon)

Select non Manifold Vertices (then select the "delete the current set of selected vertices; faces that share one of the deleted vertices are deleted too" icon)

"Fill Hole" icon (Select every hole > Trivial > Fill > Accept)

Filter Tab > **Smoothing, Fairing and Deformation**

Taubin Smooth (10 Smoothing steps)

Optionally: Filter Tab > **Cleaning and Repairing**

Remove Duplicate Faces

Remove Duplicate Vertex
Remove Unreferenced Vertex
Remove Zero Area Faces

Note 1: to extract the centerlines from a AAA "zero pressure geometry" loaded by blood pressure, the best option is to prepare the AAA outer wall as a continuous mesh with the above method. Even if an ILT is present, the resulting centerline should be accurate enough for our purposes (collagen fiber orientation, catheter initial positioning prior to deployment simulation). If for any reason, such AAA outer wall surface comes as a patchwork of several pieces, the latter need to be previously merged in Meshlab by means of the following

Filter Tab > Mesh Layer
Flatten Visible Layers

Regarding centerlines extraction, it is worthy of mention that AAA walls partitioned into several pieces may not work well, and it is strongly advised to rather use continuous closed surfaces (preferably without including ILT).

Note 2: the above indicated closing option from Meshlab should be used preferentially, however this tool might fail on occasions and an alternative solution is

Filter Tab > Remeshing, Simplification and Reconstruction
Close Holes (provide the maximum hole dimension in mm)

Both techniques can also be combined, which is very case specific. Ideally, the former ("Fill Hole" icon) should eventually return the following message "Mesh has no hole to edit.", otherwise the manifold edges and vertices must be selected and deleted anew several times (up to three loops might be required) until getting this message.

Note 3: for the VMTKCenterlines module to work properly (option *-endpoints 1*), there must be enough points/vertices on each proximal and distal sections so the selected points are truly on the centerline as opposed to near the wall. If Taubin's smooting algorithm does not provide such points then one can resort to the following (*only for the facets located on or near the concerned section*)

Filter Tab > Remeshing, Simplification and Reconstruction

Subdivision Surfaces: Midpoint (use default parameters)

The "Midpoint" remeshing usually does not perform well if applied on the whole geometry.

Note 4: face normals have to be oriented outward so Abaqus can latter create volumes based on lumen and ILT envelopes. Meshlab fulfills this requirement by default, but sometimes a single or a few facets may point inward, and the corrective operation is

Filter Tab > Normals, Curvature and Orientation

Re-Orient all faces coherently

Note 5: once the lumen and ILT meshes are cleaned and well prepared following the above guidelines, they should be exported from Meshlab with the format extension .ply which provides a better data organization (ordered list of point coordinates, followed by an ordered list of facet connectivity with the points).

Appendix C

Optimal sequence of VMTK commands to extract centerlines

The following VMTK script is to be typed in the upper window of the PypePad application (in Windows operating system). The input file *Input-Geometry.stl* must have a stereolithography (stl) format, which eventually generates the output file *Output-Centerlines.dat*. The location of both files can be specified (C:/Temp in this case).

```
vmtksurfacereader -ifile C:/Temp/Input-Geometry.stl --pipe vmtkcenterlines
-endpoints 1 --pipe vmtkcenterlineresampling -length 0.1 --pipe
vmtkcenterlinesmoothing --pipe vmtkbranchextractor --pipe vmtkbranchclipper
--pipe vmtkrenderer --pipe vmtksurfaceviewer -opacity 0.25 --pipe
vmtkcenterlineviewer -cellarray GroupIds --pipe vmtksurfacewriter -i
@vmtkbranchextractor.o -ofile C:/Temp/Output-Centerlines.dat
```

To execute this script select Run > Run all.

The "endpoint" option, ensuring a continuous centerline definition up to end sections, obviously works better if a point that is close to the actual centerline can be selected at each end section, hence the need to have enough points on these sections (Figure C.1).

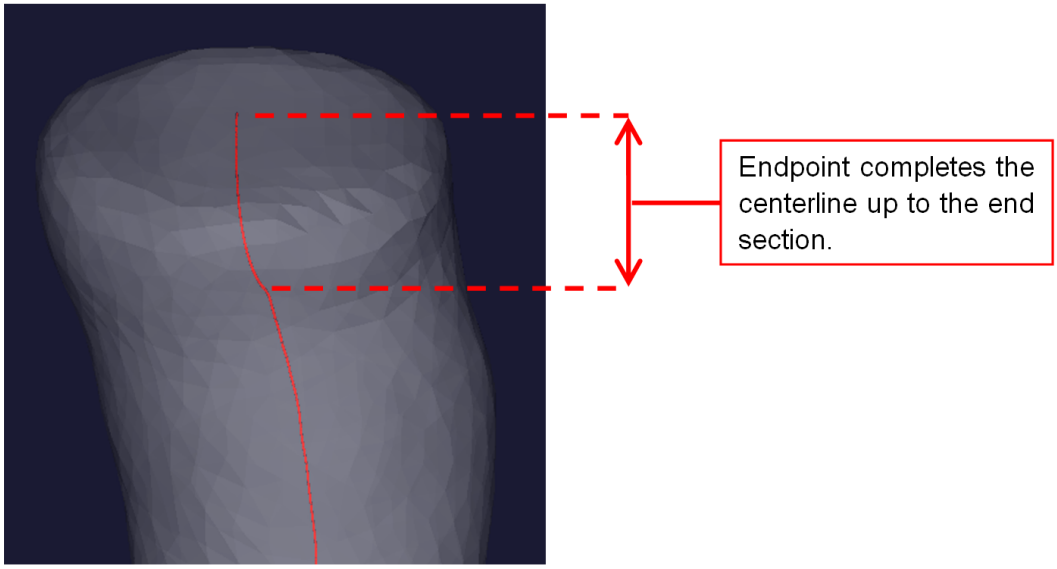

Figure C.1: Purpose of the VMTK option Endpoint for centerline extraction.

Note 1: if the .stl file defining a vascular geometry comes from an existing finite element mesh built in Abaqus, thus having open end sections (clear cuts made with Abaqus' tools), it can be imported as is into VMTK. In this case, there is no need to close the end sections, and the centerlines are well defined anyway.

Note 2: if the centerlines look too noisy, the option to further smooth them is adding the following arguments after *vmtkcenterlinesmoothing*

-factor x
where x has a default value of 0.1, and a value of 1.5 would greatly improve the centerline.

-iterations y
where y has a default value of 100, and a value of 150 might improve the centerlines, but not as efficiently as with -factor x.

Note 3: for the scripts to perform well, and as a convention, the curvilinear length of the proximal centerline should be longer than 80 mm (from the very proximal section down to the most distant renal artery ostium). This is depicted in Figure C.2.

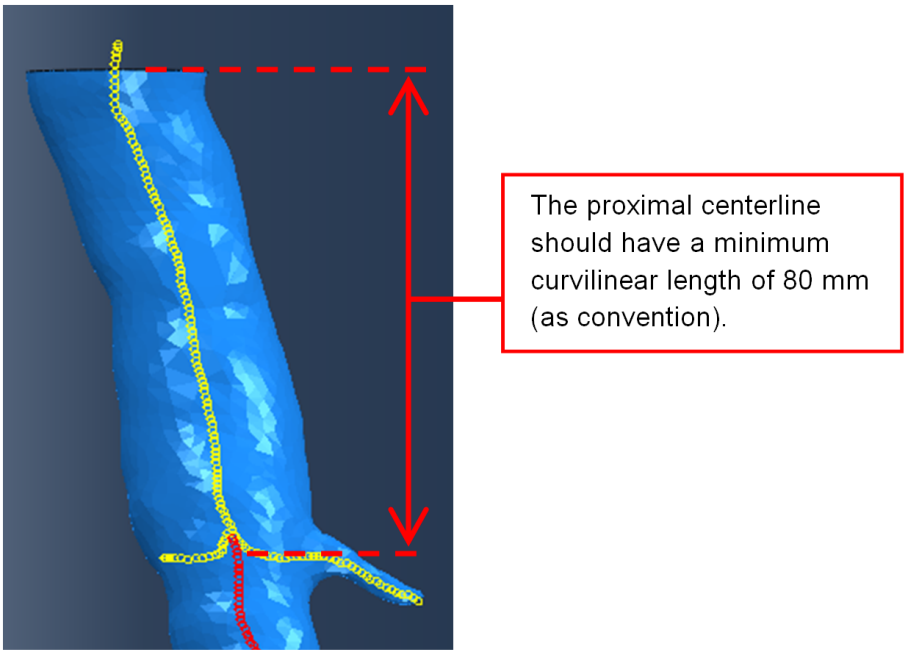

Figure C.2: Minimal distance for the proximal centerline.

Appendix D

Explicit expressions of U, S_θ and S_z for the HGO model

$$U = C_{10}\left(\lambda_\theta^2+\lambda_z^2+\frac{1}{\lambda_\theta^2\lambda_z^2}-3\right) + \frac{k_1}{k_2}\left\{\exp\left[k_2\left(\kappa\left(\lambda_\theta^2+\lambda_z^2+\frac{1}{\lambda_\theta^2\lambda_z^2}\right)+(1-3\kappa)\left(c^2\lambda_\theta^2+\left(1-c^2\right)\lambda_z^2\right)-1\right)^2\right]-1\right\} \tag{D.1}$$

$$S_\theta = 2C_{10}\left(\lambda_\theta-\frac{1}{\lambda_\theta^3\lambda_z^2}\right) + 2k_1\left[\kappa\left(\lambda_\theta^2+\lambda_z^2+\frac{1}{\lambda_\theta^2\lambda_z^2}\right)+(1-3\kappa)\left(c^2\lambda_\theta^2+\left(1-c^2\right)\lambda_z^2\right)-1\right]\left[2\kappa\left(\lambda_\theta-\frac{1}{\lambda_\theta^3\lambda_z^2}\right) + 2c^2(1-3\kappa)\lambda_\theta\right]\exp\left[k_2\left(\kappa\left(\lambda_\theta^2+\lambda_z^2+\frac{1}{\lambda_\theta^2\lambda_z^2}\right)+(1-3\kappa)\left(c^2\lambda_\theta^2+\left(1-c^2\right)\lambda_z^2\right)-1\right)^2\right] \tag{D.2}$$

$$S_z = 2C_{10}\left(\lambda_z-\frac{1}{\lambda_z^3\lambda_\theta^2}\right) + 2k_1\left[\kappa\left(\lambda_\theta^2+\lambda_z^2+\frac{1}{\lambda_\theta^2\lambda_z^2}\right)+(1-3\kappa)\left(c^2\lambda_\theta^2+\left(1-c^2\right)\lambda_z^2\right)-1\right]\left[2\kappa\left(\lambda_z-\frac{1}{\lambda_z^3\lambda_\theta^2}\right)+2\left(1-c^2\right)(1-3\kappa)\lambda_z\right]\exp\left[k_2\left(\kappa\left(\lambda_\theta^2+\lambda_z^2+\frac{1}{\lambda_\theta^2\lambda_z^2}\right)+(1-3\kappa)\left(c^2\lambda_\theta^2+\left(1-c^2\right)\lambda_z^2\right)-1\right)^2\right] \tag{D.3}$$

Appendix E

Contact controls applied during SG deployment

To further improve the contacts and make sure all grafts were fully deployed, some additional contact controls were attributed to each new definition of *general contact*. These controls were applied to surface entities undergoing very large deformations (AAA wall, grafts & sheaths), and are described below.

1. When compressing both leg SG:

```
*CONTACT CONTROLS ASSIGNMENT, TYPE=FOLD INVERSION CHECK
AAA-Inner-Face
*CONTACT CONTROLS ASSIGNMENT, TYPE=FOLD INVERSION CHECK
Body-Graft
*CONTACT CONTROLS ASSIGNMENT, TYPE=FOLD INVERSION CHECK
Body-Sheath
*CONTACT CONTROLS ASSIGNMENT, TYPE=FOLD INVERSION CHECK
L-Leg-Graft
*CONTACT CONTROLS ASSIGNMENT, TYPE=FOLD INVERSION CHECK
R-Leg-Graft
*CONTACT CONTROLS ASSIGNMENT, TYPE=FOLD INVERSION CHECK
Sheath-Body-Leg-L
*CONTACT CONTROLS ASSIGNMENT, TYPE=FOLD INVERSION CHECK
Sheath-Body-Leg-R
*CONTACT CONTROLS ASSIGNMENT, TYPE=FOLD INVERSION CHECK
Sheath-Leg-L
```

```
*CONTACT CONTROLS ASSIGNMENT, TYPE=FOLD INVERSION CHECK
Sheath-Body-Leg-R
*CONTACT CONTROLS ASSIGNMENT, TYPE=ENHANCED EDGE TRACKING
```

2. When removing the sheaths:

```
*CONTACT CONTROLS ASSIGNMENT, TYPE=FOLD INVERSION CHECK
AAA-Inner-Face
*CONTACT CONTROLS ASSIGNMENT, TYPE=FOLD INVERSION CHECK
Body-Graft
*CONTACT CONTROLS ASSIGNMENT, TYPE=FOLD INVERSION CHECK
Body-Sheath
*CONTACT CONTROLS ASSIGNMENT, TYPE=FOLD INVERSION CHECK
L-Leg-Graft
*CONTACT CONTROLS ASSIGNMENT, TYPE=FOLD INVERSION CHECK
R-Leg-Graft
*CONTACT CONTROLS ASSIGNMENT, TYPE=FOLD INVERSION CHECK
Sheath-Body-Leg-L
*CONTACT CONTROLS ASSIGNMENT, TYPE=FOLD INVERSION CHECK
Sheath-Body-Leg-R
*CONTACT CONTROLS ASSIGNMENT, TYPE=ENHANCED EDGE TRACKING
```

3. At final equilibrium:

```
*CONTACT CONTROLS ASSIGNMENT, TYPE=FOLD INVERSION CHECK
AAA-Inner-Face
*CONTACT CONTROLS ASSIGNMENT, TYPE=FOLD INVERSION CHECK
Body-Graft
*CONTACT CONTROLS ASSIGNMENT, TYPE=FOLD INVERSION CHECK
L-Leg-Graft
*CONTACT CONTROLS ASSIGNMENT, TYPE=FOLD INVERSION CHECK
R-Leg-Graft
*CONTACT CONTROLS ASSIGNMENT, TYPE=ENHANCED EDGE TRACKING
```

Appendix F

Installation of the EVARSim application and plug-in in Abaqus

This installation procedure is valid in Windows OS only. First of all, the EVARSim icon must be created on the desktop

1. Copy the following files in C:\temp
   EVARSim_App.py
   EVARSim_MainWindow.py
   EVARSim_MenuToolSet.py
   ___init___.py
   EVAR-SIM_Icon.ico

2. Right click on the destop > New > Shortcut > enter *C:\temp* as location > enter *EVARSim* as name > Finish

3. Right click on the shortcut > Properties > enter
   C:\SIMULIA\Abaqus\Commands\abaqus.bat cae -custom EVARSim_App noStartupDialog as target > enter *C:\temp* as start in > OK

4. Right click on the shortcut > Properties > Change Icon > Browse > select *EVAR-SIM_Icon.ico*

5. Copy the following files and directories in *C:\SIMULIA\Abaqus\6.10-1\abaqus_plugins*
   EVARSim_Step1_plugin.py
   EVARSim_Step2_plugin.py
   EVARSim_Step3_plugin.py

abq_EVARSim_S1
abq_EVARSim_S2
abq_EVARSim_S3

the EVARSim icon is then active, and both the application and plug-in can be used.

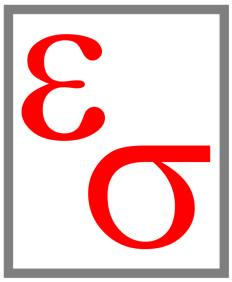

Figure F.1: EVARSim icon.

The plug-in can also be used from a classic Abaqus CAE graphic interface in parallel.

Appendix G

Mechanical properties of polyurethane

This material has the following reference *rencast 6400-1 (supplier: Huntsman)*, and was prepared as a mixture of a resine (10 volumes) and polyurethane powder (1 volume). The specimen samples were designed as per norm ISO 527-1 (or ASTM D638), and were fixed with sandpaper and cyanoacrylate glue.

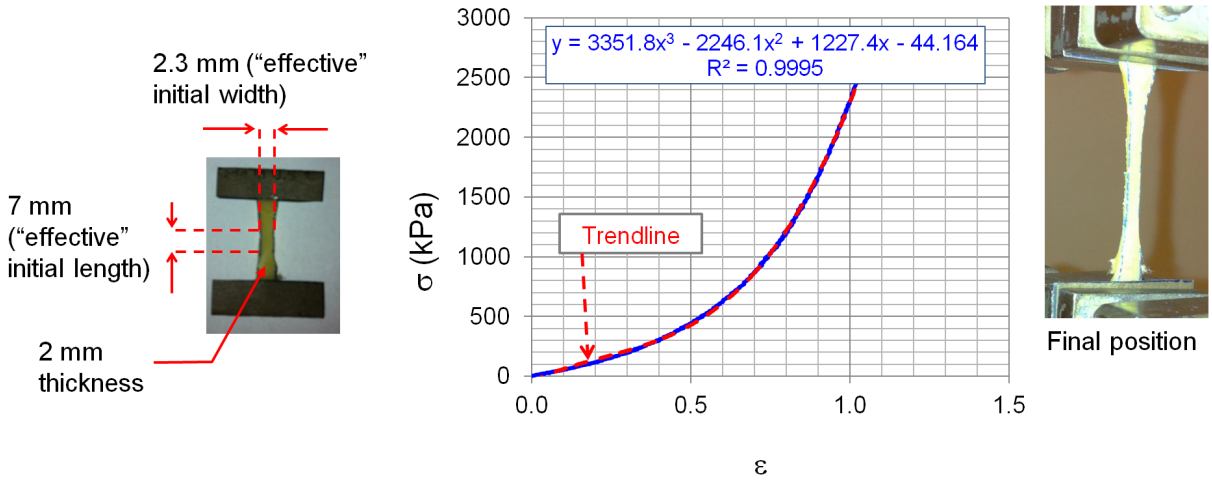

Figure G.1: True stress-strain curve for polyurethane.

This corresponded to a maximal stretch of 12.8 mm and a related force of 1.5 N.

A density of $1.18 \times 10^{-6}\,\mathrm{kg\,mm^{-3}}$ was found from *www.matweb.com* (consulted on 2014-06-14) under "Polyurethane Blend".

Appendix H

Mechanical properties of "TangoBlackPlus Shore A40"

This material is specific from the company *Proto3000*. A simple soft phantom was printed in 3D (Figure H.1).

Figure H.1: Simple vascular phantom made of TangoBlackPlus Shore A40 material.

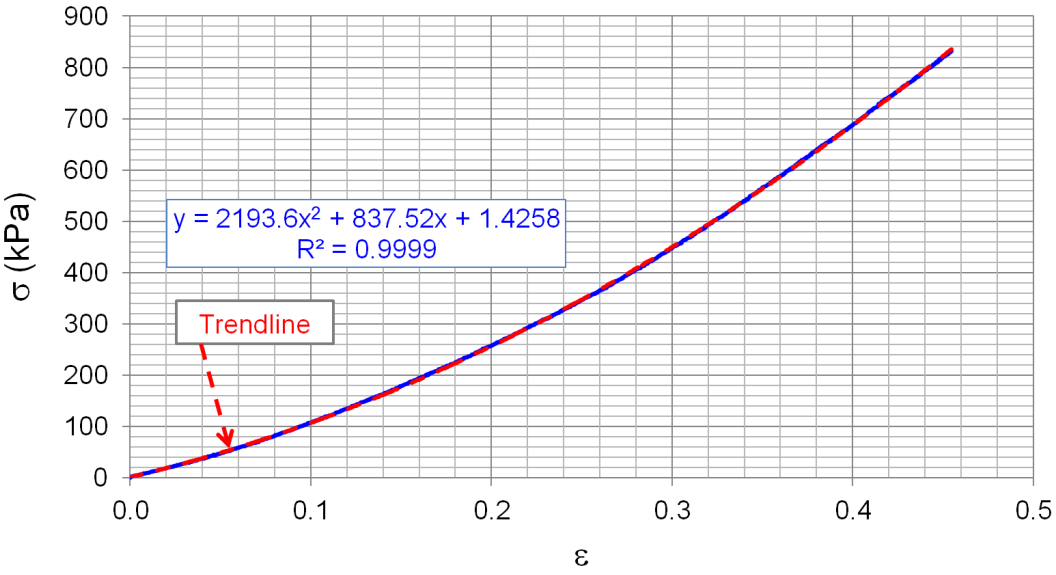

Figure H.2: True stress-strain curve for TangoBlackPlus Shore A40.

Appendix I

Mechanical properties to model the graft with a "Fabric"

In this project the graft was optimally modeled with a "Lamina" formulation. But for the sake of completeness, equivalent material properties are provided here for an implementation with the "Fabric" formulation from Abaqus. Both provide the same results. The Lamina formulation was preferred because it offered control on more material parameters, which appeared more physically sound.

```
*Material, name=Graft
*Density
 6.35e-06,
*FABRIC
*UNIAXIAL, COMPONENT=1
*LOADING DATA, DIRECTION=TENSION,
TYPE=ELASTIC
0.00E+00, 0.00
4.02E+06, 1.00E+00
*LOADING DATA, DIRECTION=COMPRESSION,
TYPE=ELASTIC
0.00E+00, 0.00
4.02E+06, 1.00E+00
*UNIAXIAL, COMPONENT=2
*LOADING DATA, DIRECTION=TENSION,
TYPE=ELASTIC
0.00E+00, 0.00
```

```
1.65E+06, 1.00E+00
*LOADING DATA, DIRECTION=COMPRESSION,
TYPE=ELASTIC
0.00E+00, 0.00
1.65E+06, 1.00E+00
*UNIAXIAL, COMPONENT=SHEAR
*LOADING DATA, DIRECTION=TENSION,
TYPE=ELASTIC
0.00,      0.00
1.17E+02,  1.00E-2
*LOADING DATA, DIRECTION=COMPRESSION,
TYPE=ELASTIC
0.00,      0.00
1.17E+02,  1.00E-2
```

Appendix J

Executing analyses on supercomputers from "Compute Canada"

After an account with Compute Canada is set, a SSH connection must be installed (the application Bitvise is recommended to do so in Windows). Once an Abaqus input file is ready, say input.inp, it must be placed into a sub-directory (named test-1 hereafter) in the local SCRATCH directory, along with a script (named script.sh hereafter) that typically contains the following lines

```
#!/bin/bash
#PBS -l walltime=168:00:00
#PBS -l nodes=1:ppn=6
#PBS -r n

module load intel-compilers/12.0.4.191
module load MPI/Intel/openmpi/1.6.5

cd $SCRATCH/test-1
# mpiexec /chemin/vers/mon/programme_mpi

module load ABAQUS
abaqus job=input cpus=6 interactive
```

where *walltime=168:00:00* stands for the maximum number of hours allowed for analysis, and *ppn=6* represents the number of CPUs.

To actually start a job, one simply has to type *qsub script.sh* (and *qdel job-ID* to kill it).

More explanations can be found on this web site
https://wiki.calculquebec.ca/w/Exécuter_une_tâche/en.

Appendix K

Permissions to reproduce figures

Hereafter are presented the required permissions to reproduce figures from “limited access” articles.

Copyright Clearance Center RightsLink®

Home | Account Info | Help | Live Chat

Title: Computational comparison of the bending behavior of aortic stent-grafts

Publication: Journal of the Mechanical Behavior of Biomedical Materials

Publisher: Elsevier

Date: January 2012

Logged in as:
David Roy
Account #:
3000349031

LOGOUT

Order Completed

Thank you very much for your order.

This is a License Agreement between David DR Roy ("You") and Elsevier ("Elsevier"). The license consists of your order details, the terms and conditions provided by Elsevier, and the payment terms and conditions.

Get the printable license.

License Number	3536501456818
License date	Dec 26, 2014
Licensed content publisher	Elsevier
Licensed content publication	Journal of the Mechanical Behavior of Biomedical Materials
Licensed content title	Computational comparison of the bending behavior of aortic stent-grafts
Licensed content author	None
Licensed content date	January 2012
Licensed content volume number	5
Licensed content issue number	1
Number of pages	11
Type of Use	reuse in a thesis/dissertation
Portion	figures/tables/illustrations
Number of figures/tables /illustrations	1
Format	electronic
Are you the author of this Elsevier article?	No
Will you be translating?	No
Original figure numbers	9
Title of your thesis/dissertation	Mechanical Simulation of the Endovascular Repair of Abdominal Aortic Aneurysms
Expected completion date	Dec 2014
Estimated size (number of pages)	200
Elsevier VAT number	GB 494 6272 12
Permissions price	0.00 USD
VAT/Local Sales Tax	0.00 USD / 0.00 GBP
Total	0.00 USD

Figure K.1: Permission to reproduce Figure 6.

Copyright Clearance Center RightsLink®

Home | Account Info | Help | Live Chat

Springer
the language of science

Title: Severe Bending of Two Aortic Stent-Grafts: An Experimental and Numerical Mechanical Analysis
Author: Nicolas Demanget
Publication: Annals of Biomedical Engineering
Publisher: Springer
Date: Jan 1, 2012
Copyright © 2012, Biomedical Engineering Society

Logged in as:
David Roy
Account #:
3000349031
LOGOUT

Order Completed

Thank you very much for your order.

This is a License Agreement between David DR Roy ("You") and Springer ("Springer"). The license consists of your order details, the terms and conditions provided by Springer, and the payment terms and conditions.

Get the printable license.

License Number	3536521383772
License date	Dec 26, 2014
Licensed content publisher	Springer
Licensed content publication	Annals of Biomedical Engineering
Licensed content title	Severe Bending of Two Aortic Stent-Grafts: An Experimental and Numerical Mechanical Analysis
Licensed content author	Nicolas Demanget
Licensed content date	Jan 1, 2012
Volume number	40
Issue number	12
Type of Use	Thesis/Dissertation
Portion	Figures
Author of this Springer article	No
Original figure numbers	8
Title of your thesis / dissertation	Mechanical Simulation of the Endovascular Repair of Abdominal Aortic Aneurysms
Expected completion date	Dec 2014
Estimated size(pages)	200
Total	0.00 USD

Figure K.2: Permission to reproduce Figure 7.

Copyright Clearance Center RightsLink®

Home | Account Info | Help | Live Chat

Title: Computational comparison of the bending behavior of aortic stent-grafts

Publication: Journal of the Mechanical Behavior of Biomedical Materials

Publisher: Elsevier

Date: January 2012

Logged in as:
David Roy
Account #:
3000349031

LOGOUT

Order Completed

Thank you very much for your order.

This is a License Agreement between David DR Roy ("You") and Elsevier ("Elsevier"). The license consists of your order details, the terms and conditions provided by Elsevier, and the payment terms and conditions.

Get the printable license.

License Number	3536681108803
License date	Dec 26, 2014
Licensed content publisher	Elsevier
Licensed content publication	Journal of the Mechanical Behavior of Biomedical Materials
Licensed content title	Computational comparison of the bending behavior of aortic stent-grafts
Licensed content author	None
Licensed content date	January 2012
Licensed content volume number	5
Licensed content issue number	1
Number of pages	11
Type of Use	reuse in a thesis/dissertation
Portion	figures/tables/illustrations
Number of figures/tables/illustrations	1
Format	electronic
Are you the author of this Elsevier article?	No
Will you be translating?	No
Original figure numbers	6
Title of your thesis/dissertation	Mechanical Simulation of the Endovascular Repair of Abdominal Aortic Aneurysms
Expected completion date	Dec 2014
Estimated size (number of pages)	200
Elsevier VAT number	GB 494 6272 12
Permissions price	0.00 USD
VAT/Local Sales Tax	0.00 USD / 0.00 GBP
Total	0.00 USD

Figure K.3: Permission to reproduce Figure 9.

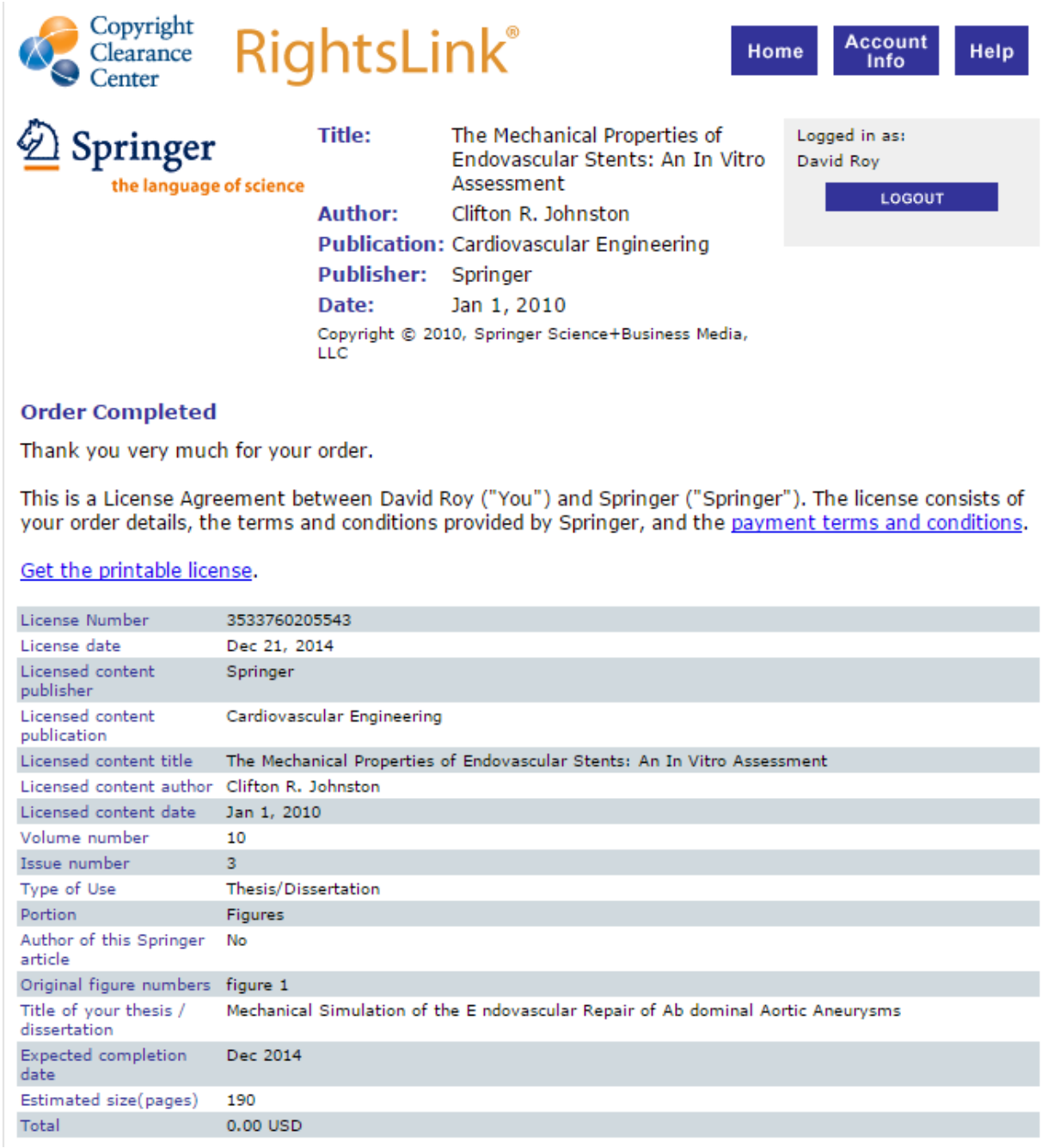

Copyright Clearance Center RightsLink®

Home | Account Info | Help

Springer the language of science

Title: The Mechanical Properties of Endovascular Stents: An In Vitro Assessment
Author: Clifton R. Johnston
Publication: Cardiovascular Engineering
Publisher: Springer
Date: Jan 1, 2010
Copyright © 2010, Springer Science+Business Media, LLC

Logged in as:
David Roy
LOGOUT

Order Completed

Thank you very much for your order.

This is a License Agreement between David Roy ("You") and Springer ("Springer"). The license consists of your order details, the terms and conditions provided by Springer, and the payment terms and conditions.

Get the printable license.

License Number	3533760205543
License date	Dec 21, 2014
Licensed content publisher	Springer
Licensed content publication	Cardiovascular Engineering
Licensed content title	The Mechanical Properties of Endovascular Stents: An In Vitro Assessment
Licensed content author	Clifton R. Johnston
Licensed content date	Jan 1, 2010
Volume number	10
Issue number	3
Type of Use	Thesis/Dissertation
Portion	Figures
Author of this Springer article	No
Original figure numbers	figure 1
Title of your thesis / dissertation	Mechanical Simulation of the E ndovascular Repair of Ab dominal Aortic Aneurysms
Expected completion date	Dec 2014
Estimated size(pages)	190
Total	0.00 USD

Figure K.4: Permission to reproduce Figure 1.15.

Copyright Clearance Center RightsLink®

Home | Account Info | Help

Springer
the language of science

Title:	Severe Bending of Two Aortic Stent-Grafts: An Experimental and Numerical Mechanical Analysis
Author:	Nicolas Demanget
Publication:	Annals of Biomedical Engineering
Publisher:	Springer
Date:	Jan 1, 2012

Copyright © 2012, Biomedical Engineering Society

Logged in as:
David Roy
Account #:
3000349031
LOGOUT

Order Completed

Thank you very much for your order.

This is a License Agreement between David DR Roy ("You") and Springer ("Springer"). The license consists of your order details, the terms and conditions provided by Springer, and the payment terms and conditions.

Get the printable license.

License Number	3376070474218
License date	Apr 25, 2014
Licensed content publisher	Springer
Licensed content publication	Annals of Biomedical Engineering
Licensed content title	Severe Bending of Two Aortic Stent-Grafts: An Experimental and Numerical Mechanical Analysis
Licensed content author	Nicolas Demanget
Licensed content date	Jan 1, 2012
Volume number	40
Issue number	12
Type of Use	Thesis/Dissertation
Portion	Figures
Author of this Springer article	No
Original figure numbers	figure 5
Title of your thesis / dissertation	Mechanical Simulation of the Endovascular Repair of Abdominal Aortic Aneurysms
Expected completion date	Dec 2014
Estimated size(pages)	200
Total	0.00 USD

Figure K.5: Permission to reproduce Figure 2.5.

Copyright Clearance Center RightsLink®

Home | Account Info | Help

Title: A New Constitutive Framework for Arterial Wall Mechanics and a Comparative Study of Material Models
Author: Gerhard A. Holzapfel
Publication: Journal of Elasticity
Publisher: Springer
Date: Jan 1, 2000

Logged in as:
David Roy
Account #:
3000349031
LOGOUT

Order Completed

Thank you very much for your order.

This is a License Agreement between David DR Roy ("You") and Springer ("Springer"). The license consists of your order details, the terms and conditions provided by Springer, and the payment terms and conditions.

Get the printable license.

License Number	3376090550490
License date	Apr 25, 2014
Licensed content publisher	Springer
Licensed content publication	Journal of Elasticity
Licensed content title	A New Constitutive Framework for Arterial Wall Mechanics and a Comparative Study of Material Models
Licensed content author	Gerhard A. Holzapfel
Licensed content date	Jan 1, 2000
Volume number	61
Issue number	1
Type of Use	Thesis/Dissertation
Portion	Figures
Author of this Springer article	No
Original figure numbers	figure 1
Title of your thesis / dissertation	Mechanical Simulation of the Endovascular Repair of Abdominal Aortic Aneurysms
Expected completion date	Dec 2014
Estimated size(pages)	200
Total	0.00 USD

Figure K.6: Permission to reproduce Figure 3.1.

Copyright Clearance Center RightsLink®

Home | Account Info | Help

Title: The effects of aneurysm on the biaxial mechanical behavior of human abdominal aorta
Author: Jonathan P. Vande Geest,Michael S. Sacks,David A. Vorp
Publication: Journal of Biomechanics
Publisher: Elsevier
Date: 2006
Copyright © 2006, Elsevier

Logged in as:
David Roy
Account #:
3000349031
LOGOUT

Order Completed

Thank you very much for your order.

This is a License Agreement between David DR Roy ("You") and Elsevier ("Elsevier"). The license consists of your order details, the terms and conditions provided by Elsevier, and the payment terms and conditions.

Get the printable license.

License Number	3376100203588
License date	Apr 25, 2014
Licensed content publisher	Elsevier
Licensed content publication	Journal of Biomechanics
Licensed content title	The effects of aneurysm on the biaxial mechanical behavior of human abdominal aorta
Licensed content author	Jonathan P. Vande Geest,Michael S. Sacks,David A. Vorp
Licensed content date	2006
Licensed content volume number	39
Licensed content issue number	7
Number of pages	11
Type of Use	reuse in a thesis/dissertation
Portion	figures/tables/illustrations
Number of figures/tables/illustrations	1
Format	electronic
Are you the author of this Elsevier article?	No
Will you be translating?	No
Title of your thesis/dissertation	Mechanical Simulation of the Endovascular Repair of Abdominal Aortic Aneurysms
Expected completion date	Dec 2014
Estimated size (number of pages)	200
Elsevier VAT number	GB 494 6272 12
Permissions price	0.00 USD
VAT/Local Sales Tax	0.00 USD / 0.00 GBP
Total	0.00 USD

Figure K.7: Permission to reproduce Figure 3.15.

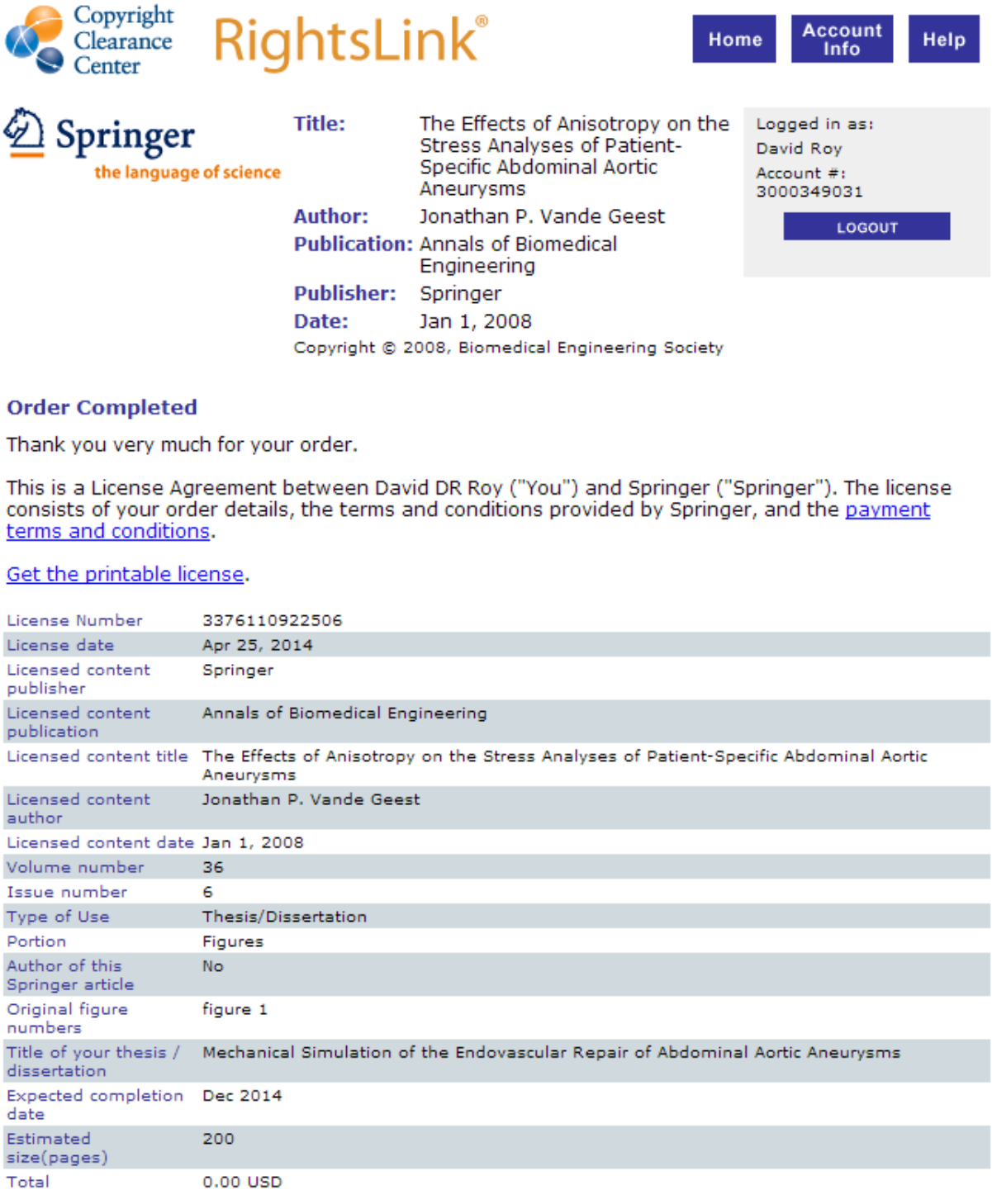

Copyright Clearance Center RightsLink®

Home | Account Info | Help

Springer
the language of science

Title: The Effects of Anisotropy on the Stress Analyses of Patient-Specific Abdominal Aortic Aneurysms
Author: Jonathan P. Vande Geest
Publication: Annals of Biomedical Engineering
Publisher: Springer
Date: Jan 1, 2008
Copyright © 2008, Biomedical Engineering Society

Logged in as:
David Roy
Account #:
3000349031
LOGOUT

Order Completed

Thank you very much for your order.

This is a License Agreement between David DR Roy ("You") and Springer ("Springer"). The license consists of your order details, the terms and conditions provided by Springer, and the payment terms and conditions.

Get the printable license.

License Number	3376110922506
License date	Apr 25, 2014
Licensed content publisher	Springer
Licensed content publication	Annals of Biomedical Engineering
Licensed content title	The Effects of Anisotropy on the Stress Analyses of Patient-Specific Abdominal Aortic Aneurysms
Licensed content author	Jonathan P. Vande Geest
Licensed content date	Jan 1, 2008
Volume number	36
Issue number	6
Type of Use	Thesis/Dissertation
Portion	Figures
Author of this Springer article	No
Original figure numbers	figure 1
Title of your thesis / dissertation	Mechanical Simulation of the Endovascular Repair of Abdominal Aortic Aneurysms
Expected completion date	Dec 2014
Estimated size(pages)	200
Total	0.00 USD

Figure K.8: Permission to reproduce Figures 3.17 and 3.25.

Copyright Clearance Center RightsLink®

Home | Account Info | Help

Springer
the language of science

Title: A Novel Simulation Strategy for Stent Insertion and Deployment in Curved Coronary Bifurcations: Comparison of Three Drug-Eluting Stents

Author: Peter Mortier

Publication: Annals of Biomedical Engineering

Publisher: Springer

Date: Jan 1, 2009

Logged in as:
David Roy
Account #:
3000349031

LOGOUT

Order Completed

Thank you very much for your order.

This is a License Agreement between David DR Roy ("You") and Springer ("Springer"). The license consists of your order details, the terms and conditions provided by Springer, and the payment terms and conditions.

Get the printable license.

License Number	3376120084675
License date	Apr 25, 2014
Licensed content publisher	Springer
Licensed content publication	Annals of Biomedical Engineering
Licensed content title	A Novel Simulation Strategy for Stent Insertion and Deployment in Curved Coronary Bifurcations: Comparison of Three Drug-Eluting Stents
Licensed content author	Peter Mortier
Licensed content date	Jan 1, 2009
Volume number	38
Issue number	1
Type of Use	Thesis/Dissertation
Portion	Figures
Author of this Springer article	No
Original figure numbers	figure 2
Title of your thesis / dissertation	Mechanical Simulation of the Endovascular Repair of Abdominal Aortic Aneurysms
Expected completion date	Dec 2014
Estimated size(pages)	200
Total	0.00 USD

Figure K.9: Permission to reproduce Figure 3.18(a).

Copyright Clearance Center RightsLink®

Home | Account Info | Help

Springer
the language of science

Title: Layer-Specific 3D Residual Deformations of Human Aortas with Non-Atherosclerotic Intimal Thickening
Author: Gerhard A. Holzapfel
Publication: Annals of Biomedical Engineering
Publisher: Springer
Date: Jan 1, 2007
Copyright © 2007, Biomedical Engineering Society

Logged in as:
David Roy
Account #:
3000349031
LOGOUT

Order Completed

Thank you very much for your order.

This is a License Agreement between David DR Roy ("You") and Springer ("Springer"). The license consists of your order details, the terms and conditions provided by Springer, and the payment terms and conditions.

Get the printable license.

License Number	3376120730922
License date	Apr 25, 2014
Licensed content publisher	Springer
Licensed content publication	Annals of Biomedical Engineering
Licensed content title	Layer-Specific 3D Residual Deformations of Human Aortas with Non-Atherosclerotic Intimal Thickening
Licensed content author	Gerhard A. Holzapfel
Licensed content date	Jan 1, 2007
Volume number	35
Issue number	4
Type of Use	Thesis/Dissertation
Portion	Figures
Author of this Springer article	No
Original figure numbers	figure 7
Title of your thesis / dissertation	Mechanical Simulation of the Endovascular Repair of Abdominal Aortic Aneurysms
Expected completion date	Dec 2014
Estimated size(pages)	200
Total	0.00 USD

Figure K.10: Permission to reproduce Figure 3.18(b).

Copyright Clearance Center RightsLink®

Home | Account Info | Help

Title: Virtual evaluation of stent graft deployment: A validated modeling and simulation study

Author: S. De Bock,F. Iannaccone,G. De Santis,M. De Beule,D. Van Loo,D. Devos,F. Vermassen,P. Segers,B. Verhegghe

Publication: Journal of the Mechanical Behavior of Biomedical Materials

Publisher: Elsevier

Date: September 2012

Logged in as:
David Roy
Account #:
3000349031

LOGOUT

Order Completed

Thank you very much for your order.

This is a License Agreement between David DR Roy ("You") and Elsevier ("Elsevier"). The license consists of your order details, the terms and conditions provided by Elsevier, and the payment terms and conditions.

Get the printable license.

License Number	3376151099155
License date	Apr 25, 2014
Licensed content publisher	Elsevier
Licensed content publication	Journal of the Mechanical Behavior of Biomedical Materials
Licensed content title	Virtual evaluation of stent graft deployment: A validated modeling and simulation study
Licensed content author	S. De Bock,F. Iannaccone,G. De Santis,M. De Beule,D. Van Loo,D. Devos,F. Vermassen,P. Segers,B. Verhegghe
Licensed content date	September 2012
Licensed content volume number	13
Number of pages	11
Type of Use	reuse in a thesis/dissertation
Portion	figures/tables/illustrations
Number of figures/tables/illustrations	1
Format	electronic
Are you the author of this Elsevier article?	No
Will you be translating?	No
Title of your thesis/dissertation	Mechanical Simulation of the Endovascular Repair of Abdominal Aortic Aneurysms
Expected completion date	Dec 2014
Estimated size (number of pages)	200
Elsevier VAT number	GB 494 6272 12
Permissions price	0.00 USD
VAT/Local Sales Tax	0.00 USD / 0.00 GBP
Total	0.00 USD

Figure K.11: Permission to reproduce Figure 3.21.

Copyright Clearance Center RightsLink®

Home | Account Info | Help

Springer the language of science

Title: Ex vivo biomechanical behavior of abdominal aortic aneurysm: Assessment using a new mathematical model
Author: M. L. Raghavan
Publication: Annals of Biomedical Engineering
Publisher: Springer
Date: Jan 1, 1996
Copyright © 1996, Biomedical Engineering Society

Logged in as:
David Roy
Account #:
3000349031
LOGOUT

Order Completed

Thank you very much for your order.

This is a License Agreement between David DR Roy ("You") and Springer ("Springer"). The license consists of your order details, the terms and conditions provided by Springer, and the payment terms and conditions.

Get the printable license.

License Number	3376101225917
License date	Apr 25, 2014
Licensed content publisher	Springer
Licensed content publication	Annals of Biomedical Engineering
Licensed content title	Ex vivo biomechanical behavior of abdominal aortic aneurysm: Assessment using a new mathematical model
Licensed content author	M. L. Raghavan
Licensed content date	Jan 1, 1996
Volume number	24
Issue number	5
Type of Use	Thesis/Dissertation
Portion	Figures
Author of this Springer article	No
Original figure numbers	figures 4 and 5
Title of your thesis / dissertation	Mechanical Simulation of the Endovascular Repair of Abdominal Aortic Aneurysms
Expected completion date	Dec 2014
Estimated size(pages)	200
Total	0.00 USD

Figure K.12: Permission to reproduce Figure 5.1.